

LBNO-DEMO

Large-scale neutrino detector demonstrators for phased performance assessment in view of a long-baseline oscillation experiment

The LBNO-DEMO (WA105) Collaboration

I. De Bonis, P. Del Amo Sanchez, D. Duchesneau, and H. Pessard
LAPP, Université de Savoie, CNRS/IN2P3, Annecy-le-Vieux, France

S. Bordoni, M. Ieva, T. Lux, and F. Sanchez
Institut de Fisica d'Altes Energies (IFAE), Bellaterra (Barcelona), Spain

A. Jipa, I. Lazanu, M. Calin, T. Esanu, O. Ristea, C. Ristea, and L. Nita
Faculty of Physics, University of Bucharest, Bucharest, Romania

I. Efthymiopoulos and M. Nessi
CERN, Geneva, Switzerland

R. Asfandiyarov, A. Blondel, A. Bravar, F. Cadoux, A. Haesler, Y. Karadzhov,
A. Korzenev, C. Martin, E. Noah, M. Ravonel, M. Rayner, and E. Scantamburlo
University of Geneva, Section de Physique, DPNC, Geneva, Switzerland

R. Bayes and F.J.P. Soler
University of Glasgow, Glasgow, United Kingdom

G.A. Nuijten
Rockplan Ltd., Helsinki, Finland

K. Loo, J. Maalampi, M. Slupecki, and W.H. Trzaska
Department of Physics, University of Jyväskylä, Finland

M. Campanelli

Dept. of Physics and Astronomy, University College London, London, United Kingdom

A.M. Blebea-Apostu, D. Chesneanu, M.C Gomoiu, B. Mitrica, R.M. Margineanu, and D.L. Stanca

**Horia Hulubei National Institute of R&D for Physics
and Nuclear Engineering - IFIN-HH, Magurele, Romania**

N. Colino, I. Gil-Botella, P. Novella, C. Palomares, R. Santorelli, and A. Verdugo

**Centro de Investigaciones Energéticas, Medioambientales
y Tecnológicas (CIEMAT), Madrid, Spain**

I. Karpikov, A. Khotjantsev, Y. Kudenko, A. Mefodiev, O. Mineev, T. Ovsianikova, and N. Yershov

Institute for Nuclear Research of the Russian Academy of Sciences, Moscow, Russia

T. Enqvist and P. Kuusiniemi

University of Oulu, Oulu, Finland

C. De La Taille, F. Dulucq, and G. Martin-Chassard

OMEGA Ecole Polytechnique/CNRS-IN2P3, route de Saclay, Palaiseau, France

B. Andrieu, J. Dumarchez, C. Giganti, J.-M. Levy, B. Popov, and A. Robert

**UPMC, Université Paris Diderot, CNRS/IN2P3, Laboratoire de
Physique Nucléaire et de Hautes Energies (LPNHE), Paris, France**

L. Agostino, M. Buizza-Avanzini, J. Dawson, D. Franco,

P. Gorodetzky, D. Kryn, T. Patzak, A. Tonazzo, and F. Vannucci

**APC, AstroParticule et Cosmologie, Université Paris Diderot,
CNRS/IN2P3, CEA/Irfu, Observatoire de Paris, Sorbonne Paris Cité,
10, rue Alice Domon et Léonie Duquet, 75205 Paris Cedex 13, France**

O. Bésida, S. Bolognesi, A. Delbart, S. Emery, V. Galymov, E. Mazzucato, G. Vasseur, and M. Zito

IRFU, CEA Saclay, Gif-sur-Yvette, France

M. Bogomilov, R. Tsenov, and G. Vankova-Kirilova

**Department of Atomic Physics, Faculty of Physics,
St. Kliment Ohridski University of Sofia, Sofia, Bulgaria**

M. Friend, T. Hasegawa, T. Nakadaira, K. Sakashita, and L. Zambelli

High Energy Accelerator Research Organization (KEK), Tsukuba, Ibaraki, Japan

D. Autiero, D. Caiulo, L. Chaussard, Y. Déclais, D. Franco, J. Marteau, and E. Pennacchio
Université de Lyon, Université Claude Bernard Lyon 1, IPN Lyon (IN2P3), Villeurbanne, France

F. Bay, C. Cantini, P. Crivelli, L. Epprecht, A. Gendotti, S. Di Luise, S. Horikawa, S. Murphy,
K. Nikolics, L. Periale, C. Regenfus, A. Rubbia,* D. Sgalaberna, T. Viant, and S. Wu
ETH Zurich, Institute for Particle Physics, Zurich, Switzerland

F. Sergiampietri
**ETH Zurich, Institute for Particle Physics, Zurich, Switzerland and
INFN-Sezione di Pisa, Italy**

*Contact e-mail: andre.rubbia@cern.ch

Executive Summary

In June 2012, an Expression of Interest for a long-baseline experiment (LBNO) [1] has been submitted to the CERN SPSC and is presently under review. LBNO considers three types of neutrino detector technologies: a double-phase liquid argon (LAr) TPC and a magnetised iron detector as far detectors. For the near detector, a high-pressure gas TPC embedded in a calorimeter and a magnet is the baseline design.

A mandatory milestone in view of any future long baseline experiment is a concrete prototyping effort towards the envisioned large-scale detectors, and an accompanying campaign of measurements aimed at assessing the systematic errors that will be affecting their intended physics programme. Following an encouraging feedback from 108th SPSC on the technology choices, we have defined as priority the construction and operation of a $6 \times 6 \times 6\text{m}^3$ (active volume) double-phase liquid argon (DLAr) demonstrator, and a parallel development of the technologies necessary for large magnetised MIND detectors.

The $6 \times 6 \times 6\text{m}^3$ DLAr is an industrial prototype of the design proposed in the EoI and scalable to 20 kton, 50 kton or more. It is to be constructed and operated in a controlled laboratory and surface environment with test beam access, such as the CERN North Area (NA). Its successful operation and full characterisation will be a fundamental milestone, likely opening the path to an underground deployment of larger detectors. The response of the DLAr demonstrator will be measured and understood with an unprecedented precision in a charged particle test beam (0.5-20 GeV/c). The exposure will certify the assumptions and calibrate the response of the detector, and allow to develop and to benchmark sophisticated reconstruction algorithms, such as those of 3-dimensional tracking, particle ID and energy flow in liquid argon. All these steps are fundamental for validating the correctness of the physics performance described in the LBNO EoI.

We anticipate that a successful operation of the double-phase $6 \times 6 \times 6\text{m}^3$ DLAr demonstrator and its campaign exposure to a charged particle beam, will provide very important and vital feedback for long baseline programmes, and in general for the field. It will represent a never-achieved milestone for LAr detectors. Its design specifically addresses and represents a concrete step towards an extrapolation of the technology to very large masses in the tens of kton range, such as the one considered and studied for several years within the EU FP7 funded LAGUNA/LAGUNA-LBNO design studies. The parameters of the demonstrator will be directly scalable and the components mass-produceable. Long drift paths will be assessed on a large scale.

As requested by SPSC, we submit a Technical Design Report, in view of a realisation of the facility and an exposure to the charged particle beam before the LHC LS2.

Contents

1. Introduction	10
1.1. Main goals of the demonstrators	10
1.2. The DLAr demonstrator	12
1.3. The MIND demonstrator	14
1.4. Location of the prototype and needed infrastructure	16
2. Scientific and technical motivations	18
2.1. Calorimetry in charge particle beams	18
2.2. Development of automatic event reconstruction	22
2.3. Charged pions and proton cross-section on Argon nuclei	24
2.4. Development and proof-check of industrial solutions	26
3. DLAr Detector overview	28
3.1. Design concept of the $6 \times 6 \times 6\text{m}^3$ prototype	28
3.2. Liquid argon as detector medium and electron drift	31
3.3. Drift velocity and diffusion in argon gas	33
3.4. Drift velocity and diffusion in liquid argon	34
3.5. Electrons extraction	37
3.6. Scintillation in liquid and gas phases	39
3.7. Charge amplification in gas - Townsend avalanche	40
3.8. Primary and secondary scintillation light	43
3.9. Electron attachment to impurities	45
3.10. Liquid argon purity requirements	47
3.11. Effect of impurities on scintillation light	48
3.12. Ionisation space charge effects	49
3.13. Convective motion of liquid argon	52
3.14. Electric breakdown in liquid argon	52
4. DLAr detector components	58
4.1. Anode Charge Readout Plane	58
4.1.1. The top anode deck	58
4.1.2. The supporting structure	58
4.1.3. The position control system	59

4.1.4. The LAr LEM TPC option	62
4.1.5. The CRP for the $6 \times 6 \times 6\text{m}^3$	77
4.1.6. The MICROMEAS option	82
4.2. Drift cage	85
4.3. Drift high voltage	87
4.4. Front-end and DAQ readout	89
4.4.1. Requirements for the large scale front-end electronics	89
4.4.2. Cold front-end electronics	92
4.4.3. Fine-tuning of the F/E dynamic range	95
4.4.4. Back-end electronics and DAQ global architecture	95
4.4.5. MicroTCA standard and crates	98
4.4.6. MicroTCA dedicated AMC	100
4.4.7. Data rate requirements	102
4.4.8. Integration of readout electronics	102
4.5. The Light Readout system	104
4.5.1. Scintillation light detection	104
4.5.2. Light readout front-end digitiser and DAQ	105
4.6. Cryogenic vessel	110
4.7. Liquid Argon process	116
4.7.1. Sources of impurities from outgassing	116
4.7.2. The desorption from real surfaces	118
4.7.3. Diffusion	119
4.7.4. Permeation	120
4.7.5. The $40 \times 80 \text{ cm}^2$ LEM TPC as an example	121
4.7.6. Leaks	123
4.7.7. Gas recirculation	125
4.7.8. Liquid argon purification	128
4.7.9. Molecular sieve	128
4.7.10. Oxygen filters	130
4.7.11. Design of the ArDM LAr purification system	132
4.7.12. Liquid argon purification in the $40 \times 80 \text{ cm}^2$ operation at CERN	134
4.7.13. Concept for the gas and liquid purification of the $6 \times 6 \times 6 \text{ m}^3$ prototype	135
4.8. Process control and monitoring	137

5. DLAr offline requirements and software	140
5.1. Overview	140
5.2. The Qscan software	140
5.3. Event simulation	141
5.3.1. Particle propagation in detector geometries	142
5.3.2. Waveform generation	144
5.4. Event Reconstruction	145
5.4.1. Signal processing	147
5.4.2. Hit identification and reconstruction	150
5.4.3. Cluster finding	152
5.4.4. Track reconstruction	153
5.4.5. Three dimensional track reconstruction	154
5.4.6. Particle flow - the PANDORA methodology	157
6. MIND500: North Area MIND	159
6.1. MIND500 overview	159
6.2. MIND reconstruction efficiencies	160
6.2.1. Muon reconstruction efficiencies	162
6.2.2. Pion reconstruction efficiencies	164
6.3. Detector modules	165
6.3.1. Detector module mechanics	165
6.3.2. Scintillators	166
6.3.3. Scintillator and fiber connectors	167
6.3.4. Choice of photosensor	170
6.4. Electronics and DAQ	173
6.4.1. Outline of electronics chain	173
6.4.2. Beam considerations for electronics	174
6.4.3. EASIROC chip	175
6.4.4. Readout modes	176
6.4.5. Data stream	176
6.4.6. Slow control	179
6.5. Iron plates	179
6.5.1. Plate dimensions	179
6.5.2. Material selection	180

6.5.3. Chemical and mechanical properties	181
6.6. Magnetization of MIND500	181
6.6.1. The Superconducting Transmission Line	181
6.6.2. Dimensioning the STL for MIND500	184
6.6.3. The STL superconducting coil	185
7. Overall layout and space requirements	186
7.1. General Requirements	186
7.2. Control room	186
7.3. Clean-room	187
7.4. Access to EHN1-X area	187
7.5. Liquid Argon filling and emptying	188
7.6. Liquid argon boiloff recondensation	188
7.7. Gas phase argon purging and purification	189
7.8. Liquid Argon filtration	189
7.9. Cranes	189
7.10. Ventilation requirements	190
7.11. Cryorefrigeration requirements	190
7.12. HVAC requirements	190
7.13. Cooling water requirements	190
7.14. Electrical requirements	190
7.15. Additional laboratory space at CERN	191
7.16. Data storage and computing requirements	191
8. Test beam requirements	192
9. Organization, cost estimate, schedule and risk assessment	194
9.1. Organisation	194
9.2. Cost estimate	195
9.3. Schedule and milestones	195
9.4. Risk assessment	197
10. Conclusions	198
A. Appendix: Event rates with neutrino beams	200
1. CENF conventional beam	200

	9
2. Muon storage ring - NuSTORM	202
B. Appendix: Test of full-scale APA's for LBNE	205
References	207

1 Introduction

1.1 Main goals of the demonstrators

The main objectives towards long baseline neutrino oscillation experiment (LBNO) in the coming years are to develop demonstrators of the neutrino detector technologies considered in the Expression of Interest (EoI) CERN-SPSC-2012-021 (SPSC-EOI-007) [1] submitted to the SPSC in 2012. Such demonstrators are needed to leverage large risks associated to the extrapolation from existing experience to the huge mass required for far detectors.

Already since almost a decade we have worked towards the realisation of a giant liquid argon underground detector for neutrino mass hierarchy (MH) and leptonic CP-violation (CPV) discovery, and neutrino astrophysics. In the recent years, two consecutive FP7 Design Studies (LAGUNA/LAGUNA-LBNO) have led to the development of a conceptual design (fully engineered and costed) for a 20kton/50kton GLACIER-type [2] underground neutrino detector. In these studies, an underground implementation has been assumed *ab initio* and such constraints have been important and taken into account in design choices.

In 2013, the SPSC has endorsed the physics case for CP-violation and neutrino mass hierarchy determination described in the EoI, the choice of the Liquid Argon (LAr) detector technology, and encourages the development of the kind of activities described in this document, requesting more detailed information (108th SPSC minutes):

“Concerning LAGUNA-LBNO, the SPSC supports the double-phase LAr TPC option as a promising technique to instrument very large LAr neutrino detectors in the future. The SPSC therefore encourages the LBNO consortium to proceed with the R&D necessary to validate the technology on a large scale. For further review of the project, the SPSC requests a technical proposal describing the R&D programme to be led at CERN”.

The successful operation of the $6 \times 6 \times 6\text{m}^3$ DLAr demonstrator presented in this Technical Report will open the way to the construction of large and affordable liquid argon underground detectors addressing the complete investigation of 3-flavours neutrino oscillations and the determination of their still unknown parameters. These detectors will as well be very powerful for important non-beam studies such as proton decay, atmospheric neutrinos and supernovae neutrinos. The $6 \times 6 \times 6\text{m}^3$ dimensions are motivated by the fact that the basic readout component of the large-scale LAGUNA/LBNO 20-50 kton detectors are $4 \times 4 \text{m}^2$ units. The $6 \times 6 \text{m}^2$ is consistent with having a fiducial volume corresponding to that readout unit. Surface operation prohibits drift lengths above 6 m. In parallel, the MIND detector will allow developing further this well-understood technology in particular for what concerns

the optical readout and the large scale integration.

More generally, the technologies addressed and the results that will be obtained during the commissioning and operation of the facility, are relevant to a broader range of experiments, which are presently being considered and could go online in the next decade. In the following we list the main experiments where our proposal would have a potentially important impact:

- The vision of the long baseline neutrino experiment (LBNE) in the USA [3] is based on a prospective 1.2 MW proton beam power at FNAL and a far detector at Homestake of 35 kton mass. The detectors proposed in this document and their successful operation could, if performed on a timescale of less than 3 years, have a positive potential impact on the design of the LBNE far detector, and represent the basis for a significant European contribution to the project.
- The Hyper-Kamiokande Detector in Japan (LOI September 2011) [4] has been proposed as a next generation underground Water Cherenkov Detector (WCD). It will serve as a far detector of a long baseline neutrino oscillation experiment envisioned for the J-PARC neutrino complex upgraded up to 750 kW, and as a detector capable of observing – far beyond the sensitivity of the Super-Kamiokande (Super-K) detector – proton decays, atmospheric neutrinos, and neutrinos from astronomical origins. The baseline design of Hyper-K is based on the highly successful Super-K, taking full advantage of a well-proven technology. However, in order to exploit the full statistical power, systematic errors have to be controlled by a set of near detectors. The technologies considered in this proposal are directly relevant for improved near detectors at J-PARC. In particular, a muon ranger behind a new WCD detector at the new 2 km position is being discussed.
- In the proposed short baseline neutrino experiment at CERN, CERN-SPSC-2012-010 (SPSC-P-347) [5], a new conventional neutrino beam (CENF) has been discussed. The location of the DLAr and MIND demonstrators described in this proposal is made compatible with the “near” station of the eventual CENF neutrino beam. Exposure to the CENF would allow to collect a large number of neutrino interactions in the range of 500 k/year, as illustrated in Appendix A.
- NUSTORM [6] (“Neutrinos from STORed Muons,”) is a proposed facility, which, with an appropriate far detector for neutrino oscillation searches at short baseline, could provide a confirmation or rejection of the LSND/MinBooNE results. The DLAr and MIND detectors proposed in this document exposed to a NUSTORM-like beam, could be used to make precision neutrino interaction cross section measurements important to the next generation of long-baseline neutrino

oscillation experiments. This would result in the detection of 100 k/year neutrino interactions, as illustrated in Appendix A.

- In the recent proposal to Search for Heavy Neutral Leptons at the SPS, CERN-SPSC-2013-024 (SPSC-EOI-010) [7], the neutrinos produced in the dump are a source of background, whose rate and spectra are not very well known. A recent calculation finds a discrepancy of a factor four with CHARM data. The DLAr and MIND demonstrators would directly measure these backgrounds, which could be used to predict the rates and features of these interactions in the muon shield and decay volume of the SHIP experiment.
- The Neutrino Factory (see e.g. [8]) is conceived as the facility for the ultimate long baseline neutrino oscillation experiment. As explained in the LBNO EOI, the choice of baseline 2300 km is optimised for the neutrino factory, and the LBNO far detector infrastructure is a first milestone towards such a facility. In this proposal, the DLAr and MIND demonstrators will assess the scalability and costs of the far detectors of the neutrino factory.

1.2 The DLAr demonstrator

The concept of the LAr Time Projection Chamber (LAr TPC) [9] and its excellent tracking-calorimeter performances allow for massive neutrino detectors with higher signal efficiency and effective background discrimination compared to other techniques. The pioneering work of ICARUS on prototypes of ever increasing mass (0.003 [10], 0.05 [11], 3 [12], and 10 tons [13]) has culminated in the construction and operation of the T600 detector (478 tons) on surface [14], its characterization [15–20], and eventually to its underground commissioning [21]. The so-called GLACIER design [2, 22], based on the double phase Large Electron Multiplier (LEM) readout “sandwich” with charge extraction and amplification, coupled to a very long drift paths in a single non-evacuated LNG-type tank has been advocated as an attractive solution to reach very large detector masses, beyond what is realistically achievable by linear extrapolation of the ICARUS design. The successful phases of R&D and prototyping on small-scale double phase LAr LEM TPC setups [23–26], benefitting from the worldwide effort on the general development of Micro Pattern Gas Detectors (MPGD) [27] – in particular GEMs [28], MicroMegas [29] and LEMs/THGEMs [30] – already demonstrated the significantly improved performance of this novel concept. The collection-only readout mode (avoiding the use of induction planes) is also an important asset in the case of complicated topologies, like e.g. in electromagnetic or hadronic showers. Three examples of cosmic events obtained with typical electric field configurations (the drift field of ≈ 0.4 kV/cm) and 35 kV/cm in the LEM holes are presented in Figure 1. Using a simple event

display images for two projections, i.e. xt - and yt -projections, can be obtained for each event: x - and y -coordinates are two horizontal coordinates orthogonal to each other and t -coordinate corresponds to the vertical coordinate z .

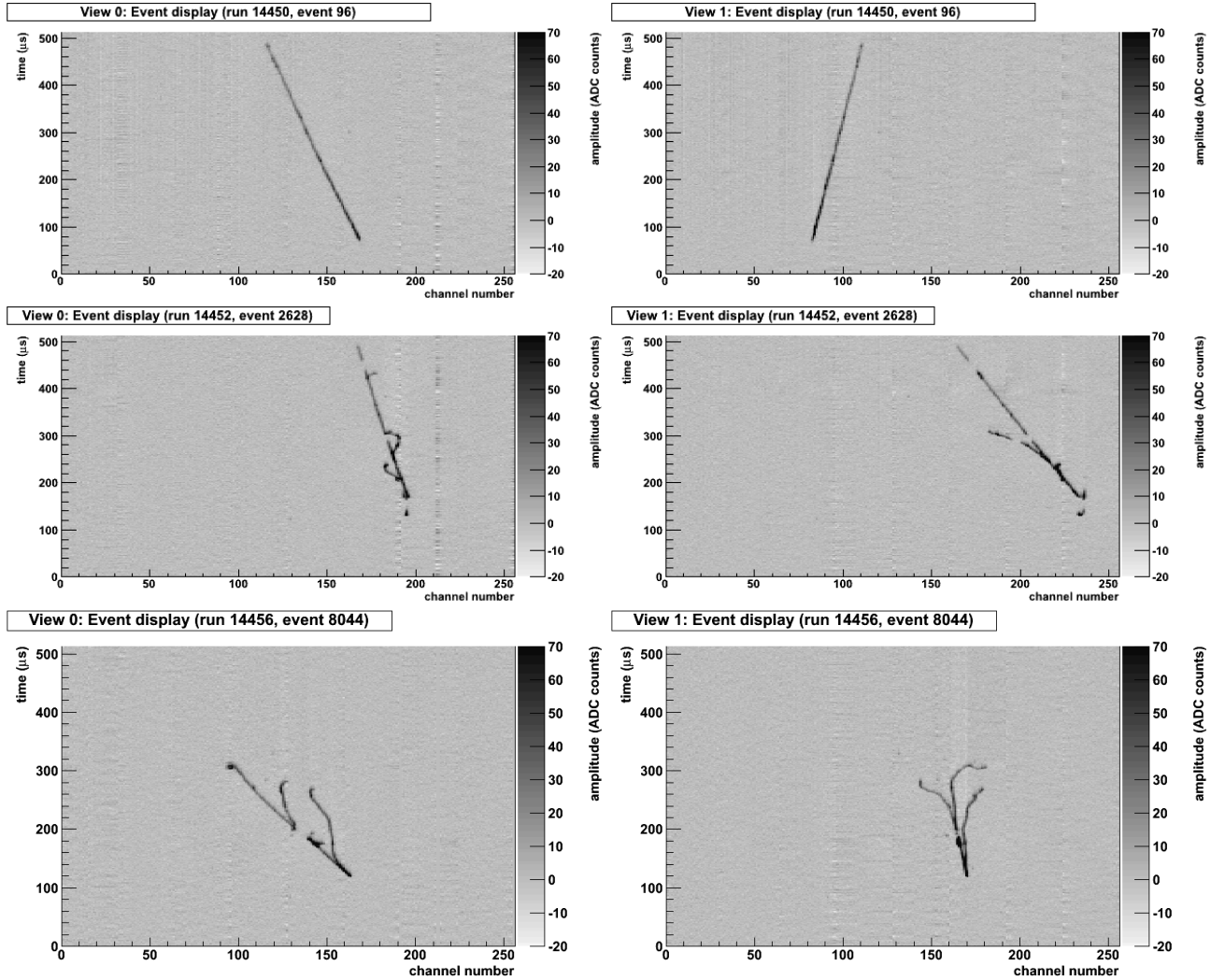


FIG. 1: Event display for three cosmic events recorded using the $40 \times 80 \text{ cm}^2$ LAr LEM-TPC [24]. The left and right columns correspond to the xt - and yt -projections, respectively. Top: a straight muon track crossing from top to bottom of the field cage. The time of the start ($t_0 \sim 60 \mu\text{s}$) and the end ($t_{\text{max}} \sim 490 \mu\text{s}$) of the extraction are clearly visible. Middle: an example of a “grazing” muon track with delta rays, where the extraction starts later at $t \sim 150 \mu\text{s}$. Bottom: interacting event.

The LAGUNA and LAGUNA-LBNO EU FP7 design studies have been focussed on the GLACIER concept, a large double phase Liquid Argon TPC with a long drift and charge-sensitive detectors in the gas phase. According to these studies it is technically feasible to build a large (20-100 kt) underground tank, based on the LNG industrial technology, in which the detector is composed of a large number of independent basic readout units of $4 \times 4 \text{ m}^2$ [31]. In a more recent related development these studies have also considered a novel technique for the tank construction involving the membrane technology for

the tank. In this technology, the functions of structural support, insulation and liquid containment are all realised by different components, namely an outer concrete structure, specially designed insulating panels and a thin layer of steel plates. These development are very promising for the realisation of a large underground detector, however several areas need to be verified on a large scale prototype.

In order to measure and assess the detector performance for LBNO, we consider dedicated test beam campaigns, to test and optimise the readout methods and the calorimetric performance of such detectors. The proposed test beam will address the following points:

1. Electron, neutral pion, charged pion, muon reconstruction: A crucial feature of the LAr TPC is the possibility for a very fine sampling, which should deliver unmatched performances in particle identification and reconstruction.
2. Electron/ π^0 separation: Another central feature of the LAr TPC is the possibility to precisely measure and identify electrons from neutral pion backgrounds.
3. Calorimetry: A specific feature of the LAr TPC is its 100% homogeneity and full sampling capabilities. As an extension of the measurements performed in above, more refined measurements with low energy particles will yield actual calorimetric performance and determine the ability to reconstruct full neutrino events in the GeV-range.
4. Hadronic secondary interactions: With the large statistics expected, an exclusive final state study of pion secondary interactions will be attempted. Comparison of the data obtained with MC (e.g. GEANT4) will allow to cross-check and eventually tune these models.

The reconstruction of electrons, neutral and charged pions and muons will be demonstrated in the dedicated test beam campaign. The obtained results will optimise the readout parameters to be used in the far detector. They will represent a major milestone in the definition of LAGUNA/LBNO, which relies on low energy neutrino beams and sensitive searches for proton decay. They will complement direct measurements in a low energy neutrino beam. The reconstruction software with a fully automatised reconstruction will be developed. Samples of hadronic interactions produced by particles of well-known momentum will allow benchmarking these software tools and determining their performance with high precision.

1.3 The MIND demonstrator

MIND-type detectors have been successfully designed, built and operated over several decades. They are particularly well suited for charge current (CC) neutrino interactions with an outgoing muon

in the final state, see Figure 2. A MIND is the baseline detector for a Neutrino Factory, where a muon of opposite charge to that expected from the neutrino content of the beam, is detected through CC interactions of the oscillated ν_μ [32]. Along with the performance of detectors obtained online, dedicated test runs have provided valuable information, for example the calibration detector tests or CalDet carried out for MINOS at the CERN-PS, which measured the energy resolution for the setup to be $21.42\%/\sqrt{E}$ (GeV), $56.6\%/\sqrt{E}$ and $56.1\%/\sqrt{E}$ (GeV) for electrons, protons and pions respectively.

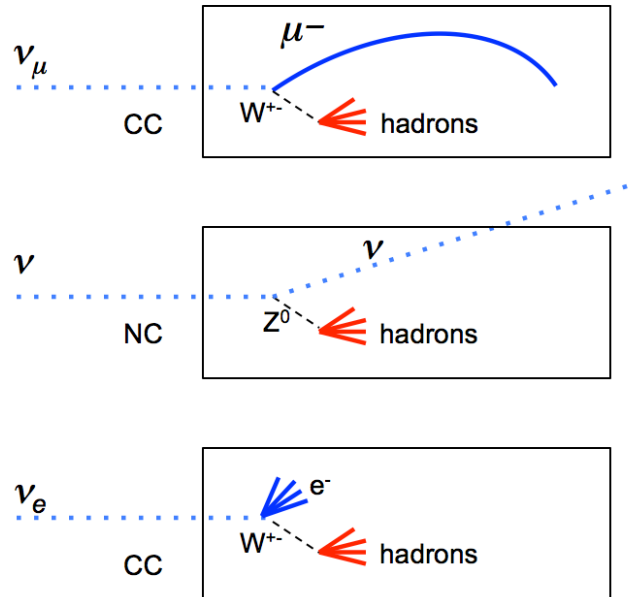


FIG. 2: Sketch of event topologies in a MIND. The dashed lines with the W/Z bosons are for illustration only and do not represent tracks.

Despite the considerable amount of experience gained on this detector technology, there are several gaps in our knowledge which merit further detailed studies. A MIND prototype located downstream of the DLAr demonstrator would enable the following studies:

- Charge ID efficiencies specifically for low energy interactions (< 1 GeV/c): Reconstruction tools such as the Kalman filter, work very well for high energy muons, where a typical event has several hits through several planes well away from the initial hadronic activity. When the muon range is comparable to the range of the hadronic shower, we have more of a challenge. Cellular automaton techniques are a possibility. We would benchmark new reconstruction techniques against test beam data. This will include testing how fast reconstruction and charge ID efficiencies drop as a function of decreasing momentum in a MIND, and establishing at which point an alternative detector (e.g. air core magnet) would be better suited.
- Backgrounds in MIND analyses: backgrounds to wrong sign muon events come from secondary

muons arising from decays of the initial hadronic activity (e.g pions, kaons). A charged particle beam incident first on a 6 m DLAr would generate several scenarios in the MIND, especially given the beam is typically composed of several particles (e.g. > 10% pions in a muon beam). Simulations can be benchmarked against these.

- Momentum reconstruction for charged particles crossing the DLAr: the DLAr cannot reconstruct muons above a few GeV/c. Secondary particles arising from interactions of the primary charged particle beam in the DLAr may not stop in the DLAr, so event reconstruction would be complemented by the MIND.

MIND-type detectors are planned downstream of a liquid argon detector at LBNO but also downstream of a water cherenkov at a near detector facility for Hyper-Kamiokande.

1.4 Location of the prototype and needed infrastructure

The cryogenic vessel required for a detector of the size of $6 \times 6 \times 6\text{m}^3$ is hardly transportable, and is most conveniently constructed *in situ*. On the other hand, the detector components will be assembled and tested elsewhere, transported sealed onsite, and installed inside the vessel, equipped during the installation phase as a clean-room.

An extension of the CERN EHN1 experimental hall (See Figure 3) would provide an appropriate location to host the $6 \times 6 \times 6\text{m}^3$ prototype. This extension fulfils the following requirements:

- possibility to host the infrastructure needed during the construction and installation phase, such as crane, access, electricity, services, by extending the presently existing services in EHN1;
- controlled area for safe cryogenic operation;
- charge particle test beam by extension of the existing lines in EHN1.

The infrastructure should be provided by CERN, via their technical experimental area support teams. Refer to ?? for a general list of space and infrastructure requirements.



FIG. 3: Areal view of the foreseen extension of the CERN EHN1 (Bat 887) building to host the LAGUNA/LBNO detector demonstrators.

2 Scientific and technical motivations

2.1 Calorimetry in charge particle beams

Besides its tracking capabilities, the LAr TPC can also be considered as a fully homogeneous liquid argon ionization chambers, allowing the energy measurement by total absorption, in the spirit of the liquid argon calorimeter proposed by Willis and Radeka [33]. As was pointed out in their pioneering work, liquid argon is a medium that satisfies all requirements better than many other materials. All the energy is ideally converted into ionization through the development of the cascade showers, which is then drifted across a gap and readout electronically. The integral charge, once calibrated, yields the incoming particle energy. In practice, the precision of the ionization measurement is limited by (i) particle leakage out of the surface of the detector, such as high energy neutrons or neutral strange kaons, (ii) energy carried off by neutrinos, (iii) nuclear interactions releasing or absorbing binding energies, (iv) charge recombination (v) charge quenching of heavy nuclear fragments, alpha particles and nuclear evaporation products (saturation of response on densely ionizing particles) and (vi) electronic noise. The energy resolution of the calorimeter will be determined by the fluctuations in the above effects.

Just as in the case of the liquid argon ionization chamber, the LAr TPC is a single-carrier device as far as charge collection is concerned, since only the drifting electrons induce visible signals as they arrive nearby the readout electrodes in the LAr TPC, which is picked up by a charge sensing preamplifier, and then sampled and converted to digital information. Offline the integrals of the digitized signal waveforms yield the full amount of charge of the ionization electrons. This situation is similar to that of calorimeters where positive ions, due to their very low mobility, contribute little to the signal charge in the short time electrons take to drift across the gap (which for uniformly distributed ionization across the gap yields half the charge).

In order to study the calorimetric response of the LAr TPC, Monte Carlo simulations with the GEANT3/GFLUKA and GEANT4 (QGSP_BERT physics list) were performed in the full geometry of the LAr detector. Charge recombination R was taken into account according to the Birks law:

$$R = \frac{A}{1 + k/E_{drift}(dE/dx)} \quad (2.1)$$

where $A = 0.8$, $k = 0.0486 \text{ kV/cm} \frac{\text{g/cm}^2}{\text{MeV}}$ and E_{drift} is the drift field [18]. For 1 kV/cm, about 30% of the produced ionization charge recombines in the case of minimum ionizing particles. The digitization of the charge is performed using the expected response of the charge preamplifier. The charge is reconstructed using the same automatic reconstruction algorithm as used for data.

The electromagnetic and hadronic responses were studied with 1, 3, 5, 7 and 10 GeV/c electrons and charged pions. Since pure liquid argon is a non-compensating medium, electromagnetic and hadronic showers require different calibrations. The e/π compensation is performed offline and the reconstructed energy is therefore defined as

$$E_{reco} = \alpha E_{had} + \beta E_{em} \quad (2.2)$$

where E_{had} is the reconstructed hadronic component, E_{em} is the reconstruction electromagnetic component and α, β are tunable parameters. Neglecting the electromagnetic components from the charged pions, the parameters α and β are measured from the hadronic and electromagnetic energy response. The results are shown for the case of GEANT3 and GEANT4 in Figure 4 on the left. Both simulations

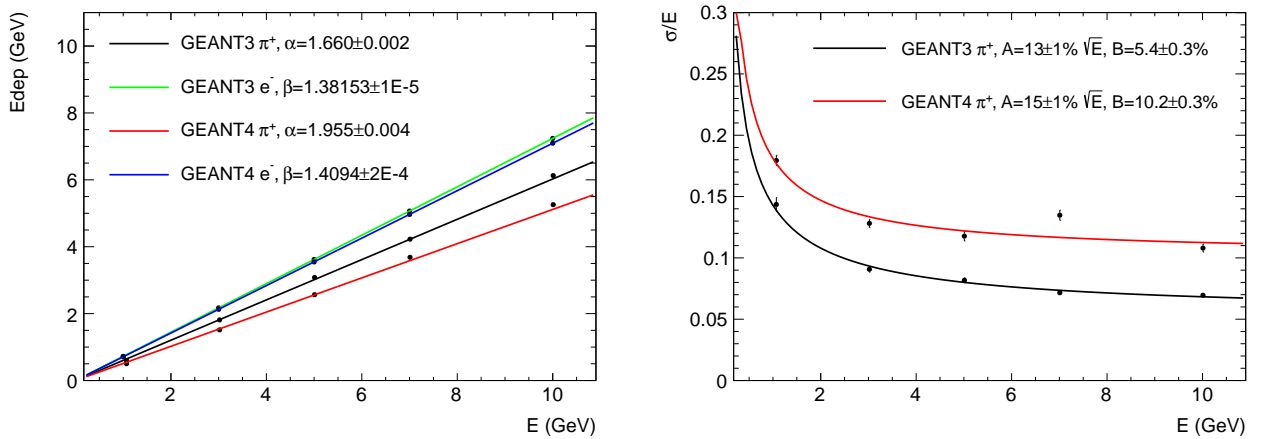


FIG. 4: LAr energy response of MC generated (GEANT3/GEANT4) e^- and π^+ events for energies up to 10 GeV. The left plot shows the obtained results for the correction factors α and β . On the right the reconstructed energy resolution for π^+ particles is shown.

are in agreement for the electron showers, with a consistent value for $\beta \simeq 1.4$, as expected from the charge recombination effect. On the other hand, the results differ for hadronic showers, with GEANT4 predicting about 30% less ionization than GEANT3. This difference is also reflected in the predicted hadronic energy resolutions. The right plot shows the energy dependence of the hadronic shower resolution, superimposed with the fit $\sigma/E = A/E \oplus B$. The stochastic terms are similar at the level of 15%, while the predicted constant term is significantly larger with GEANT4 which predicts 10% than with GEANT3/GFLUKA which gives 5%. The study of calorimetry will be performed with the LAGUNA/LBNO prototype with unprecedented statistics of charged particles crossing the detector of well-defined energy and direction. The understanding of calorimetry is a fundamental milestone to achieve the required level of precision in the reconstruction of the neutrino energy, fundamental in the future oscillation experiments at long baselines.

As specified above, the calorimetric resolution of the chamber is limited by particle leakage out of the surface of the detector. The best energy resolution is obtained if the resulting cascade shower is fully contained within the fiducial volume of the detector. The containment of the showers in the $6 \times 6 \times 6\text{m}^3$ were studied by comparing the reconstructed energy[159] of π^+ events with two other simulated detector geometries: (i) LBNO/GLACIER 20kton, which is the far detector described in the LBNO expression of interest [1]. Here the event is generated at the center of the detector and the volume is large enough that the event is fully contained (ii) $3 \times 1 \times 1\text{m}^3$ which is a chamber of 3 m along the beam direction 1m transverse and 1 m drift.

Figure 5 shows an event display of a shower initiated by a 3 GeV π^+ in each of those detectors. For a detailed discussion on the simulation of detector geometries and particle transport please refer to ???. The distributions of reconstructed energies were compared for generated π^+ of 0.2, 0.5, 1, 3, 5 and 10 GeV in the three detector geometries. The distributions of reconstructed energies are shown in Figure 6 for pions of 1 and 10 GeV. If the event is fully contained, as is the case with the LBNO/GLACIER 20kton geometry, the distribution of reconstructed energy is centered on the initial energy of the particle. On the other hand if the fiducial volume is not large enough (e.g in the $3 \times 1 \times 1\text{m}^3$), the distribution is shifted to lower energies. The mean of the distribution of reconstructed energy versus the initial energy of the pion is plotted in Figure 7. It shows that the $6 \times 6 \times 6\text{m}^3$ detector is large enough to contain pion showers at least up to 10 GeV, and is adequate for energies up to 20 GeV as envisioned. On the other hand, the smaller $3 \times 1 \times 1\text{m}^3$ is not adequate to contain hadronic showers.

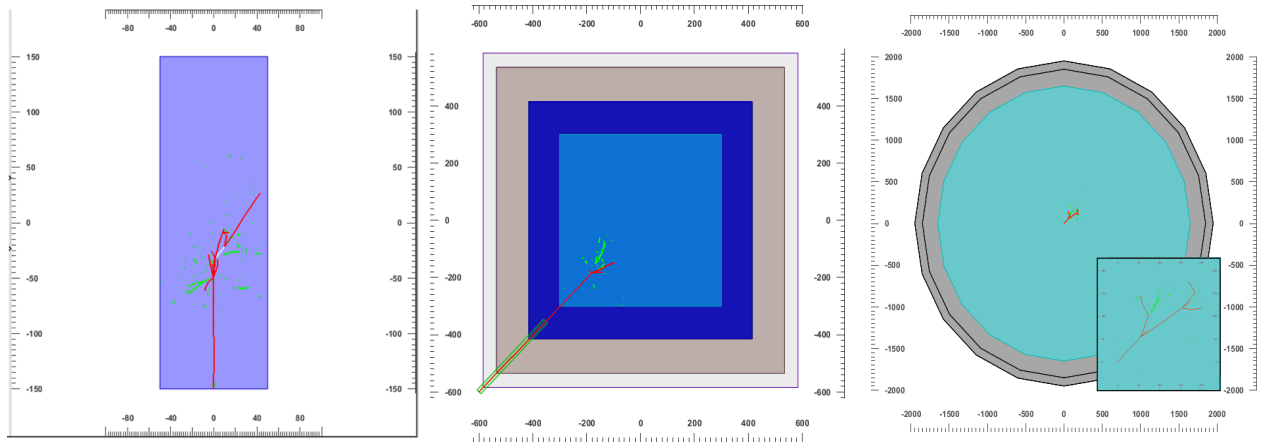


FIG. 5: Topview of a simulated 3 GeV π^+ in the $3 \times 1 \times 1\text{m}^3$ (left), the $6 \times 6 \times 6\text{m}^3$ (middle) and the LBNO/GLACIER 20kt with a zoom on the shower (right).

Beyond neutrino physics, the high statistics data sample of hadronic interactions collected by the DLAr demonstrator and its detailed comparison with the predictions of the hadronic showers models will be of general interest, in particular for the next generation collider experiments. These experiments aim at very accurate hadronic calorimetry, based on particle showers imaging and on the application

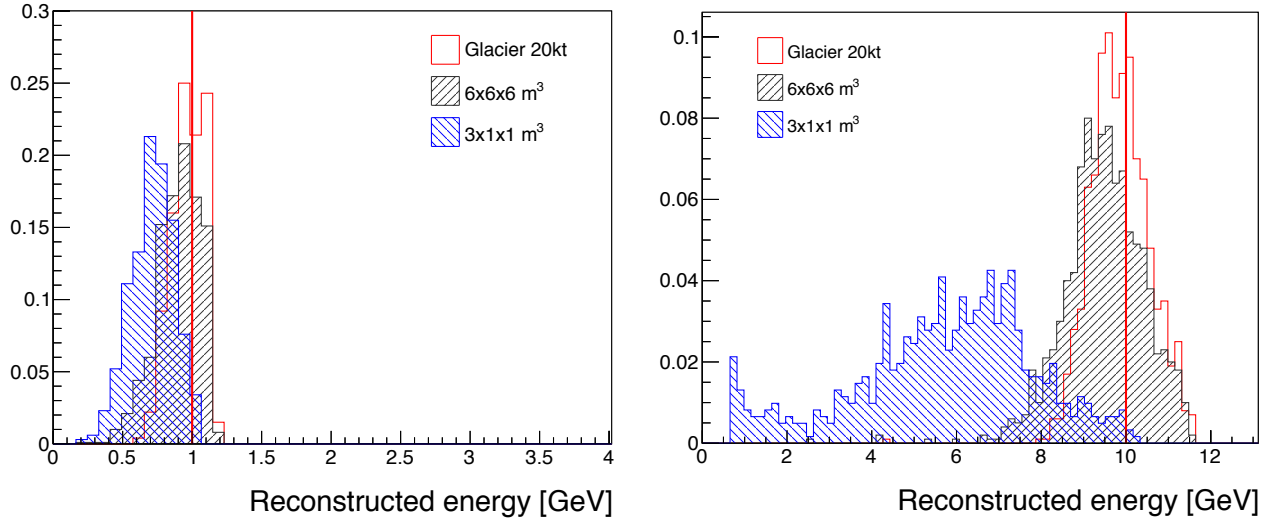


FIG. 6: Distribution of reconstructed energy for a π^+ event of 1 GeV/c (left) and 10 GeV/c (right) for three different detector geometries. The initial energy of the particle is indicated by a red line.

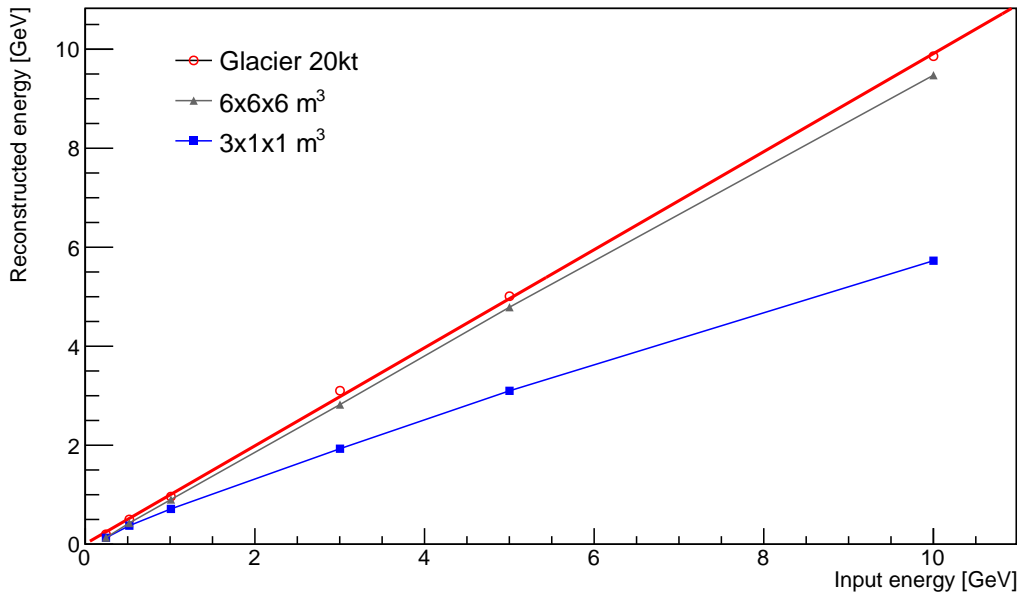


FIG. 7: Mean of the reconstructed energy as a function of the π^+ initial energy for the three considered geometries.

of the particle flow approach (PFA) [34].

The recent R&D activity on calorimetry for the future Linear Collider brought to the construction of prototypes with unprecedented granularity, bringing detailed information on the properties of hadronic showers. The CALICE collaboration constructed an analog hadronic calorimeter prototype (AHCAL) [35] (iron/scintillator with SiPM readout) with a maximal granularity of $3 \times 3 \text{ cm}^2$. The high granularity allowed studying, with high precision, properties of the hadronic showers, such as the longitudinal and transverse profiles, tracks multiplicities and angular distributions. These data were compared to Monte

Carlo models and used to develop software e/h compensation techniques.

The DLAr demonstrator is a completely homogeneous calorimeter with granularity of $3 \times 3 \text{ mm}^2$ granularity with full containment of hadronic showers. Its data sample of interactions from the charged particle beam will represent the ultimate tool for the high accuracy studies of the hadronic showers. They could bring a real breakthrough in the improvement of the showers simulation models useful, for a large number of applications in high energy physics. The granularity is two orders of magnitude finer than the one achieved in the AHCAL prototype [35] and it is also accompanied by other very powerful handles:

- the dE/dx measurements in LAr allow also for the identification of the secondary hadrons produced in the showers. This information will complement the multiplicity and angular distribution measurements;
- the electromagnetic component of the shower can be identified and measured with very high resolution;
- the energy and transverse momentum P_t balance of the secondary vertices can be measured as well and compared to simulations bringing to improved comprehension of the sources of invisible energy in the hadronic showers;

All these features will allow for unprecedented studies of the hadronic showers development and very thorough data comparisons and validation of the simulation models.

2.2 Development of automatic event reconstruction

The LAr TPC technology provides an “imaging” of the events with a bubble-chamber-like quality. Due to the large amount of information, the automatic reconstruction of such complex events is an important task that needs to be addressed, in order to move towards an unbiased reconstruction and analysis, not required an intense human intervention (in the spirit of the analysis of the large sets of photographs collected in the bubble chambers).

While we have already shown that minimum ionising particles and tracking are well understood and reproduced by our Qscan reconstruction [36], and that electromagnetic showers are rather well modelled by Monte-Carlo codes such as GEANT, the main difficulty lies in the reconstruction of hadronic showers. Indeed, the response is affected by nuclear debris which are highly quenched, and offline reconstruction algorithm that can automatically handle the e/pi compensation must be developed.

The collection of charged particles in a test beam configuration, as opposed to a neutrino beam, is very important (and sufficient) to assess the performance and response of the detectors. ?? compares the event produced by a muon neutrino interaction of 5 GeV with the one of a 5 GeV pion interaction. The MC tracks are coloured according to their type (blue=muon, green=electron, red=proton, cyan=pion). The secondary particles produced in the two interactions have very similar characteristics

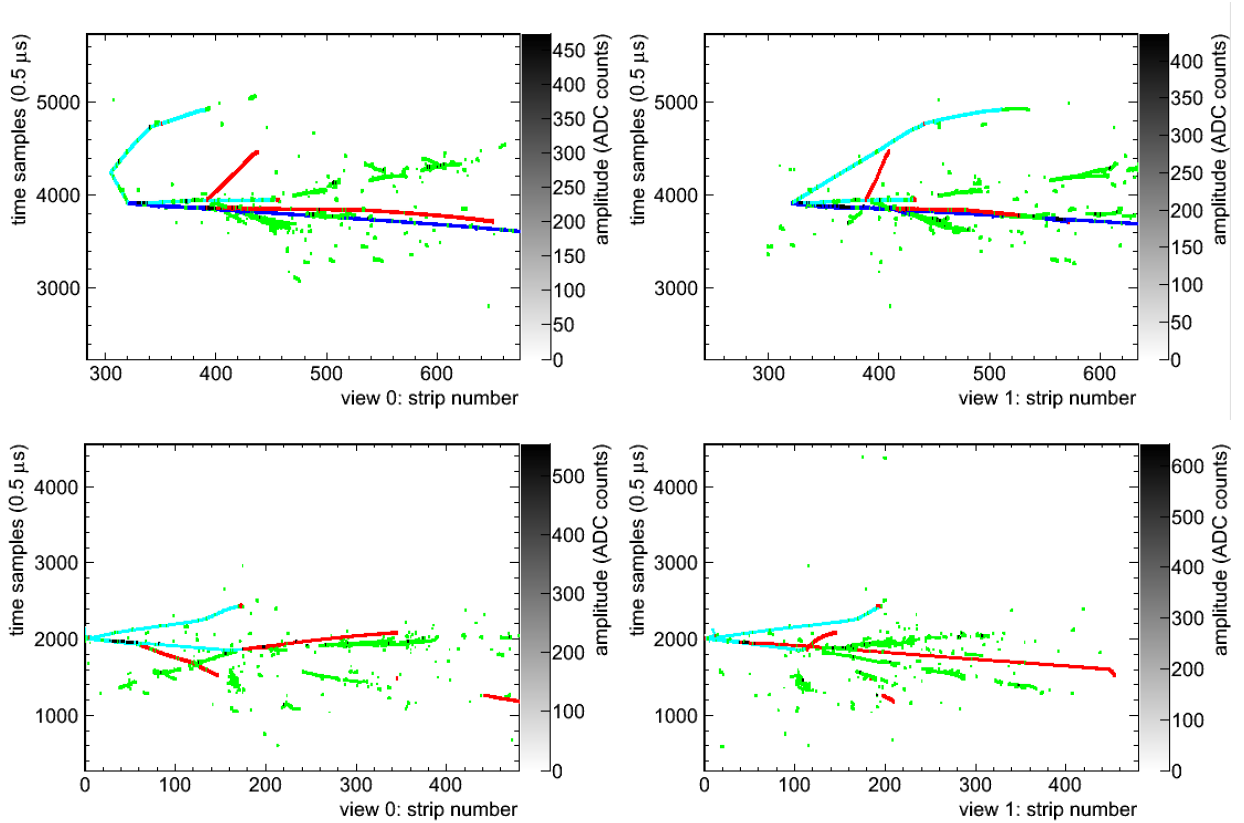


FIG. 8: MC comparison of neutrino and pion interactions: (top) 5 GeV muon neutrino interaction (bottom) 5 GeV pion interaction. The secondary particles produced in the two interactions (blue=muon, green=electron, red=proton, cyan=pion) have very similar characteristics (except for the muon in the case of the neutrino charged current (CC) interactions) and can be used to assess the performance of the detector and test the energy flow reconstruction algorithms. A precise knowledge of the incoming particle energy (not possible in a neutrino beam) is necessary to calibrate and check the linearity of the the response.

and topologies (except for the muon in the case of the neutrino CC interactions) and can be used to assess the performance of the detector and test the energy flow reconstruction algorithms.

In the case of the charged particles, the well-known momentum of the incoming particle (not accessible on an event-by-event basis in a neutrino beam) is necessary to precisely calibrate the energy and to check the linearity of the response.

2.3 Charged pions and proton cross-section on Argon nuclei

The neutrino energy reconstruction is a challenge for current and future long-baseline neutrino oscillation experiments. Several elements contribute to the neutrino energy reconstruction, such as the detector response (see ??), the interaction of charged particles emitted in the interaction with matter and the re-interaction of hadrons within the nucleus. Concerning this latter, the high density in the nucleus changes both the nature and the energy of the hadrons produced in the interaction affecting the total energy reconstruction of the event. Traditionally neutrino interaction cross-section Monte Carlo simulate these re-interactions base on a cascade model tuned by external pion-Nucleus cross-section data (see [160] for the description of the implementation for T2K).

There are three type of interactions considered in the cascade models:

- Elastic scattering, the particle changes momentum and direction.
- Absorption, the particles are absorbed emitting low energy nucleons.
- Charge exchange, the charged particle is absorbed and reemitted with different charge (i.e. proton \rightarrow neutron, $\pi^+ \rightarrow \pi^0, \dots$)

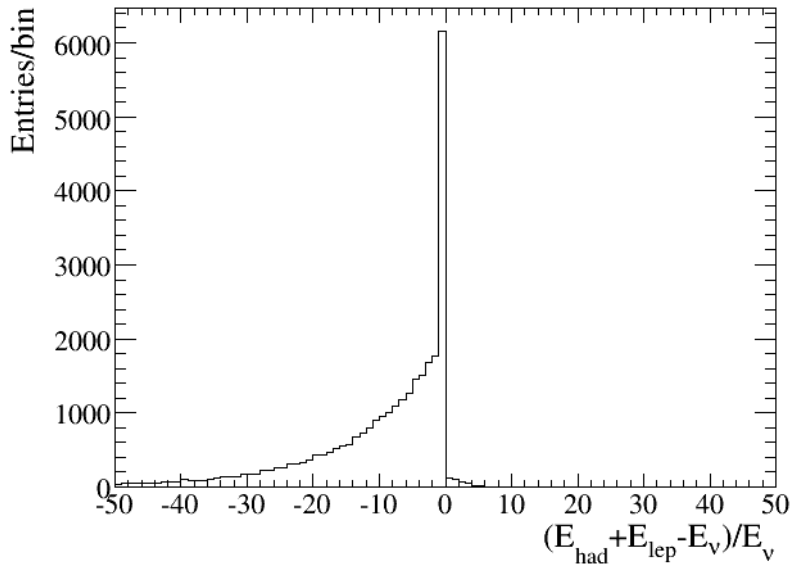


FIG. 9: Fraction of the neutrino energy visible at the detector following a charge current neutrino nucleus interaction as predicted by GENIE Monte Carlo.

The last two processes affect the neutrino energy reconstruction by smearing or removing energy from the final state. Figure 9 shows the fraction of the neutrino energy visible at the detector after

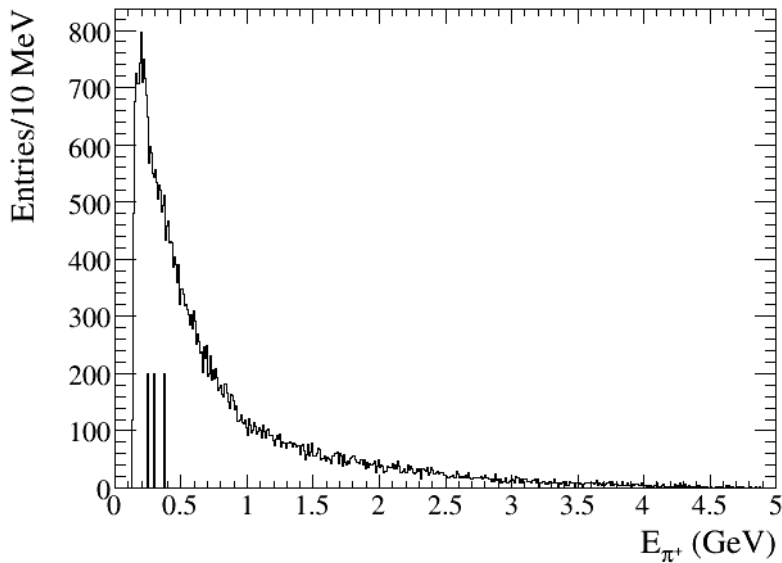


FIG. 10: Pion momentum emitted in neutrino argon interactions as predicted by GENIE Monte Carlo.

a charge current neutrino interaction as simulated by the GENIE MC [37] for the typical LBNO beam neutrino spectrum. The reconstructed neutrino energy shows lower energy than the original one producing an asymmetric distribution. This distribution needs to be known to reconstruct precisely the oscillations parameters such as the mass difference squared.

The current knowledge about π^+ argon cross-section at low energy is limited. The most recent result [38] provides the total cross-section and the final state multiplicity for three values of the pion kinetic energy (118, 162 and 239 MeV). These values do not cover, see ??, the full spectrum of π^+ emitted by the neutrino interactions. Another limitation is that the results in [38] do not distinguish between the three interactions modes described above, each one with a different contribution to the energy reconstruction bias.

These interactions modify the reconstruction of the event worsening the neutrino energy reconstruction and increasing the probability of lower energy reconstruction. This effect is much stronger for the interactions happening inside the nucleus. The direct measurement of the hadron-nucleus cross sections in liquid argon will be helpful in the improvement of the nuclear cascade models which are based on these data.

The DLAr will help in reducing these uncertainties for future experiments by means of measuring the strength of the exclusive interaction channels and the properties of the final state particles. The cross-section can be studied via the response to beam particles. An alternative method is to study the low energy products of the interaction of high-energy hadrons inside the detector volume by reconstructing

the full cascade history of the event. This is illustrated in ?? where the event display of a 5 GeV pion interaction is displayed, in which a secondary pion of 2.58 GeV has re-interacted. The MC tracks are coloured according to their type (blue=muon, green=electron, red=proton, cyan=pion). A full kinematical reconstruction (fit) of such events will yield information on the exclusive interactions cross-sections of secondary particles of lower momenta.

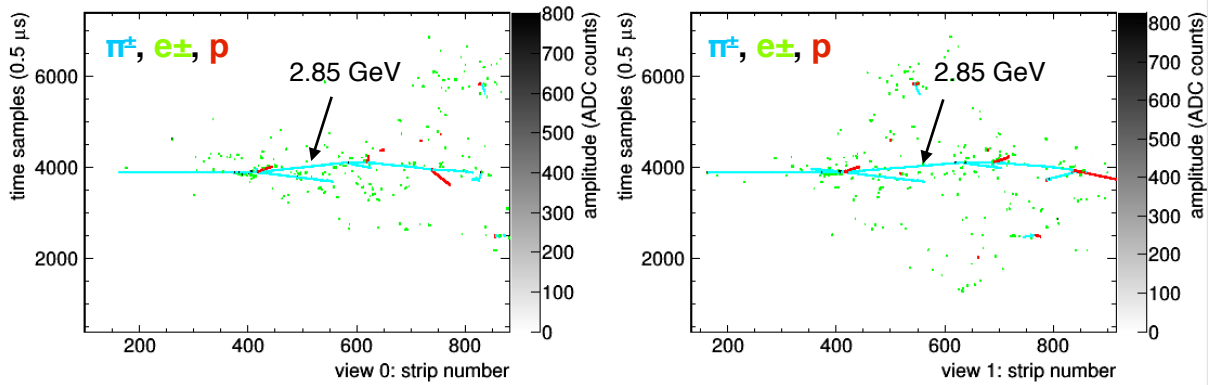


FIG. 11: A 5 GeV pion interaction, where a secondary pion of 2.85 GeV reinteracts in the detector.

2.4 Development and proof-check of industrial solutions

Several years of studies and engineering efforts in the context of the LAGUNA/LBNO design studies (funded by EC) have led to the conceptual design of the 20 and 50 kton GLACIER detectors. Further steps beyond these efforts require the actual demonstration of the techniques on a smaller scale, ideally in an optimal laboratory environment as CERN. The technical goals are to develop and assess the design in view of an extrapolation to tens of kton mass scales and a long-term stable operation (>10 years), as necessary to accomplish the LBNO physics programme [1]. One fundamental issue is the drift length, whose optimisation involves the interplay of several technical components, such as the high-voltage (for the drift field), the purity, the mechanical aspects of the field cage, etc. It can only be addressed with a prototype with a drift length of several meters. To test the feasibility and the performance of an ultimate drift length of 20 m [2], a minimum length of 6 m is required, where the longer drift conditions expected at a drift field of 1 kV/cm can be reproduced by the shorter drift length of 6 m at a field of about 0.3 kV/cm. From the technological point of view the most urgent questions to be addressed are summarised in the following:

- **Very high purity.** The drift of ionization electrons over a distance of 20 m requires a very clean environment, with impurities at the level of 100 ppt O₂ equivalent for an electron lifetime of 3-10 ms. While this has been achieved on small prototypes, this will be the first test with a

large scale non-evacuatable prototype and the same tank construction technique foreseen for the far detector.

- **Large field cage.** This is a large and hanging structure with demanding requirements on its mechanical precision and capable of sustaining a large potential difference (up to 500 kV).
- **Very high voltage generation.** A very low noise and stable power supply able to reach 600 kV to generate an uniform drift field of 1 kV/cm (300 kV power supplies with the required specification are commercially available).
- **Large area micropattern charge readout.** A large 36 m² surface will be instrumented with a charge sensitive device providing gas amplification in ultra pure argon vapour.
- **Cold front-end charge read-out electronics.** A good S/N is crucial to reach the required physics performances, especially for the low energy neutrino physics. An innovative solution with preamplifiers located as close as possible to the charge-sensitive anode, but yet accessible without opening the inner vessel, will be tested.
- **Long term WLS coating.** A method based on WLS deposition with very long stability (> 10 years) will be implemented and tested.
- **Integrated light readout electronics.** New integrated devices will be developed for the digitisation of argon scintillation light, scalable to very large detectors.

3 DLAr Detector overview

3.1 Design concept of the $6 \times 6 \times 6\text{m}^3$ prototype

The $6 \times 6 \times 6\text{m}^3$ prototype is illustrated in ???. Following the GLACIER concept, the LAr detector has the shape of a vertically standing volume, where electrons are drifted vertically towards the liquid-vapor interface, extracted from the liquid into the gas phase, amplified and collected at a segmented anode [23–25]. The main parameters are summarised in Table I. The horizontal and vertical sections are shown in ?????.

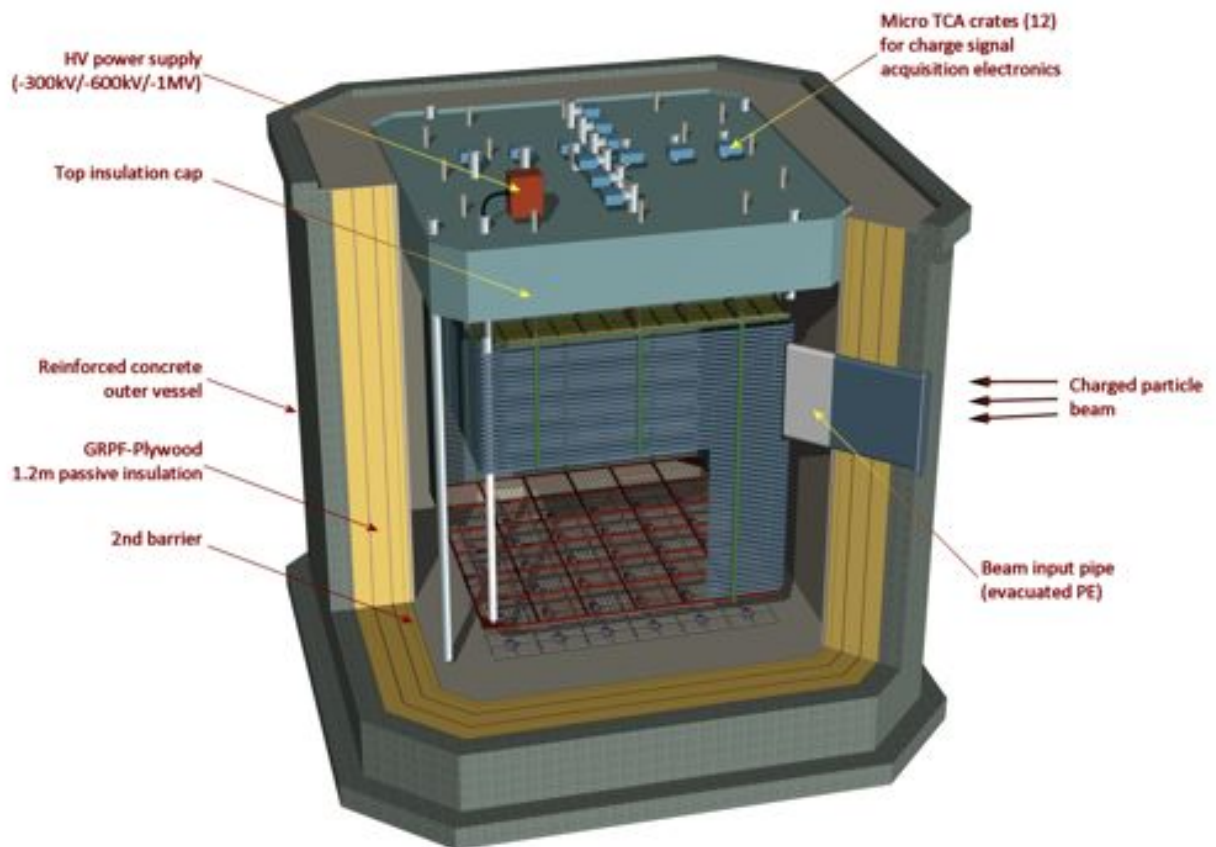
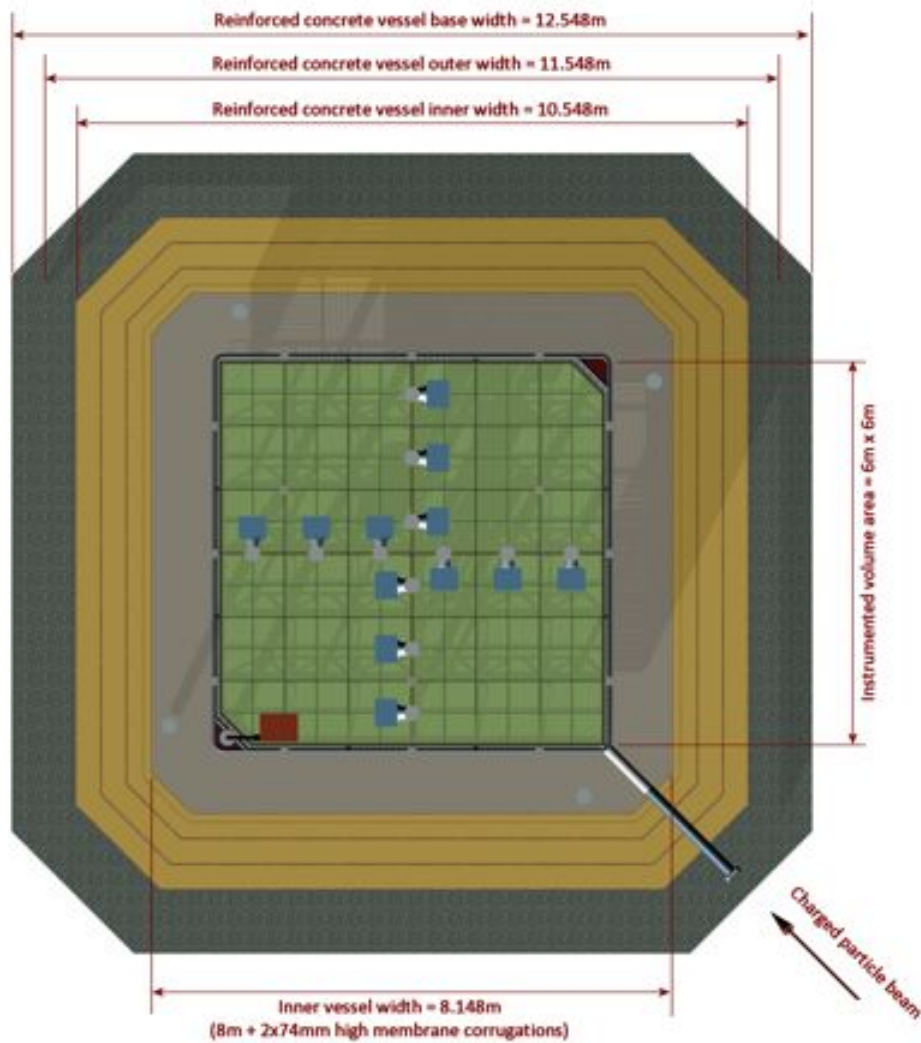


FIG. 12: Illustration of the $6 \times 6 \times 6\text{m}^3$ with the inner detector inside the cryostat.

The uniform drift field is created by a field cage composed of several equally-spaced stainless-steel tubes, held in place by insulating mechanical structures which are hanged from the top cap of the vessel. The anode deck is also suspended with stainless-steel ropes linked to the top roof. The bottom field is closed by a transparent cathode and the top field by an anode, which also serves as the charge readout. The light readout consists of PMTs uniformly distributed below the cathode.

Liquid argon density	T/m ³	1.38
Liquid argon volume height	m	7.6
Active liquid argon height	m	5.99
Hydrostatic pressure at the bottom	bar	1.03
Inner vessel size (WxLxH)	m ³	$8.3 \times 8.3 \times 8.1$
Inner vessel base surface	m ²	67.6
Total liquid argon volume	m ³	509.6
Total liquid argon mass	t	705
Active LAr area	m ²	36
Charge readout module ($0.5 \times 0.5 \text{ m}^2$)		36
N of signal feedthrough		12
N of readout channels		7680
N of PMT		36

TABLE I: Main parameters of the LBNO prototype.

FIG. 13: Plan view section of the $6 \times 6 \times 6\text{m}^3$.

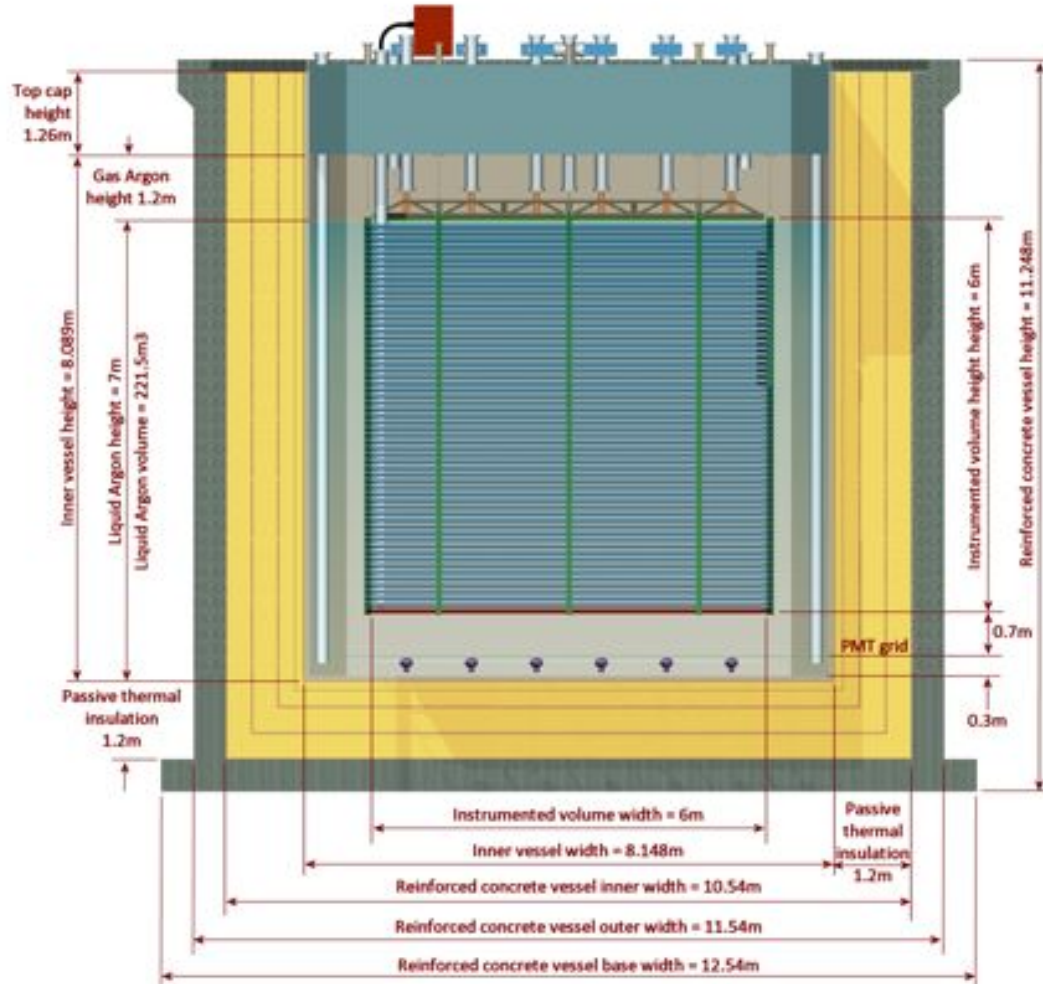


FIG. 14: Vertical cross section of the $6 \times 6 \times 6 \text{ m}^3$.

The detector is configured as a $6 \times 6 \times 6 \text{ m}^3$ liquid argon TPC with liquid-to-gas ionisation electron extraction and multiplication before collection. The ionisation charge is collected in a 2-dimensional readout plane on the top of the volume with an area of $6 \times 6 \text{ m}^2$ and finely segmented with a 3 mm strip pitch. The full active volume of $\sim 216 \text{ m}^3$ is under an uniform electric field $E \approx 0.5 - 1.0 \text{ kV/cm}$ generated from a bottom cathode plane (also $6 \times 6 \text{ m}^2$) operated at $\approx 300-600 \text{ kV}$ and kept uniform by a stack of field shaping electrodes (round pipes along a square path, with rounded corners) polarised at linearly decreasing voltage from the cathode voltage to ground.

The cathode plane is gridded and transparent to light to allow the detection of the scintillation light by an array of photomultipliers located at a distance of $\sim 1 \text{ m}$ under it. Ionization charge signals

are sent to a set of signal feedthroughs (12), located on the top face of the hosting LAr vessel and hosting the cold readout electronics. Other chimneys/feedthroughs are foreseen for HV (1 or 2), top readout plane suspension and level regulation (3), PMT high voltage and signal readout (4), monitoring instrumentation (level, temperature, 1 or 2). The front-end electronics is based on analog preamplifiers implemented in CMOS ASIC circuits for high integration and large scale affordable production. The baseline design is to integrate this electronics on the feed-through flange terminating the chimneys on the roof of the tank, under the insulation layer in order to be cooled to a temperature near that of liquid argon. Cathode and field shaping electrodes are kept in their position by a set of insulating supports/spacers resting on the inner vessel floor. The inner vessel has a cubic shape with chamfered vertical edges. Its walls are built with the so-called corrugate membrane technique, to compensate thermal shrinkage. A manhole and a detail-introduction hole are located in its top face. Thermal insulation is passive, based on GRPF (glass reinforced polyurethane foam) layers, interspersed with pressure distributing layers of plywood. Its thickness and composition are such to reach a residual heat input of 5 W/m^2 . The estimated total heat input including also the losses through the feed-throughs, cables, etc., and introduced by the LAr process, is $\sim 4 \text{ kW}$ at liquid argon temperature, to be dissipated by cryocooler(s). The passive insulation is contained in a reinforced concrete “vessel” with $\simeq 0.5 \text{ m}$ thick walls. The top outer ceiling is made by a framework reinforced stainless steel plane, able to support the inner anode and outer instrumentation (electronics, cryogenics, control).

A charged beam pipe (evacuated) is indicated as crossing the concrete outer vessel and the thermal insulation layers. Its vertical orientation is adapted to the charged beam vertical axis in its last section.

3.2 Liquid argon as detector medium and electron drift

Liquid argon, and liquid noble gases in general, have interesting properties for detecting particles, what makes them a good choice as target material. A summary of the most important argon properties is given in ???. Because of its density of 1.4 g/cm^3 , liquid argon is a good stopping material with an average energy loss dE/dx of 2.12 MeV/cm for a minimum ionizing particle (mip). Also, an interaction of a particle with an argon atom excites it and creates scintillation light, or the atom is ionized. The mean excitation energy of $W_\gamma = 19.5 \text{ eV}$, and the mean ionization energy $W_{ion} = 23.6 \text{ eV}$, give a very good energy resolution also for detecting low energetic particles. The possibility to drift charges within the liquid noble gas along the electric drift field, without big diffusion, gives the option to read out ionising tracks with a high spacial resolution. The basic principle of every time projection chamber is that free charge carriers are produced in a relatively large volume and then drifted towards an electrode. The time needed between the initial ionisation and the moment the signal is read out from

General properties	
Atomic number	18
Molecular weight	39.948 g/mol
Most important stable isotopes	³⁶ Ar (0.34%) ³⁸ Ar (0.06%) ⁴⁰ Ar (99.60%)
Concentration in air	0.934%
Melting point (1 atm)	83.8 K
Boiling point (1 atm)	87.3 K
Triple point	83.8 K and 0.687 bar
Ratio LAr/GAr (1 atm)	835 vol/vol
Gaseous phase properties	
Gas density (at boiling point resp. 15 °C)	5.85 resp. 1.67 kg/m ³
Heat capacity at constant pressure C_p (1 bar and 25 C°)	0.02 kJ/mol · K
Heat capacity at constant volume C_v (1 bar and 25 C°)	0.012 kJ/mol · K
Thermal conductivity of GAr (1 atm and 273 K)	16.36 mW/m · K
Thermal conductivity of GAr (boiling point and 1 atm)*	5.66 mW/m · K
Ionization energy in gas W_{ion}	26.4 eV
Liquid phase properties	
Liquid density (at 87.3 K)	1392.8 kg/m ³
Latent heat of vaporization L_v (1 atm)	160.81 kJ/kg
Thermal conductivity of LAr (87.3 K)*	127 mW/m · K
dE/dx_{min} for mip	2.12 MeV/cm
Ionization energy in liquid W_{ion}	23.6 eV
Excitation energy W_γ	19.5 eV
Maximum of emission spectrum	~ 128 nm
Radiation length X_0	14 cm
Molière radius	9.28 cm
Nuclear interaction length	84 cm
Maximal breakdown strength	1.1 – 1.4 MV/cm

* Value linear extrapolated from [39]

TABLE II: Physical and chemical properties of argon.

the electrode defines, together with the drift velocity, the distance between the interaction and the electrode along the lines of the electric field. In case of the double phase LAr TPC, the drift velocity in gas argon as also in liquid argon have to be taken in account.

Argon is a byproduct from the air liquefaction process and therefore relatively cheap compared to other noble gases. This makes it the only viable candidate for very large detectors of several tens of kilotons of active volume.

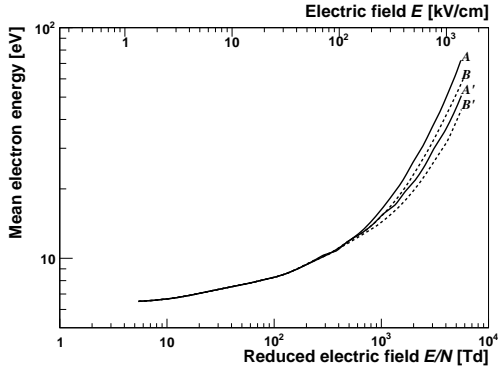


FIG. 15: The mean energy in argon gas as a function of the external (reduced) electric field. In case A, both the elastic and inelastic scatterings are according to the elastic differential cross-section. In case B the inelastic scattering is isotropic. A and B are the values before and A' and B' after scattering [41]. The scale of the electric field E is given for 1 bar and 20 °C.

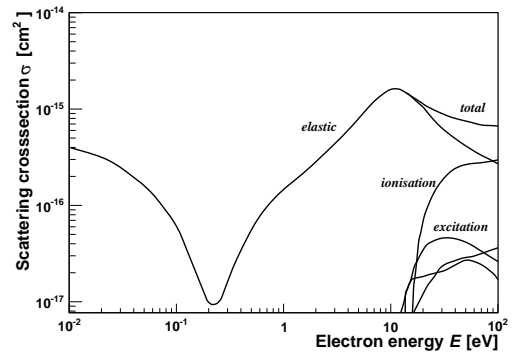


FIG. 16: The cross-section between electrons and argon gas as a function of the total energy of the electron, calculated with Magboltz [42]. Clearly visible is the Ramsauer-minimum around 0.2 eV.

3.3 Drift velocity and diffusion in argon gas

Applying an electric field, the electron is drifted along the field line and the total energy depends on the electric field strength as shown in ???. The Figure is normalized to a reduced electric field E/N with Townsend unit ($\text{Td} = [E/N] = 10^{-17} \text{ V cm}^2$), where E is the electric field and N the molecular density. The top label indicates the values for SATP conditions (Standard Ambient Temperature and Pressure: 20 °C and 1 bar).

For electrons drifting in gas, the energy gained between two collisions is, because of their small mass, rather large. The drift velocity hence depends strongly on the total scattering cross-section between the electrons and the atoms of the medium, as shown in ???. It is not uniform but has a minimum around ~ 0.2 eV caused from quantum mechanical effects (Ramsauer-minimum [40]). In the energy range relevant for the drifting electrons, there is mainly elastic scattering. In a first approximation the drift velocity u is given by the acceleration in the electric field E and the characteristic time τ_c between two collisions

$$u = \frac{e E \tau_c}{m} \equiv \mu E \quad (3.1)$$

where μ is the mobility. The characteristic time τ_c is a function of the electric field E [43]. This is only an approximation since it is assumed that the electron completely stops after each interaction. An actual measurement of the drift velocity is reported in [44] and shown in ???.

An important property is the electron cloud diffusion. In case of an electric field, we have to distinguish between the diffusion in drift direction and the diffusion normal to it. The longitudinal

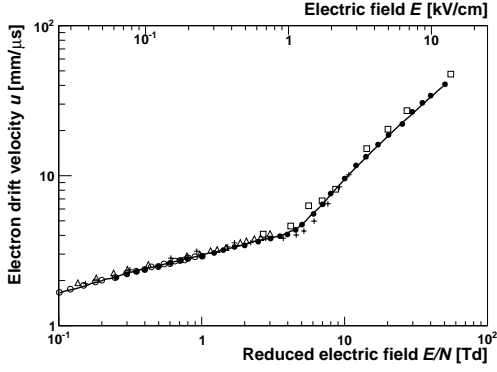


FIG. 17: The electron drift velocity u in gaseous argon as a function of the normalized electric field ($[Td] = 10^{-17} Vcm^2$) according to [44]. The scale for the electric field E is derived for SATP conditions.

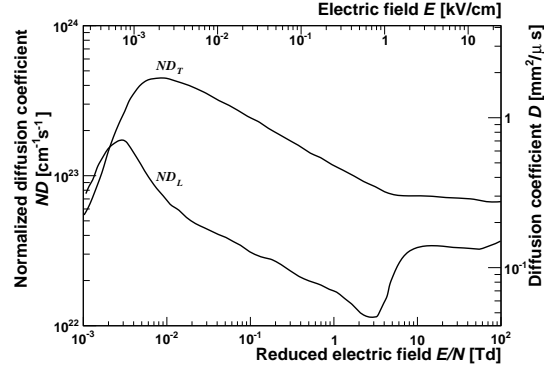


FIG. 18: The normalized longitudinal and transversal diffusion coefficient ND for gaseous argon according to [45]. The scale of the diffusion coefficient D and the electric field E are under SATP conditions.

and transversal diffusions are given by

$$\sigma_{l,t}^2 = 2D_{l,t} t = 2D_{l,t} L/u \quad (3.2)$$

where L is the drift length, u the drift velocity along the electric field lines and $D_{l,t}$ the diffusion coefficients in longitudinal and the transversal directions, respectively. As shown in ??, the diffusion coefficients are depending on the electric field. Also it is shown that for low electric fields the diffusion in the transversal direction is almost one order of magnitude bigger than the one in longitudinal direction.

3.4 Drift velocity and diffusion in liquid argon

The liquid phase changes the properties for drifting electrons. Electrons drift through a non-polar medium and locally, the argon atoms are polarised by the charge. The local field is no longer only given by the distance between the electron and the scattering atom but also by the sum of all other fields due to the induced dipoles in the neighbouring atoms. This interaction changes the scattering cross-section and the Ramsauer-minimum disappears [46]. Other parameters besides the electric field affect the drift velocity. A relatively large effect is due to the temperature of the liquid argon. In [47] an average temperature gradient of u has been reported to be

$$\frac{\Delta u}{\Delta T \cdot u} = (-1.72 \pm 0.08) \% \cdot K^{-1} \quad (3.3)$$

Experimentally, the drift velocity of electrons in liquid argon is measured by their drift time in a known electric field. One possibility for the measurement is to use crossing muons through the detector.

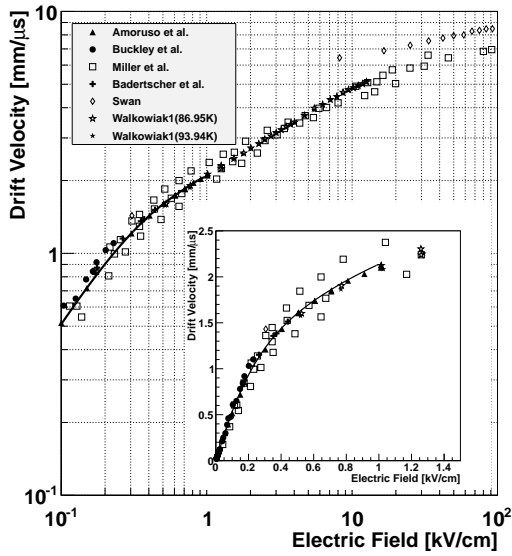


FIG. 19: Drift velocity in liquid argon for fields up to 100 kV/cm. The general plot (data collected from [47, 49–53]) is in log-scale to give a good overview, while the zoom-in, in the interesting region of the electric field for ArDM, is in linear scale. The solid line is a 5th order polynomial proposed by [49]. It is fitted between 0 and 2 kV/cm and includes all the presented data. All data are corrected according to Eq. ?? to a common temperature of 87 K.

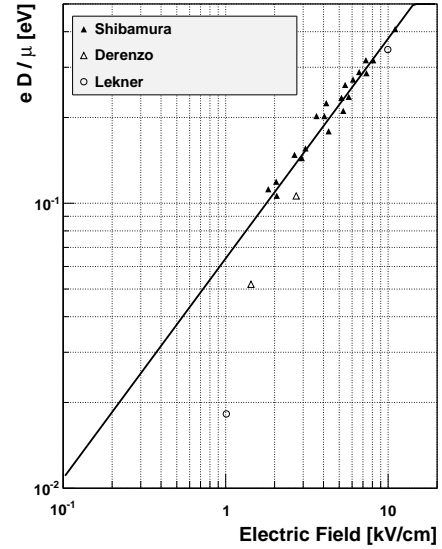


FIG. 20: Field dependence of the ratio $\frac{eD}{\mu}$ in liquid argon [54], where D is the diffusion coefficient and μ the electron mobility. The different sets of data are described in [54].

There is a trigger on the primary scintillation light and the stopping trigger is either on secondary scintillation light or on the charge extracted and read out by an anode [48]. Another option is to knock out the electrons from the HV cathode by the use of a laser [47] or a pulsed xenon lamp [49]. The trigger is the pulse from the cathode when an electron is knocked out, and, as a stopping signal, again the arrival of the charge on the anode is used. ?? shows the drift velocity as a function of the electric field, compiled from the literature [47, 49–53]. The data from the different sources are corrected to a common temperature of 87 K and fitted with a polynomial function [161], as proposed by [49].

The electron cloud diffusion in the liquid is an important parameter to determine the maximum drift length of a detector, which is presently not fully known experimentally. The theoretical background for diffusion is similar to the diffusion in gas. It is derived from Einstein’s theory about the molecular kinetic motion of particles suspended in a fluid [55]. Electrons in the liquid and with an electric field below ~ 200 V/cm can be assumed to be thermal electrons, and the ratio between diffusion coefficient and mobility is given by:

$$\frac{eD}{\mu} = kT = \frac{2}{3} \langle \epsilon \rangle \quad (3.4)$$

where D is the diffusion coefficient. ?? shows the ratio $\frac{eD}{\mu}$ as a function of the electric field measured by [54]. The transversal diffusion σ_t can be derived by multiplication of the coefficient with the electron mobility μ and dividing it by the drift velocity u (Eq. ??). The expected diffusion is shown as a function of the drift distance in ??, assuming different electric drift fields ranging from 0.5 to 1.5 kV/cm. For the needed ratio of the diffusion coefficient and the mobility, the data presented in [54] and shown in ?? are fitted with a simple power law, $eD/\mu = 0.064 \cdot E^{0.77}$ where E is the electric field in kV/cm. This might not be true for low electric fields, as shown by the data points in ??, but the proposed function is giving an upper limit of the ratio. The points measured at lower electric field(empty triangle) might be too low due to space charge effects [54]. The empty circles are theoretical values derived from Eq. ?? with $\langle \epsilon \rangle$ -values calculated in [46].

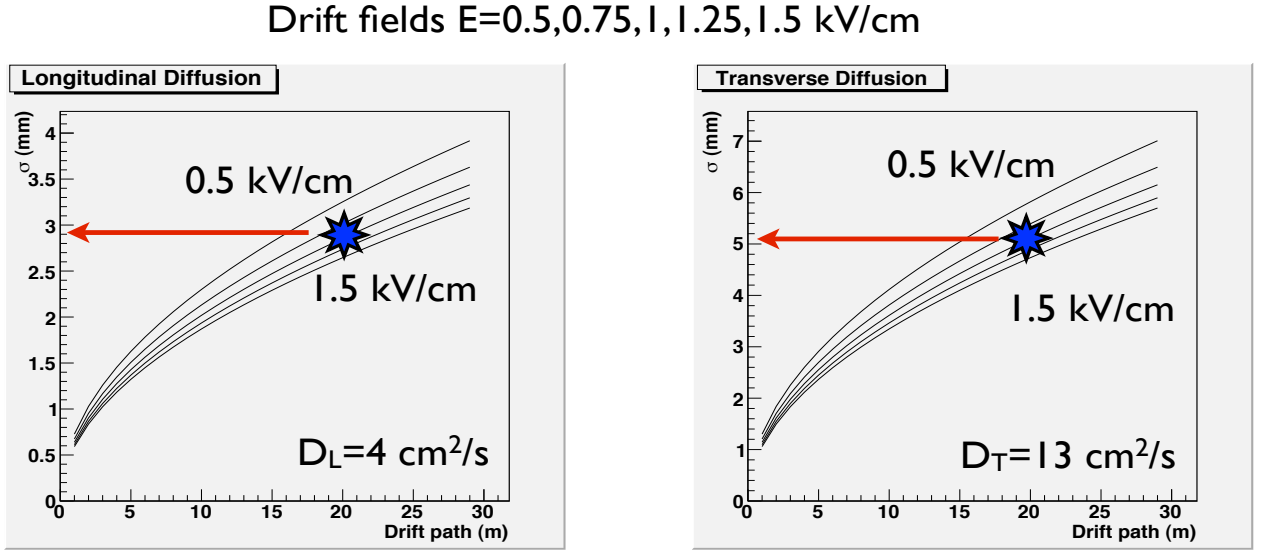


FIG. 21: Expected longitudinal and transversal diffusion in liquid argon as a function of the drift distance, for various drift fields.

From ?? it is clear that even for long drifts of 10 or 20 m the diffusion is still small and a charge readout with a pitch of the readout of ~ 3 mm can be used. Electric drift fields in the range 0.5-1 kV/cm are optimal from the point of view of the resolution and are sufficient for a wide range of detectors, up to a total drift length of up to 20 m [2]).

The $6 \times 6 \times 6\text{m}^3$ will be a fundamental tool to investigate experimentally the effect of very long drift distances. To reach a goal corresponding to drift times of about 10 ms, one is considering a shorter drift distance with a reduced drift field in order to obtain similar drift times and therefore similar diffusions.

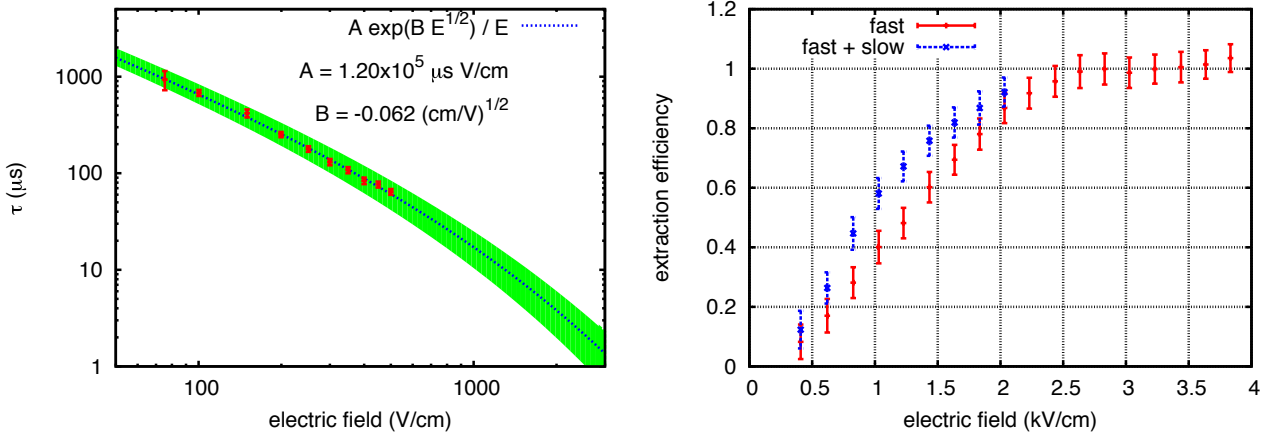


FIG. 22: The left picture shows the dependence of the extraction time on the electric field in liquid argon ($T = 87.4 \text{ K}$) as reported in [58]. The picture on the right [57] shows the extraction efficiency for fast and slow components as a function of the electric field in liquid argon ($T = 90 \text{ K}$). As described in the paper, due to limitations of the electronics the measurement of the slow component has a semi-qualitative character.

3.5 Electrons extraction

The $6 \times 6 \times 6 \text{ m}^3$ will be operated in double-phase conditions [23–25], involving the transfer of the electron cloud from liquid to the gas phase. The transfer of electrons in excess from a condensed non-polar fluid to its saturated vapor using an electric field is a phenomenon investigated since the seventies [56]. In particular, in argon it is experimentally shown that the electrons are extracted in two stages. Near the triple point part of the charge is emitted on time scales that can be as high as 1 ms, strongly dependent on the electric field applied [57, 58], while at larger temperatures the emission takes less than 100 ns. At high electric fields the slow extraction time reduces, and the fraction of the slowly extracted electrons becomes negligible (see Figure 22). This behavior can be understood in the framework of the Schottky model of electric field enhanced thermionic emission [59].

An electron in the vicinity of a dielectric surface feels the force of the charge induced on the surface by its presence. In analogy to a conductor surface one can compute, with a method similar to the mirror charge method [60], the potential energy of the electron. In the presence of an external electric field orthogonal to the liquid-vapor interface of argon, the energy potentials in the liquid (Φ_l) and in the vapor (Φ_v) as a function of the vertical position z (the surface is set at $z = 0$) are [57, 58, 61]:

$$\Phi_l = -V_0 - q_e \mathcal{E}_l z - A_l / z \quad \text{and} \quad \Phi_v = -q_e \mathcal{E}_v z - A_v / z,$$

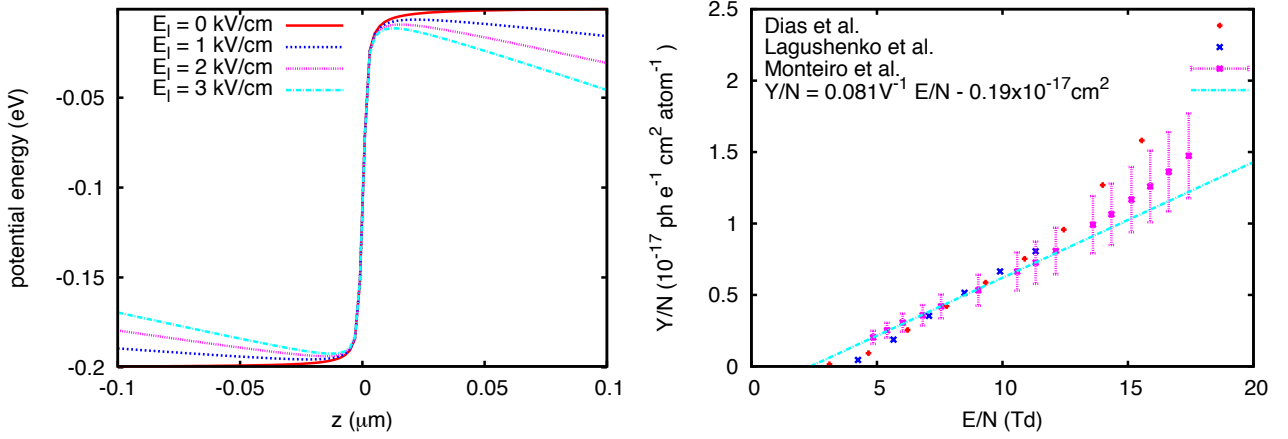


FIG. 23: Left: potential energy of an electron at the liquid vapor interface (at $z = 0$). Right: reduced proportional scintillation yield in pure argon gas simulated by Lagushenko and Dias [62, 63] and measured by Monteiro and collaborators [64].

with

$$A_l = \frac{q_e^2}{16\pi\epsilon_0\epsilon_l} \frac{\epsilon_l - \epsilon_v}{\epsilon_l + \epsilon_v} \text{ and } A_v = A_l\epsilon_l/\epsilon_v,$$

where the terms inversely proportional to z are due to the presence of the dielectric, $-q_e$ is the charge of the electron, \mathcal{E}_l and $\mathcal{E}_v = \mathcal{E}_l\epsilon_l/\epsilon_v$ are the electric fields in the liquid and in the vapor respectively, ϵ_l and ϵ_v are the dielectric constants of the liquid and of the vapor respectively, ϵ_0 is the permittivity of the vacuum, $-V_0$ is the minimum of the conduction band in the liquid with respect to the vapor (about -0.2 eV [61]). The discontinuity of the potential on the surface is unphysical, but also not relevant for the discussion. The regulated potential around $z = 0$ is shown in the plot on the left in Figure 23 for different externally applied electric fields.

The minimum and the maximum of the potential in the liquid and in the vapor phase are:

$$\begin{aligned} \Phi_l^{min} &= 2\sqrt{A_l q \mathcal{E}_l} - V_0, & \text{for } z_l^{min} &= -\sqrt{A_l/(q\mathcal{E}_l)}, \\ \Phi_v^{max} &= -2\sqrt{A_v q \mathcal{E}_v}, & \text{for } z_v^{max} &= \sqrt{A_v/(q\mathcal{E}_v)}. \end{aligned}$$

It is interesting to notice that the presence of the electric field reduces the potential barrier by:

$$\Delta\Phi = 2(1 + \epsilon_l/\epsilon_v)\sqrt{A_l q \mathcal{E}_l},$$

so that the gap becomes $V = V_0 - \Delta\Phi$.

An electron with momentum p_z perpendicular to the liquid argon surface for which $p_z^2/(2m_e) > V$

(with m_e the mass of the electron) is transferred to the vapor. The electrons with kinetic energy $T > V$, but not satisfying the requirement on p_z , are reflected towards the liquid. They undergo several elastic collisions that randomize the momentum direction almost without loss of energy, and they reach the liquid surface again. If p_z is not yet big enough, they repeat the process until all electrons are extracted in few tens of nanoseconds. These are the so called *hot* electrons (or fast component).

The electrons with $T < V$ are thermalized on the liquid surface and are emitted according to the thermionic emission with a characteristic time that depends on the energy gap [58]. These electrons are the *cold* ones (or slow component).

The electrons in liquid argon gain energy from the electric field. At around 1 kV/cm, the electron average kinetic energy is of the order of 0.1 eV [46, 65], larger than the thermal energy and comparable to the liquid-vapor interface energy gap.

The experimental facts can be summarized and explained:

1. at low temperature the electrons are emitted also slowly because their energy is not always larger than the potential barrier,
2. increasing the electric field the fraction of electrons with energy above the potential barrier increases,
3. the extraction time for the *cold* electrons decreases at high field because the energy gap reduces.

The electrons can be trapped by electronegative impurities diluted in the liquid argon and never be emitted in the vapor. Similarly to what happens to the scintillation light in the presence of impurities, the amount of charge extracted decreases by a factor $\tau_{imp}/(\tau_{ext} + \tau_{imp})$, and the effective extraction time can be written as $\tau_{ext}^{eff} = (1/\tau_{ext} + 1/\tau_{imp})^{-1}$, where τ_{ext} is the extraction time with no impurities and τ_{imp} is inversely proportional to the electronegative impurity concentration.

3.6 Scintillation in liquid and gas phases

Ionizing radiation in liquid noble gases leads to the formation of excimers in either singlet or triplet states [66, 67], which decay radiatively to the dissociative ground state with characteristic fast and slow lifetimes ($\tau_{fast} \approx 6$ ns, $\tau_{slow} \approx 1.6\mu\text{s}$ in liquid argon with the so-called second continua emission spectrum peaked at 128 ± 10 nm [68]). This prompt 128 nm scintillation light is exploited in liquid Argon TPCs to provide the absolute times (T_0) of the ionisation signals collected at the anode, thereby after matching providing the absolute value of the drift coordinate of fully contained events, as well as a prompt signal used for triggering purposes.

The proportional scintillation in argon, also referred to as secondary scintillation and luminescence, is the phenomenon of generating photons in gas or vapor in the presence of free charges and an electric field. In a defined electric field window, that depends on the density of the argon, the amount of photons is proportional to the number of electrons, to the electric field and to the length of the path covered by the electrons.

The electric field range is defined such that between two successive collisions the drifting electrons, accelerated by the electric field, gain enough energy to excite argon atoms, but not ionize them. In the case the electric field is lower, no photons are produced, in the case it is larger, because new charge is created, the amount of light grows nearly exponential with the field and the path length. For the discussion on the charge amplification in gas, see ??.

In order to take into account the argon density, the quantity used is the reduced electric field, defined as the electric field divided by the argon atomic density ($1 \text{ Td} = 10^{-17} \text{ V cm}^2$), and the reduced light yield, defined as the number of photons produced per electron per unit path length divided by the argon density. On the right of Figure 23 the simulated [62, 63] and measured [64, 69] reduced light yield at room temperature and pressure are plotted versus the reduced electric field. The measured proportional scintillation threshold and ionization threshold are respectively 2.34 Td and 12.4 Td [69], slightly lower than the simulated ones, but still in good agreement.

The electrons, when extracted from the liquid argon to the vapor, produce proportional scintillation. From the data at room temperature and pressure one can extrapolate that in an electric field of 4.5 kV/cm, corresponding to an extraction field of 3 kV/cm in liquid, over 1 cm one electron generates about 200 photons. Since the total amount of light produced is proportional to the charge extracted, this method is used by some double phase noble gas experiments for the direct Dark Matter searches [70–72] to detect the ionisation charge. In the $6 \times 6 \times 6 \text{ m}^3$, they will be detected by the scintillation light system to provide a secondary trigger.

3.7 Charge amplification in gas - Townsend avalanche

In a gas an electron accelerated under the action of an electric field (E) gains energy that is released in collisions against neutral atoms. In addition to the diffusive random motion of the electron, the net drift velocity (u) in the direction of the field (but opposite) is obtained. Under the assumption that the duration of the scattering is short compared to the average time between collisions τ_c , and that the electrons undergo elastic collision only, so that the absolute magnitude of their speed does not change appreciably (the mass of the atom is much larger than the electron mass), the drift velocity can be written as in Eq. ?? [73]. τ_m is inversely proportional to the gas density ρ and the momentum transfer

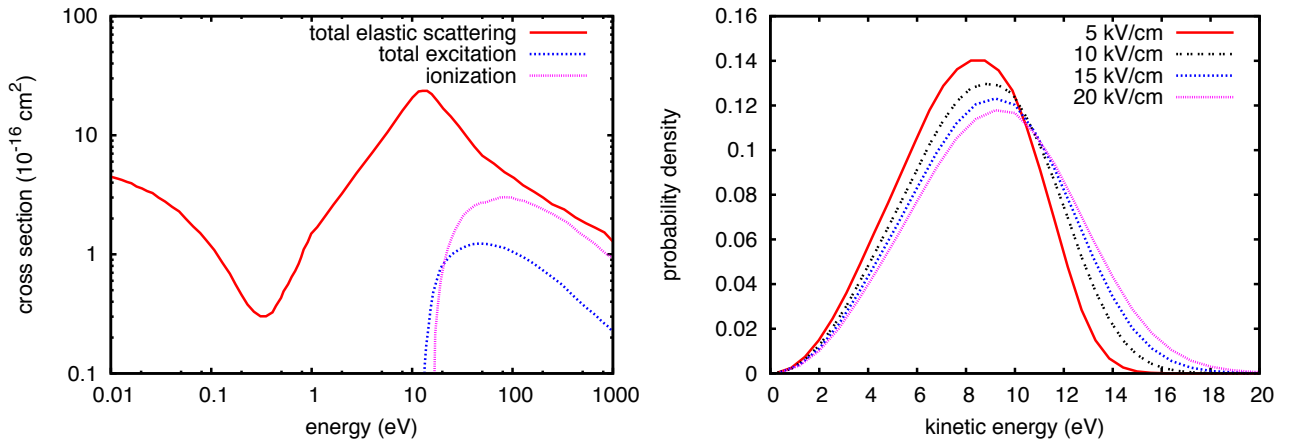


FIG. 24: Left: electron argon atom cross sections for different kind of interactions [75]. Right: energy distribution of free electrons under the action of an external electric field in pure argon gas at 1 atm and 20° C simulated with Magboltz 8.4 [74].

cross-section σ_m [73]. In general, it depends on the energy of the electrons and therefore on E . This makes u proportional to E only for low electric fields. The kinetic energy due to the drift is much smaller than the kinetic energy due to thermal motion. A more realistic computation should take into account the details of the electron velocity distribution. The kinetic energy of the electrons increases by (1) decreasing the gas density and the electron-atom cross section and (2) increasing the electric field. In other words, the peak of the electron energy distribution moves to higher energies with the increase of the electric field, as shown in the right plot of Figure 24. It displays the results of a computation done using Magboltz 8.4 [74] in pure argon gas at 1 atm and 20° C. Magboltz calculates diffusion coefficients, drift velocities and first Townsend coefficients (see later in the text) for gas mixtures in the presence of electric and magnetic fields. The program inputs are tables of cross sections like the one reported on the left plot of Figure 24, provided in [75].

The high energy tail of the electron energy distribution extends beyond the first ionization potential, that for the argon is about 15.7 eV [76]. This means that a fraction of collisions gives rise to ionization of neutral atoms and to the production of new free electrons. This process is called Townsend avalanche and is at the base of all the signal amplification techniques in gas chambers. The larger the electric field is, the more populated becomes the tail above the ionization energy, and the larger the ionization rate is. When the electric field is high enough that the majority of the electrons have an energy above the ionization potential, the ionization rate saturates, and its behavior reflects the ionization cross section dependence on the electron energy. The first Townsend coefficient (α) is the quantity that describes the number of ion-electron pairs created by an electron per unit drift length. A very useful empirical approximation of the first Townsend Coefficient as a function of the electric field and the gas density

is:

$$\alpha(\rho, E) = A\rho e^{-\frac{B\rho}{E}}, \quad (3.5)$$

where A and B are constants depending on the gas. The expression α/ρ is a function of E/ρ (also called reduced electric field). The reason of this comes from the following considerations:

1. The electron mean free path (λ) can be written as $(\sigma\rho)^{-1}$, where σ is the electron-atom total cross section (generally dependent on the electron energy, see Figure 24).
2. The energy gained by a free electron between two collisions is proportional to the product of the electric field E and the mean free path λ , i.e. $E/(\sigma\rho)$.
3. $\alpha\lambda$, i.e. $\alpha/(\rho\sigma)$, can be regarded as a quantity proportional to the number of electron-ion pairs produced by an electron *per collision*.

Given a defined gas, in conditions where E and ρ are changed, but E/ρ is kept constant, the electron-atom collisions are not distinguishable, i.e. same energy and, therefore, same ionization probability per collision (proportional to α/ρ). For the very weak assumption that the mean free path of the electrons is much smaller than the size of the avalanche, the total number of electrons n_e created along a drifting electron path \mathcal{S} starting from n^0 electrons can be written as:

$$n \equiv Gn^0 = n^0 \exp \left[\int_{\mathcal{S}} \alpha(E(s)) ds \right], \quad (3.6)$$

and G is the gain, under the assumption that the gas amplification device is operated in proportional mode, meaning that the detected charge is proportional to the initial charge. In a parallel plate gap of length x with a uniform electric field, where the Townsend coefficient is constant, the gain is:

$$G = e^{\alpha x}. \quad (3.7)$$

The above cited quantities must be considered as average values. In fact, the Townsend avalanche is a stochastic process with the following behavior. When $n_e < 10^5$, the number of electrons involved in an avalanche generated by a single electron follows the so called Furry distribution [77]. The probability that an electron frees a second electron traversing an infinitesimal distance dx is αdx . As computed in [78], given one initial particle entering into the uniform field of the multiplication region,

the probability that n particles emerge is

$$P(n) = (1 - 1/G)^{n-1}/G.$$

The most probable number of particles at the end of the path is one, the average is $G = e^{\alpha x}$, and the variance is $G^2(1-1/G)$. For large gains the standard deviation of the distribution can be approximated with G , and for the central limit theorem, given a large number n_e^0 of electrons at the beginning of the multiplication path, the distribution of the number of emerging electrons is a Gaussian with average Gn_e^0 and standard deviation $G\sqrt{n_e^0}$. To be noticed is that the relative width of the distribution is independent of the gain, and it decreases the larger the number of electrons at the beginning is.

While the gain is mainly due to the described Townsend mechanism, also secondary effects, caused by the simultaneously produced ions and photons have to be taken into account: although the energy of the produced scintillation light is not sufficient to ionize directly argon atoms, photons can extract electrons from electrodes by photoelectric effect. A similar feedback, though much slower, is due to back drifting ions, which can eject further electrons when they impinge on the collection electrode. Obviously any of the described feedback mechanisms can turn into a continuous current, that may lead to the formation of an electron-ion plasma or a *streamer*. Due to the fact that such a streamer persists until the amplification device is completely discharged, a detector would be paralysed until the fields are back at the working point. As a consequence of the heat production, heavy discharges may also damage the amplification device. In order to decrease the rate of discharges or to increase the maximum achievable stable gain, typical gas detectors work with a gas mixture, including a so-called quench gas that absorbs scintillation light and thus reduces the feedback. However, since the LAr TPC requires extremely low levels of contaminations of less than 1 ppb in order to drift electrons over large distances in LAr, chemical quenchers cannot be used. In the LAr LEM TPC option described in ??, mechanical quenching is important to stabilise the system and allow high gains to be achieved.

3.8 Primary and secondary scintillation light

Primary scintillation light is produced promptly by the passage of ionising particles through the liquid argon volume. The formation of excimers in either singlet or triplet states [66, 67], which decay radiatively to the dissociative ground state with characteristic fast and slow lifetimes ($\tau_{fast} \approx 6$ ns, $\tau_{slow} \approx 1.6\mu\text{s}$ in liquid argon with the so-called second continua emission spectrum peaked at 128 ± 10 nm [68]). Secondary scintillation light is produced in the gas phase of the detector when electrons, extracted from the liquid, are accelerated in the electric field. Because the gas is less dense and the mean free path of the electron is longer than in liquid, the extracted electrons can gain enough

energy to excite argon atoms in collisions so that scintillation light appears. For appropriate electric fields, the amount of light is directly proportional to the amount of charge. Measurements show a reduced secondary scintillation yield in pure argon per electron and per cm, according to [64]:

$$(Y/p) = (81E/p) - 47 \quad \text{photons}/(\text{electron cm bar}) \quad (3.8)$$

where $[E/p] = \text{kV}/(\text{cm bar})$. This formula is valid for room temperature. For the operation at cryogenic temperatures of about 90 K (e.g. argon vapor at 1 bar) the pressure has to be multiplied by a factor 3.36 due to the higher density.

?? shows a screenshot from the oscilloscope of a cosmic track crossing the $40 \times 80 \text{ cm}^2$ LAr LEM TPC with 60 cm drift length[23]. The track ionised a straight track through the detector. As a result, there is a continuous extraction of electrons as long as the track drifts towards the liquid-gas interface. The time between the occurrence of the primary scintillation light and the secondary scintillation light is equivalent to the drift time of the electrons from the vertex to the liquid argon surface. The yellow and red traces correspond to two PMTs located below the cathode with a timebase of $100 \mu\text{s}/\text{div}$. They show a continuous extraction signal for a total duration of $400 \mu\text{s}$, which can be translated in a drift velocity of $\sim 1.5 \text{ mm}/\mu\text{s}$. With the given electric field of $\sim 480 \text{ V}/\text{cm}$ the measurement agrees with values from literature as also the curve in ??. The violet trace is the persistence of the signals from previous events and signals after $400 \mu\text{s}$ are from pile up events.

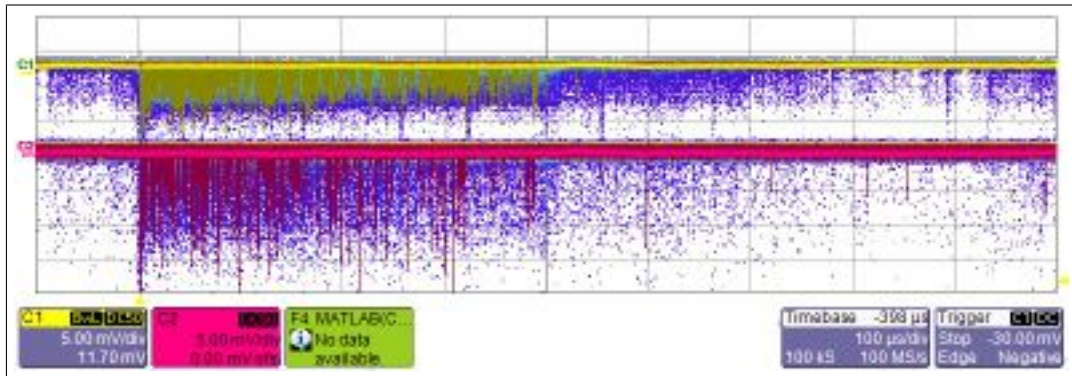


FIG. 25: Oscilloscope screen shot of the primary and secondary scintillation light of a crossing track during the operation of the $40 \times 80 \text{ cm}^2$ LAr LEM TPC with 60 cm drift length[23] (see text).

In the $6 \times 6 \times 6 \text{ m}^3$ and for an extraction field of 2.5 kV assuming the liquid level in the middle of the gap between the extraction grid and the lower electrode of the CRP, the secondary light yield is $Y \approx 75 \gamma/e$. In addition, the avalanche inside the LEM holes create light.

3.9 Electron attachment to impurities

The amount of charge collected at the anode is affected by the amount of electronegative molecules (for example O₂) dissolved in the liquid argon. By capturing free electrons these latter become negative ions which slowly drift towards the anode. Due to their larger mass and scattering cross-section with the argon atoms, they move much slower than electrons. Attached electrons therefore do not contribute to the readout signal. Thus, purity is a fundamental requirement and a possible contamination has to be kept at an extraordinary low level. This means the vessel needs to be sealed and absolutely vacuum tight, with a typical leak rate upper limit of 10⁻⁹ mbar l s⁻¹ to prevent molecule contaminants from entering the argon volume.

In practice, the most common impurities in the welding-grade liquid argon are oxygen, nitrogen and water. In absence of leaks to the outside, the majority of the electronegative impurities come from the outgassing of the detector material itself. Special attention has to be given to composite materials like glue, for they might have chlorine or fluorine compounds. These materials must be prevented from contaminating the liquid argon, since chlorine and fluorine are the most electronegative molecules and immediately capture the drifting electrons.

In general, the attachment in liquid is a three-body process that involves the electron and the molecule to which it is attached. When attaching an electron, the molecular ion is excited and loses its energy to a third body through vibrational states [79].



where M is the electronegative molecule and X the third body, in our case the argon atom. k_s is the rate constant and it is given as a function of the electric field E by

$$k_s(E) = \int v \cdot \sigma(v) \cdot f(v, E) dv, \quad (3.10)$$

with v the electron velocity and $f(\epsilon)$ the Maxwell distribution [80]. If the capture cross section $\sigma(\epsilon)$ is a function of the energy ϵ , the rate constant is given by

$$k_s(E) = \int \sigma(\epsilon) \cdot f(\epsilon, E) d\epsilon \quad (3.11)$$

For $E = 0$ the distribution $f(\epsilon)$ is

$$f(\epsilon) = \frac{2}{\sqrt{\pi} k_B T} e^{-x} x^{1/2} \quad (3.12)$$

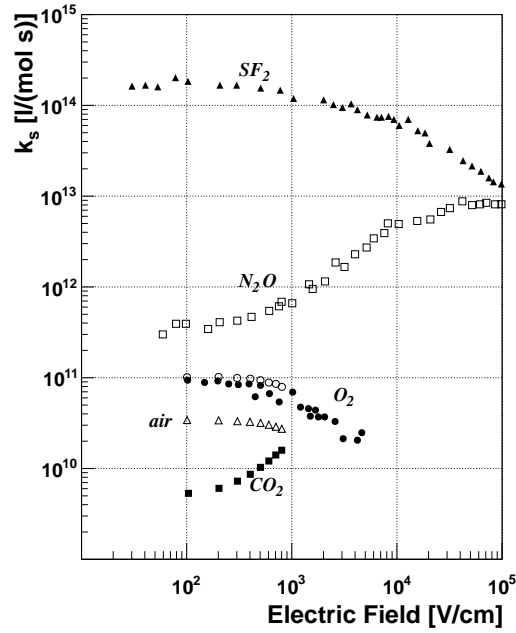


FIG. 26: Rate constant for the electron attachment to different molecules. The data points for SF_6 (\blacktriangle), N_2O (\square) and O_2 (\bullet) are from [80], the data points for O_2 (\circ), air (\triangle) and CO_2 (\blacksquare) from [81].

with $x = \epsilon/(k_B T)$. The effects of an external electric field on the rate constant k_s are described in [80] and shown in ?? for different molecules. Experimentally, the rate constant k_s can be obtained by looking at the decay of the electron current after a controlled release of electrons from the cathode or inside the liquid argon by ionization.

In case of a small number of released electrons N_e with respect to the amount of impurities N_s ($[N_s] = \text{mol/l}$), the number of electrons captured per time interval is

$$\frac{dN_e}{dt} = -k_s \cdot N_s \cdot N_e \quad (3.13)$$

and therefore, for a homogeneous impurity contamination and drift field, the number of electrons N_e as a function of time is

$$N_e(t) = N_{e0} e^{-t/\tau} \quad (3.14)$$

where τ is the mean electron lifetime and N_{e0} the initial number of released electrons. The lifetime is directly related to the amount of impurities.

$$\tau = \frac{1}{k_s N_s} \quad (3.15)$$

As shown in ??, the rate constant k_s for attaching electrons is not only depending on the kind of molecule but also on the electric field strength. For electric fields up to ~ 1 kV/cm, k_s is approximately constant for oxygen and Eq. ?? can be written as [50]

$$\tau[\mu\text{s}] \approx \frac{300}{\rho_{O_2}[\text{ppb}]} \quad (3.16)$$

where $\rho_s = N_s/N_{Ar}$ is the amount of impurities of the molecule s with respect to the amount of argon.

Recent measurements of the electron lifetime in liquid argon have brought attention to water [82]. Derived from the presented data, a lifetime of

$$\tau[\mu\text{s}] = \frac{17.4 \pm 0.5}{\rho_{H_2O}[\text{ppb}]} \quad (3.17)$$

has been found. This measurement has been presented without any information about the electric field, used for drifting the electrons. In general, impurities are given as “oxygen equivalent” impurities. In that case, 1 ppb of water corresponds to ~ 17 ppb of oxygen.

3.10 Liquid argon purity requirements

As discussed in the previous section, a long drift path requires an ultra-high level of purity in the medium. The expected ionisation charge attenuation due to attachment to impurities as a function of the drift path for various oxygen-equivalent impurity levels and electric fields is shown in Figure 27. The arrows indicate the drift length of the ICARUS T600 [14], MicroBOONE [83], LBNE [84] and LAGUNA-LBNO GLACIER [22, 85]. The free of electro-negative molecules (like O_2 , H_2O , etc.) must reach a level below 100 ppt O_2 level. An impurity level of < 30 ppt O_2 -equivalent is needed to obtain an electron lifetime greater than 10 ms. Compared to commercially available bulk liquid argon deliveries which typically contain ppm-level purities, the goal is to reduce those impurities by a factor 10^4 – 10^5 before filling the main vessel tank. Excellent purity has been reproducibly achieved in various setups always relying on commercially available techniques, of various sizes and capacities, and should not pose a show-stopper for long drift paths.

Several independent groups performed numerical simulations and concluded that the vacuum evacuation of the main detector volume could be avoided for larger detectors, thanks to (1) a more favourable surface / volume ratio for larger volume (also larger volumes are less sensitive to micro-leaks), (2) a purification from ppm to $\ll 1$ ppb is anyhow needed since the initial purity of argon when delivered is typ. ppm O_2 (see above), and (3) the outgassing of material is mostly from hot components and impurities frozen at low temperature. GAr flushing and purging were shown to be effective ways to

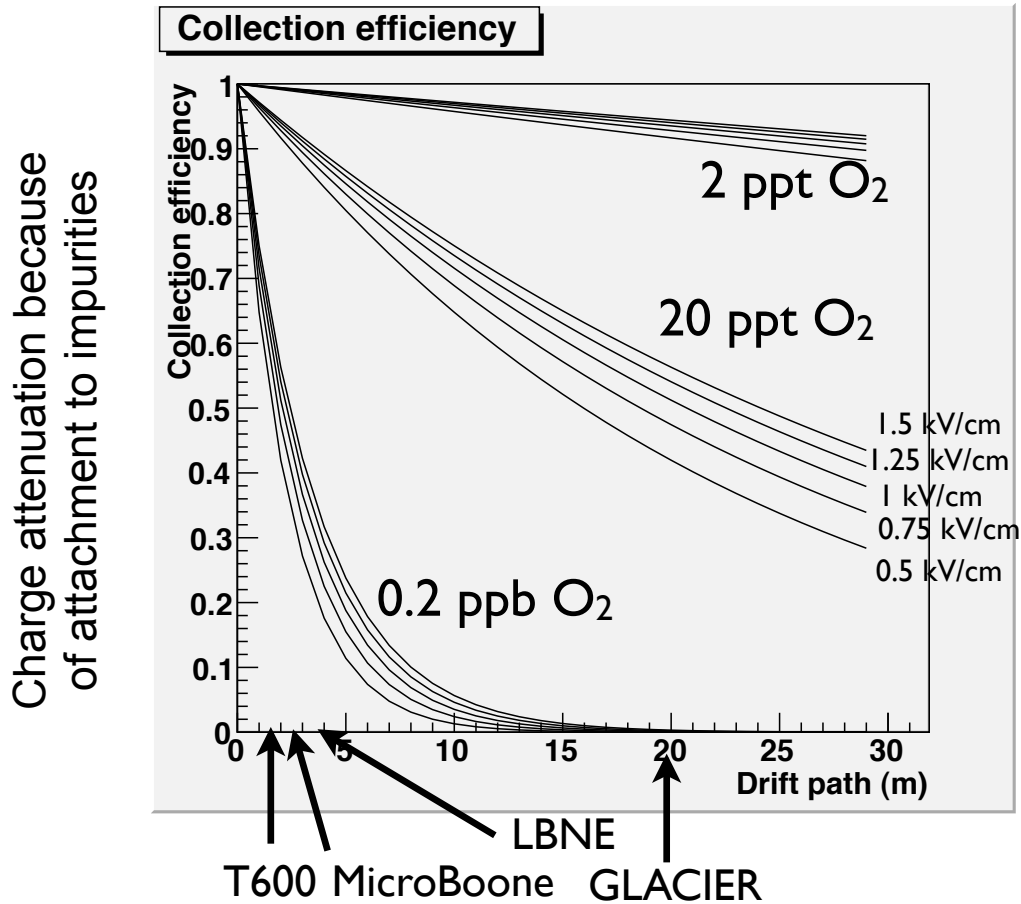


FIG. 27: Expected ionisation charge attenuation due to attachment to impurities as a function of the drift path for 0.2 ppb, 20 ppt and 2 ppt Oxygen-equivalent impurity levels and electric fields in the range 0.5–1.5 kV/cm. The arrows indicate the drift length of the ICARUS T600, MicroBOONE, LBNE and LAGUNA-LBNO GLACIER.

remove air and impurities. Purging on 6 m³ volume has been successfully demonstrated [86]. The piston effect was seen in gas and the impurities reached 3 ppm O₂ after several volumes exchange.

Although the 6 × 6 × 6m³ adopts a drift length which is significantly longer than the others such as ICARUS T600, MicroBOONE or LBNE as mentioned above, it should be noted that all experiments require in order to collect efficiently ionisation charges a liquid argon purity in the range below 0.1 ppb = 100 ppt of oxygen equivalent (See ??). Hence, the challenge to reach the required level of purity starting from commercially available ppm-level bulk argon is not mitigable by a shorter drift length in the meter range. It exists for all considered detectors.

3.11 Effect of impurities on scintillation light

Electronegative impurities in the liquid argon do not only affect the lifetime of the free electrons but also quench the scintillation light, especially its slow component. In pure argon the total scintillation

light emission rate $l(t)$ is given by the simple exponential equation

$$l(t) = \frac{A_S}{\tau_S} \exp\left(-\frac{t}{\tau_S}\right) + \frac{A_T}{\tau_T} \exp\left(-\frac{t}{\tau_T}\right), \quad (3.18)$$

with A_S the relative amplitude of the singlet and A_T the relative amplitude of the triplet state. The sum of the two is normalized to $A_S + A_T = 1$. In case of impurities, mainly O_2 , N_2 and H_2O , the argon excimer Ar_2^* is de-excited by collisions with the impurity molecules and the average lifetime is therefore reduced [87].

$$\tau_T' = \frac{\tau_T}{1 + k[X_2]\tau_T} \quad (3.19)$$

with $k[X_2]$ the rate constant of the light quenching for different molecules X_2 . The measured values for oxygen and nitrogen are $k[O_2] = 0.54 \pm 0.03 \mu s^{-1} ppm^{-1}$ and $k[N_2] = 0.11 \mu s^{-1} ppm^{-1}$ respectively [87]. Comparing the actual measured lifetime and the maximum lifetime of the triplet state of $\sim 1.6 \mu s$, the purity of the liquid argon can be measured down to a contamination of $\sim 10 - 100$ ppb.

In the case of a detector that reads out charge and light, the quenching of the light is not important, since the purity needed for drifting large distances is the limiting factor. It is much lower than the purity needed to recover all the light produced. For example, drifting over 1 m with an electric field of 1 kV/cm gives, according to ??, a total drift time of $\sim 500 \mu s$ and therefore, according to Eq. ?? a maximum allowed O_2 equivalent contamination in the order of ~ 0.6 ppb. This is too small to affect the lifetime of the scintillation light. The light quenching is useful for quickly checking the quality of the commercial argon when delivered. It also gives an immediate alarm in case of a leak in the cryostat, since the lifetime can be analyzed in every PMT signal instantaneously without time consuming processing of the data.

3.12 Ionisation space charge effects

Cosmic ray muons and other natural radiation create ionisation charge with a constant rate and uniformly distributed in the liquid argon. Electron and positive argon ion pairs are separated by the applied electric field and drift towards the anode and the cathode respectively.

In a steady state, the charge concentration is proportional to the evacuation time, and, therefore, inversely proportional to the drift speed v_x . The drift velocity of ions in liquid argon is known to be influenced by the self-motion of the liquid (in particular see convective motions in the next Section 3.13). Although the lowest measured mobility was about $3.6 \times 10^{-4} cm^2 V^{-1} s^{-1}$, Dey and Lewis have reported an extrapolation to zero current suggesting a true ion mobility, uninfluenced by liquid motion, of about

$2 \times 10^{-4} \text{ cm}^2 \text{V}^{-1} \text{s}^{-1}$ [88]. In practice, the velocity of the ions is influenced by the movement of the liquid, generally due to the convective motion (see ??).

In a uniform electric field, the spatial charge distribution ρ_x can be written as a function of the drift length z as

$$\rho_x = \Phi \langle dQ/dl \rangle z / v_x,$$

where Φ is the cosmic muon flux (considered the main contribution to the ionisation during surface operation), $\langle dQ/dl \rangle$ is the average charge per unit length created after the ion-electron recombination, and the subscript x refers to the electron e^- and positive ion Ar^+ . Assuming for the positive argon ions $v = 1 \text{ cm/s}$ and $E = 1 \text{ kV/cm}$, $\Phi = 200 \text{ m}^{-2}/\text{s}$ and $\langle dQ/dl \rangle = 10 \text{ fC/cm}$, for a drift of 6 m the ion concentration is of the order of 10^6 ion/cm^3 , which is enough to distort the drift field. Due to the fact that electrons move much faster than ions, their contribution is negligible.

There are other processes that may have an impact on the final charge distribution. Electrons and ions may recombine during the electron drift. The recombination rate is proportional to the local densities of the two species

$$d\rho_x/dt = -K\rho_{e^-}\rho_{Ar^+},$$

with the constant $K = 10^{-4} \text{ cm}^3/\text{s}$ [89]. This results in a decrease of the amount of charge in the volume and, consequently, in a decrease of the signals from the TPC.

Electronegative molecules diluted in the liquid argon may trap drifting electrons. Since the amount of electronegative impurities is much greater than the amount of drifting electrons, the formation of the negative ions (O_2^-) [162] can be expressed as

$$d\rho_{O_2^-}/dt = \rho_{e^-}/\tau,$$

where τ is the very well known drifting electron lifetime (assumed 5 ms for the computations performed here). The negative ions have a drift velocity similar to the argon ions, but they move on the opposite direction, and they partially cancel the effects of the positive charges.

The TPC signal amplification and readout system (consisting of the extraction grid, the LEM and the two views anode) is based on the charge multiplication in argon vapour due to the Townsend effect, i.e. drifting electrons gain enough energy in a strong electric field to further ionise argon atoms. In the process, there is a formation of positive argon ions, that drift back towards the active volume. A significant part is collected on the bottom electrode of the LEM and on the extraction grid. The ions

that enter into the liquid phase contribute to the positive charge distribution.

The solution to this problem can be computed with a Finite Element Analysis (FEA) approach. The model was implemented in COMSOL Multiphysics [163]. Figure 28 shows the computed absolute value of the electric field and the field lines in a cylindrical volume of 6 m of diameter and 6 m long with a nominal electric field of 1 kV/cm. For the computation the charge gain in the LEM was assumed to be 20, and the two images refer to the case where all the ions are collected on the extraction grid and on the LEM (left), and to the case where 20% of the ions leaks into the liquid argon bulk. In the model the $O_2^- - Ar^+$ recombination is neglected. The nominal drift field is distorted: the value varies

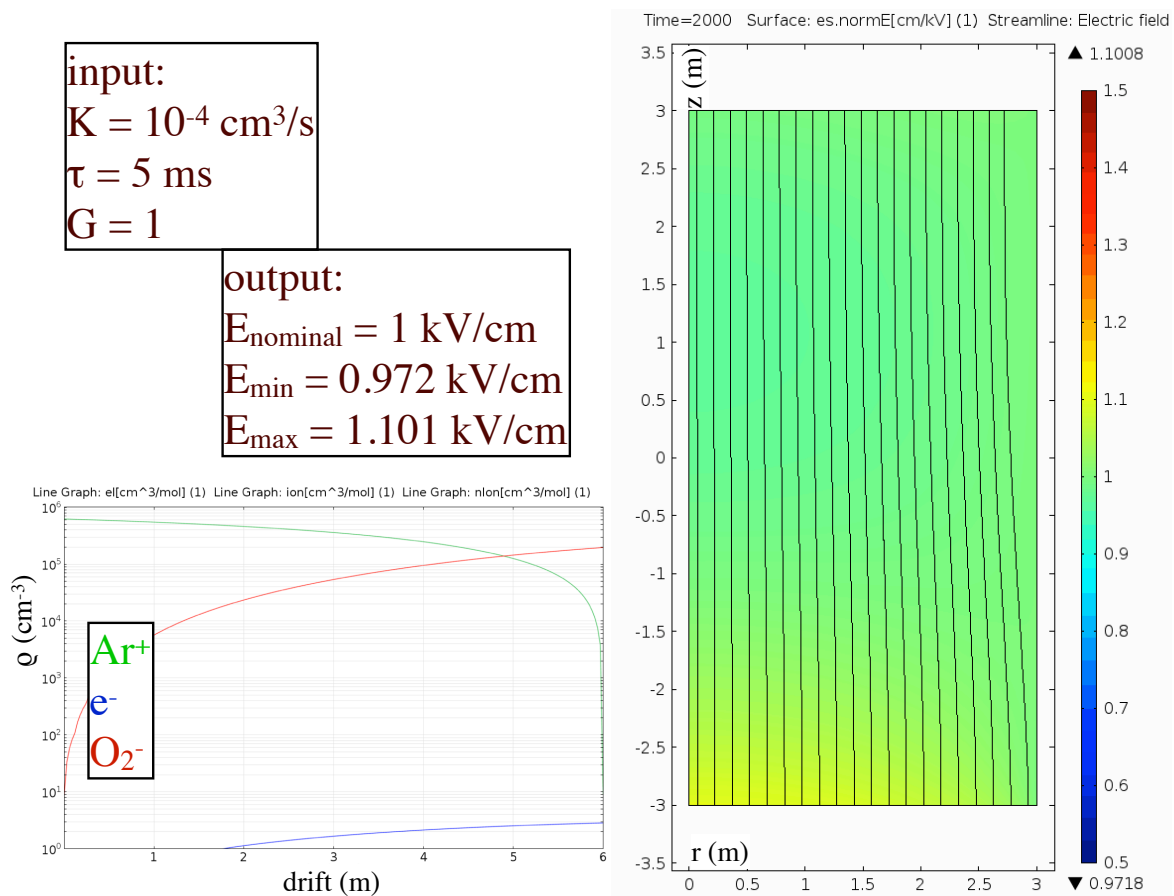


FIG. 28: Steady state computation in cylindrical coordinates of the electric field with space charges without (left) and with (right) argon ions from the signal amplification system. The colour scale represents the absolute value of the electric field and the curves are the field lines. See text for the details.

between -44% and +27% in the worst case, and the field lines followed by the drifting electrons are squeezed towards the centre of the volume. This prevents the charge to be lost because exiting from the sensitive volume. The drift field distortions can be mapped with straight cosmic muons, and at sea level the cosmic ray flux is large enough to provide the required statistics. Another important aspect, neglected up to now, is described next.

3.13 Convective motion of liquid argon

Since liquid argon density decreases with its temperature, convective fluxes due to the buoyancy may occur in the presence of temperature gradient of liquid argon. Thermal gradients are due to heat input and cooling power. As an example, in ?? the convection of liquid argon in a 6 m diameter and 6 m long cylinder is computed with COMSOL, assuming a constant 5 W/m^2 heat input from the walls. The three figures are snapshots of the convection velocity every 100 s at $t=4000 \text{ s}$.

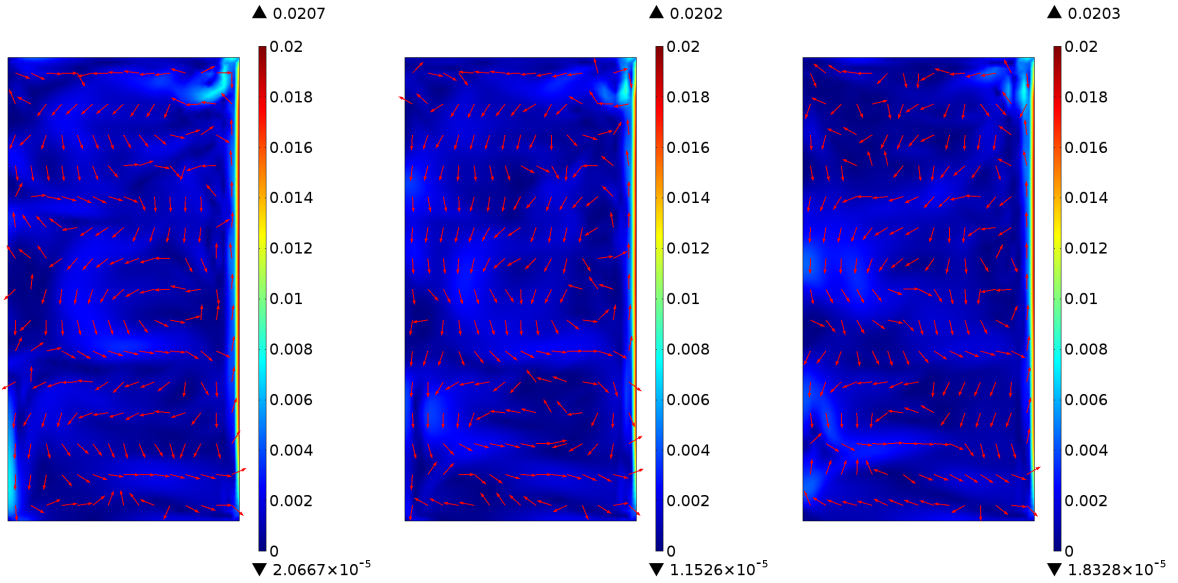


FIG. 29: Liquid argon velocity distribution at three times spaced by 100 s. The colour scale represents the magnitude of the speed and the arrows the direction.

The liquid argon is mixed by convection and, since the ion drift speed is of the same order of magnitude of the argon convection speed, also the Ar^+ distribution is affected. While in the space charge computation described before, the argon is supposed still, in this case the liquid argon motion must be considered to compute the ion motion. The net effect of the convection is to even out the positive and negative ion distributions and to speed up the evacuation of the charges by neutralising them on the conducting surfaces. This results in a decrease of the total amount of space charges in the volume and in a decrease of the electric field distortion.

3.14 Electric breakdown in liquid argon

The loss of the dielectric properties (of a gas, liquid or solid) as a result of application of a strong electric field greater than a certain critical magnitude is called dielectric breakdown. The critical field at which the breakdown occurs is the dielectric strength of the material (or breakdown voltage). It depends on the geometry, on the thickness, the rate of the voltage increase, the shape of the voltage as

a function of time, etc. In (pure) liquids, the breakdown mechanism is similar to that in gases where current carriers are free electrons and ions generated by external radiation. In the strong electric field, these particles acquire kinetic energy, large enough to ionise further molecules or atoms, potentially leading to streamers. Compared to gases, the liquid has the advantage of a much higher density, so in a first approximation one can expect the dielectric strength of liquids to be much higher than those of gases (proportional to their relative densities). However, it is known that breakdown in liquid can occur at much lower electric fields due to the formation of bubbles. The geometry of these latter is altered by the field lines and ellipsoids can form and merge into larger high-conductivity channels prone to discharges. A local increase of conductivity increases the temperature in the channel, the liquid can boil, the vapour enlarging further the canal. Such phenomena have for example been observed in liquid under the sudden application of strong electric fields, where electrostriction generates by cavitation a gaseous phase prone to discharges [90]. In general, the influence of a strong electric field in a liquid is noticeable when the electric field density is comparable to the external pressure p :

$$\frac{1}{2}\epsilon\epsilon_0 E^2 \geq p \quad (3.20)$$

where E is the electric field. For liquid argon and in absence of bubbles, a field of 1 MV/cm=100 MV/m leads to ≈ 0.5 bar, which will have a noticeable effect. For comparison, the dielectric strength of polyethylene is in the range 20–160 MV/m. A field of 100 kV/cm in liquid argon yields a pressure of about 5 mbar. By assuming that the liquid argon in the $6 \times 6 \times 6 \text{ m}^3$ will be sub-cooled by e.g. 10 mbar via the liquid argon process system, the condition on the field strength to prevent formation of bubbles is set to $E \leq 100$ kV/cm.

The assumed electron drift length for GLACIER is 20 m, with an electric field of 1 kV/cm, corresponding to the path after which the spread due to the electron diffusion becomes larger than the readout pitch of 3 mm. This requires a voltage at the cathode of -2 MV. In the current design of GLACIER, a distance of 1.5 m is foreseen between the cathode structure and the bottom of the tank at ground, giving an average electric field of 13.3 kV/cm (See ??). In the vicinity of the cathode tubes the electric field reaches 50 kV/cm over distances of the order of centimetre.

A dedicated test to measure the maximum electric field (up to 100 kV over 1 cm) that the liquid argon can sustain was performed [91]. Figure 31 shows the schematic representation of the test setup, which consists of a vacuum insulated dewar hosting a high voltage feedthrough and a couple of electrodes, in between which the high electric field is generated.

During operation, the dewar is filled with liquid argon purified through a molecular sieve (ZEOCHEM Z3-06), which blocks the water molecules, and a custom-made copper cartridge, which

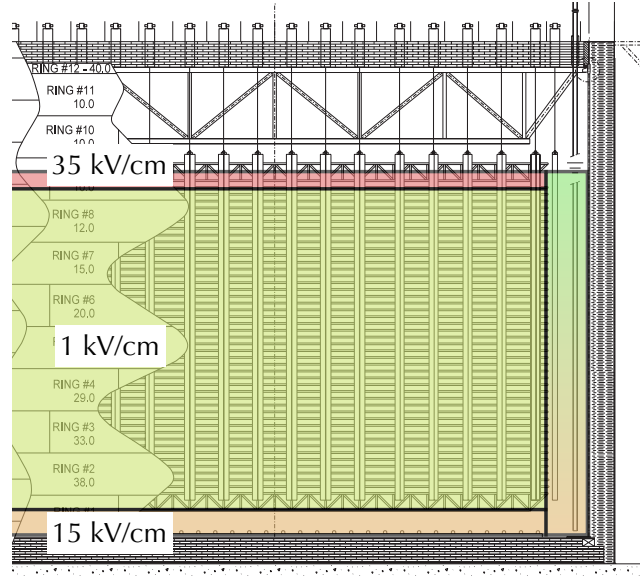


FIG. 30: Representation of the electric fields in a GLACIER-type detector with a 20 m drift distance.

absorbs oxygen molecules. Before the filling, the vessel is evacuated to residual pressure lower than 10^{-4} mbar in order to remove air traces, favour the outgassing of the materials in the dewar, and check the absence of leaks towards the atmosphere. During the filling, the argon *boil off* is exhausted to control the pressure in the dewar. The pressure is always kept at least 100 mbar above the atmospheric pressure, so that air contaminations are minimised. Once the detector is completely full, the exhaust is closed, and the liquid argon is kept cold by means of liquid nitrogen flowing into a serpentine, which acts as heat exchanger that condenses the argon *boil off*. The liquid argon level is visually checked through a vacuum sealed viewport.

The voltage is provided by a negative 100 kV power supply from Heinzinger [164] though a HV coaxial cable modified to inductively couple the HV wire to an oscilloscope via a 1:1 transformer.

When a pulsed current flows through the cable, it is detected on the scope. This sensor is used to monitor the frequency of small discharges (not necessarily happening between the electrodes, e.g. the feedthrough and the cable may have leakage currents). It is also used to monitor the current delivered by the power supply during the charging up. The cable enters into a custom-made HV feedthrough (see figure 32 left), which is vacuum tight and designed to sustain voltages larger than 150 kV.

High electric fields can be achieved with low potentials and electrodes with small curvature radii, but, since the breakdown is a random process, it is important to test a sizeable region of the electrodes. For these reasons, a system that provides a uniform electric field over 20 cm^2 area was used. A picture of the electrodes structure is shown in figure 32 right. The two 10 cm diameter electrodes have the same shape and are facing each other at a distance of 1 cm. The top electrode is connected to the live

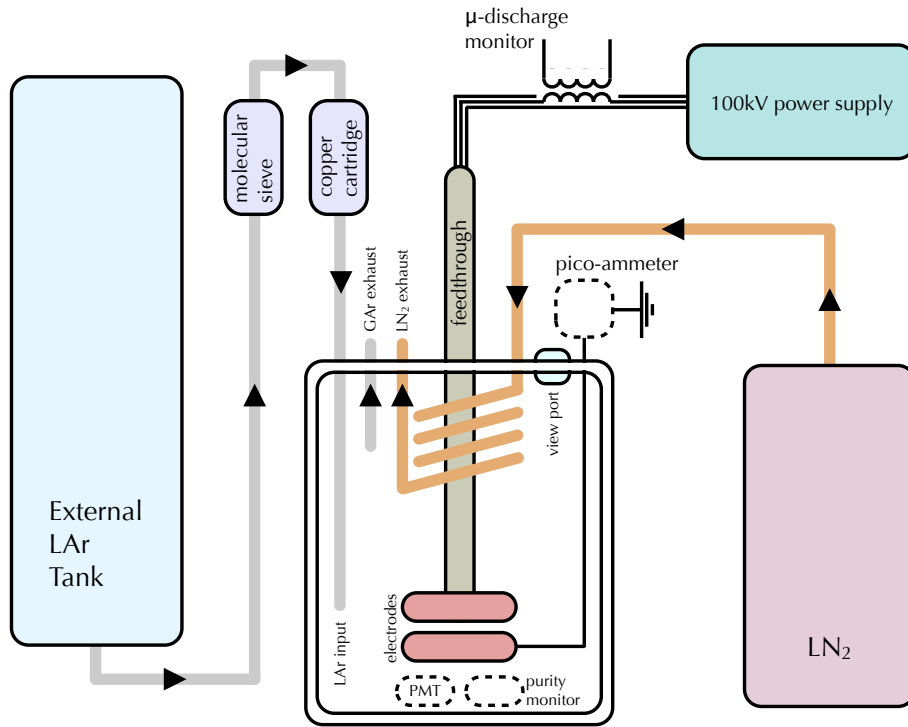


FIG. 31: Schematic representation of the apparatus. See text for the description.

contact of the HV feedthrough, and the bottom one is connected to ground through the vessel. The electrodes, made out of mechanically polished stainless steel, are shaped according to the Rogowski profile [92] that guarantees that the highest electric field is almost uniform (in a region of about 5 cm in diameter), and confined in between the two electrodes, as shown in figure 33. The left image shows, in cylindrical coordinates, the absolute value of the electric field in the vicinity of the electrodes, computed with COMSOL. On the right the electric field along the profile of the top electrode as a function of the radius is shown.

The two electrodes form a standalone structure, that is assembled first and then mounted. By construction, the structure ensures the parallelism of the electrodes when cooled down to the liquid argon temperature. The shrinkage of the materials in cold is computed to affect the distance between the electrodes less than 1%.

With the liquid argon temperature below the boiling point at a given pressure, a voltage of -100 kV was applied to the top electrode. This value was limited by the maximum voltage of the power supply. This configuration corresponds to a uniform electric field of 100 kV/cm in a region of about 20 cm² area between the electrodes. Several cycles of discharging and charging up of the power supply were

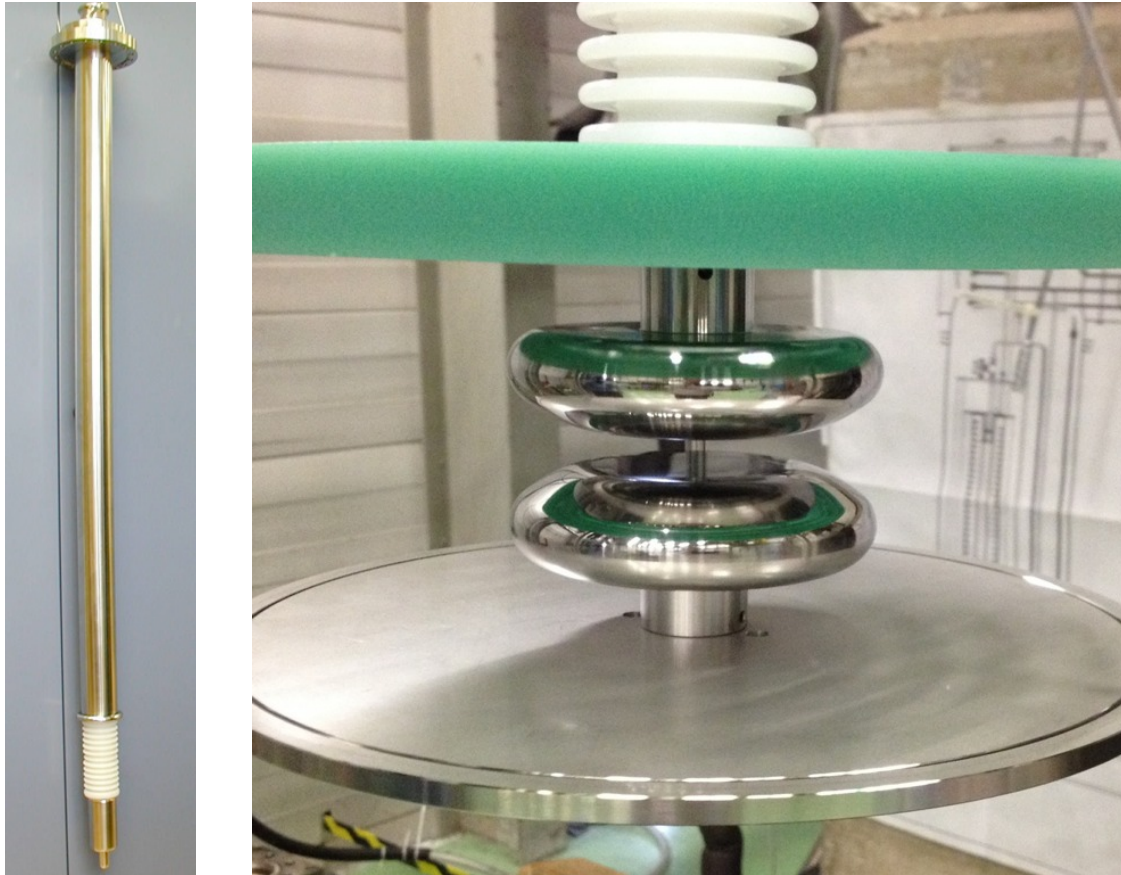


FIG. 32: Left: Image of the High Voltage feedthrough. Right: figure of the electrodes structure.

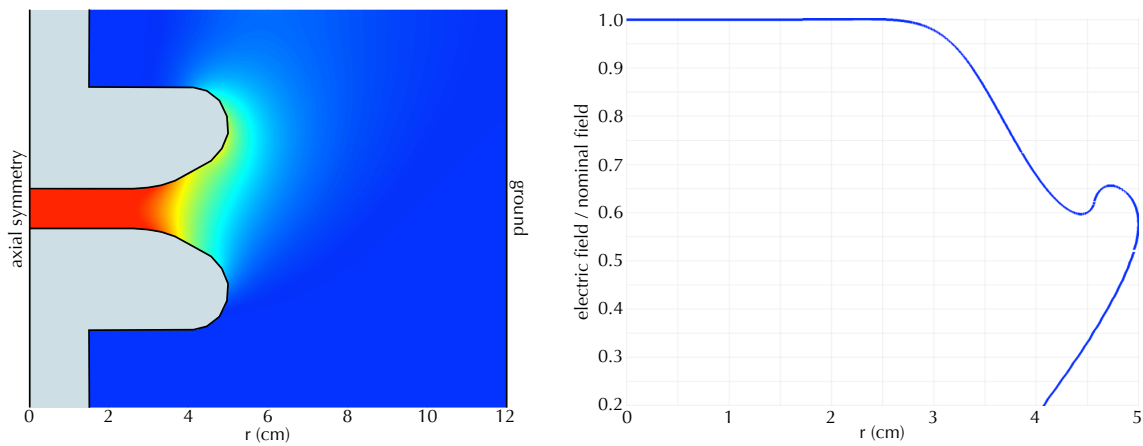


FIG. 33: Left: Computed electric field. The cross sections of the electrodes are shown in grey, and the colour pattern is proportional to the absolute value of the electric field. The electric field is essentially uniform in the central region. Right: Computed electric field on the profile of the top electrode as a function of the radius. The largest field is attained between the electrodes.

performed. The system could also be stressed several times by ramping up the voltage from 0 V to -100 kV in about 20 s without provoking any breakdown. At the centimetre scale, the dielectric rigidity of non-boiling liquid argon is larger than 100 kV/cm (See ??).

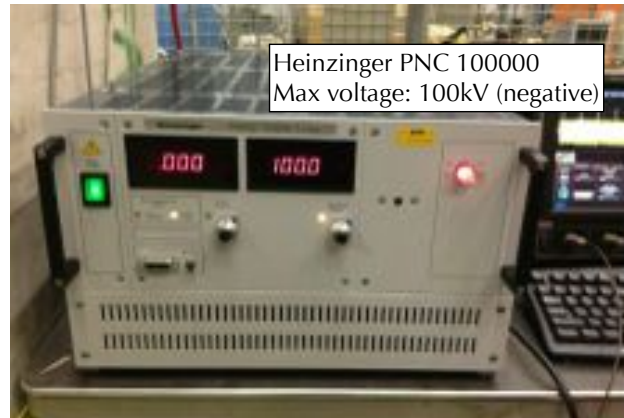


FIG. 34: Negative PNC 100000 power supply from Heinzinger in operation with 100 kV across a 1 cm liquid argon gap and no current. See text.

A completely different behaviour was observed with boiling argon. Several breakdowns between the electrodes at fields as low as 40 kV/cm occurred. The stillness of the liquid argon was controlled by varying the pressure of the argon vapour and was monitored visually by looking through the viewport. The pressure was regulated by acting on the flow of the liquid nitrogen passing through the heat exchanger. In fact, the thermal inertia of the liquid argon bulk makes temperature variations very slow, hence increasing the cooling power translates in a rapid decrease of the vapour pressure. When the pressure is above the boiling one, the liquid argon surface becomes flat and still. On the contrary, the more the pressure decreases below the boiling point, the more the liquid argon boils.

The occurrence of breakdowns was found to be significantly sensitive to the presence of bubbles. Above about 1000 mbar the argon was not boiling and 100 kV/cm could be achieved. Around 930 mbar breakdowns occurred at 70 kV/cm and below 880 mbar at 40kV/cm. This is interpreted as the evidence that breakdown can be triggered by bubbles in the liquid: the bubbles convey the breakdown forming a preferred channel for the discharge development, since argon gas has a much lower dielectric rigidity compared to the liquid.

Results from a similar test [93] with a different electrode geometry show that the maximum electric field (in a non uniform field) for a breakdown free operation is 40 kV/cm. A strong dependence of the behaviour of the setup on the presence of bubbles is also observed. In addition, the breakdown point is only weakly dependent on the liquid argon purity: the maximum electric field increases of 30% changing the oxygen-equivalent contamination from 1 ppb to 20 ppm.

4 DLAr detector components

4.1 Anode Charge Readout Plane

4.1.1 The top anode deck

The top anode deck is composed of a reinforced frame holding the independent Charge Readout Planes (CRPs). The deck is suspended via ropes passing through dedicated Feedthroughs as explained in ???. The height of the deck is controlled externally and positioned precisely above the liquid level. The 36 m² surface is to be instrumented with a large number (144) of individual modules. This will require a semi-industrial production with external suppliers and a dedicated QA/QC validation and calibration effort. The anode modules provide two independent coordinate views, and are segmented with strips of 3 mm pitch. The baseline option for the CRP is based on the LAr LEM TPC technique, as described in the ??. In addition, we are also developing a second option based on the MicroMEGAS technique, as described in ??.

4.1.2 The supporting structure

The anode deck structure is made of a sandwich of elements holding the independent Charge Readout Planes (CRP). ?? shows an exploded view of the different components, whereas ?? shows the assembled structure. Note that for clarity reason, the closing plate on the second figure has been partially removed to make the frame visible.

The structure is made of a connection structure for CRP on which is fixed a frame made of beams called structural frame. Then a plate is used to close this frame, playing the role of an upper skin. The combination of the frame, whose vertical dimension (~250mm) is clearly of prime importance, associated with a closing plate gives the desired stiffness of the final assembly. Moreover, the deck is suspended via four ropes fixed in the structural frame using dedicated feedthroughs. The use of four ropes makes the boundary conditions symmetric and is decisive to achieve the requirement in term of CRP deformations. Finally several feedthroughs for the CRP cables (electronics) are foreseen in the closing plate. The mechanical support structure is designed to get a very small sag under gravity, but also to maintain the read out plane into positioning tolerance when going from ambient mounting temperature to liquid argon temperature (+22°C to -186°C). During this almost two hundred degree cooling phase, even small differences between materials thermal expansion coefficient could modify drastically the planarity of the structure because of bi-material thermal effects. Consequently, in order to avoid as much as possible the use of different material the retained proposal is to produce the whole mechanical structure in G10.

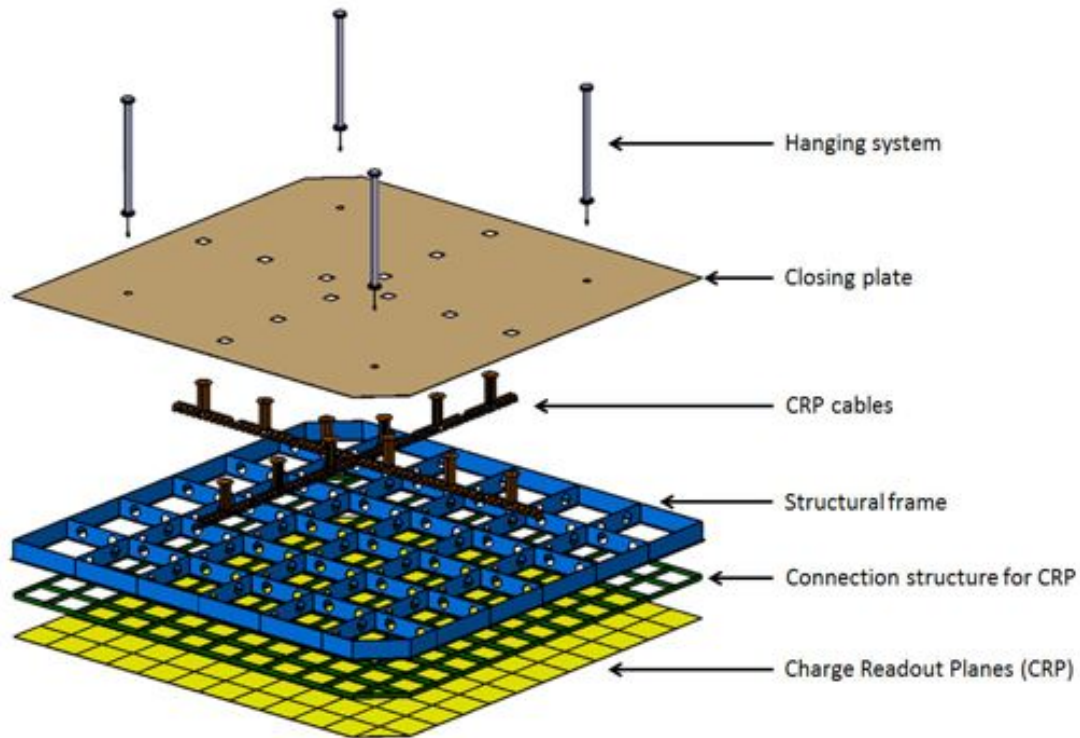


FIG. 35: Exploded view of the anode deck structure and naming conventions.

In order to minimize sagging, the design is based on a sandwich structure composed of two G10 plates separated by the G10 frame. The lower plate is composed of LEM detection plane and associated connection structure supporting frame. The upper one is purely dedicated to mechanical stiffness and structure symmetry. The later guarantees an in-plane thermal deformation of readout plane (displacements almost reduced to X and Y components), CRP and holding structure assembly.

A pre-sizing finite element study has been carried out to evaluate the thermo-mechanical behaviour of the proposed structure. The anode grid, tensioning system and electronic readout weight have been estimated to be about $10\text{kg}/\text{m}^2$. In this model a vertical zero displacement boundary condition has been applied to each hanging rope. The loading used consists of a gravity load and a uniform temperature change from $+22^\circ\text{C}$ to -186°C . As shown on ??, the CRP vertical displacements are in the range $+0.52\text{ mm}$ to $+1.016\text{mm}$ equivalent to a peak to peak vertical displacement of 0.5 mm . Moreover for better illustration of CRP vertical displacements, the upper closing plate has not been shown. These displacements are in agreement with the $\pm 0.5\text{ mm}$ CRP plane planarity specification.

4.1.3 The position control system

The aim of the control system is to manage the position of the anode plane with respect to the liquid argon surface. The system will have to cover a displacement range of the order of 100 mm and

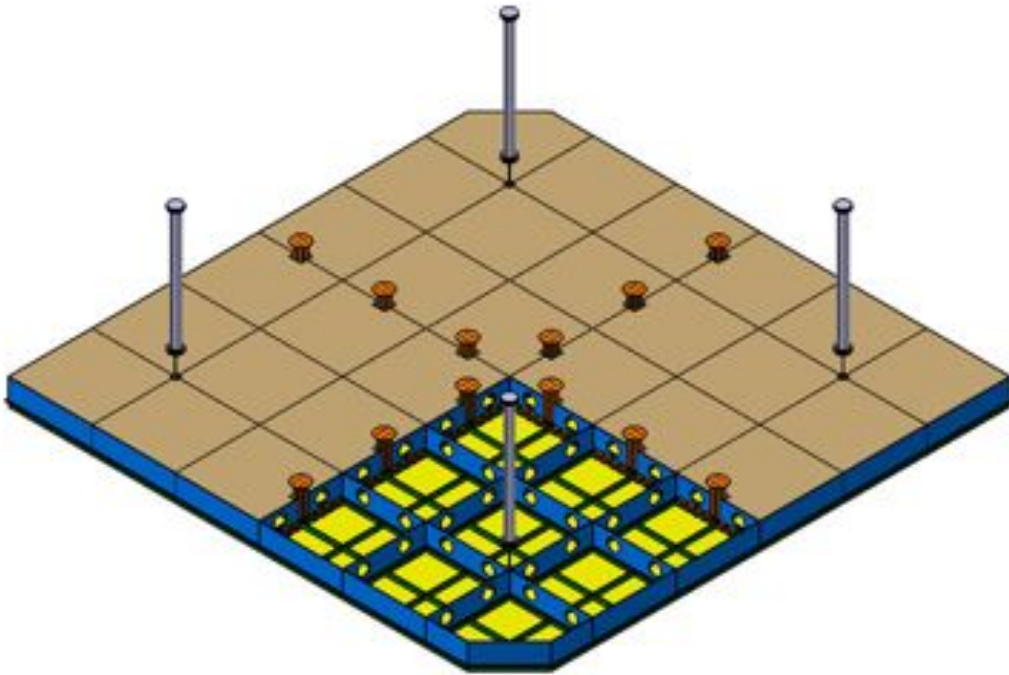


FIG. 36: Assembled structure (with closing plate partially removed for viewing purpose).

to keep the distance of the anode plane to the liquid equals to 10 mm at a sub mm precision. The speed and acceleration are not an issue due to the slow change of the argon liquid level with time.

The real time monitoring and control will be carried out assuming that the position of each CRP pad (1 m^2 unit; total 36) is available thanks to capacitive measurement between the argon liquid level and the pads with an accuracy of 0.1mm. The position is proportional to the capacitive measurement signal.

The anode plane, weighting approximately 2 tons, will be hanged up by means of 4 rigid cables as described earlier and the action and control of the anode plane will be carried out outside of the tank to avoid the environment problems (temperature, vacuum). The thermic dilatation of the cables is expected to be less than 10mm.

Positioning process:

The positioning of the anode plane will be decomposed in two different steps.

The first one will be the displacement of the whole anode plane to move it as close as possible to the liquid argon level. This motion is named Translation Motion (TM) and will be based on a multi-axes coordinated motion. The control set point of each axis will be done via a virtual axis used as a master. The 4 physical axes will be the slaves (??). In such manner, the motion will be accurately and safely performed during the complete process. Note that this technology is commonly used in automation

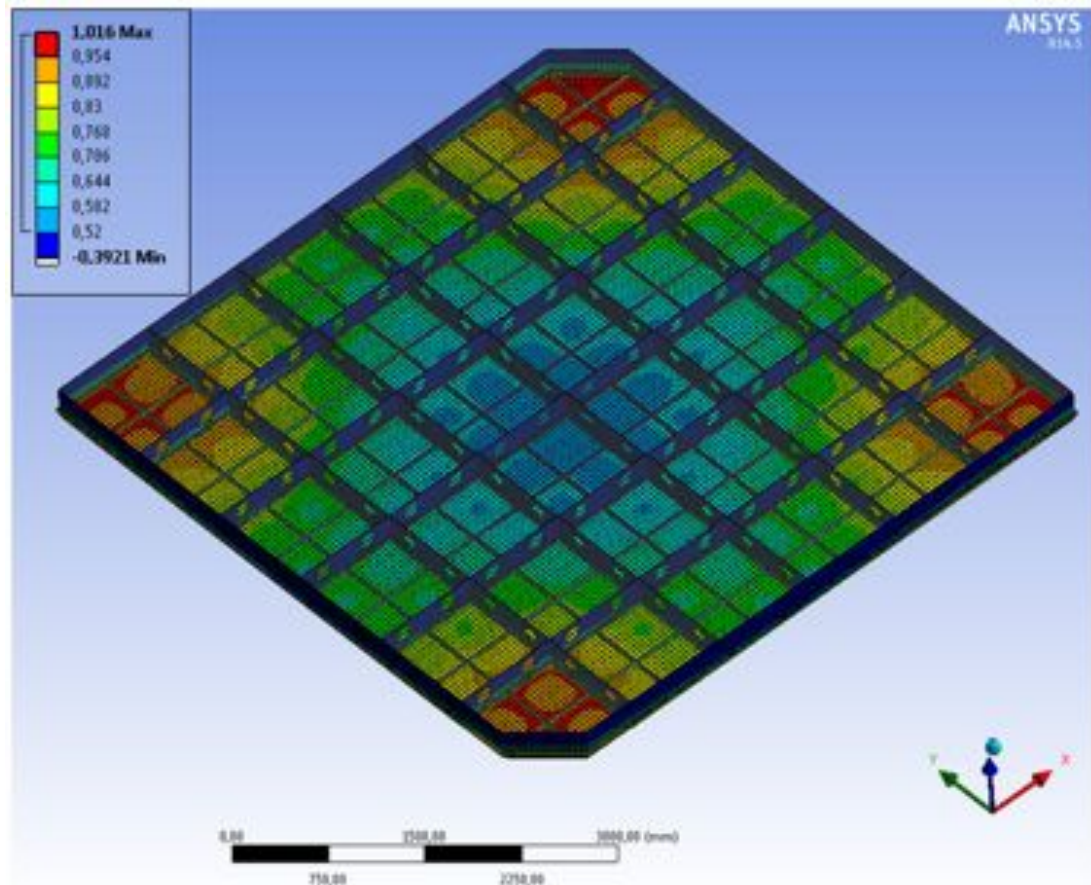


FIG. 37: Vertical displacements under gravity and thermal loading.

when requiring multi-axes motion control.

The second step, named Tilt Adjustment (TA), will be the correction of the anode plane tilt. In this case, the four axes will be decoupled and independently managed. The capacitive measurement of each pad will allow interpolating the shape and the planarity of the anode plane. A dedicated algorithm will be developed in order to generate the needed rotations and translations, and thus to obtain a charge readout plane as parallel as possible to the liquid argon level. In this way, the system will be able to manage rotation and deformation of the anode in accordance to the specifications.

The advantage of this setup is that the axes could be managed simultaneously like if they would be mechanically coupled for the whole plane positioning (TM) or completely independent for the tilt plane adjustment (TA). In parallel, constrain gauges could be installed all along the anode plane to guarantee that the applied forces won't generate any damages.

Technology of the control system and actuators:

The control architecture will be based on a Programmable Logic Controller (PLC) which is composed of two central processing units (one for the classical cycles and a second one for the drive

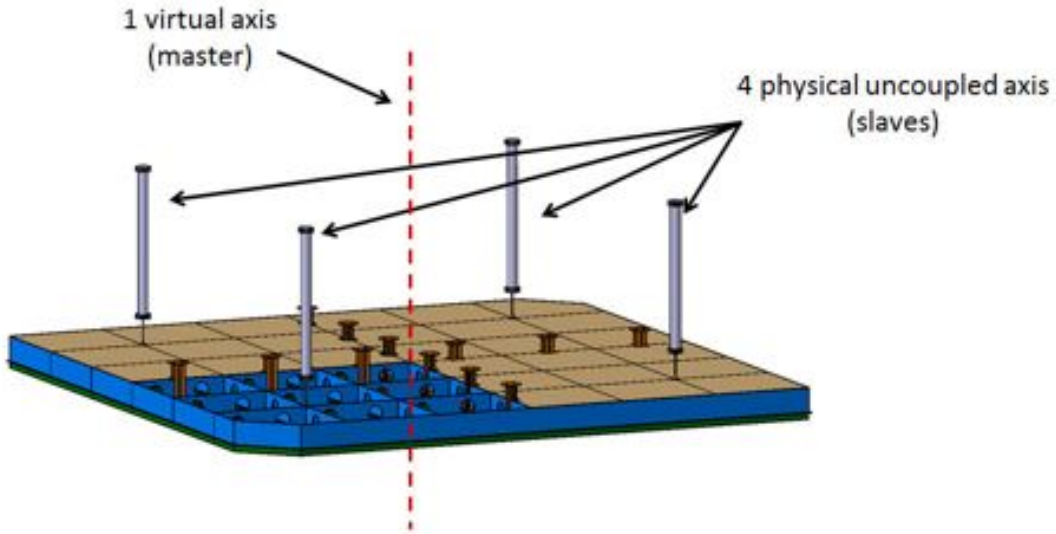


FIG. 38: Anode plane controlled by four physical axes managed which are managed by a virtual axis.

part management), two fieldbus (one of which is dedicated to the drive) for the deported devices (input/output modules, touch panel) and specific variators which are able to manage power cuts and synchronized displacements.

The actuators have to be able to manage accurately tiny displacements of a few millimeters with a relative heavy load. In this prospect, electric jacks are foreseen. This type of device coupled with an electrical gear-motor (brushless equipped by absolute encoders) thanks to an industrial integrated system (example: ESBF jacks models produced by Festo, EMC jacks models produced by Bosch with a range of 200 mm) will allow such linear displacement. Note that the jack supplier could be different from the motor supplier.

4.1.4 The LAr LEM TPC option

The design concept of the novel Liquid Argon Large Electron Multiplier Time Projection Chamber (LAr LEM TPC) and its promising performances have been demonstrated experimentally with a detector prototype having an active area of $10 \times 10 \text{ cm}^2$ [25, 26] and $40 \times 80 \text{ cm}^2$ [23, 24]. This new type of LAr-TPC, operating in the double-phase (liquid-vapor) mode in pure argon, is characterized by its charge amplifying stage (LEM) and its projective anode charge readout system. Situated in the vapor phase on top of the active LAr volume, these latter provide an adjustable charge gain and two independent readout views, each with a canonical and optimal pitch of 3 mm, since the amplification stage produces sufficient charge to be shared among several readout electrodes (smaller pitch sizes

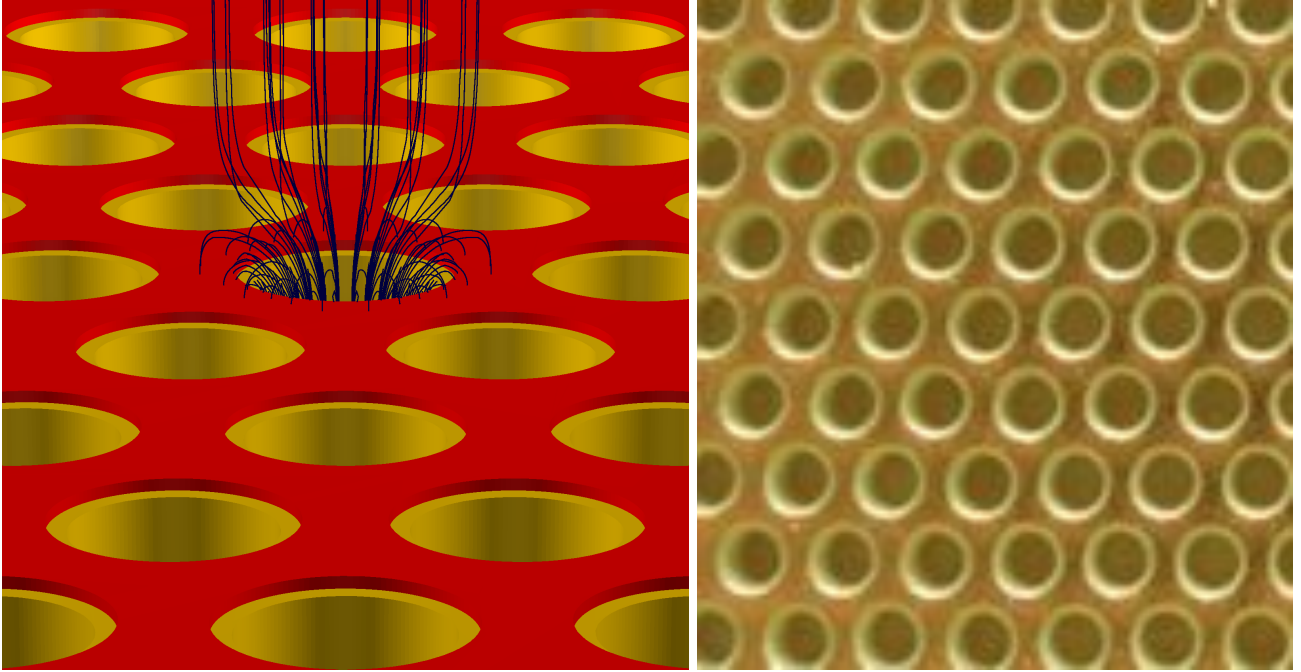


FIG. 39: Left: schematic drawing of the LEM, consisting of the copper electrode (red) and the insulating material FR4 (yellow). The field lines passing through the central hole are drawn in black. Right: closeup picture of a manufactured LEM. As in the schematic drawing on the left, the dielectric rim is clearly visible. [See text for more details.]

could be considered). With T_0 time information provided by the LAr scintillation, they provide a real-time three-dimensional (3D) track imaging with dE/dx information and the detector acts as a high resolution tracking-calorimeter. A high signal-to-noise ratio can be reached in the LAr LEM-TPC thanks to the gas amplification stage. This significantly improves the event reconstruction quality with a lower energy deposition threshold and a better resolution per volumetric pixel (voxel) compared to a conventional single-phase LAr-TPC [26]. In addition the charge amplification compensates for potential loss of signal-to-noise due to the charge diffusion and attachment to electronegative impurities diluted in LAr, which both become more important as the drift length increases. The collection-only readout mode (avoiding the use of induction planes) is also an important asset in the case of complicated topologies, like e.g. in electromagnetic or hadronic showers.

The extracted drift electrons in the vapor phase are finally drifted towards a collection plane where they are detected. Due to the applied electric field, electrons are accelerated in between two collisions with argon atoms and produce the *Townsend avalanche* (see ??). Being positioned on top of the LAr TPC in the vapor phase, the LEM is responsible for the multiplication of the ionization charges. Similar to the more established Gaseous Electron Multipliers (GEMs) [28], the basic idea of the LEM is to create electron avalanches in the gap of two holed metal planes, which are spaced by an electrical insulator. While the GEMs are made of 50 μm thick Kapton foils that are likely not applicable to

cryogenic double phase detectors, the LEM or THGEM (for THick GEM) is a macroscopic, sturdy structure, made with standard PCB techniques. It consists of a 1 mm thick FR4 substrate with thin copper sheets laminated on both sides. The electrode-insulator-electrode sandwich is perforated with 800 μm spaced cylindric holes with a diameter of 500 μm . The view from top is shown in the scheme on the left and the picture on the right of ???. The scheme shows that the hole diameter of the electrode (red) exceeds the diameter of the hole through the insulator (yellow). As demonstrated in [94] these so-called dielectric rims, typically about 50 μm thick, significantly reduce the occurrence of discharges and therefore increase the maximum achievable gain. Besides the dielectric rims, the discharge probability is further reduced by the hole geometry of the LEM. Since the avalanche is happening inside the 1 mm long and 0.5 mm wide holes that are only surrounded by insulating material and no metal surfaces, secondary effects due to emitted scintillation light are suppressed. This is sometimes called *mechanical quenching*. A very detailed discussion of the discharge mechanisms, including finite element simulations, can be found in [95].

Figure 40 illustrates the structure of the $40 \times 80 \text{ cm}^2$ LAr LEM-TPC hanging inside the ArDM detector vessel, that was successfully operated at CERN in 2011. The field cage, which defines the active LAr target and drift volume, is constructed with four PCB side walls in a shape of rectangular box with dimensions 76 cm (L) \times 40 cm (W) \times 60 cm (H). On the inner surface of each PCB 31 horizontal field shaping strips, which hereafter are called field shapers (FS), are formed by etching at a constant pitch of 20 mm. The top (FS0) and the bottom (FS30) field shapers have a width of 9 mm while the ones in between have 18 mm, with a gap of 2 mm between neighboring ones. Negative high voltages linearly decreasing from bottom to top are distributed to the field shapers so that a vertical drift electric field is created uniformly over the full drift length of 60 cm.

On top of the field cage two horizontal extraction grids are mounted with a gap of 10 mm in between. The grid is a 0.15-mm-thick stainless-steel mesh, where square holes with a size $2.85 \times 2.85 \text{ mm}^2$ are etched at a pitch of 3 mm all over the active area. The lower grid is positioned at the top face of the field cage. For the double-phase operation mode the LAr surface is adjusted at the middle of the two grids. The liquid level at each of the four corners can be monitored with a precision of $\sim 0.5 \text{ mm}$ with the aid of four capacitive level meters. Ionization electrons produced by ionizing particles are drifted upwards to the liquid surface. These electrons are extracted across the liquid-vapor interface into the gas argon (GAr) phase with the aid of a strong extraction field of typically 3–4 kV/cm between the two grids. They are then collected by the charge readout system incorporating the LEM. The bottom face of the field cage is covered by the cathode grid that is a stainless-steel mesh of the same type as used for the extraction grids. The top (FS0) and the bottom (FS30) field shapers are electrically

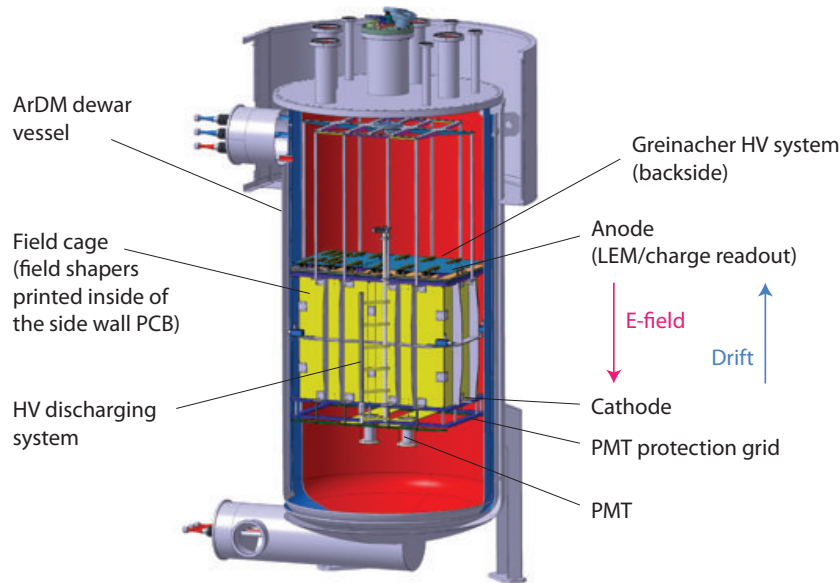


FIG. 40: 3D CAD model of the LAr LEM-TPC prototype installed in the ArDM LAr vessel. The field cage has dimensions 76 cm (L) \times 40 cm (W) \times 60 cm (H). The LEM charge readout system is mounted on top of the field cage. Negative HVs linearly decreasing from bottom to top are generated by the built-in Greinacher HV multiplier and distributed to 31 field shapers formed by etching on the inner surface of the side wall PCBs. A vertical drift electric field thus is created uniformly over the full drift length of 60 cm.

coupled to the lower extraction grid and respectively, to the cathode.

The HV for creating the drift field is generated using a built-in 30-stage Greinacher HV multiplier [24]. The circuit is integrated in the design of one of the side-wall PCBs and the components are mounted directly on the outer surface of the PCB, as can be seen in Figure 41. As already mentioned the generator itself avoids the use of a voltage divider, since each multiplying stage provides a characteristic DC voltage. The various multiplying stages generate a monotonously increasing potential to supply the electrodes surrounding the drift volume. In our setup, the DC output of each of the 30 Greinacher stages is connected to each field shaper via a wire through the PCB.

As displayed in the scheme of Figure 45, each electrode is connected independently via SHV feedthrough and a low pass filter to a separate channel of the power supply. This configuration allows to apply arbitrary field configurations. In order to be able to operate the anode at positive voltages, each of the 512 readout strips is connected via 500 M Ω resistors to the guard ring of the anode. They are mounted on a first *signal routing plane*, which is positioned on top of the anode. The 270 pF HV decoupling capacitors connect this first plane to a second one, where a discharge protection circuit is installed as well as the connectors for the sixteen signal cables. Finally, the signal cables are fed through the cryostat and connected to the charge acquisition system. Both the discharge protection

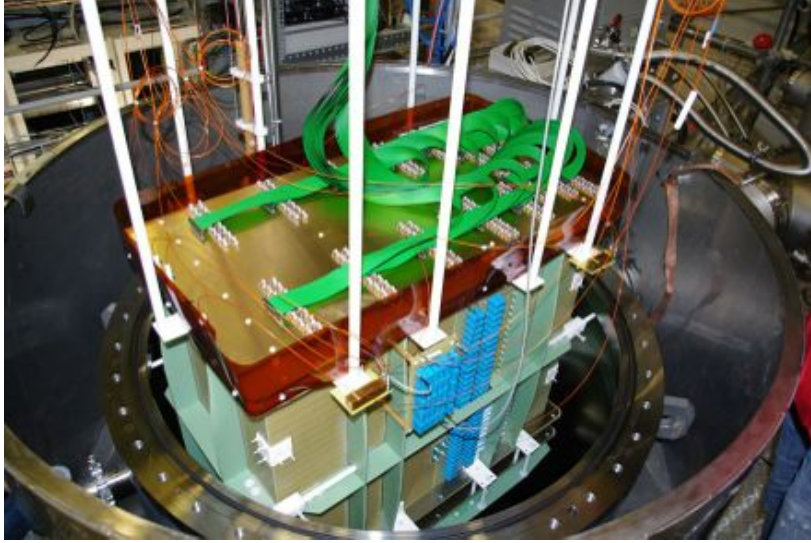


FIG. 41: Picture of the LAr LEM-TPC with readout sandwich and drift field cage, which are about to be inserted into the ArDM vessel. The stack of blue capacitors on the front side wall shows the Greinacher HV multiplier.

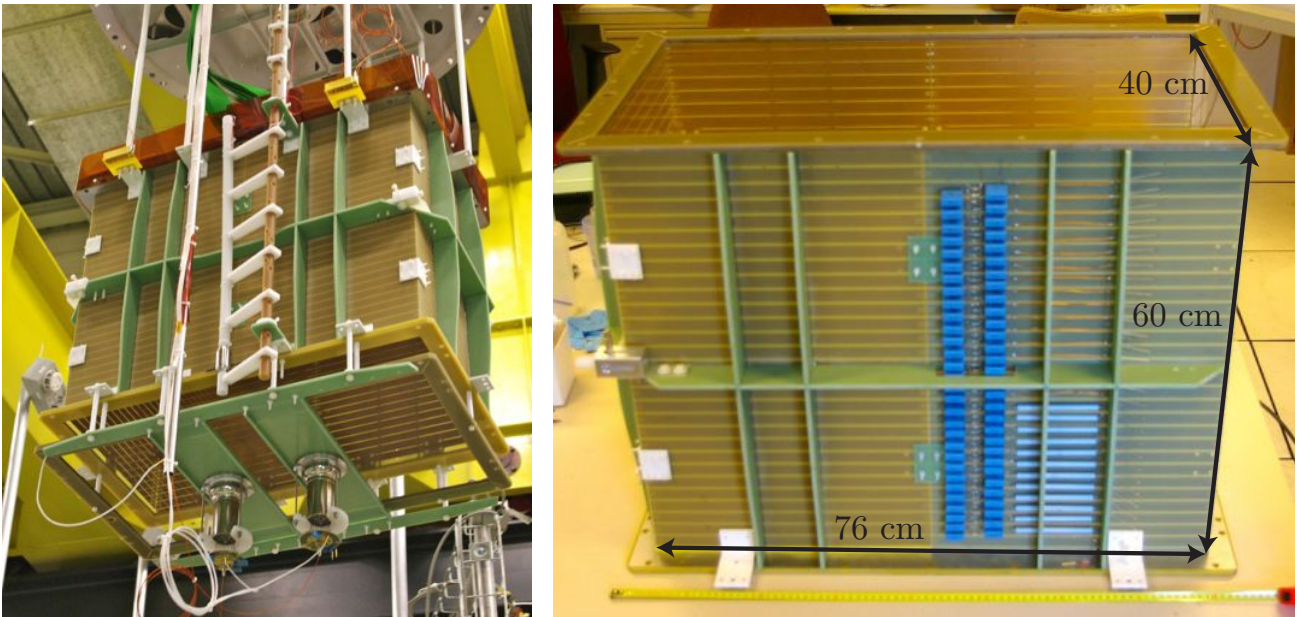


FIG. 42: Pictures of the detector. Left: fully assembled detector hanging from the top flange of the ArDM vessel. Right: TPC during the assemblage phase.

circuit as well as the readout electronics and acquisition system are detailed in the following section.

Under the field cage two photomultiplier tubes (PMTs) are installed to detect scintillation light produced by charged particles crossing the LAr target (primary scintillation, S1), as well as the secondary scintillation light (S2) produced via electro-luminescence by the electrons extracted to the GAR phase [96]. We employed Hamamatsu R11065 cryogenic 3" PMTs having a high quantum efficiency of $\sim 30\%$, specifically designed for the use in LAr [97]. The quartz window of the PMT was coated with a

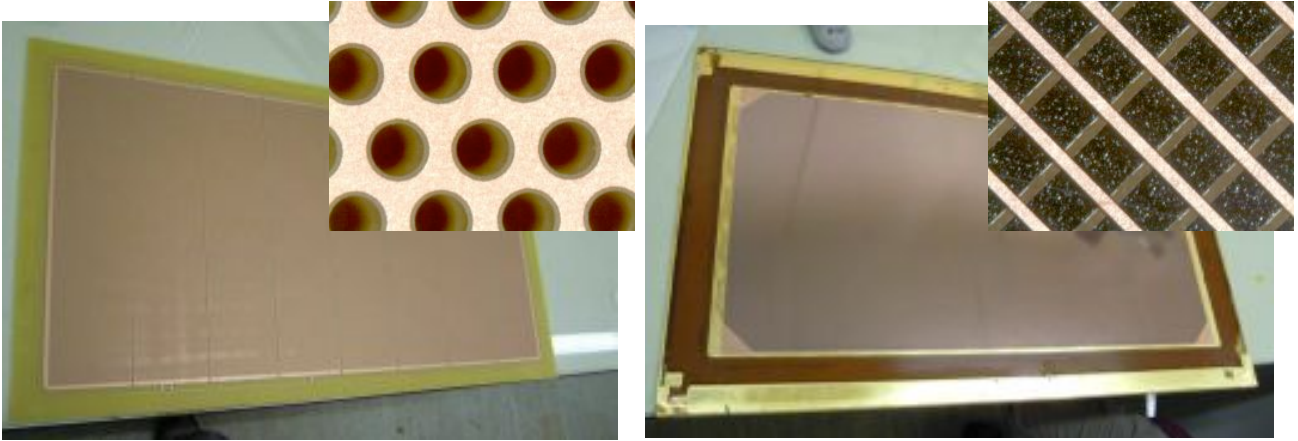


FIG. 43: Picture of the $76 \times 40 \text{ cm}^2$ LEM with close-up of its holes (left) and picture of the 2D anode with close-up of its strips (right).

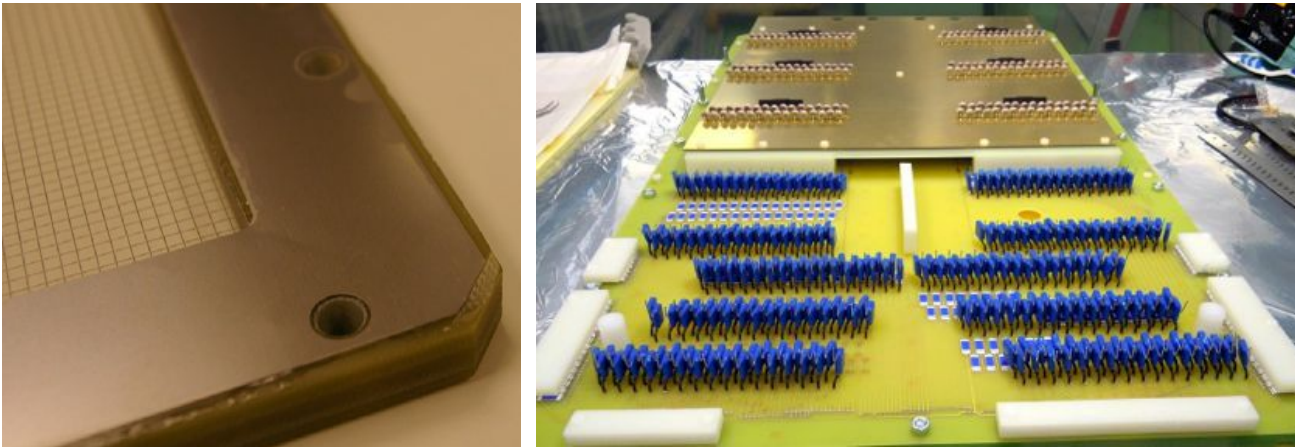


FIG. 44: Pictures of the details of the detector: one of the extraction grids (left) and the charge readout sandwich during the assembling (right): the half in the back is already covered with the signal plane, in the foreground the HV distribution plane with the decoupling capacitors and the $500 \text{ M}\Omega$ resistors is seen.

wavelength shifter, 1,1,4,4-Tetraphenyl-1,3-butadiene (TPB) [98], in a Paraloid™ B-72 polymer matrix to detect deep ultra violet photons of the argon scintillation (peaked around 128 nm) . The PMT signal is used primarily for triggering and for determination of the event T_0 absolute time. To protect PMTs from possible discharges from the parts at HV, another mesh electrode, which is grounded to the detector vessel, is inserted between the cathode grid and the PMTs. The distance between the cathode and the protection grid was 9 cm and that between the protection grid and the PMTs was 1 cm.

The $10 \times 10 \text{ cm}^2$ and $40 \times 80 \text{ cm}^2$ are characterised by (1) a single 1-mm-thick LEM amplification stage and (2) a 2D readout anode realized on a single PCB. The system has a multi-stage structure consisting of two extraction grids, a LEM, a 2D readout anode and two signal collection planes as illustrated in Figure 46. The distances between the stages and typical configurations for the potentials

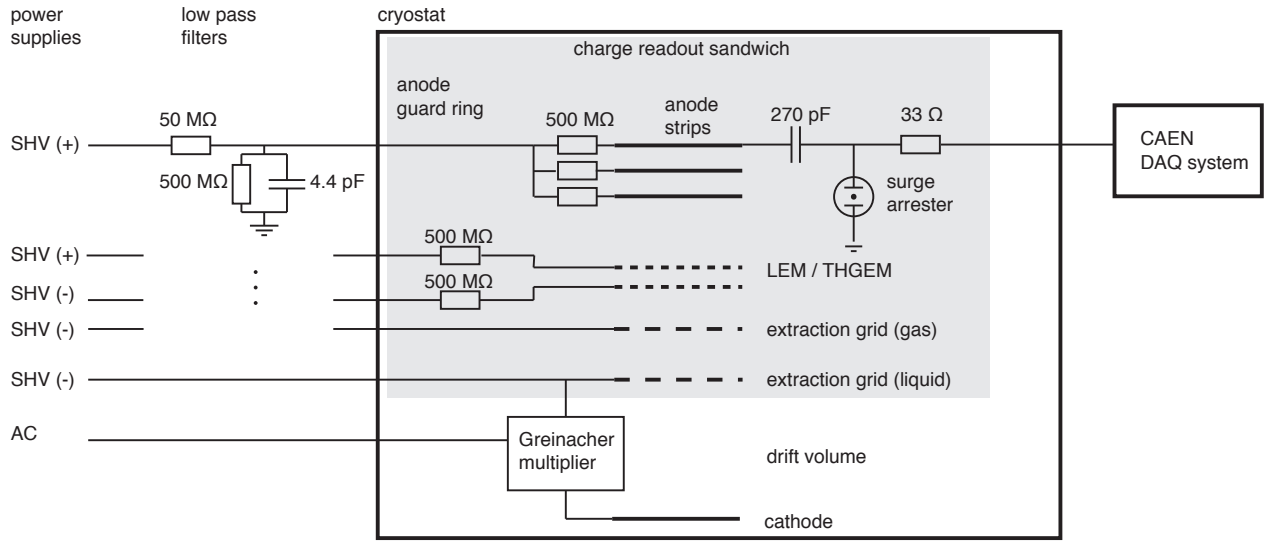


FIG. 45: Electrical scheme of the TPC with the HV connections on the left and the data acquisition system on the right. The gray box shows the components which are embedded in the charge readout sandwich.

and the inter-stage electric fields are summarized in Table III. In typical configurations a positive HV of ~ 1 kV is applied to the anode while the extraction grid in liquid is operated at a negative HV of ~ -7 kV, resulting in a virtual ground within the LEM plane. The LEM is a macroscopic hole

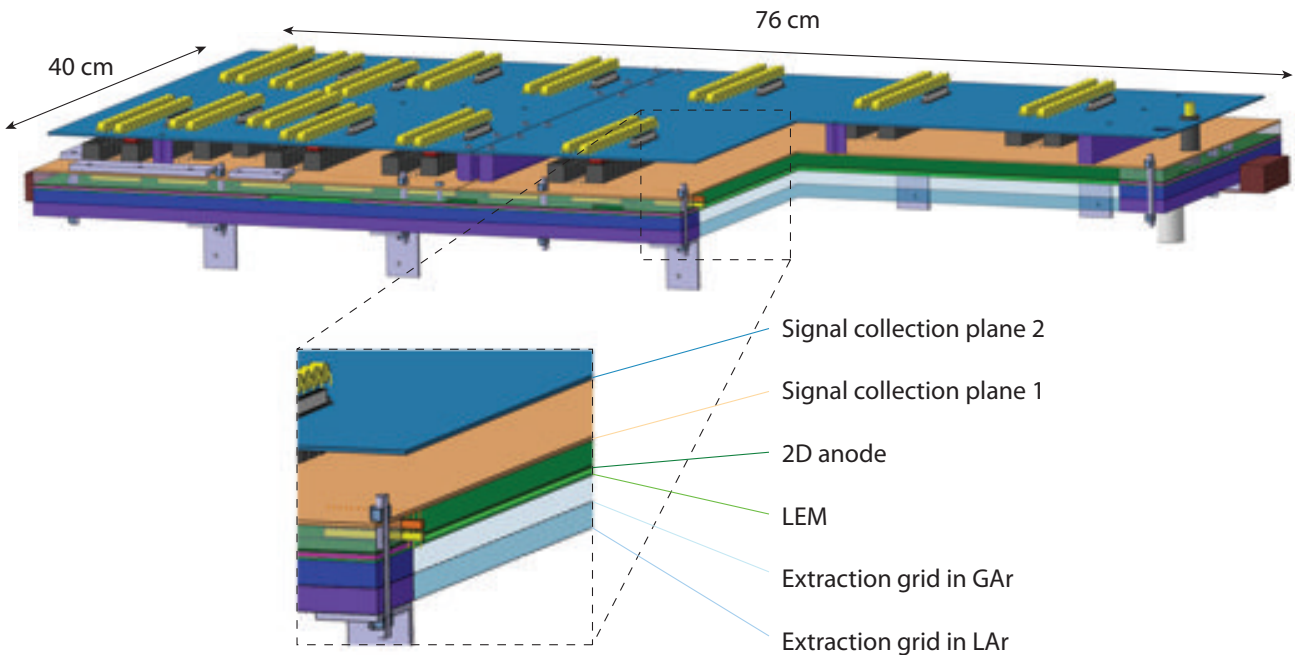


FIG. 46: Structure of the 40 × 80 cm² charge readout system incorporating a LEM (Large Electron Multiplier) and a 2D anode successfully built and operated. Right-front corner is cut in the illustration to present different stages in the multi-stage structure.

electron multiplier built with standard PCB techniques[165]. It is a 1-mm-thick FR4 plate, double-

	Distance to the stage above (cm)	Typical operating potential (kV)	Field to the stage above (kV/cm)
Signal collection plane 2	–	0	–
Signal collection plane 1	2	+1	–
2D anode	1	+1	–
LEM (top electrode)	0.2	+0.5	2.5
LEM (bottom electrode)	0.1	–3	35
Extraction grid in GAr	1	–4	1
Extraction grid in LAr	1	–7	3
Cathode	60	–31	0.4

TABLE III: Baseline LAr LEM charge readout system configurations.

side clad with a passivated copper layer. Of the order of half a million holes $500\ \mu\text{m}$ in diameter are CNC (Computer Numerical Control) drilled through the plate at a pitch of $800\ \mu\text{m}$ between the centers of adjacent holes. After the PCB has been manufactured and drilled, the copper layers are further chemically etched to create $40\ \mu\text{m}$ wide rims around the holes. A HV of typically $3.5\ \text{kV}$ is applied across the two faces creating a strong electric field of $35\ \text{kV/cm}$ in the LEM holes leading to multiplication of electrons by avalanches. The 2D anode plane has two orthogonal sets of readout strips on the bottom face providing two independent readout views. On top of the strips for one view, those for the other view are laid with a thin ($50\ \mu\text{m}$) polyimide (Kapton) insulating bed underneath. For each view, copper strips are formed by etching at a pitch of $600\ \mu\text{m}$ covering nearly the full area of $76 \times 40\ \text{cm}^2$. The readout pitch of $3\ \text{mm}$ is obtained by bridging five strips at one end. The strips on top are narrower ($120\ \mu\text{m}$) than those lying underneath ($500\ \mu\text{m}$) optimizing for an equal charge collection by the two views operating at the same potential. A more detailed description of the 2D anode can be found in Ref. [25] and references therein. The strips for both of the views are tilted by 45° with respect to the sides of the rectangular plate, to have symmetric conditions for both views. We use two signal collection planes, between which HV decoupling capacitors ($270\ \text{pF}$) are connected. Each readout channel is routed to a collective 32-channel connector to a flat cable. A surge arrester protecting the readout electronics from discharges is mounted for each channel. The cables bring the signals through a custom-made feedthrough on the upper flange, connected to the readout electronics placed outside of the vessel. The LEM charge readout system is assembled as a multi-layered “sandwich” unit with precisely defined inter-stage distances and inter-alignment. The multiplied charges coming from the ionization in LAr are finally collected on a charge readout plane. The *2D anode* basically consists of two perpendicular sets of electrode strips (or: *views*), which are separated by a very thin insulating layer. Due to the semi-transparent design of the device, arriving charges produce a similar response on both sets of strips, finally delivering the two coordinates of the detected charges. Although the concept was adapted from the readout for GEM detectors [99], the

design parameters had to be optimized for the application in a LAr TPC. In order to define an optimal electrode geometry, we have considered the response of a point-like energy deposition in LAr. As a consequence of the electric field focussing and defocussing by the extraction grids and the LEM but also the diffusion in gaseous argon, a δ -function like charge distribution in LAr arrives at the anode as a 1 mm extended charge cloud. Given this assumption, the induced signals on both views of the anode have to be mono-polar, fast and with similar amplitudes. Mono-polarity is guaranteed, since all the electrodes act in charge collection mode. As can be shown using the method of W. Shockley and S. Ramo [100, 101], electrons always drift against the weighting field of the corresponding collection electrode, inducing an entirely negative replacement current. Since the current is proportional to the electron drift speed in gas, the expected signal rise times are $< 0.5 \mu\text{s}$.

As sketched on top of ??, the readout consists of a FR4 substrate with $500 \mu\text{m}$ wide copper strips (*covered strips*), spaced by $600 \mu\text{m}$. On top of them, thin Kapton strips provide the electrical separation from the second set of $120 \mu\text{m}$ wide readout strips (*exposed strips*). The intrinsic readout pitch of $600 \mu\text{m}$ for each view ensures that even point-like charge deposits in the detector induce signals on both views, guaranteeing a correct reconstruction of the (x, y) coordinates. In order to collect in average equal amounts of charges on both views (exposed and covered strips), the local electric field was simulated with finite element methods[166]. It can be seen in the cut through the anode shown on the bottom left plot of ?? that the exposed electrodes have a focusing effect on the electric field lines. Simulating different geometries, we have found that roughly half of the field lines end up on each of the two views if the width of the exposed strip equals $120 \mu\text{m}$, as shown in the figure. The picture on the bottom right of ?? shows the anode of the 3L prototype. It can be seen that the desired readout pitch of 3 mm is obtained by connecting five consecutive strips with the intrinsic pitch of $600 \mu\text{m}$ together. Published performance obtained with these kind of detectors can be found in Refs. [23–26]. The $40 \times 80 \text{ cm}^2$, the largest detector operated so far, has been operated during more than 1 month in 2011 under controlled pressure of $\pm 1 \text{ mbar}$. The effective gain in stable condition was 14.6 with a $S/N = 30$ for m.i.p. The charge sharing between the two views was within 8%.

Figure 48 shows four typical cosmic ray events, taken from the highest gain run with an amplification field of 35 kV/cm . From top to bottom, there are two cosmic muons crossing the detector, a deep inelastic interaction and an electromagnetic shower candidate. These plots show the usual representation of events with the drift time as a function of the strip number for both views. The greyscale represents the signal amplitude for each sample in a linear scale. It can clearly be seen that both views show symmetric unipolar signals which are clearly distinguishable from the noise. As a consequence of the good signal to noise ratio and the spatial resolution, small structures like knock-on electrons – also

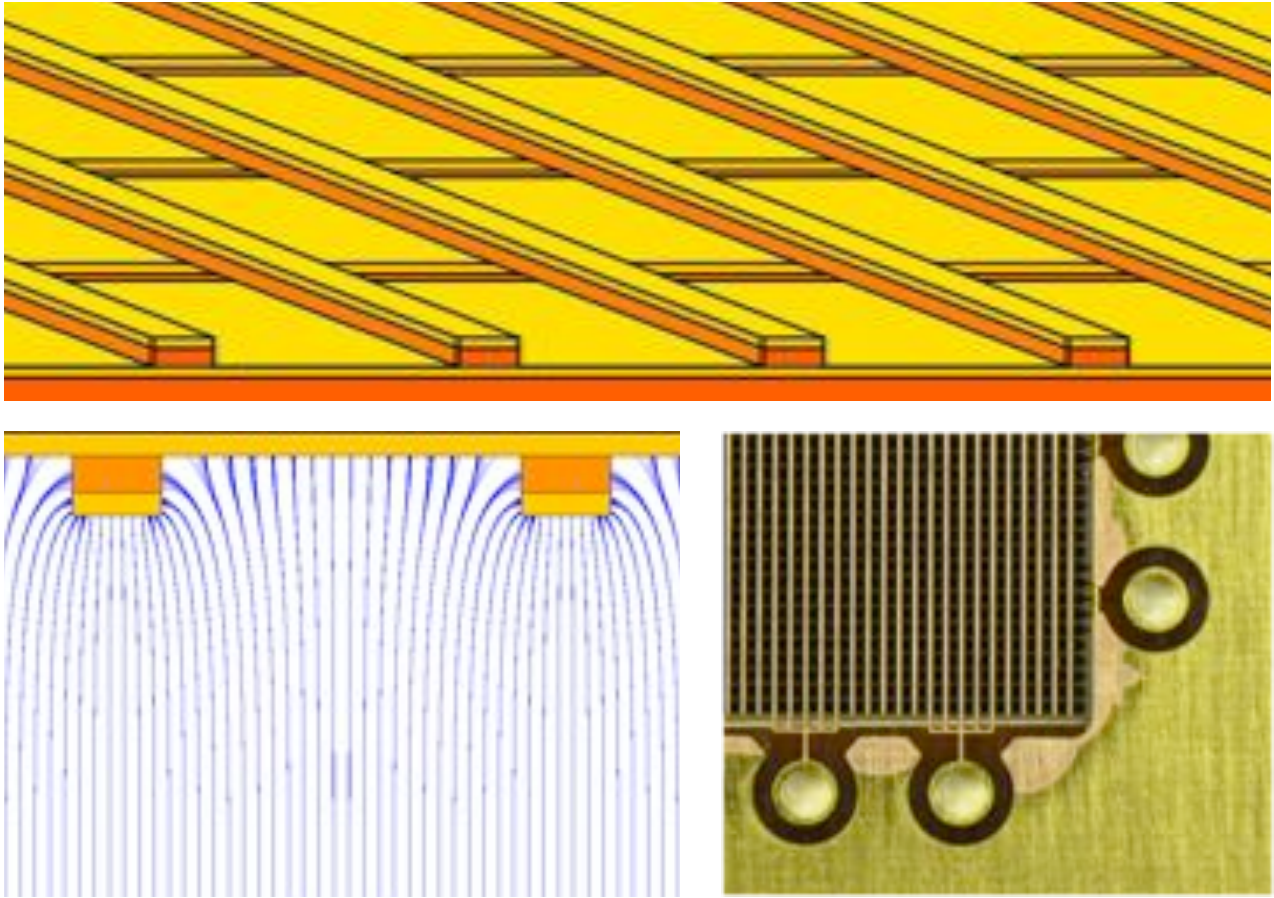


FIG. 47: Top: scheme of 2D anode (upside-down) with the FR4 substrate on the bottom (orange), followed by two perpendicular sets of electrodes (yellow), which are separated from each other by a thin Kapton layer (orange strips underneath the thin copper electrodes). Bottom left: electric field simulation to show that equal amount of charges are collected by both electrode sets. Bottom right: picture of manufactured 2D anode of the 3 L prototype [25].

called δ -rays – can be identified and reconstructed in three dimensions as demonstrated below. Since cosmic muons produce straight crossing tracks and the energy deposition is known to be ~ 2.1 MeV/cm, the events can be used to characterise the detector in terms of free electron lifetime and amplification. An obvious limitation of this charge readout was the inactive area introduced by the segmentation of the LEM. The 1.6 mm wide gaps between the LEM electrode segments appear as equally spaced missing charge, as seen in the two muon events in Figure 48.

In view of the extrapolation of the double phase technique to the large surfaces foreseen in the DLAr detector further studies were conducted to simplify the design and reduce the electrical capacitance of the readouts. First, as explained in Ref. [102], we were able to extract the drifting electrons from the liquid to the gas by means of a single grid placed just below the liquid surface. In this configuration the LEM is positioned 50 mm above the liquid surface and the extraction field is directly provided by the LEM-grid system over the 10 mm distance. This configuration offers the advantage of 1. simplifying the

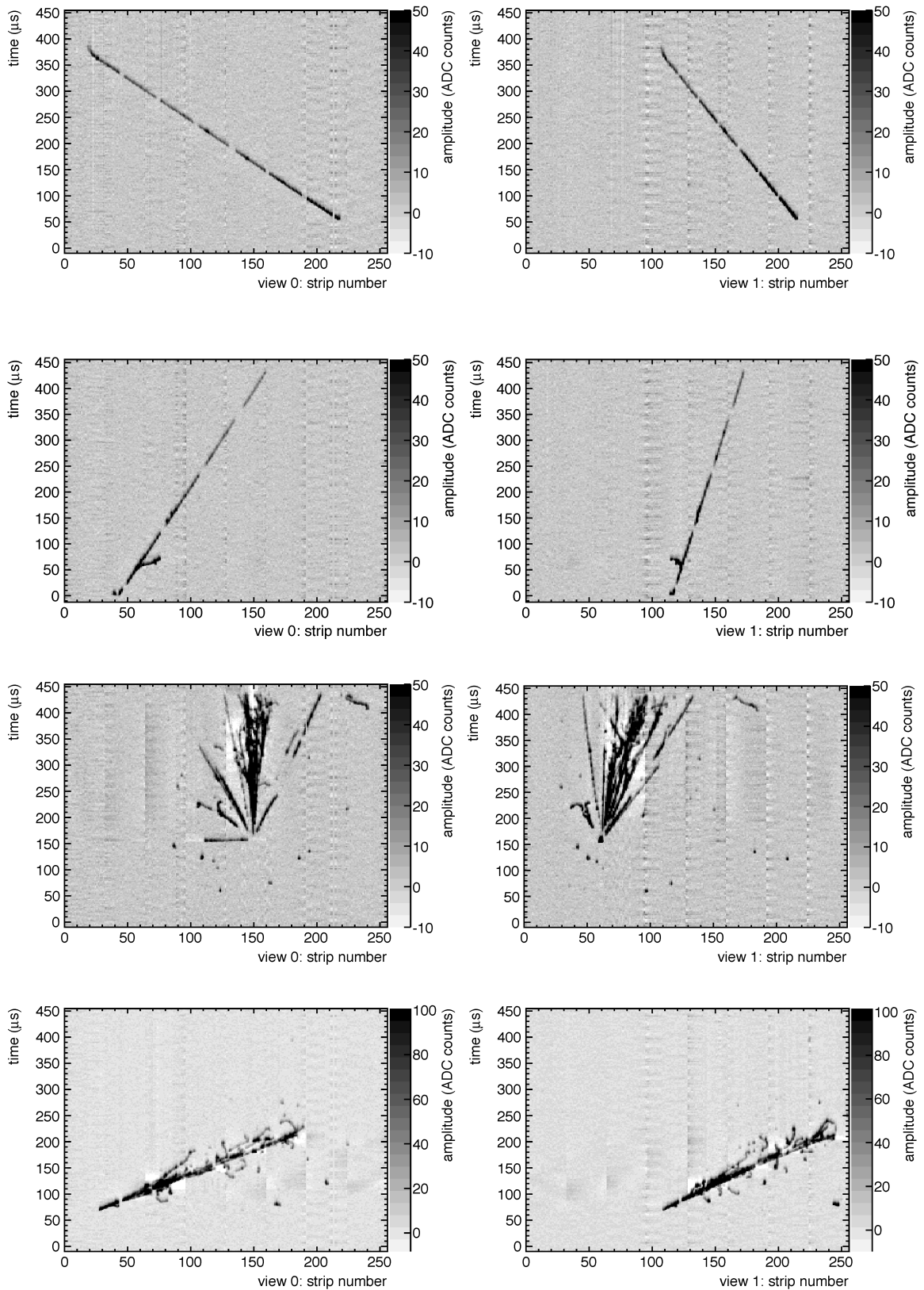


FIG. 48: Cosmic ray event displays (left: view 0, right view 1), recorded in double phase conditions with a LEM field of 35 kV/cm. The four event displays show from top to bottom two muons, a hadronic and an electromagnetic shower candidate. [See text for more details.]

overall design, 2. reducing the absolute required high voltage and removing a high voltage connection in the gas phase and 3. improving the electrical transparency of the system by avoiding the collection of the electrons on the top grid. The typical high voltages applied across each stage with the single grid configuration are summarised in Table IV. The DLAr detector will follow a similar high voltage scheme. In the single grid configuration the anode is kept at ground while the extraction grid is operated at a

	Distance to the stage above (cm)	Typical operating potential (kV)	Field to the stage above (kV/cm)
2D anode	-	0	-
LEM (top electrode)	0.2	-1	5
LEM (bottom electrode)	0.1	-4.4	34
Extraction grid	1	-6.4	2
Cathode	20.5	-16.7	0.5

TABLE IV: LAr LEM charge readout system configurations for the 10×10 cm² detector equipped with a single extraction grid.

negative HV of ~ -7 kV. An electric field of 34 kV/cm is applied across the LEM which produces an effective gain of about 20.

With the aim of easing the manufacturing process for large scale production and reducing electrical capacitance of the readout we designed and tested two dimensional projective readout anodes, manufactured from a single multilayer printed circuit board (PCB). A picture of the anode used in the 10×10 cm² setup together with a close up look and a schematic drawing is shown in ???. Its design parameters are listed in Table V.

Copper thickness (μm)	Readout pitch (mm)	Track pitch (mm)	Track width (mm)	Pad diameter (mm)	Via diameter (mm)
35	3.125	1.5625	0.1	0.4	0.2

TABLE V: Characteristics of the 2D multilayer PCB anode.

The 3 mm readout pitch of each view is segmented in two interconnected gold plated copper tracks which are printed on a multilayer PCB. As seen in the schematic drawing, the basic pixel contains 8 pads equally distributed between two views in order to guaranty a fully symmetric charge sharing. The response of the anode was tested by fitting it to the 10×10 cm² prototype and exposing the chamber to cosmic muons. We tested that the charge is efficiently shared between both views which is one of the important requirements of the anode. Moreover the fine segmentation of the readout strips should ensure that the response in terms of charge collected per unit length is independent of the angle at which the track crosses the strips. All these requirements are demonstrated in ????: the left plot shows the collected charge per unit length on view 0 ($\Delta Q_0/\Delta s_0$) as a function of the track azimuthal angle ϕ (see ??? for a definition of ϕ). As can be seen from the projections (middle plot)

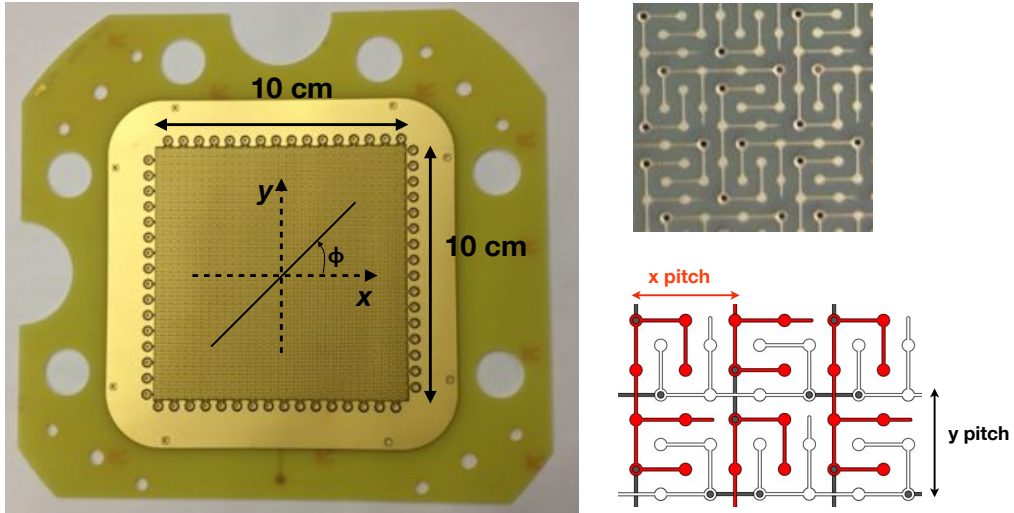


FIG. 49: *Left:* Picture of a $10 \times 10 \text{ cm}^2$ multilayer PCB anode tested in our chamber with dimensions and coordinate system super-imposed. *Right:* close up picture of the anode showing the copper track pattern that allows a 2 view readout on the same circuit board. A schematic explaining the interconnections between both views is also shown. The 3 mm readout pitches are indicated by arrows. View 0 is filled in red and view 1 in white.

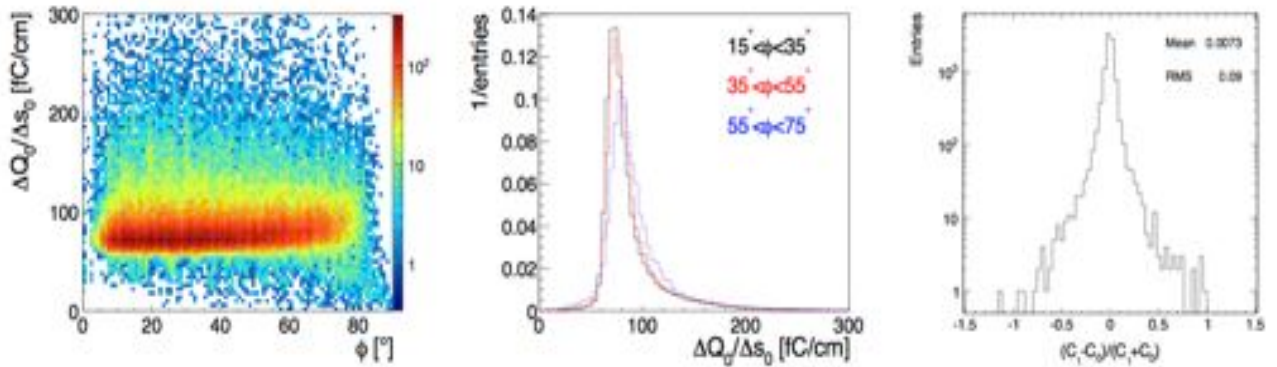


FIG. 50: Charge deposition measured on view 0 ($\Delta Q_0/\Delta s_0$) as a function of the track angle ϕ (left) and projection of the $\Delta Q_0/\Delta s_0$ distribution in three ϕ intervals (middle). The right plot shows the distribution of the difference between the total charge collected on both views normalised to their sum.

the $\Delta Q_0/\Delta s_0$ distributions are close to a Landau function as expected from the fluctuations of the collected charge per unit length. The width and mean value of those distributions are also similar for all angular intervals illustrating a uniform response. To illustrate the charge sharing between both views the right plot shows the distribution of the difference between the total charge collected on both views normalised to their sum. The distribution has an RMS of 9 % and is centered around 0.7 % indicating that the anode is indeed perfectly $x - y$ symmetric and that the charge is equally shared between both views. Thanks to the spacing between the pads and tracks of both views, the anode has a measured capacitance per unit length of about 150 pF/m between neighbouring channels.

Compared with the Kapton type anodes used previously in the $10 \times 10 \text{ cm}^2$ and $40 \times 80 \text{ cm}^2$ which had a capacitance per unit length of $\sim 600 \text{ pF/m}$, this anode offers a significant noise reduction and satisfies our needs in terms of signal-to-noise ratio for the 3 m long readouts foreseen in the DLAr detector. Other anodes with alternate geometries have also been tested. Their designs and the results are presented in Ref. [102]. The goal is always to reduce the capacitance per unit length without degrading the imaging capabilities of the TPC. From that point of view, the one presented here offered the best performance and was hence chosen as the final readout option.

In order to define the optimal high voltage settings across each stage we systematically tested the response of the chamber in terms of effective gain and resolution on the deposited charge for different electric field settings. For that matter, we define the effective gain of the device as the ratio of the measured charge (corrected for the drifting electron lifetime) collected on both views to the initially produced charge of the ionising particles. Under the assumption that only MIP events are present in our selected sample, the average charge deposition along a track, predicted by the Bethe-Bloch formula and accounting for electron-ion recombination [18] is $\langle \Delta Q / \Delta s \rangle_{MIP} = 10 \text{ fC/cm}$. The effective gain is hence defined as

$$G_{eff} = \frac{\langle \Delta Q_0 / \Delta s_0 \rangle + \langle \Delta Q_1 / \Delta s_1 \rangle}{\langle \Delta Q / \Delta s \rangle_{MIP}} \quad (4.1)$$

where the indices correspond to view 0 and 1. As example we show in ?? the response of the chamber as a function of the electric field applied across the LEM. On the same figure we show the effective gain and the resolution on the charge deposition measurement. The resolution is obtained by fitting the distributions with a Gaussian convoluted Landau function and is defined as $\sigma_{gauss} / \langle \Delta Q_i / \Delta s_i \rangle$. As can be seen the measured effective gain exhibits the expected exponential dependence with the LEM field (see Refs. [95, 102] for details) and the resolution on both views are similar and stay constant at around 8%. We achieved an effective gain of 90 by setting the amplification field to 35 kV/cm. The signal-to-noise ratio is then defined as the mean amplitude of the waveforms produced by the cosmic tracks divided by the average value of the noise RMS. Given our noise value of about 4-5 adc counts RMS, a gain of 90 corresponds to a signal-to-noise ratio S/N of about 400 for minimum ionising particles, or $S/N \sim 10$ for an energy deposition of 15 keV on a single readout channel.

As discussed in detail in [102] the effective gain stabilises after an initial decrease of about 1.5 days due to the charging up of the dielectric of the LEM. Once a state of equilibrium is reached, the gain is however stable for long periods. We showed that with a LEM field of 33kV/cm the detector was in stable operation for about a month at the gain 15. This means that we can run the chamber in a stable operation mode with a S/N of at least 60 for minimum ionising particles. ?? shows a typical cosmic

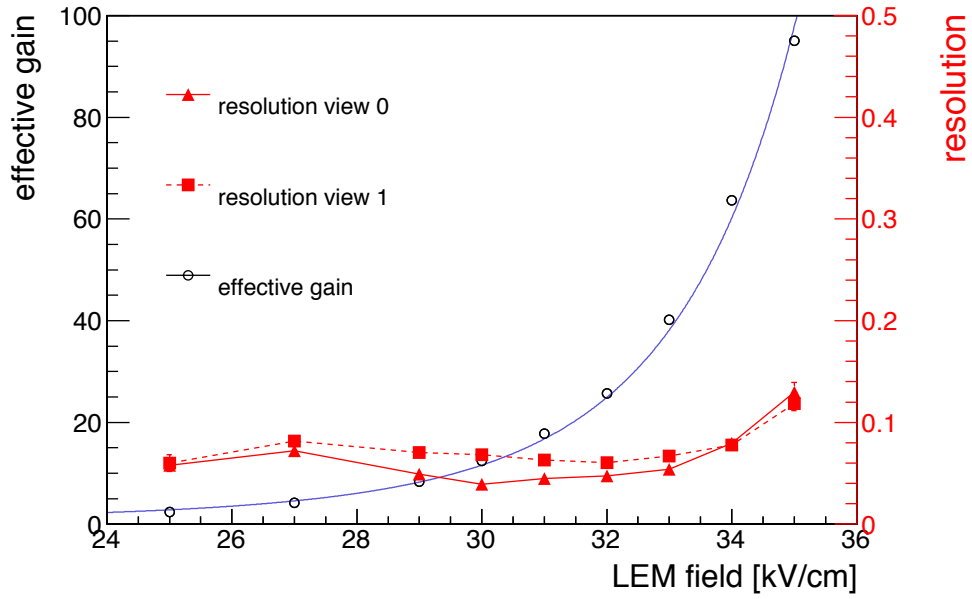


FIG. 51: Effective gain and resolution of the charge deposition measurements on both view as a function of the LEM electric field.

event acquired with a gain of 15. Further studies will be performed to check whether the chamber can be continuously operated at larger LEM fields and if higher gains in stable conditions can be reached.

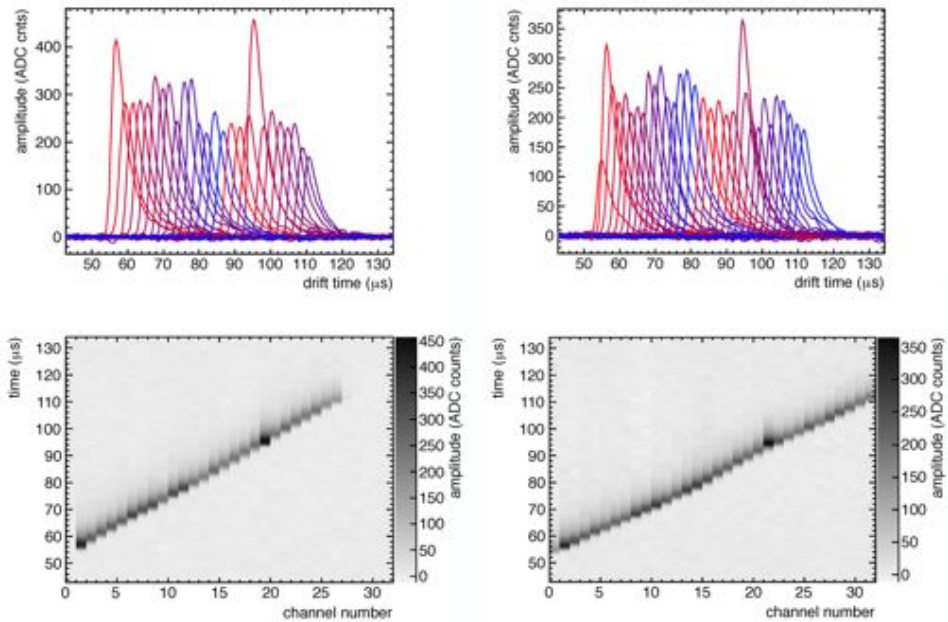


FIG. 52: Event display of a cosmic track with a gain of ~ 15 obtained in the 3 liter chamber. (top): the raw waveform showing the amplitude of the signals on both views. (bottom): drift time versus channel number of the reconstructed hits.

Based on those studies in Table IV we summarise the typical high voltages applied across each stage of the detector equipped with the new anode and operated in the single grid configuration. An electric

field of 33 kV/cm is applied across the LEM which produces a stable effective gain of about 15. The DLAr detector will follow a similar high voltage scheme.

4.1.5 The CRP for the $6 \times 6 \times 6\text{m}^3$

The Charge Readout Plane (CRP) module of the $6 \times 6 \times 6\text{m}^3$ is a direct extrapolation of the successful $10 \times 10 \text{ cm}^2$ prototype with the single extraction grid configuration to an active area approximately as large as $600 \times 600 \text{ cm}^2$. In the LAr LEM TPC configuration, the CRP consists of the low capacitance 2D anode, LEM and extraction grid assembled as a multi-layered “sandwich” unit with precisely defined inter-stage distances and inter-alignment. The distances, tolerances and nominal electric fields between each stage are shown in ?? and summarised in Table VI. In this configuration we successfully operated the $10 \times 10 \text{ cm}^2$ prototype at a constant gain of about 15 for around a month with very few discharges [102].

	[mm]	electric field [kV/cm]	tolerance [mm]
anode-LEM	2	5	0.1
LEM	1	34	0.01
LEM-grid	10	2	1
liquid level	5 (from grid)	-	1

TABLE VI: distances and tolerances between each stage. The tolerance on the LEM refers to the thickness of the LEM insulating material (FR4).

The tolerances are calculated to keep the gain stable within 5% over the entire active area of the readout. We used the $10 \times 10 \text{ cm}^2$ prototype to scan the fields applied between the different stages and we checked the effect on the gain. As example we show in ?? the gain for different values of the extraction field. The extraction field is defined as the electric field across the LEM-grid stage calculated in the liquid. As can be seen the gain is rather stable around the chosen operating value of 2kV/cm in the liquid and variations of the extraction field do not have a dramatic impact on the gain. The fact that the gain reaches a stable level indicates that at about 2kV/cm all the electrons are efficiently extracted from the liquid to the gas phase. The allowed variation of the extraction field define a region of tolerance for the LEM-grid distance as shown in ??-right. The quoted tolerance of 1 mm on the grid-LEM distance lies well within the allowed variation of the extraction field specified on the figure.

The design concept of the CRP is illustrated in ?. The final design of the CRP for the $6 \times 6 \times 6\text{m}^3$ will be guided by many studies and prototyping. One important aspect is to ensure that the various mechanical components have an adequate rigidity in order to respect the tolerances reported in Table VI. For that matter the mechanical structure is being tested on a $1 \times 1\text{m}^2$ mockup. In a next step we

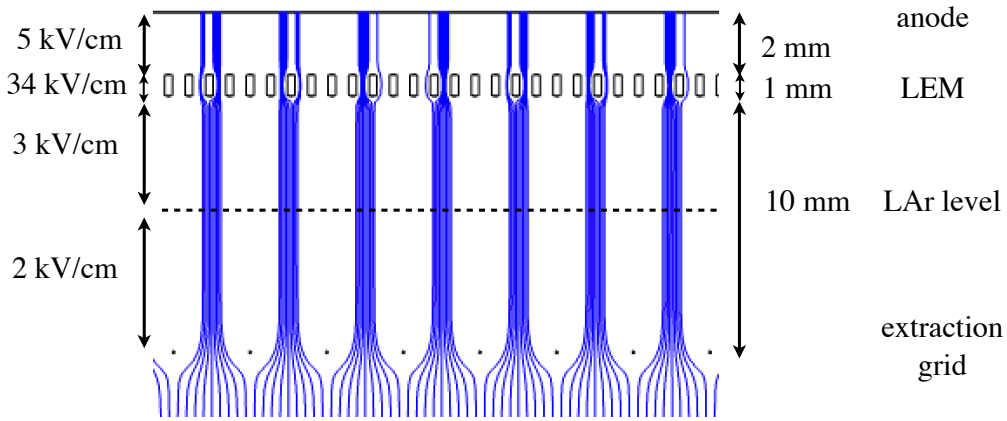


FIG. 53: Simulated geometry of the readout showing the distances and nominal electric fields. The field lines followed by the drifting charges (not taking into account diffusion) are also shown.

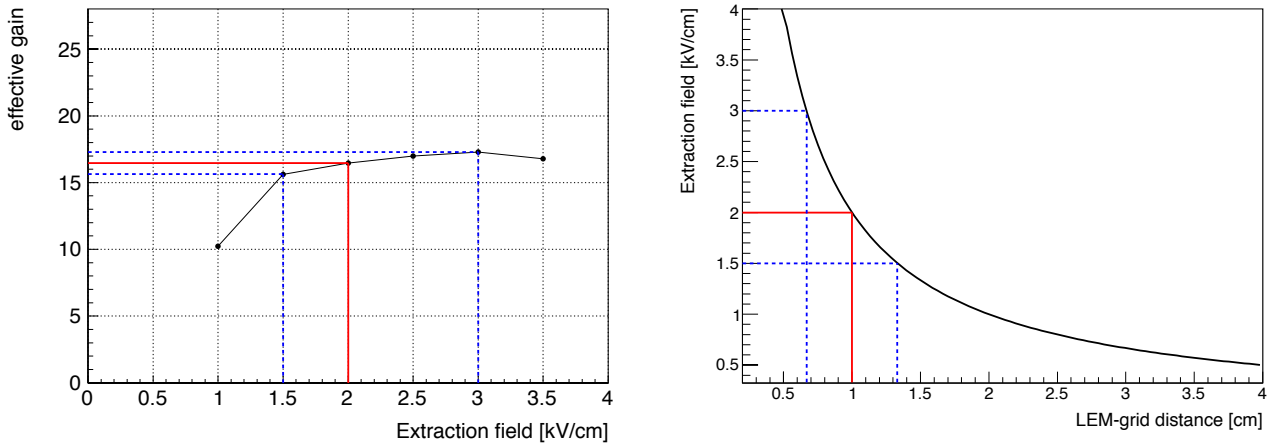


FIG. 54: *Left*: measured gain in the $10 \times 10 \text{ cm}^2$ prototype as a function of the extraction (LEM-grid) field. The red line shows the nominal electric field and the dotted blue lines the electric field corresponding to a $\pm 5\%$ variation of the gain. *Right*: calculated extraction field as a function of the LEM-grid distance. The dotted blue lines indicate the variations around the nominal 1 cm distance that keep the gain within $\pm 5\%$.

will construct a larger $1 \times 3 \text{ m}^2$ module which will be fitted on a LAr LEM TPC of a $3 \times 3 \times 1 \text{ m}^3$ active volume.

$1 \times 1 \text{ m}^2$ CRP

In order to test the structural rigidity of the CRP and optimise the overall design a mechanical mockup of the CRP module with an active area of $1 \times 1 \text{ m}^2$ was constructed as shown in ???. The mockup consists of a rigid frame reinforced by precisely machined external and internal FR4 bars. In addition to hosting the anode and LEM modules, the frame serves as external suspension. The readout is composed of four independent modules of $50 \times 50 \text{ cm}^2$. Each module is composed of a $50 \times 50 \text{ cm}^2$ anode and a

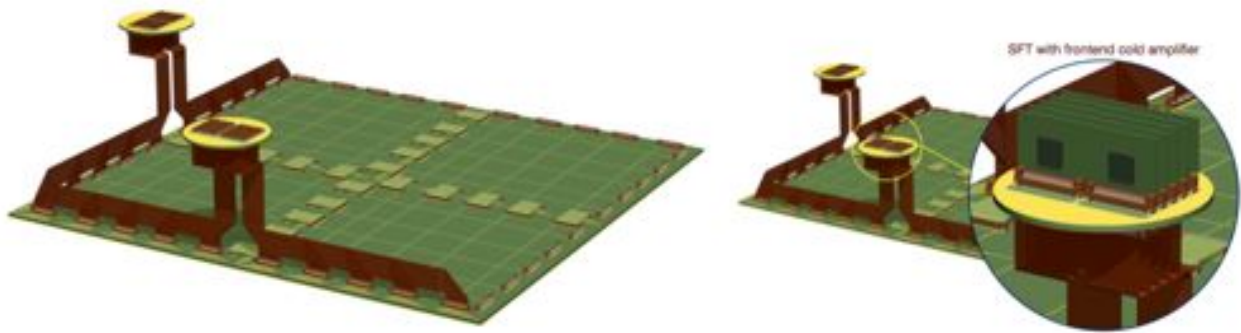


FIG. 55: Design concept of the $1 \times 1 \text{ m}^2$ CRP: (left) overall view and zoom on a signal feedthrough (SFT) with cold frontend preamplifier;

$50 \times 50 \text{ cm}^2$ LEM panel. The anode is designed to have 5 connectors at the edges which provide the function of either bridging the anodes or sending out the signal. The set of connectors in between two anodes are used to bridge them together in order to form a fully active 1 m^2 readout while the others are used to send the signal to the front-end electronics.

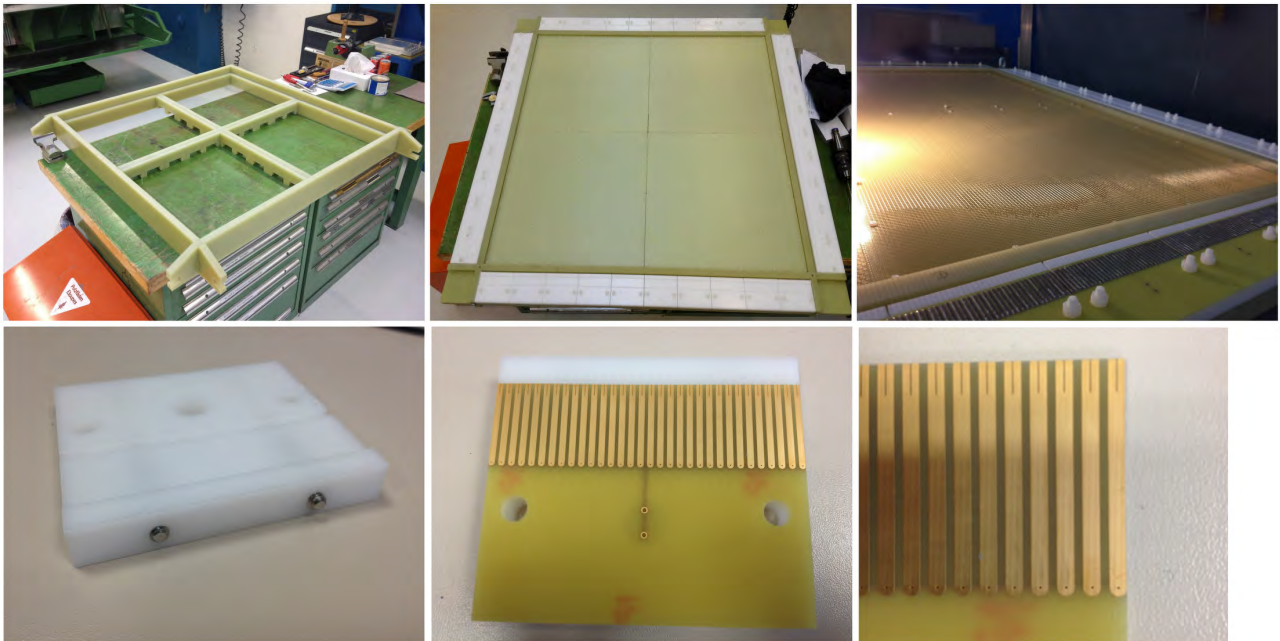


FIG. 56: Pictures of the 1 m^2 CRP mockup. The top pictures show the frame structure made out of G10 which holds the four anode-LEM modules and the CRP assembled with a fake LEM (1 mm sheet of FR4). The wire tensioning pads made are also positioned. The CRP is then equipped with the four $50 \times 50 \text{ cm}^2$ anode modules and the tensioned wires of the extraction grid. The bottom picture shows the details of one wire tensioning pad: the wire holder made out of POM (Polyoxymethylene) is equipped with two stainless steel screws that provide the tension to the wires by pushing the holder against the FR4 frame. A close up picture of the wire soldering PCB shows the $200 \mu\text{m}$ grooves that allow a precise positioning of the wires.

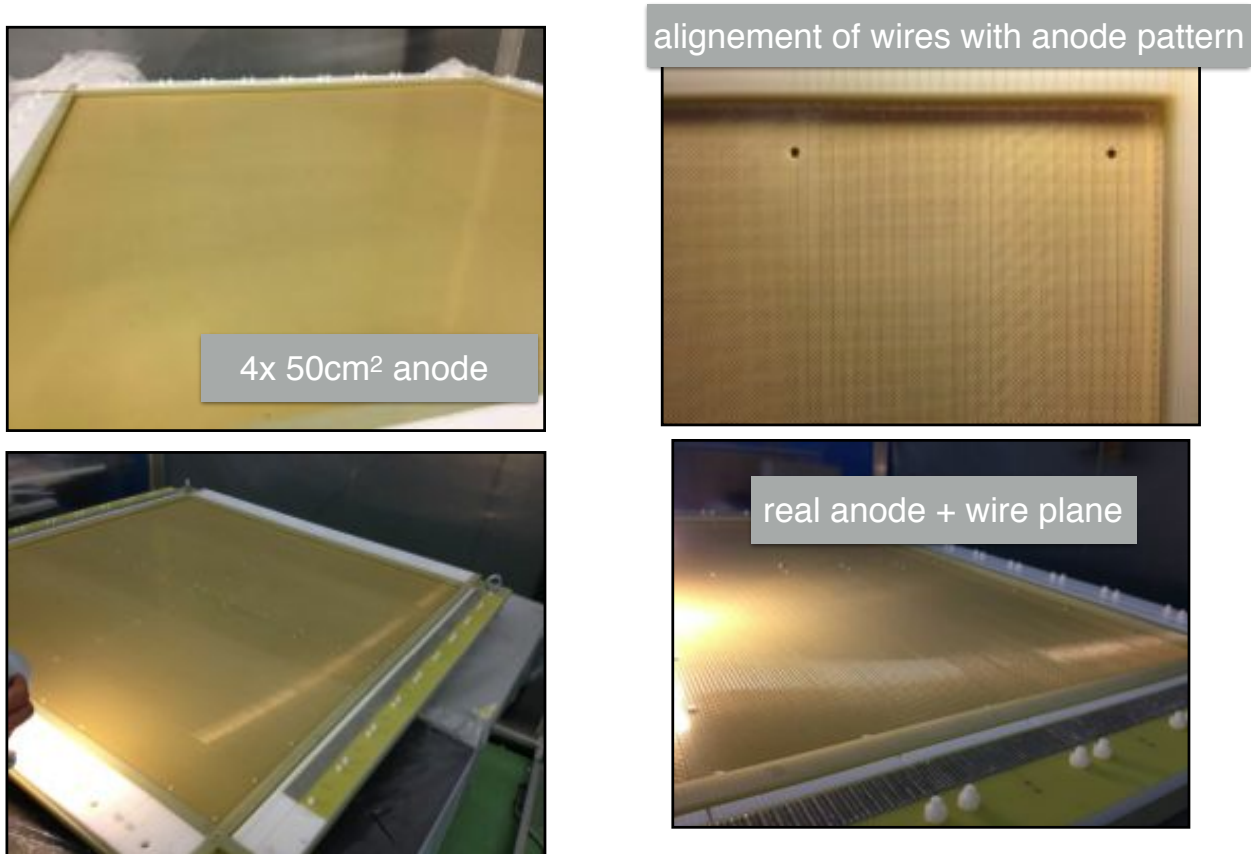


FIG. 57: Pictures of the 1 m² CRP mockup: anode details.

The extraction grid consists of 100 μm diameter stainless steel wires tensed in both x and y directions. They are soldered by group of 32 on independent wire tensioning pads spaced on the side of the frame as shown in ???. Each wire tensioning pad consists of a PCB precisely fixed on a mechanical wire holder machined from POM (Polyoxymethylene)[167]. The PCB hosts the high voltage connection and has 32 soldering pads with 200 μm grooves to precisely position the wires. During the wire soldering process each wire is tensioned by 150 g lead weights and precisely positioned inside the grooves. With this method the precision on the wire pitch, measured under the microscope, was better than 50 microns. The PCB is then fixed on the wire-holder and the whole system can provide precise tension to the group of 32 wires by pushing the holder against the CRP FR4 frame with two stainless steel screws (see ??).

$1 \times 3 \text{ m}^2$ CRP

A CRP of $1 \times 3 \text{ m}^2$ will soon be assembled and tested on a LAr LEM TPC of $3 \times 1 \times 1 \text{ m}^3$ active volume. The mechanical design is shown in Fig 60. It follows the basic concept of the $1 \times 1 \text{ m}^2$ mockup. The support structure is made from stainless steel and houses three G10 frames to which the $50 \times 50 \text{ cm}^2$

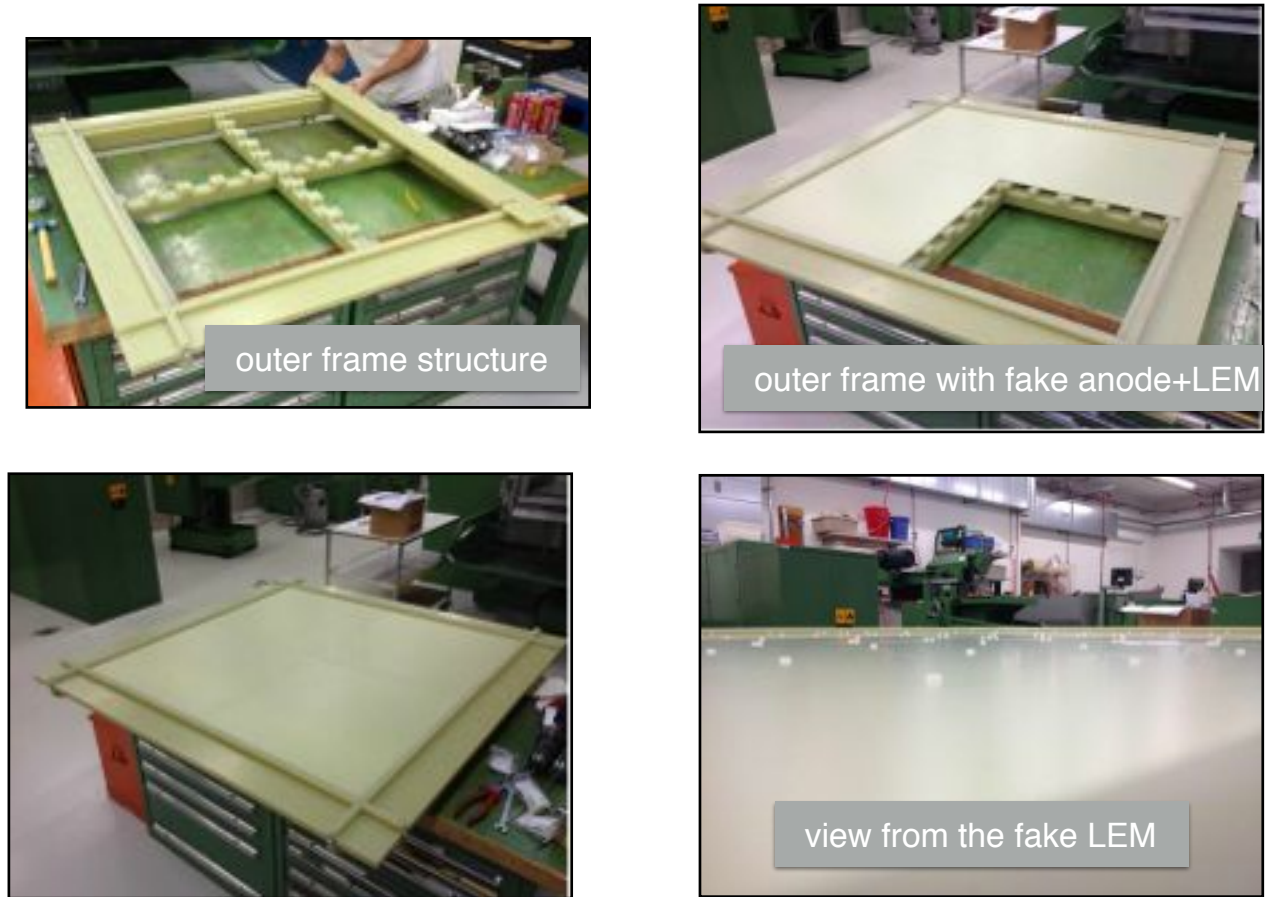


FIG. 58: Pictures of the 1 m² CRP mockup: frame details.

anode and LEM modules will be attached creating a fully 1 × 3m² active area. The frame also holds on its side the wire holders for the extraction grid.

6×6 m² CRP

The 6×6×6 m³ CRP design follows the basic concept of the 1×1 m² mockup and 1 × 3m² module as shown in ???. The frame contains 4 external reinforcement bars of 6 meters and 22 internal ones. The external bars define the 6×6 m² total area and the internal bars divide the total area into 144 identical 0.5×0.5 m² sub-areas. As for the 1×1 m² CRP, each of the 144 sub-areas has one anode and one LEM panel. The extraction grid will be made by tensioning and fixing 6 m stainless steel wires to the outer frame in both directions. The same method as the 1×1 m² mockup will be used to fix and tension the wires. In total the 7680 channels are sent to the cold front-end preamplifiers inserted in the 12 signal feedthrough chimneys. The signal feedthroughs chimneys are positioned to make 4 groups of 3 meter long readout strips as explained in ???. In this configuration, adjacent 0.5×0.5 m² anode panels are bridged by groups of 36 to form the maximal readout lengths of 3 meters. The suspension feedthrough

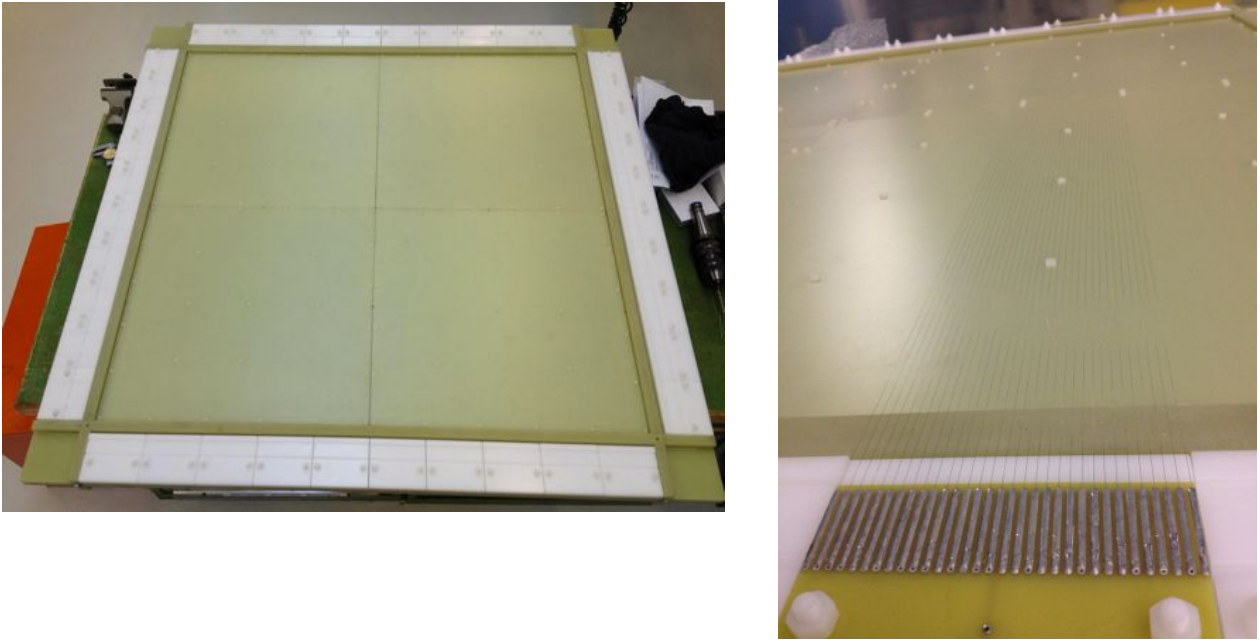


FIG. 59: Pictures of the 1 m² CRP mockup: extraction grid details.

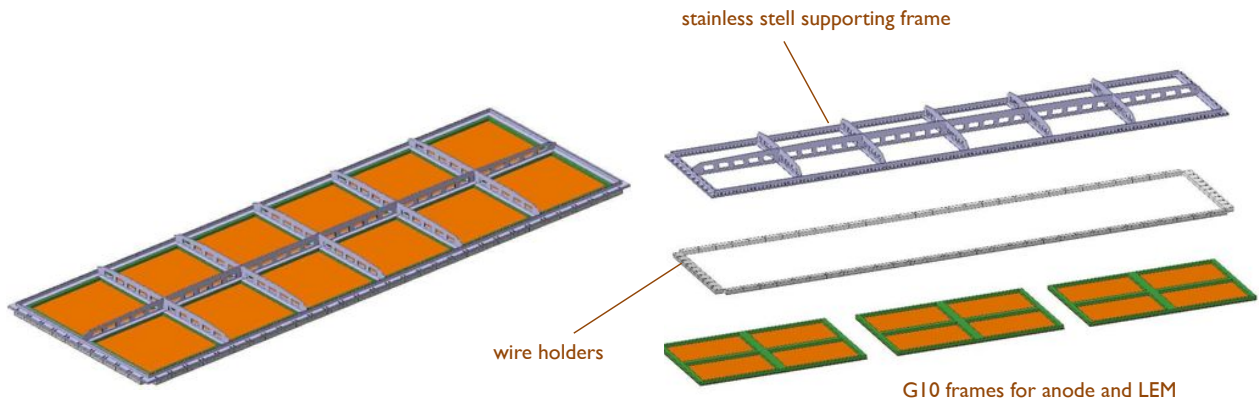
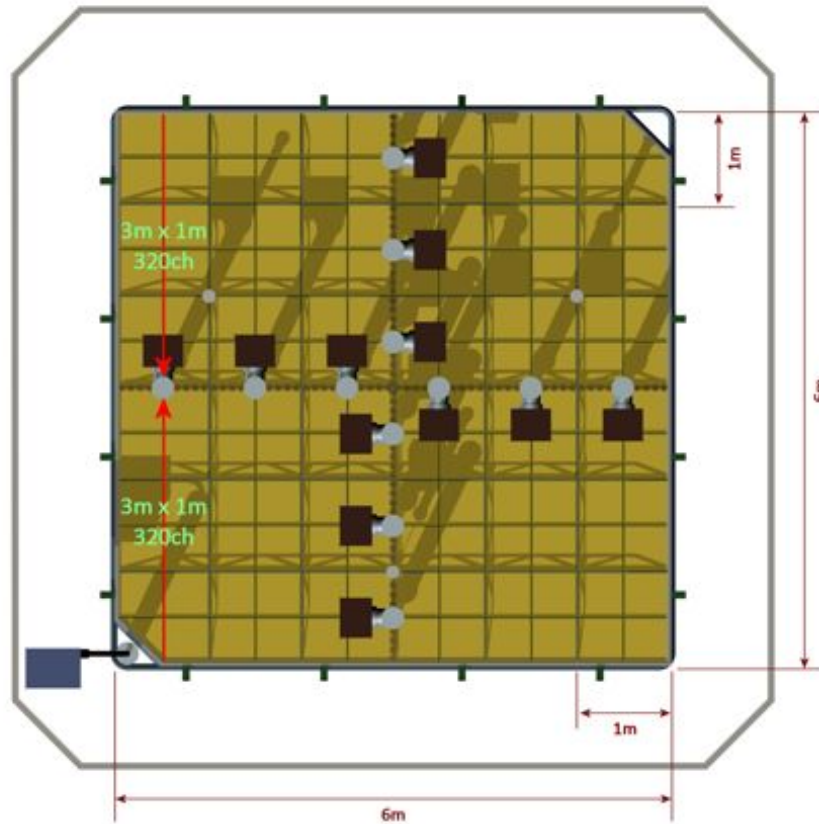


FIG. 60: 3D drawing of the 1×3 m² CRP.

chimneys provide the function of hanging the whole structure from the tank deck and precisely aligning the CRP to the liquid argon level. A detailed description of the anode deck suspension system is given in Section 4.1.1. Table VII summarises the basic components of the $6 \times 6 \times 6\text{m}^3$ CRP.

4.1.6 The MICROMEAS option

Micro-Pattern Gaseous Detectors (MPGDs) such as GEM/THGEM/LEM are well established and high performance devices widely used in particle physics experiments. The MICRO-MESH GASeous

FIG. 61: Top view of the $6 \times 6 \times 6\text{m}^3$ CRP.

Component	Anode panel	LEM panel	Signal feed-through	Suspension feed-through
	144	144	12	3

TABLE VII: Components of the $6 \times 6 \text{m}^2$ CRP.

Structure or MICROMEGAS is a MPGD invented in 1996 which amplifies electrons in a typical $100 \mu\text{m}$ gap defined by a metallic micromesh placed on top of an anode Printed Circuit Board (PCB)[103]. In 2004, a new method to build this detector was introduced and called the bulk-MICROMEGAS[104]: a woven micromesh is embedded on top of the segmented anode plane of the MICROMEGAS by use of standard photolithographic techniques. This technology was chosen to instrument the 3 TPCs of the ND280 near detector of the T2K experiment for its performance in terms of gas gain uniformity, energy resolution and space point resolution, as well as for its capability to efficiently pave large readout surfaces with minimized dead zones. Eighty six $128 \mu\text{m}$ gap $34 \times 36 \text{cm}^2$ bulk-MICROMEGAS modules were produced in 18 months. Eighty of them, for an equivalent total surface of 9m^2 , passed the quality

and performance tests. The dispersion of gas gain and energy resolution at 5.9 keV within the whole surface of each module were respectively 2.8% and 6% r.m.s. The dispersion of mean gain and mean 5.9 keV energy resolution over the eighty modules were found to be respectively 8% and 3% r.m.s[105]. These facts illustrate the maturity of the bulk-MICROMEGAS technology for a high quality mass production at a moderate cost.

One advantage of the MICROMEGAS technique is thus the possibility to easily produce large detectors, with a quality suitable for the instrumentation of a large area HEP detector. The industrial production of large area detectors is being adopted by the ATLAS Collaboration who will construct about 1200 m² of resistive MICROMEGAS detectors for the upgrade of the first station of the ATLAS muon end-cap system (New Small Wheel) [168].

In 2010, the T2K IRFU group started an R&D project to investigate the feasibility of using bulk-MICROMEGAS to instrument a double phase LAr. Gas amplification process was first tested tested in argon at room temperature up to a pressure of several bars. Then, a 10×10 cm² bulk-MICROMEGAS with an amplification gap of 100 μm was tested in the 3L ETHZ Liquid Argon TPC at CERN[106] (see ??). The anode was made of 32 1D strips with a 3 mm pitch. The device operated successfully in this cryogenic environment for several days. In particular the following points were demonstrated:

- compatibility with the high purity environment;
- operation in a cryogenic environment;
- successful charge readout, with observation of tracks from cosmic rays;
- charge amplification, up to approximately 5.

In 2013, three bulk-MICROMEGAS prototypes with amplification gaps of 115, 128 and 192 μm were built and tested in a 40 liter LAr cryostat at the University of Liverpool. Each detector had an active area of 10.8×10.8 cm² and the anode subdivided into 36 readout strips with a 3 mm pitch. Tests performed at room temperature in pure argon provided a good understanding of the gain dependance as a function of the gap size. Using a ²⁴¹Am source, gain values were measured for applied voltages on the micromesh up to values near the detector breakdown operation point. The 115 μm gap prototype was also successfully tested in the Liverpool double phase LAr TPC[107]. Clean cosmic tracks could be observed (see ??) and a gain of about 4, comparable to the one measured during the 2010 test at CERN, was obtained.

Further R&D activity will be pursued in 2014 in order to optimize the amplification gain of such MICROMEGAS devices. The main directions of development are: the use of thinner gaps (e.g. 64 μm),

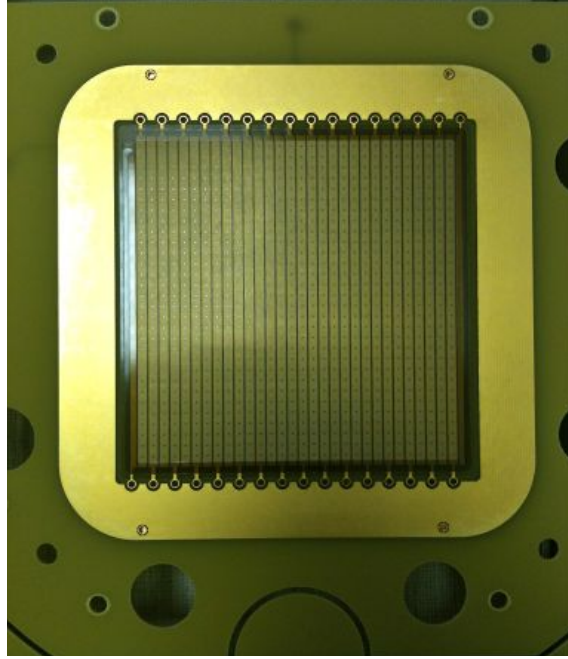


FIG. 62: The $10 \times 10 \text{ cm}^2$ bulk-MICROMEGAS prototype tested in a Liquid Argon TPC. The anode has 32 strips with a 3 mm pitch.

tests of resistive bulk-MICROMEGAS detectors and the use of a modified anode-micromesh structure to better absorb UV photons produced in the amplification region.

4.2 Drift cage

The function of the drift cage is to create a uniform electric field in the inner part of the detector, with a strength between 500 and 1000 V/cm, resulting in a drift velocity of the quasi-free electrons ranging between 1.6 and 2.0 mm/s. This mechanical structure supports also the negative HV cathode, towards the bottom of the tank, 1m above the surface of the PMT.

A full engineering design for the drift cage and the cathode has been produced in the context of the LAGUNA-LBNO design study, for detectors of fiducial mass of 20 and 50 kton. For the demonstrator, most of the technical solutions introduced there will be retained.

The drift cage is composed of 60 equally spaced electrodes, in the form of stainless-steel tubes with a diameter of 69 mm and a pitch of 100 mm. Each tube will be electrically connected to its neighbours through resistors to provide a graded electric field. The structure will be supported by 16 FR4 vertical pillars. These pillars might be replaced by insulated links, cut out of FR4 plates. These links could provide a lighter structure and an easier assembly inside the tank.

The cathode is made of a strong frame with a mesh of tubes. The diameter of the tubes is 60 mm and their spacing is 500 mm. The mesh is filled with meshed grids with a wire diameter of 5 mm and

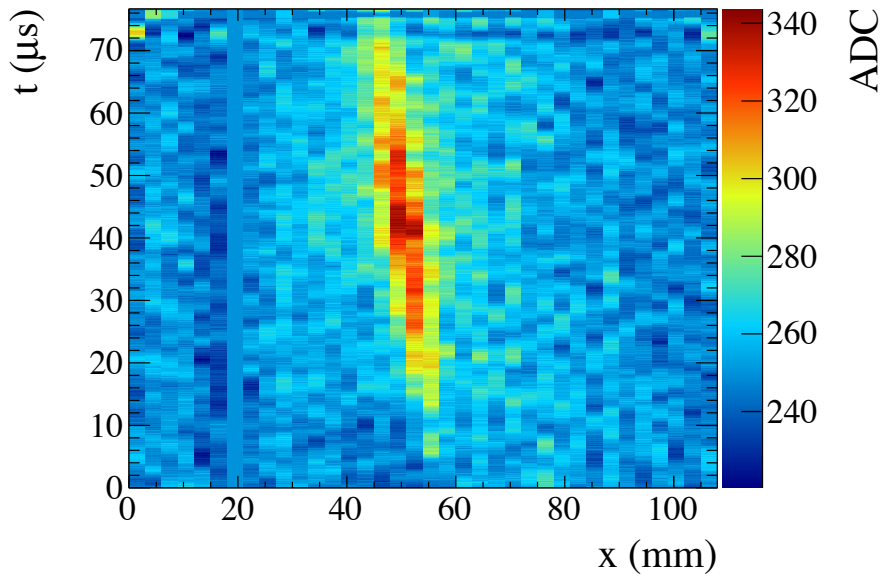


FIG. 63: Event display of a cosmic ray track observed with a $115 \mu\text{m}$ gap bulk-MICROMEGAS detector in the Liverpool LAr setup. The horizontal axis gives the position of the collected charge on the strip while the vertical axis indicates the corresponding electron drift time in liquid argon.

pitch 50 mm. The transparency to light is about 80%, such that scintillation light produced within the liquid argon fiducial volume can be detected by the PMTs located at the bottom of the vessel.

The whole structure will be hanging from the tank deck with support rods housed in special bellows. As an alternative design option, it could also be supported on the floor by feet adapted to the corrugation of the membrane tank. The drift cage is illustrated in ???. The HV feedthrough is placed in a corner of the field-cage. The top of the field cage is closed by the CRP anode deck. It should be noted that the anode deck is actually independently hung from the top via the supporting feed-through. The field-cage and the anode are therefore mechanically independent components, and the anode deck level is adjusted to the level of the liquid-gas argon interface.

We have performed an electrostatic field calculation to optimise the geometry of the field cage for a drift field of 1 kV/cm (equivalent to 600 kV on the cathode). As can be seen from ??, the field uniformity is excellent inside the drift volume. The calculation took also into account the corrugation of the membrane tank (shown as green dots on the picture). The zoomed region around the region of the cathode, where the highest field is expected, is also shown. It reaches a maximal value of 30 kV/cm nearby the last shaper forming the cathode, a value which is very acceptable according to our measurements of rigidity in liquid argon (see ??).

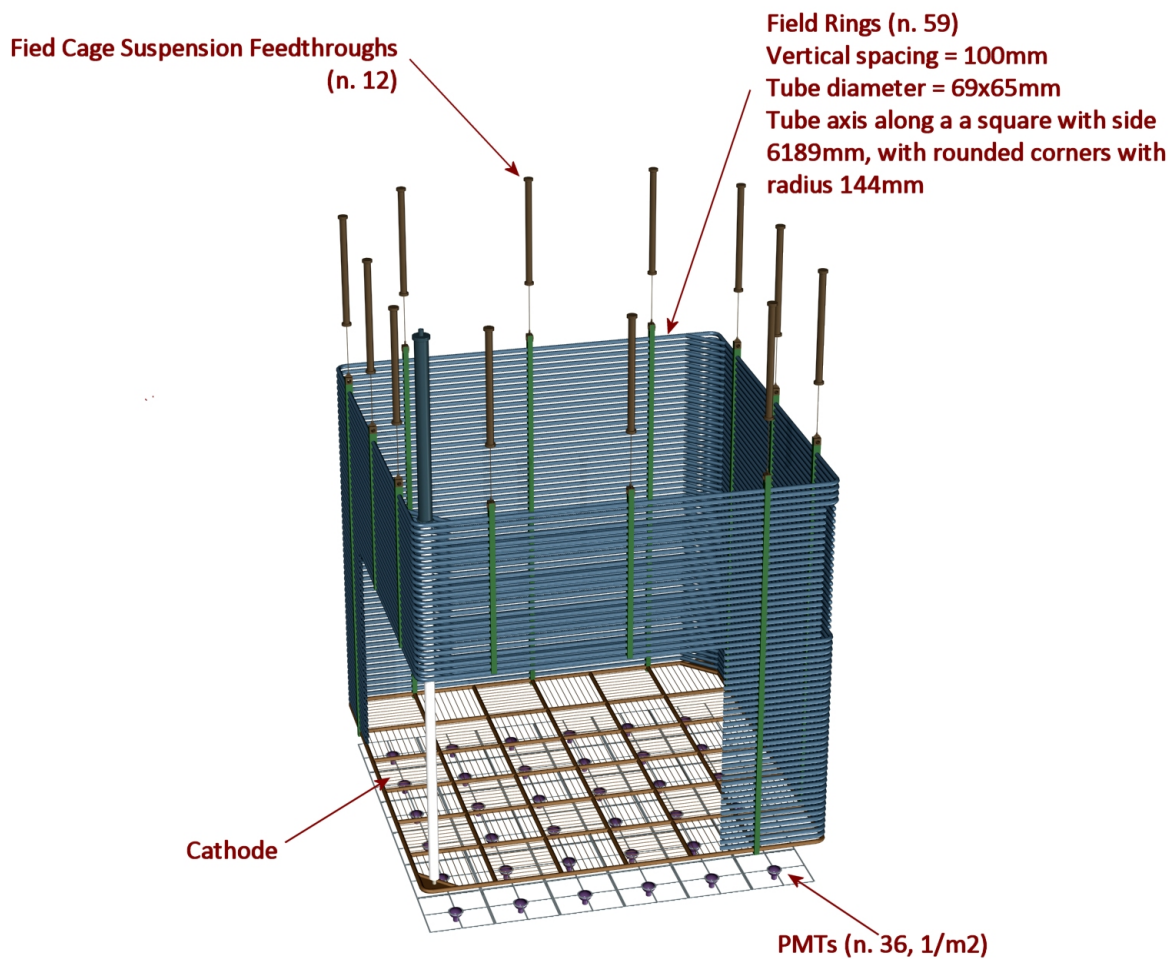


FIG. 64: Conceptual design of the field cage. The high-voltage feed-through is located in the left corner of the cage.

4.3 Drift high voltage

The intensity of the drift electric field is one of the important design parameters for liquid argon time projection chambers (LAr-TPCs). A better collection of ionisation charges is attained by increasing the field intensity because: (1) more electron-ion recombination is prevented [18] and (2) attenuation of the drift electrons due to their attachment to residual electronegative impurities such as oxygen decreases. The dependence of the attachment cross section on the electric field is known to be weak in the practical range of the intensity (0.5–1 kV/cm) [17]. The attenuation then is described well by an exponential decrease with drift time, characterised by the drift electron lifetime τ which is determined dominantly by the impurity concentration. The mean drift velocity of the electrons increases with increasing electric field, leading to the shorter collection time and consequently to the less attenuation (see ??). The drift velocity increases by 30% by doubling the electric field intensity from 0.5 to 1 kV/cm,

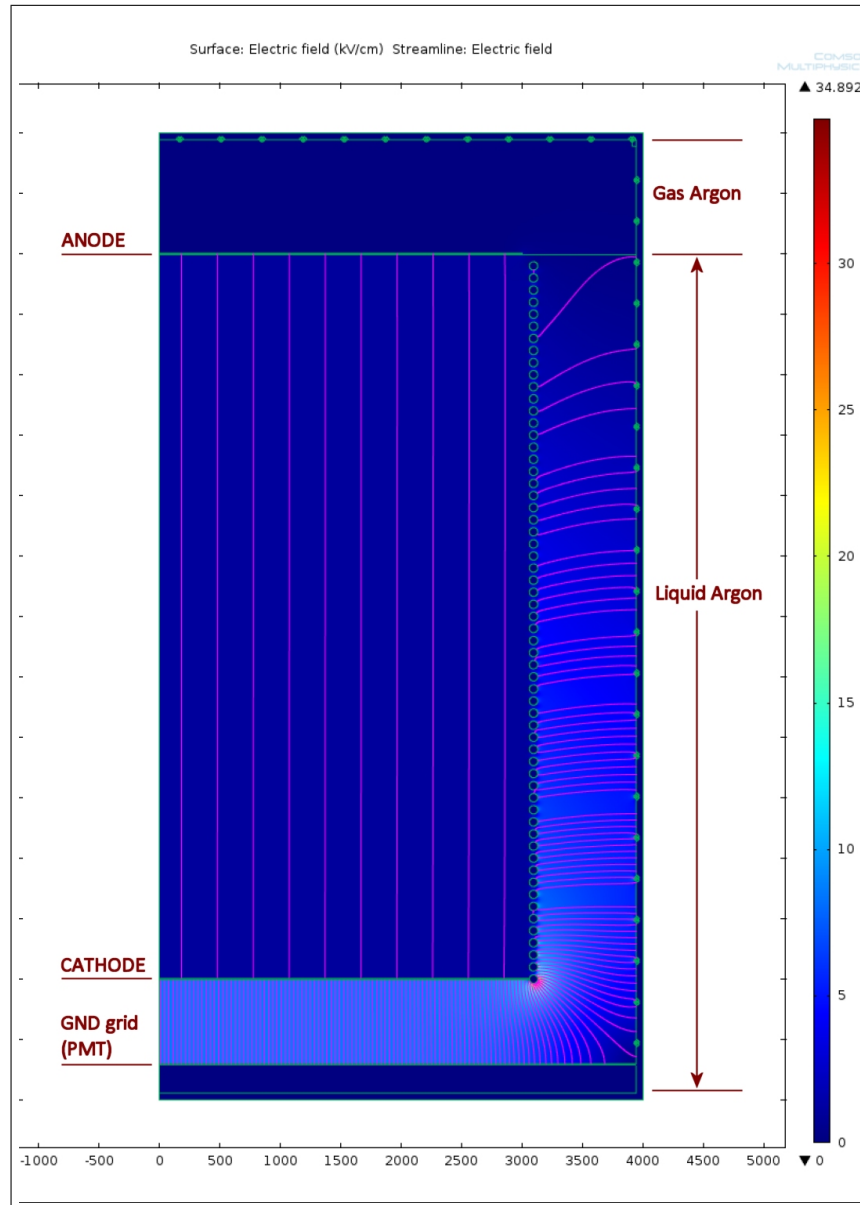


FIG. 65: Electrostatic field calculation of the field cage: global view of the field cage embedded in the vessel. The simulation takes into account the corrugation of the membrane vessel which is display by the green dots.

and again 30% from 1 to 2 kV/cm [108]. From a technical point of view, however, difficulties increase with increasing field intensity which requires higher voltages. Therefore, it should be determined by a right compromise between the detector performance and the practicality of the high voltage. A field intensity between 0.5 and 1 kV/cm is a reasonable compromise for very long drifts.

For the $6 \times 6 \times 6 \text{ m}^3$, a drift field in the range 0.5 – 1 kV/cm requires a potential difference at the cathode in the range of 300–600 kV. In comparison, the GLACIER drift length of 20 m [22] would require 2 MV. Two different approaches have been considered and realised for the drift field system for very large LAr-TPCs. The first type uses an external HV power supply and feed it into the detector

volume using HV feedthroughs [14]. The second type has an internal HV generator directly inside the LAr volume as the Greinacher HV multiplier of the ArDM-1t detector [24, 109]. Its advantages are: (1) all the HV parts are immersed in LAr which has a large dielectric strength as discussed above, (2) thus feedthroughs for very HV are not needed, (3) the circuit itself can be used as a voltage divider, so the system needs no resistive load, (4) thus the power dissipation is virtually zero and (5) this allows a low frequency (e.g. 50 Hz) of the AC input signal which is fully outside of the bandwidth of the charge amplifiers used for this type of detectors. However, a major drawback is the difficulty to access the device in case of failure of a component, such as something that could realistically happen in case of discharge given the amount of energy stored in the circuit.

A HV feed-through and an external power supply will be adopted for the $6 \times 6 \times 6 \text{m}^3$. Power supplies up to 300 kV with the required specifications in terms of stability, noise and low residual ripple, are commercially available in catalog (see e.g. Heinzinger electronic GmbH, Rosenheim(D)). We have already ordered the 300 kV (See ??) and will perform tests during 2014. The performances for the voltage stabilisation are a reproducibility to $< 0.1\%$, a stability of $< 0.001\%$ over 8 hours, a ripple of $< 0.001\%$ pp, and a temperature coefficient $< 0.001\% / \text{K}$.

Heinzinger has also indicated that unique units for 400 kV have been successfully produced and operated. An R&D phase with industrial partners is considered to develop a 600 kV-able power supply. We note that the 300 kV would be sufficient to operate the $6 \times 6 \times 6 \text{m}^3$ with the canonical drift field of 500 V/cm. However, in view of the longer drift paths, the $6 \times 6 \times 6 \text{m}^3$ facility will be used to perform R&D on higher voltages, with the aim to reach a drift field of 1 kV/cm over 6 m.

As far as the HV feedthrough is concerned, it will be a direct extrapolation of existing design, with an insulating polyethylene thickness of 10 cm. Laboratory tests are been prepared.

4.4 Front-end and DAQ readout

4.4.1 Requirements for the large scale front-end electronics

One of the goals of the WA105 demonstrator is to establish the large scale readout systems being developed for the far site LBNO LAr detectors in a configuration as close as possible to their foreseen final architecture. The large scale deployment of the readout systems in the demonstrator will allow testing their performance with high statistics samples of hadronic interaction showers, their stability and reliability over long time periods and on large data volumes, develop lossless noise-tolerant zero-suppression schemes on real data, as well as optimizing the full integration in the detector. The large number of charge readout channels, needed for the 20-50 kton LAr detector sizes for LBNO with channel count in the range of 500'000 to 1'000'000, naturally called during the last years for R&D efforts in



PNChp 300kV, 0.5mA, 100ppm

FIG. 66: The 300 kV power supply from Heinzinger electronic GmbH to be tested in 2014. This power supply can provide the canonical 500 V/cm drift field over the full 6 m drift distance.

view of the development of large scale readout solutions. These are characterized by high-integration levels, significant cost reduction and aims to performance improvement. The R&D activities focused on two main axes:

- the developments of cold front-end ASIC electronics;
- the optimization of the data acquisition system based on modern telecommunication technologies.

Both efforts aim to improving the effectiveness and the integration level of the complete readout chain and to cost reductions for the large number of channels to be implemented in the detector. Shortening of cables needed to bring the analog signals outside the cryostat and reduction of the electronic noise can be achieved using analog amplifiers operating at cryogenic temperatures. The current R&D on the front-end electronics is based on analog preamplifiers implemented in CMOS ASIC circuits for high integration and large scale affordable production [110]. The noise is reduced by

exploiting its behaviour as a function of temperature, which has a minimum around 100 K, and thanks to the suppression of the cables used to bring signals outside the cryostat, which otherwise increase the capacitance at the input of the preamplifier. In our present baseline the ASIC analog amplifiers can be integrated on the feed-through flange terminating the chimneys on the roof of the tank, under the insulation layer, in order to be cooled to a temperature near that of liquid argon (see ??). This solution fully preserves all the benefits of the cold electronics, as described above, while guaranteeing at the same time accessibility to the amplifiers without affecting the inner volume containing ultra-pure LAr.

For what concerns the DAQ, solutions based on Ethernet capable “smart sensors” were developed. The “smart sensors” are Ethernet capable front-end DAQ/processing units acquiring large groups of channels. They are integrated with a time distribution system needed to align the data taken by different units operating independently. Data are output on a Ethernet network and collected with a system of switches to a computing farm which builds the events on the bases of the time stamps associated to the data packets by the different sensors. This concept was further developed for the LAr readout, since the time of its first implementation in the OPERA experiment, with the following technical improvements [111]:

1. porting it to the Gigabit Ethernet standard;
2. adopting FPGA based virtual processors, in order to achieve cheaper implementation costs and become independent on the market of Ethernet capable front-end processors;
3. integrating the electronics in the micro-TCA form factor, becoming very popular in the world of commercial telecommunication applications;
4. developing a special time distribution system, derived from the Precise Time Protocol standard, integrated in a synchronous Ethernet network. This time distribution scheme achieves a synchronization accuracy among different nodes at better than 1 ns.

This DAQ scheme allows benefiting of the large-scale integrations developments of the telecommunication industry and decoupling from the market lifetime of commercial processors since it relies on a completely virtual implementation of the processors in the FPGA. A complete setup built out of this R&D was developed in 2010 for 128 channels (See ??). The proposed DAQ version for the LBNO prototype detector is an evolution of that system, further increasing the channels density and reducing the costs.



FIG. 67: Picture of a micro-TCA crate containing DAQ boards with 32 ADC channels/board as developed in 2010.

4.4.2 Cold front-end electronics

Since 2006 till 2012, six generations of prototypes of ASIC 0.35 microns CMOS multi-channel preamplifier chips operating at cryogenic temperatures, typically reached in the gas phase above the LAr, were developed. This development was oriented to performance improvement for large size detectors and low cost production. See ??.

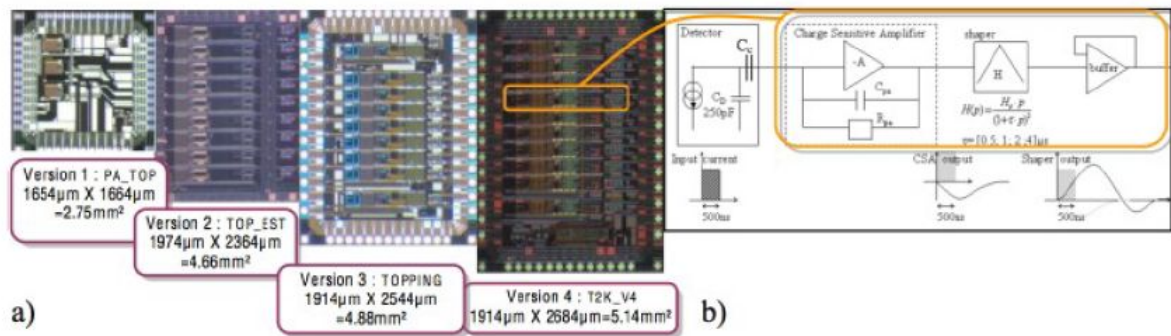


FIG. 68: Four ASIC chip die pictures (a) following the development of the different versions since 2007 and one channel block schematic (b) of the fourth version (V4)

Each amplifier channel on a ASIC chip includes a complete chain with a pre-amplifier, a shaper and a buffer. Some parameters of the analog chain response, as the shaping time, may be controlled for the group of channels in the same chip with a distributed I2C bus. The ASICs have a power dissipation of 18 mW/channel. The equivalent noise is around 1400 ENC for an input capacitance of 250 pF. The linear dynamic range extends up to 50 m.i.p. The ASIC configuration was mainly optimized for the most critical configuration of a detector with unitary gain, as a LAr TPC with wires

readout, and the related possibility of dealing with bipolar signals as from induction planes.

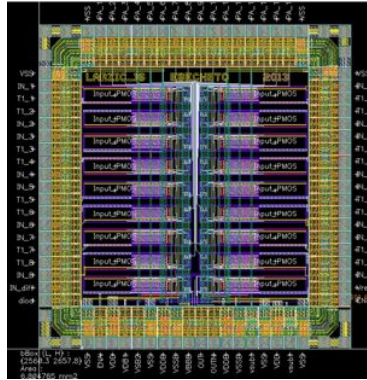


FIG. 69: 16 channels version, adapted to the LEM signals, of the ASIC preamplifier(V7) produced during fall 2013.

The current ASIC development version (V7), produced in the fall 2013, was upgraded to 16 channels and included as well the adaptation of the pre-amplifier dynamic range to LEM detectors operating at a gain of about 20 and generating unipolar signals from X and Y anode collection strips with 3 mm pitch (See ??, ??). The baseline scheme for the production version of the ASIC for the WA105 demonstrator is based on this development version, including its dynamic range adjustment, adapted to cope with the LEM detector gain, with the addition of an optimization of the resolution over the full dynamic range with a double slope regime (see Fig. 70). The double slope regime is characterized by a high gain region extending up to 10 m.i.p. signals. After 10 m.i.p. the gain is reduced by a factor 3 in order to overall match a dynamic range of 40 m.i.p. This solution provides the best resolution in the m.i.p. region without limiting the dynamic range for showers, which can still reach 40 m.i.p. The

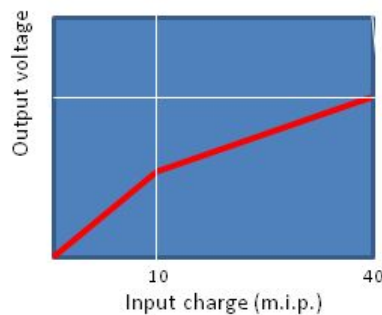


FIG. 70: Double slope gain adjustment for an extended dynamic range of the amplifiers.

total strips capacitance at the input of each preamplifier channel, will be around 300 pF, for 3 m long strips. Taking into account 20 m attenuation length of the charges during the drift, the S/N ratio for a m.i.p. signal will vary from 45 to 120 (m.i.p. tracks occurring at the beginning of end of the drift

space) for the full size detector of LBNO, and from 90 to 120, for the prototype detector, which has a maximum 6 m drift space instead of 20 m. The front-end electronics will be coupled to the DAQ system, described in the following, based on 12 bits ADC, well matching the needed dynamic range.

The design of the $6 \times 6 \times 6\text{m}^3$ demonstrator includes a total number of 7680 channels for the charge readout of the X and Y strips views. The strips have a pitch of 3.125 mm and a length of 3 m per channel. Channels are then arranged in groups of 640 per chimney.

The 40 ASIC amplifiers needed for the readout of each group of 640 channels will be arranged on cards hosted on the feed-through at the bottom of each chimney (see ??). The total power dissipation

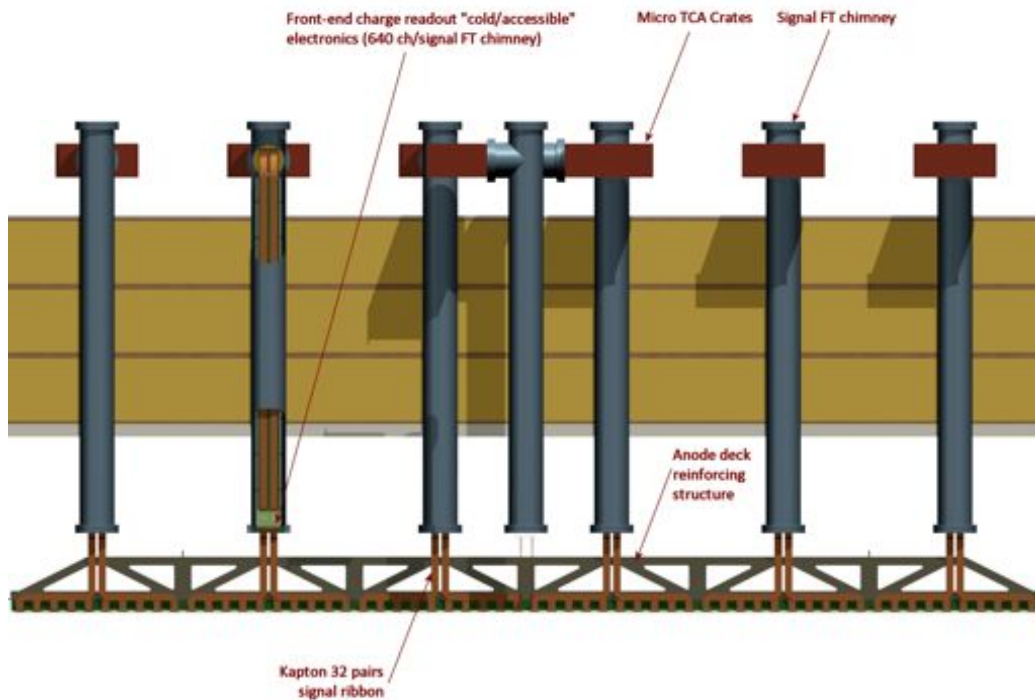


FIG. 71: Location of the FE cards at the bottom of the chimneys.

of the front-end electronics will be of about 11.5 W per chimney. The structure of the chimneys allows for heat dissipation in the cryostat and for minimising the connection length from the cards hosting the ASIC chips to the double phase detectors down to half a meter.

The ASIC chips needed to equip the final LBNO far detectors can be produced in a dedicated run including 6 wafers for a cost going from 0.28 to 0.37 eur/channel, including encapsulation. This cost varies depending on the fact that the production version will be based on 16 or 32 channels per ASIC. This dedicated production can handle up to 28k ASIC chips in the 16 channels version (14k in the 32 channels version). The production volume needed for the LBNO prototype is much smaller and it will rely on an extended multi-project run with a consequently higher cost (3.91 eur/channel). The total cost per channel for the prototype detector goes up to 6.1 eur per channel when including also the

front-end cards and the power supplies. The total cost for the demonstrator front-end electronics will amount to 54.2 keur, including 15% spare elements.

4.4.3 Fine-tuning of the F/E dynamic range

In order to fine-tune the dynamic range of the preamplifiers the amount of charge collected on the strips was studied with the simulated $6 \times 6 \times 6\text{m}^3$ geometry. The dynamic range should be large enough to allow the digitisation of highly ionising events while still providing good enough resolution for particles that deposit a small amount of charge on the strips (typically a fraction of a m.i.p). To understand the amount of charge collected on each strips, pions and electrons of energies up to 10 GeV were sent through the beam pipe and a distribution of the maximal charge deposited on each strip was retrieved. The results are shown in ?? for the strips belonging to one of the views. Since the beam pipe is orientated at 45 degrees with respect to the strips the distributions for the other view is identical. Most of the collected charge is below ~ 10 (resp. ~ 20) fC for pion and electron showers. The tails extend to about 50 fC and 100 fC for 10 GeV events. The dynamic range proposed in Section 4.4.1 is therefore suitable as it extends up to signals of 40 m.i.p (≈ 120 fC). In addition the double slope configuration of the preamplifier allows to adjust a range of increased sensitivity. This range is chosen for signals between 0 and 10 m.i.p (≈ 30 fC) as it is the region where most charge is collected.

4.4.4 Back-end electronics and DAQ global architecture

The DAQ system uses micro-TCA standards which offers a very compact and easily scalable architecture to manage a large number of channels at low cost. Those constraints are indeed very close to the one existing in the network telecommunication industry. This has been driving the very first developments based on this type of standards in constant technological evolution and applied to large scale neutrino experiments. A generic scheme of the DAQ architecture is displayed in ??.

The main component of this DAQ system is an Advanced Mezzanine Board (AMC) reading out the input signals from the front-end electronics and sending the formatted data through a micro-TCA backplane using a Gigabit or a 10 Gigabit Ethernet link. In the following, details are given on the design of this AMC and the possible alternatives existing to the Ethernet link on the backplane (e.g. PCI express). The connections from the front-end use the Very High Density cable interconnect (VHDCI) standard to minimize the number of cables.

A micro-TCA crate (or shelf) interconnects a fixed number of AMC cards through the backplane to collect the data and send them through a standard 10 Gbe MicroTCA Carrier Hub (MCH) and to distribute a common clock signal issued from a single, stable, GPS-locked Master Clock (MC).

The clock is made available on the backplane through a dedicated AMC (one per crate) which

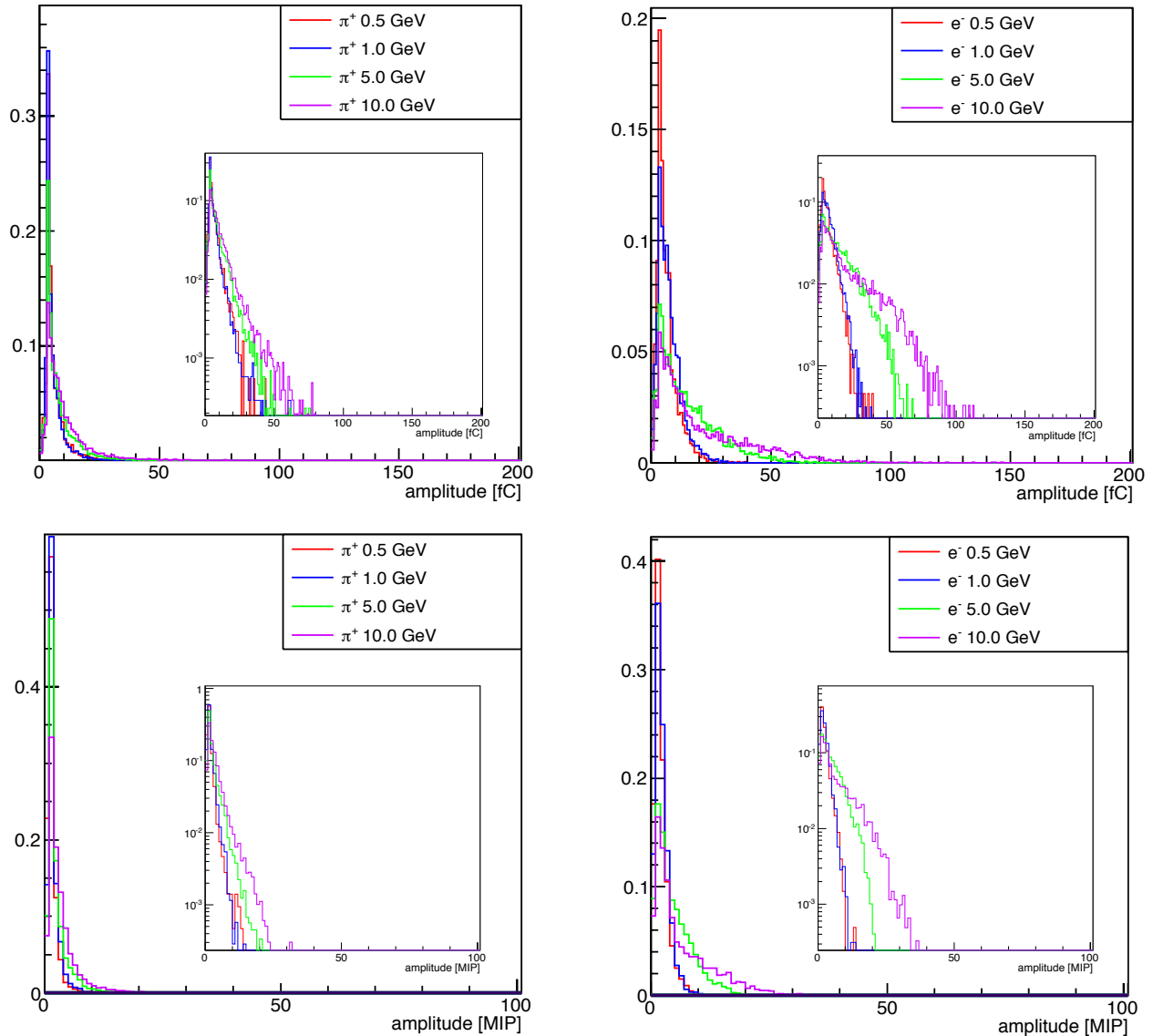


FIG. 72: Distributions of the maximal charge deposited on the strips for π^+ (left) and electron (right) showers of various energies. The distributions are given in unit of fC (top) and m.i.p (bottom).

receives it from an external connection, together with the trigger signals (internal trigger from the PMT array and external beam trigger). Those triggers are split and distributed through conventional systems.

A network hierarchical structure is implemented where all crates are interconnected to a dedicated Bittware FPGA processing board (S5-PCIe-HQ, Figure 74). This board has two QSFP+ cages to bring the data direct to the FPGA for lowest possible latency. Up-to 8x10Gbe links w/o data loss are available per board. The board performs further data processing, filtering and transmission to the highest level for storage. This type of board is widely used in the massive processing systems and the present generation, based on the Altera Stratix V, will evolve to the Aria X and

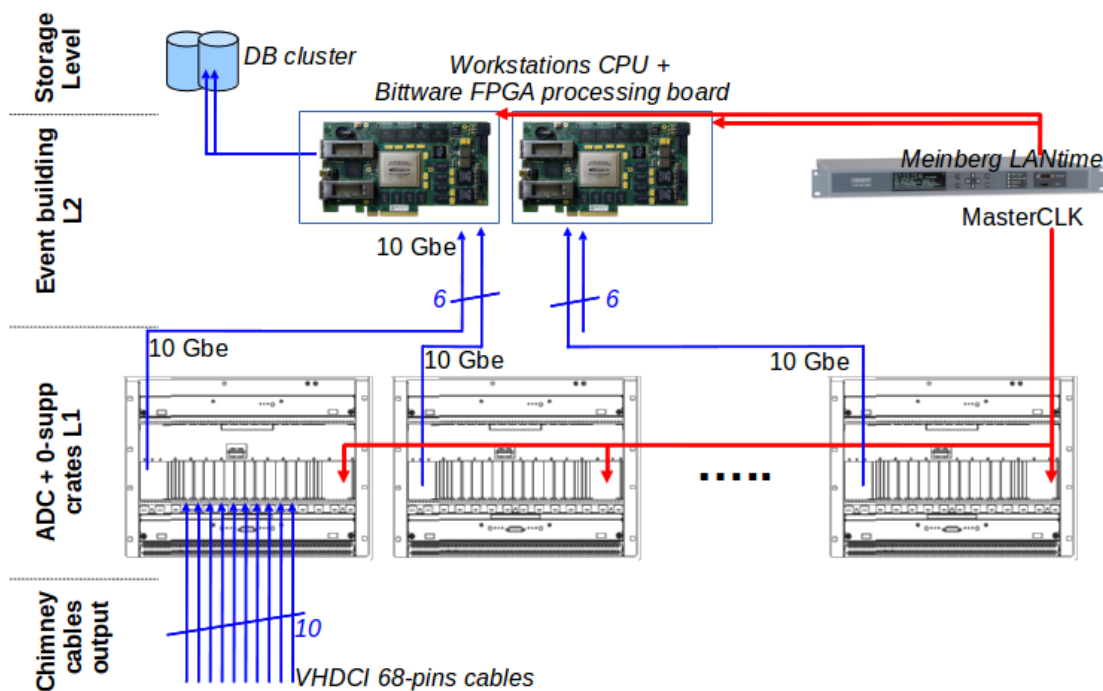


FIG. 73: Global DAQ scheme. At the bottom the DAQ receives the cables from the F/E electronics. 10 VHDCI cables are connected on each rack. One crate is foreseen per chimney, leading to 12 racks in total for the 1st level (L1). Each crate is connected through a 10Gbe uplink to the next level (L2). The L2 directly connects the racks to the event builder workstation via a 10Gbe network link on a Bittware FPGA processing board. This board may connect up to 8-10Gbe links or 2-40Gbe links. A lossless transmission scheme is therefore foreseen down to the processing board which performs the zero suppression and the event building. A stable common clock is distributed to L1 and L2, as well as the trigger signals (from PMT and beam). The master clock generator may be derived from a Meinberg LANtime generator.



FIG. 74: FPGA processing board based on Stratix V from Altera. The board features a dual QSFP+ cages for 40GigE or 10GigE links, 16 GBytes DDR3 SDRAM, 72 MBytes QDRII/II+, two SATA connectors and is programmable via OpenCL.

the Stratix X. This version will be probably available at the time of the construction of the DAQ system.

Programming of the processing board is achievable through the OpenCL software suite where a kernel code allows, on top of a host code, to program directly the FPGA without a classical VHDL synthesis chain. OpenCL is a high level language for massive parallel processing transparent to its

hardware implementation (CPUs, GPUs, FPGAs). Under OpenCL FPGAs provide large computing power for data processing at low power consumption. This highly flexible feature is fully adapted to the requirements of the large DAQ systems where conditions of filtering, event building etc... may evolve with time.

The storage is defined as the highest level of the DAQ chain and implies the use of a redundant 2-servers cluster linked to a RAID-5 disks array system.

4.4.5 MicroTCA standard and crates

MicroTCA offers the possibility to interconnect distributed applications while offering a standard, compact and robust form factor with simplified power supply management, cooling and internal clocks distribution. The microTCA backplane is based on high speed serial links arranged in various possible topologies. Lanes on a microTCA backplane support a large variety of protocols like for example Ethernet 1G or 10G, PCI Express or SRIO.

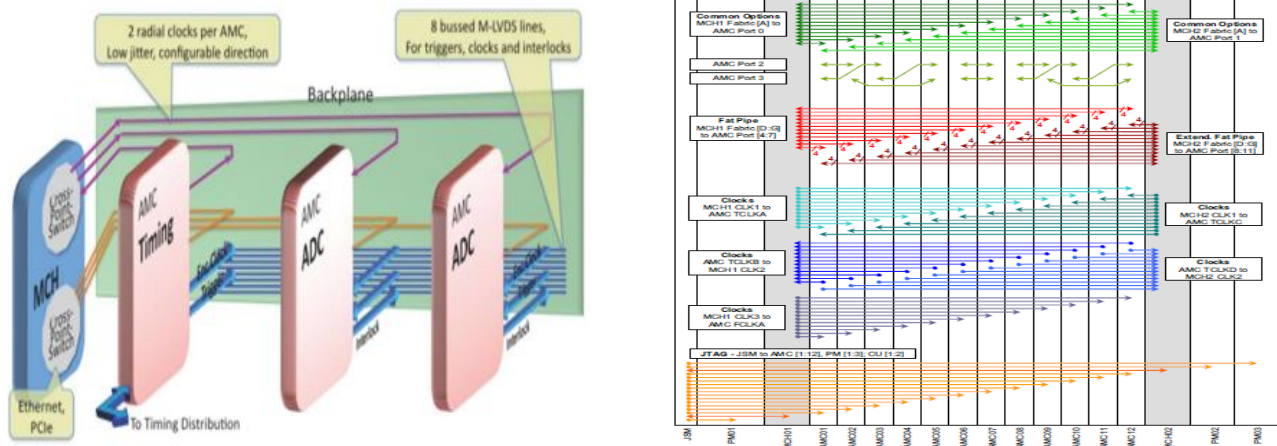


FIG. 75: Left: global microTCA crate organization. AMC cards (providing basic ADC functions) are connected to the crate controller or MCH which uplinks the external systems. A dedicated AMC for the clock receives dedicated signals (masterclock, trigger signals) from the timing distribution system and transcript them onto the backplane. Right: backplane technology of the Schroff 11850-015 reference.

The boards plugged into a microTCA shelf are called Advanced Mezzanine Card (AMC) [112]. Each AMC board is connected to one or two MicroTCA Carrier Hub (MCH) through the backplane serial links which provides a central switch function allowing each AMC to communicate with each other or towards external systems through an uplink access. The backplane also provides the connectivity for the clock distribution allowing the AMC board synchronisation. ?? provides a sketch of the backplane technology and its implementation in one retained shelf reference.

The first developments performed for the LAr TPC readout with the microTCA systems were based on the microTCA.1 standard with connections to the user input signals from the front side only. In

the baseline option we stay as close as possible to this standard although additional standards have emerged like the microTCA.4 offering the possibility to enter in a crate both from front and rear sides.

In the microTCA.1 baseline option, one has 1 crate per output chimney, handling 640 channels dispatched over 10 AMC. A candidate crate is the 11850-015 8U shelf from Schroff (??). We are also considering other references from various providers (like the NATIVE-R9 from NAT) in the spirit of evolving to the microTCA.4 standard. In this case each crate will be located between 2 nearby chimneys. As shown in ??, the crates are implemented on the top layer of the prototype detector. Each brown box features a crate. The inter-chimney distance, of the order of 1 meter, allows this type of crate disposal which minimizes the constraints on cables lengths.



FIG. 76: Picture of the Schroff 11850-015 8U shelf.

The main features of the 11850-015 Schroff crate references are listed below:

- 8 U microTCA Shelf, 12+2+3+1 slot for AMC double Mid-size modules,
- 19" rack mountable,
- 12 AMC Double Mid-size slots,
- 2 redundant MicroTCA Carrier Hub (MCH) slots (Double Full-size),
- 2 Power Module (PM) slots (6 HP Double) at the right side,
- 1 Power Module (PM) slots (12 (9) HP Double) at the left side,
- 1 slot for a JTAG module (Double compact),
- 5 splitting kits to install single module in a double slot.

Various MCH references may be used in that design. We selected the NAT MCH with additional hardware for optical fibres connections (NAT-MCH-Base12-GbE, NAT-MCH-XAUIx48, NAT-MCH-UPLNK-SFP+, NAT-MCH-UPLNK-SFP+850). The optical link will go down to the FPGA processing board. This MCH has SRIO (Gen2), PCIe (Gen3), 1GbE and 10GbE (XAUI), central management up to 13 AMCs, 2 cooling units and 4 power modules, e-keying, redundancy and load sharing.

4.4.6 MicroTCA dedicated AMC

a) AMC board design

The idea is to develop only the user AMC offering the desired functions. The generic functional diagram of the AMC is displayed in ???. The AMC chosen is a double-size module (also compatible with microTCA.4 standard) with a single input connector and a 10GbE or PCIe link to the backplane. The input stage performs the 64 channels digitization through 8 8-channels 14-bits ADC readout at a 2.5MHz frequency. The ADC readout sequence is controlled by 2 EP3C40 FPGA from Altera which makes the data available on a double port memory (DPRAM with 9k-samples width from IDT). Two banks (B0/B1) are attached to each channel and work in ping pong mode. The write state machine manages the bank address working as a circular buffer. If no trigger conditions is detected the samples are written continuously into the memory, the oldest ADC being overwritten by the newest ones. The ADC values and the address location in the bank are written into an intermediate FIFO for each bank (B0/B1). If a trigger occurs, the write state machine keeps on storing the event corresponding to the TPC drift. If the second bank is available, the main state machine tells the write state machine to continue to store the samples into this new active bank. The read state machine sets a flag corresponding to the availability of an event in a bank. All the read state machines are interconnected through a token ring like structure. The zero-suppression algorithm is applied on all samples available in the bank, the pedestals (mean and width) being computed on the samples themselves. The recorded samples are then formatted and sent out. These operations are managed by a third FPGA (EP5CE from Altera), which sends the data on the backplane. The baseline option foresees to send the data directly through a 10GbE link (UDP was used in the first prototype). The readout scheme and hardware implementation is very close to the first prototype designed in IPNL (??) with slight changes: replacement of the single FPGA by three cost-effective FPGA's and direct implementation of the ADC layer on the motherboard (in the first version ADC's were on a mezzanine board).

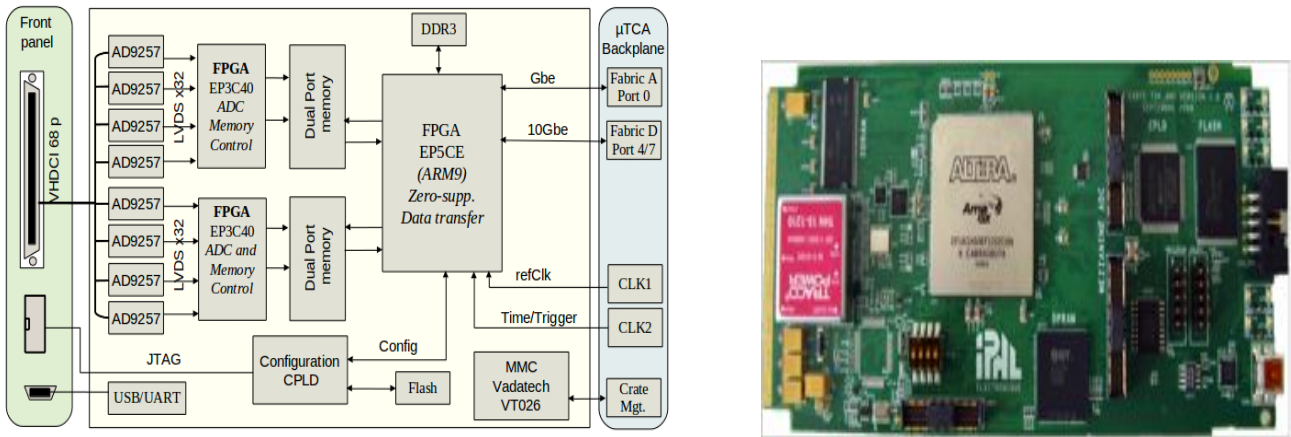


FIG. 77: Left : AMC bloc diagram scheme. The input stage digitizes the 64 input channels. The ADC readout sequence is controlled via 2 FPGA (one for 32 channels) which handles also the writing into a double bank memory. The management of the trigger input, data output, and link to the backplane if performed by a third FPGA. The link to the backplane may be direct 10GbE or PCI-e. Right: the first AMC version, single height for 32 channels. Present design is an extension of this board.

b) ADC readout chain

The analog signals from the F/E ASICs are connected to the AMC front-panel through a 68 pins VHDCI connector. The 8×14-bits ADC 8 ch. AD9257 ADC from Analog Device, including a serial LVDS output, has been chosen. The translation from single ended to differential signals is performed upstream of the ADC. The readout scheme is displayed on ???. This design offers a high integration level required by the large density of input signals.

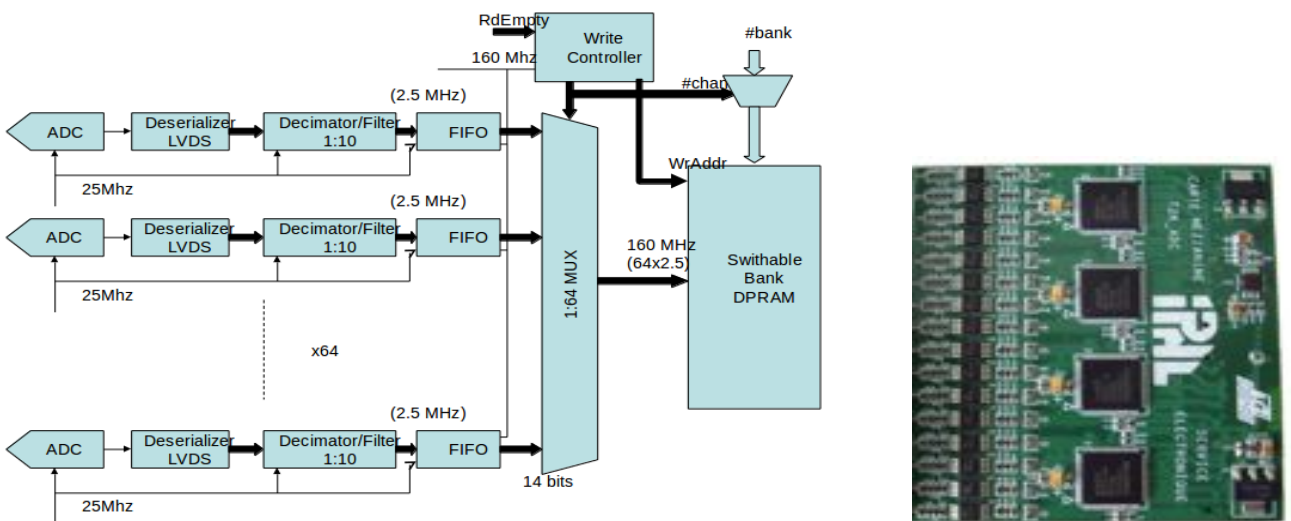


FIG. 78: Left : ADC readout chain block diagram. The AD amplifier is used to translate the inputs to differential levels. Right: implementation of a 32 channels ADC readout chain in the first prototype version.

4.4.7 Data rate requirements

a) Data reduction

In the present design the useful ADC will be 12-bits resolution and each sample will have 16-bits size. The readout frequency of 2.5 MHz (400ns steps) requires a maximum of 10k samples for the maximal drift time of 4000 microseconds that we want to cover. Given the 6 microseconds shaping of the F/E electronics for a single hit, one obtains: $6(\mu\text{ s})/400(\text{ns})\sim 15$ useful samples for a single hit over the 10k of a full bank. To be conservative we assume in the following a reduction factor 100 given by the zero suppression algorithm if implemented at the AMC level. In the lossless data transmission scheme we will assume the total 10ksamples.

b) Data rate constraints

In this context we may compute the saturation limits for one crate and for the full detector. One crate is used to readout a full chimney, that is 640 channels (10 AMC). In the case the zero-suppression is not applied, the maximal affordable data rate to saturate the 10GbE uplink of the crate is therefore: $10(\text{GbE})/(16(\text{bits})\times 640(\text{ch.})\times 10\text{k}(\text{samples}))\simeq 100\text{Hz}$. Since the crates are readout in parallel by the FPGA processing boards, this rate corresponds to the maximal rate for the full detector. This mode is adapted to a beam-only data readout. In the case the zero suppression is applied we may reach a maximal rate of 10kHz, compatible with the surface cosmic rays rate ($\simeq 6\text{kHz}$). In this mode we may readout beam data and cosmic rays between the beam cycles.

4.4.8 Integration of readout electronics

In the LBNO far detector, several hundred thousands channels will need to be routed from the charge readout plane located inside the vessel to the front-end charge preamplifiers and digitisers to be placed outside the vessel. Given the large number of channels, it will be necessary to pack as many of them into a single flange.

Signal cables of the $6\times 6\times 6\text{m}^3$ will be similarly routed towards the top of the detector and connected to the signal feed-through flange at the bottom of a chimney. Each chimney will be terminated with a feed-through that must be absolutely ultra-high vacuum leak-tight not to contaminate the pure liquid argon. ?? shows some details about the chimney and the inserted F/E electronic cards, and the foreseen cables layout.

The dimension of the chosen flange is an ISO CF 200/250 to host 640 channels (20 KEL corporation connectors (<http://www.kel.jp/>) with 20×32 channels) as shown in ?. The flange is actually made of a SS ring, in which a several mm-thick multilayer PCB is glued or sealed. The multilayer PCB is

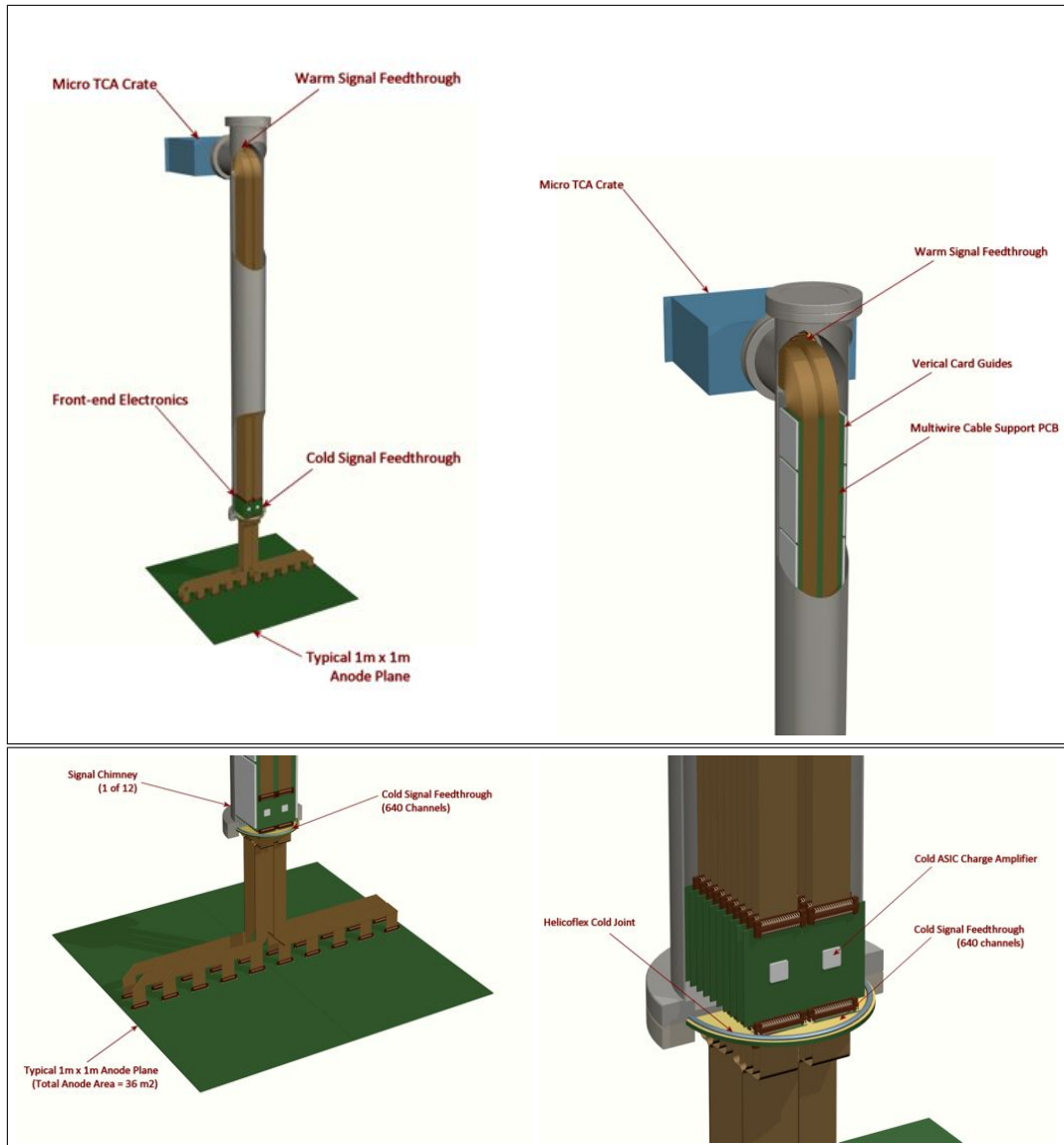


FIG. 79: Details about the chimney, the signal feed-throughs, the inserted F/E electronics cards, and the foreseen cables layout.

designed in order to accommodate connectors on both faces, but internally signals are routed along a U-shaped path, where the an inner PCB layer is shifted with respect to the top and bottom layers, in order not to have passing through holes. A prototype with 4 connectors has been built and tested (see ??).

As mentioned, the signal flanges will be located at the bottom of their chimneys, and below the thermal insulation panel (See ??). The temperature of the F/E electronics will be close to that of liquid argon and will be monitored remotely. The F/E cards with the preamplifiers will be inserted vertically into the KEL connector. The power dissipation per chimney is 11.5 W which will be taken away to the main vessel. The chimney will be flushed with dry nitrogen and sealed at the top of the chimney. This



FIG. 80: Signal feedthrough and connectors from the CRP (left) 3D view (right) 2D top view.

concept will be further developed as to allow access and exchange of the front-end electronic boards, independently of the main vessel which can remain filled with liquid argon. We believe that this is an important requirement for the potential long-term (>10 years) operation of the underground detector.



FIG. 81: Prototype of the signal feedthrough flange with 4 connectors.

4.5 The Light Readout system

4.5.1 Scintillation light detection

Efficient methods to detect the scintillation light in the DUV range have been studied in the context of ArDM-1t for several years [72, 98, 113]. The practical technique for photo-detection based on large area cryogenic photomultipliers coated with a wavelength-shifter is thus well understood. For the WLS, we seek a fast response of the light readout system not to distort the pulse shape of the liquid

argon scintillation light. Most organic wave shifting materials are well known for their fast optical response caused by the rapid process of radiative recombination of electron hole pairs at the benzene rings in their chemical structure. The best WLS and commonly used for its well matched emission spectrum to alkali photocathodes is the Tetraphenyl-butadiene(1,1,4,4-tetraphenyl-1,3-butadiene or TPB). Different methods for coating the WLS have been studied in Ref. [98]. TPB coatings can be made durable with good adherence to the substrate and high resistance to mechanical abrasion. The light collection efficiency is also well reproduced by simulations [113].

Based on this expertise, we have developed a baseline design for the light readout of LBNO which is composed of large area cryogenic PMTs placed uniformly below the (transparent) cathode. We have estimated that the number of PMT needed to have an efficient light threshold above several MeV is approximately 1000 for the 20 kton detector, if we adopt 8" photomultipliers with a conservative quantum efficiency at liquid argon temperature of about 10%. The PMT are uniformly located with a coverage of about 1 per square-meter. Their buoyancy in liquid argon (approx 4 kg) is compensated by appropriately adjusting the weight of their support. They are anchored at the bottom of the tank, or possibly to the side of the inner shell wall. See Figure 82. The HV cathode is placed at a height of 2 m above the bottom of the tank and the PMT plane will be distant enough from the cathode plane, taking into account the high electrical rigidity of the liquid argon phase. In order to protect the PMTs an additional mesh plane will be installed and placed at an identical potential as the PMT photocathode. The PMT will be negatively polarized to about 1 kV such that the PMT signal can be readout in DC. We are presently in contact with Hamamatsu Photonics to define the most optimal configuration of PMT satisfying our requirements, in particular large area (8" or 12" PMT options are being discussed), cryogenic operation, high pressure operation (the PMTs will feel about 2 bar absolute), and potentially high QE photocathodes. These solutions will be compared and one will be adopted for the $6 \times 6 \times 6\text{m}^3$.

A picture of the PMT installation and the final layout of the array developed for the ArDM experiment is shown in ???. The PMT were coated with WLS by TPB evaporation. The aluminium crosses over the final array are only for protection during the transport to the Canfranc Underground Laboratory (LSC).

4.5.2 Light readout front-end digitiser and DAQ

In view of the large scale application for the 20 kton detector, the $6 \times 6 \times 6\text{m}^3$ prototype will allow developing and testing low-cost and high-integration level solutions for the photomultiplier signal digitisation on large equipped surfaces. Solutions of this kind have been studied, in the framework of the R&D programme PMm2 [115, 116], for the instrumentation of giant water Cherenkov detectors.

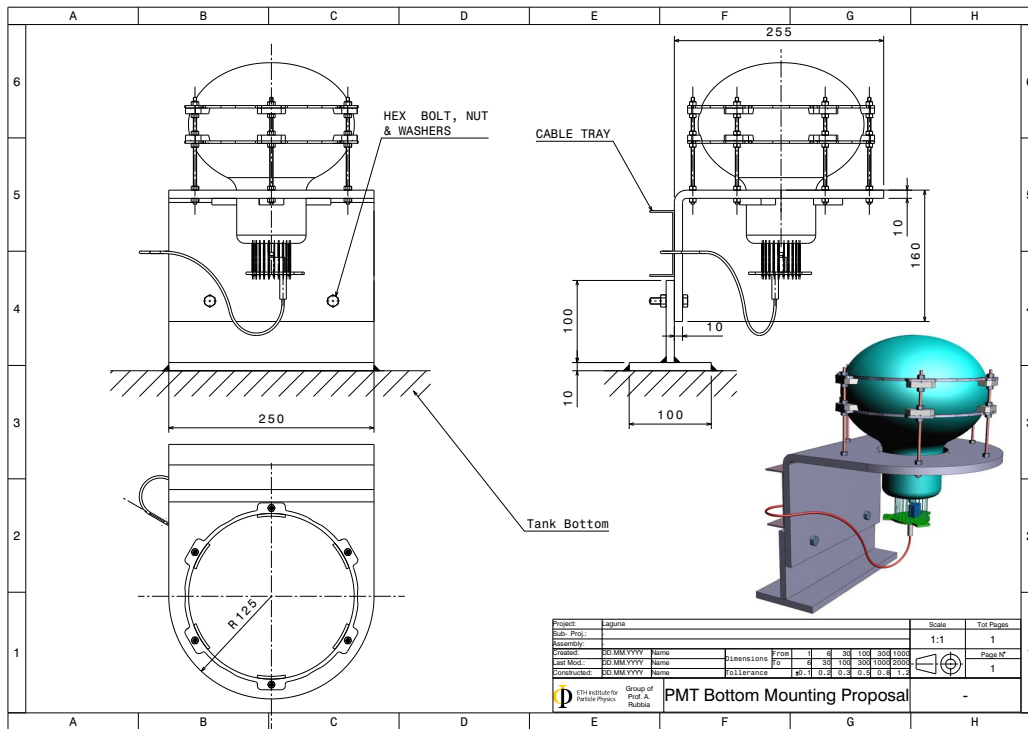


FIG. 82: PMT mounting arrangement on the bottom of the vessel and its fixation.

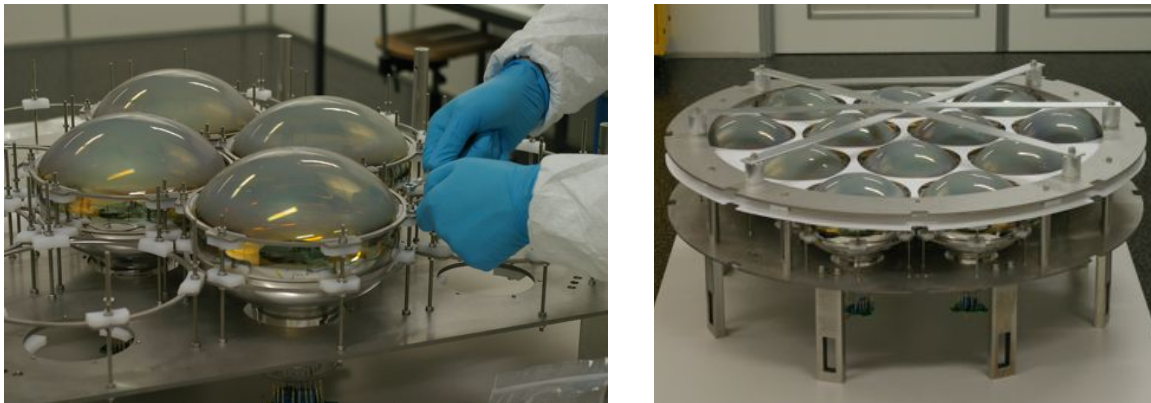


FIG. 83: The installation and final PMT array for the ArDM experiment [72, 114] in the ETHZ clean room. The aluminium crosses over the final array are only for protection during the transport to the Canfranc Underground Laboratory (LSC).

The front-end electronics for the light readout of the DLAr detector will be based on the solution developed within the PMm2 R&D. The PARISROC ASIC, as described in the following, will be adapted to the time structure of the scintillation light produced in the interactions of secondary particles in interactions in LAr. The detection of the direct scintillation light is the main purpose of the electronics in order to provide the absolute time. The system will also be capable to detect the so-called proportional scintillation light produced by the electrons extracted and amplified in the gaseous phase, see ??.

The solution developed by this R&D represents an important handle for costs reduction. The signal digitization is performed by grouping the photomultipliers in arrays of 16. Each photomultiplier array is then read out by an ASIC (Application Specific Integrated Circuit) chip in AMS SiGe 0.35 μm technology. The ASIC, which is called PARISROC (Photomultiplier ARrray Integrated in Si-Ge Read Out Chip) [115, 117], provides a complete readout system for trigger-less acquisition.

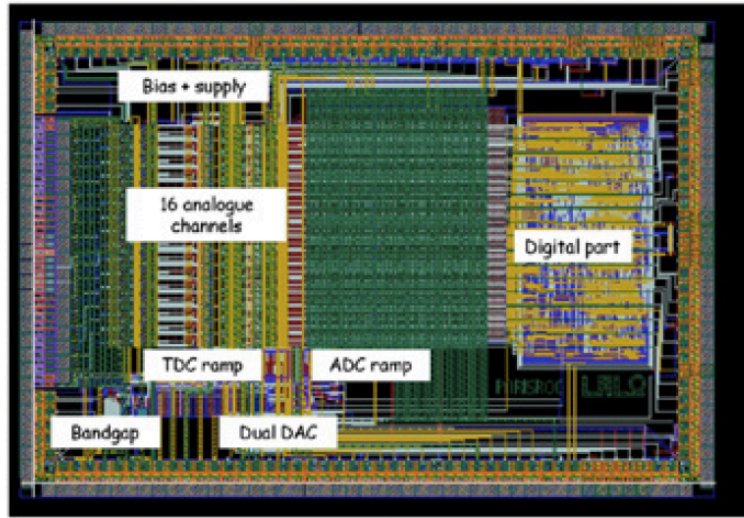


FIG. 84: Layout of the PARISROC ASIC used for the production of the second iteration of the chip. (from Nucl.Instrum.Meth. A623 (2010) 492-494).

The PARISROC chip reads the signals of 16 photomultipliers totally independently from each other. Each analogue channel consists of a low-noise preamplifier with variable and adjustable gain (8 bits) to compensate the relative photomultiplier gain differences powered by a single high voltage. The preamplifier is followed by a slow channel for the charge measurement in parallel with a fast channel for the trigger output. The slow channel includes a variable (50-200 ns) slow shaper followed by an analogue memory with depth of 2 to provide a linear charge measurement up to 50 pC; this charge is then converted by a 10-bit Wilkinson ADC. The fast channel is composed of a fast shaper (15 ns) followed by a low offset discriminator to auto-trigger down to 10 fC. This auto-trigger feature makes the PMT array completely autonomous from the other PMT arrays. The threshold is loaded by an internal 10-bit DACs common for the 16 channels.

Each output trigger is latched to hold the state of the response until the end of the clock cycle. It is also delayed to open the hold switch on the peak output of the slow shaper. The digital part of PARISROC is built around 4 modules which are acquisition, conversion, readout and top manager. Currently, PARISROC is based on 2 memories: during acquisition, analogue signals are stored into the analogue memory and then, during the analogue to digital conversion, analogue charges and times

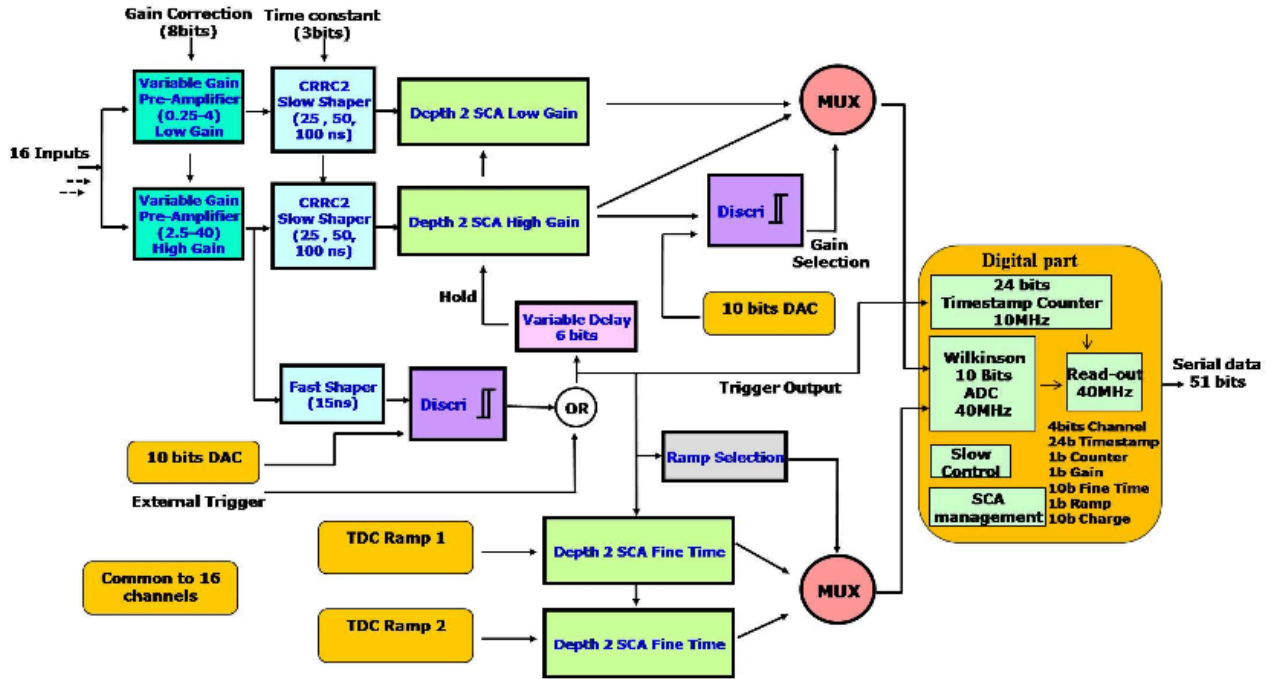


FIG. 85: Block diagram of the PARISROC ASIC.

are converted and stored into a digital memory. At the end of each cycle, data from this memory are readout to an external system. The analogue to digital conversion is made via a Wilkinson converter. It is made around a common ramp and discriminators which sample a digital counter at 40 MHz (for charge and fine time). The ASIC also provides a complete time stamping solution with a 24-bit coarse time counter at 10 MHz and a fine time measurement with an analogue ramp of 100 ns. Data are formatted by the ASIC and sent through network cables, which are tight and include also the clock and slow control connections, to the external data storage. This contributes in appreciable savings in the connection cables and feedthroughs. The power consumption of the chip is 15 mW per channel. Figure 6 shows the block diagram of the ASIC. A traditional digitization scheme with one cable per photomultiplier and external fast digitizers could be easily setup for the LBNO 6x6x6 m³ prototype, however, in view of the large scale application for the final detector it is certainly worth to test this high-integration solution which contributes to reduce the cabling connections and feedthroughs. A mixed configuration can be envisaged, where different PMT groups can be read out in different configurations, such as location of the readout cards directly in the argon on the back of the PMTs, or in the evacuation chimneys on top of the readout plane.

The front end electronics board hosts two main components: the PARISROC chip coupled to an FPGA that manages the dialog with the surface card. A series of DC/DC converters transform the 48 V brought in by the cable to provide the different low voltages for the electronics and the high voltage

power supply common to the 16 PMTs. This reduces by 16 the cost of the PMT power supply. This high voltage is tunable remotely by a 12 bit DAC. The PARISROC chip is hosted on a daughter board including its own regulators and supply filters to avoid noise coupling with the mother board. All the output digital data are read out in serial mode at a rate of 40 MHz by a FPGA. Special care was taken in the design of the Printed Circuit Board (PCB) to meet rules of isolation due to the high voltage, rules of filtering, cooling and Electro Magnetic Compatibility (EMC).

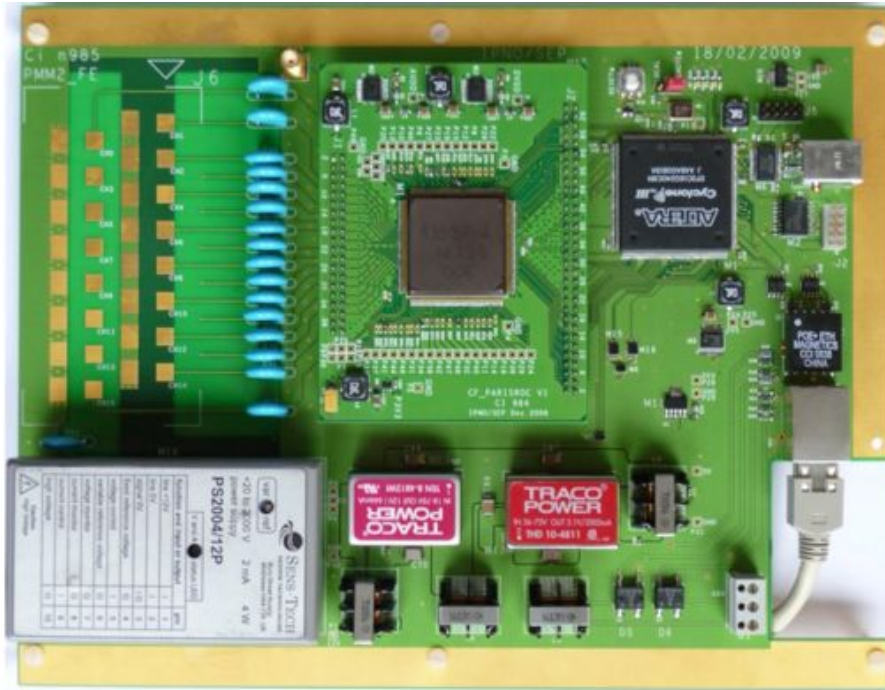


FIG. 86: Photo of the complete card of the light readout system under test.

The front end card has been successfully tested at room temperature in a dedicated facility at the APC Laboratory in Paris, shown in Figure 87. The gain linearity has been measured and the result is shown in Figure 88. The PARISROC ASIC can in principle work in liquid argon. An ongoing development foresees to test and adapt it for this application by possibly increasing the depth of the Single Channel Analyzer (SCA) and speeding up the digital readout section.

We envisage to study different solutions for the adaptation to operation in liquid argon. Because of the high electrical rigidity of liquid argon, the system could be brought into the liquid without a liquid-tight box. The current solution for the HV, common to all (16) PMTs in a matrix, needs to be adapted: each PMT will receive the HV individually. The heat dissipation in liquid argon and the local formation of bubbles around the electronics will be addressed.

The second part of the system, situated on surface at room temperature, receives the data via Ethernet cable. It provides the interface to the global DAQ, the Power Over Ethernet (POV) for the

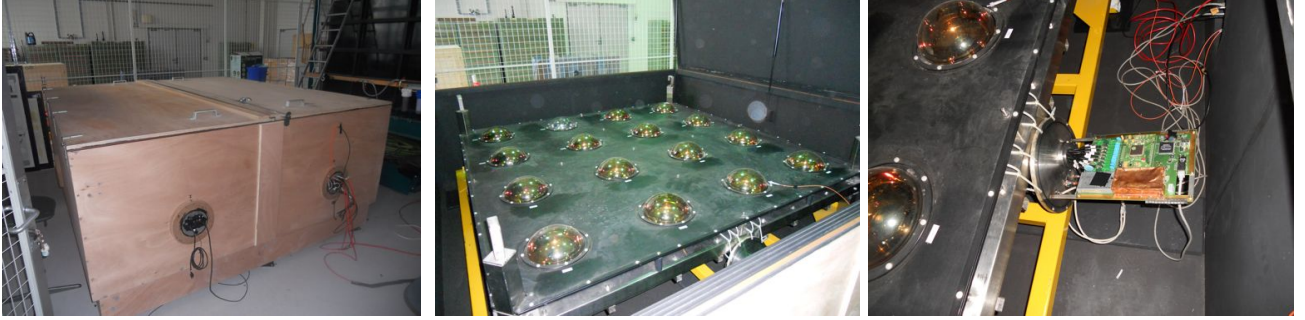


FIG. 87: The test bench for the PARISROC chip with 16 PMTs. From left to right: Light-tight box of 2x2x1,5 m³, matrix of 16 PMTs, front-end card.

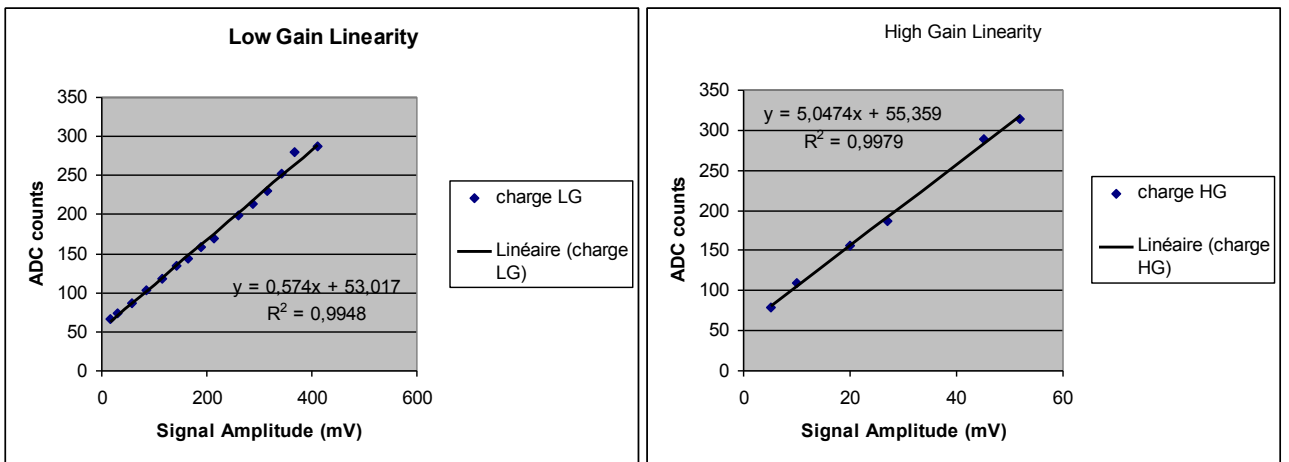


FIG. 88: Measured gain linearity of the front-end electronic board.

HV generator, the GPS. This surface card will be redesigned as a dedicated acquisition card imbedded in the microTCA technology used for the general experiment DAQ. The card is shown in Figure 89.

4.6 Cryogenic vessel

The LAGUNA and LAGUNA-LBNO EU FP7 design studies have been focusing on the GLACIER concept [2], a large double phase Liquid Argon TPC with a long drift and charge-sensitive detectors in the gas phase. According to these studies it is technically feasible to build a large (20-50-100 kt) underground tank, based on the LNG industrial technology. In a more recent related development, these studies have also considered a novel technique for the tank construction involving the membrane technology for the tank. This topic has been the subject of several developments between LAGUNA and industry over many years. In this technology, the functions of structural support, insulation and liquid containment are all realised by different components, namely an outer concrete structure, specially designed insulating panels and a thin layer of steel plates. These development are very promising for



FIG. 89: Surface card of the light readout system.

the realisation of a large underground detector, however several areas need to be verified on a large scale prototype.

Therefore, the so-called corrugate membrane panels technique (licensed by GTT/France[169]), has been envisaged as an attractive solution for the LAGUNA LAr prototype. The inner vessel has a cubic shape with inner dimensions $8.3 \times 8.3 \times 8.3 \text{m}^3$. This volume ensures enough space surrounding the drift cage, acting as electric insulation ($\sim 1 \text{ m}$ of LAr), for safe operation at HV with up to 300 kV at the cathode (and possibly up to 600 kV, to be tested as part of the demonstrator). This volume shall also be used for access and movement inside the vessel during the construction phase. A manhole and a detail-introduction hole are located at the top face of the vessel. During the inner detector assembly, additional chimneys are used to install a controlled air circulation. These additional chimneys are available for the implementation of the liquid argon process during normal operation.

For practical reasons, we adopt the panels that come in standard sizes and shapes. A preliminary panel configuration, developed specifically for us by GTT, is shown in ???. The membrane is 1.2mm thick stainless steel. The thermal insulation is passive, based on GRPF (glass reinforced polyurethane foam) layers, interspersed with pressure distributing layers of plywood. The pressure from the product is transmitted to a concrete envelope through polyurethane foam. Its thickness and composition is such to reach a residual heat input of 5 W/m^2 in cold operation. The total heat input (including the input from the roof and the cables) in cold operation at LAr temperature is $\sim 2 \text{ kW}$. The passive insulation is contained in a reinforced concrete “vessel” with $\sim 1.2 \text{ m}$ thick walls. The top outer ceiling

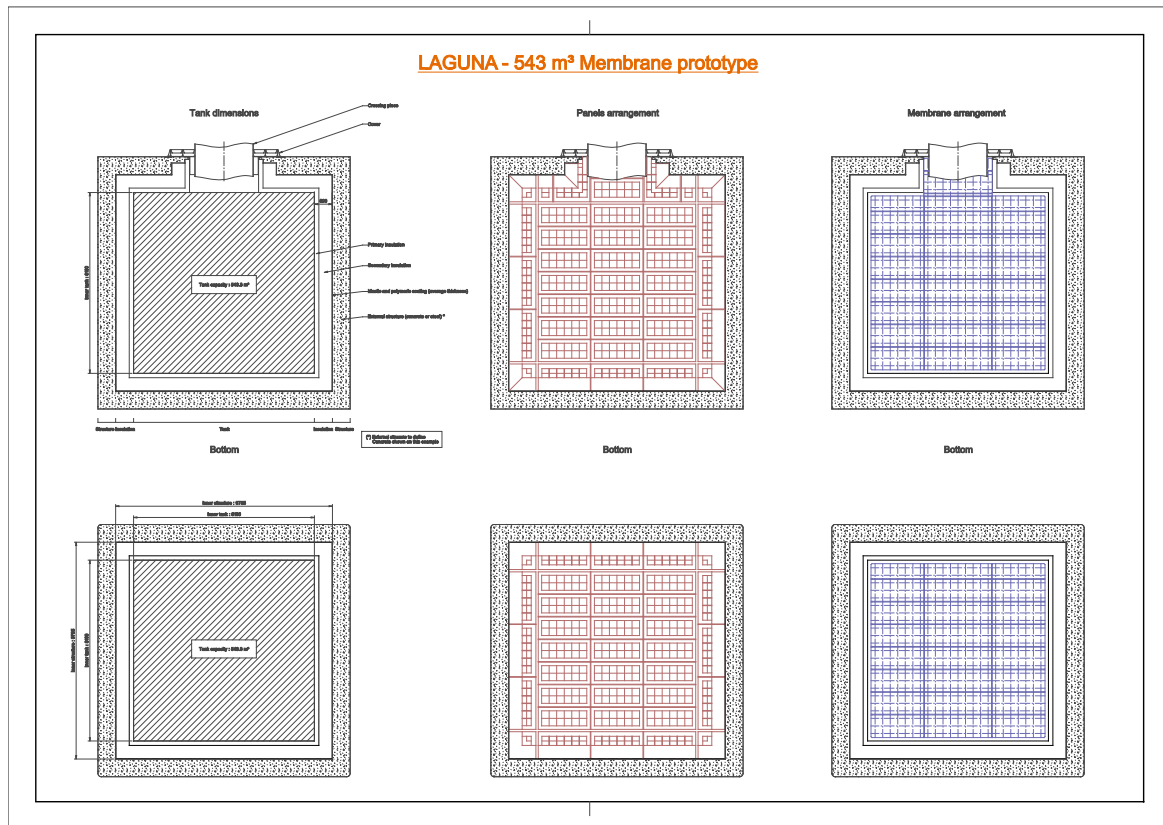


FIG. 90: Schematic of the 540 m³ membrane vessel developed specifically for this proposal by GTT/France. The top cap is not considered at this stage (copyright GTT).

is made by a framework reinforced stainless steel plane, able to support the inner anode and outer instrumentation (electronics, cryogenics, control). A beam pipe (evacuated) for the charged particles is crossing the concrete outer vessel and the thermal insulation layers. Its vertical orientation is adapted to the charged beam vertical axis in its last section. A top closed space (“penthouse”) is constructed for hosting the electronic equipment, and various control and monitoring devices. A gap space shall remain between the reinforced concrete vessel and the walls of the pit. The airflow created by the ventilation and conditioning system of the hall will be sufficient to keep the temperature of the walls of the pit constant and avoid condensation on the walls.

In order to understand in more details the use of the corrugated membrane technology, we have asked GTT to develop the conceptual design of a 17 m³ vessel (See ??), with a central area of 3 × 1 m², also exploitable for mechanical mockup tests of 3 CRP modules, (See Figure 91). The vessel is presently under procurement, and is planned to be finalised in 2014. A 3 × 1 × 1 m³ chamber is under preparation. The outer structure (number 1) ensures the structural resistance to contain the LAr, to resist to gas pressure and structural weight loads. It will work at ambient temperature and therefore will not be submitted to thermal stresses. The current design has considered that this structure will be set on

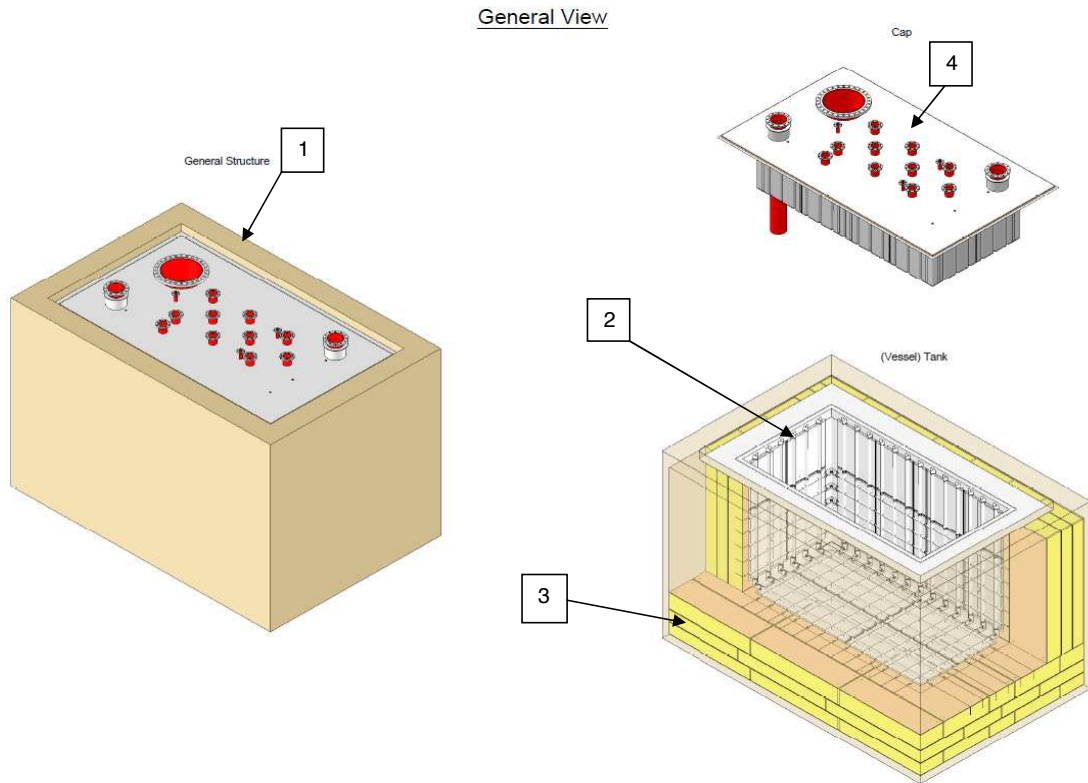


FIG. 91: General view of the 17 m³ tank solution presently under construction. Note that the cap has been specially designed and was the main focus of this development (copyright GTT).

pedestal to allow bottom convection.

The corrugated membrane (number 2) acts as primary barrier. It is a liquid and gas tight barrier. The membrane is not a structural component of the system and has a tightness function only. It is a double network of orthogonal corrugations allowing its free contraction/expansion, in two directions, under thermal solicitations.

The insulating structure (number 3) located between the membrane and the outer structure, maintains the outer tank structure at ambient temperature and keeps the thermal fluxes within the required limit; the insulation is said to be "load bearing" in the sense that it transmits the LAr loads from the inner containment to the outer structure. This insulation compartment is tight from inside (by the membrane) and outside by the outer structure. It is considered as a closed space (insulation space). This space is permanently maintained under nitrogen atmosphere, which enables a permanent monitoring. Nitrogen breathing allows a control of the integrity of the inner containment tightness.

The Cap (number 4) will ensure the tank tightness from the top and will allow instrumentation to be supported. In addition it has been designed specifically for this Project in order to limit as much as possible the thermal fluxes. The cap will entirely be made out of steel so as to prevent any pollution

of LAr and lateral sides will have corrugations in order to compensate for thermal contractions.

The principle of the membrane system is to uncouple the structural, thermal and tightness functions of the tank. The insulating panels are sandwich type made of rigid closed cells polyurethane foam inserted between two plywood faces bonded to the foam. See ??.

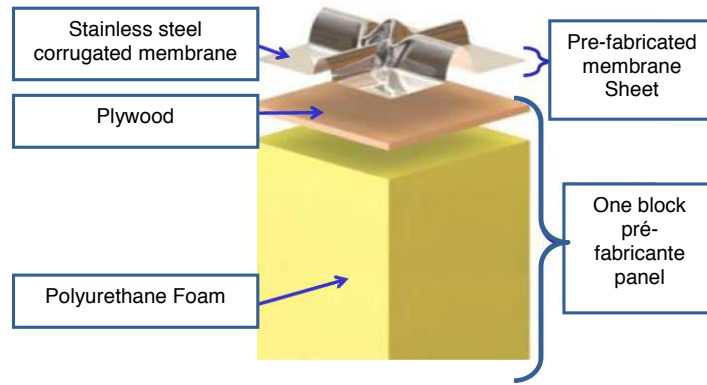


FIG. 92: Detail of the GTT insulation panel (copyright GTT).

The insulating structure protects the structural elements from the extreme temperatures. Moreover, it enables to limit ingress of heat and moisture inside the tank. The insulation system is composed of prefabricated insulating panels and flat joints (See ??). The thickness of the insulating panels has been determined upon the required thermal fluxes. The total thickness is 1m divided into three panels (as illustrated: 300 + 300 + 400 mm). The definite specific thicknesses can be adapted to suppliers requirement. The size and shape of the panels are optimized to fit easily and properly the whole area of the inner side of the tank. After panel erection, the gap must be filled with glass wool blankets (flat joints) to ensure that no convection effects or thermal bridges occur.

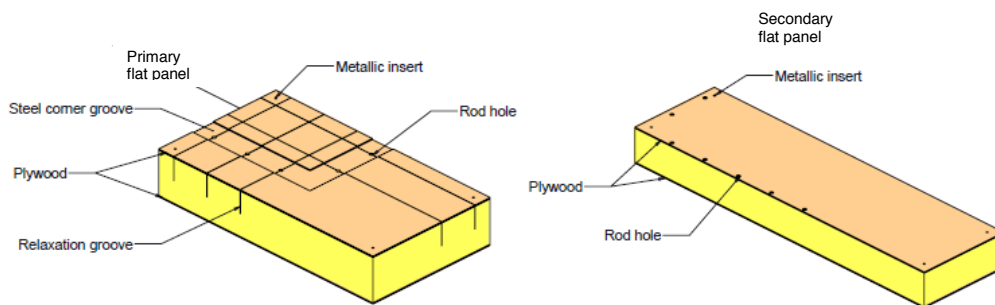


FIG. 93: Detail of the GTT insulating panel (copyright GTT).

The metallic membrane ensures the containment of the liquid and the tightness of the inner container under normal operating condition. It consists of a stainless steel corrugated membrane on top of the

insulating structure all over the tank surfaces (See ??). The membrane panels will be displayed on top of the inner containment and lap welded together for liquid and gas tightness. The corrugations are continuous and cross each other in the form of knots. The corrugations are formed by dedicated tools using a cold folding process in order to minimize the thickness reduction in the folded parts. One of the families of corrugations is larger than the other one. The sheets shape are optimized to fit easily and properly the whole area of the inner tank. The metallic membrane consists mainly of flat rectangular sheets. Other shapes are used in the angles of the tank to achieve a proper covering of the corners. When necessary, the corrugations are terminated with dedicated pieces. The junctions between the corrugations of two adjacent walls are achieved by dedicated angle pieces.

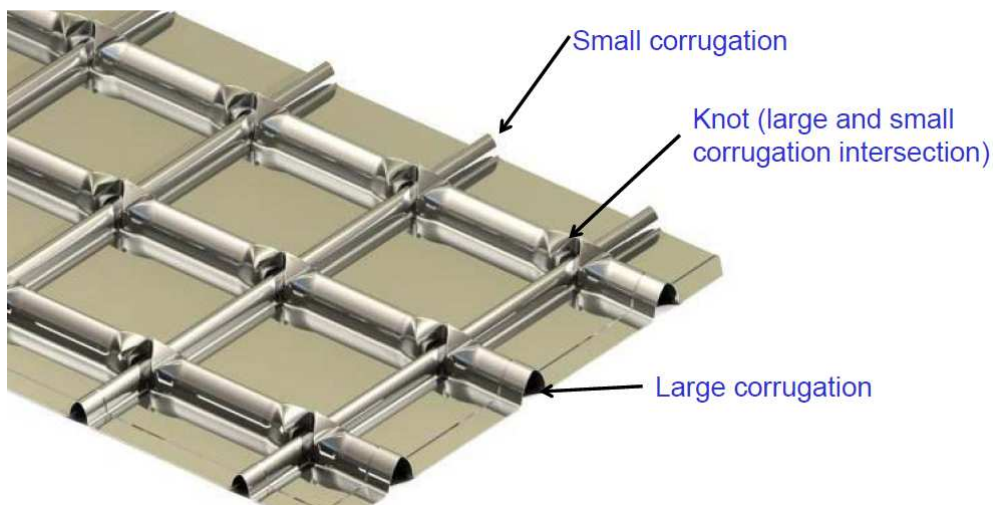


FIG. 94: Detail of the GTT metallic membrane panel (copyright GTT).

After the assembly, the tightness of the vessel will be certified. The standard GTT procedure for testing the tightness is as follows: after the inner container erection is completed, the tightness of all the welds of the membrane is tested by ammonia test. A mixture of nitrogen (75%) and ammonia (25%) is introduced in the insulating space, behind the membrane. Welded membrane joints are coated with a reactive paint which changes colour in case of leak in the membrane. All leak test points must be checked to ensure a complete distribution of the N_2/NH_3 mixture. Detected leaks must be repaired, leak test points are welded and a new full or global tightness test is carried out. After completion of the test, the insulation space is purged using nitrogen, several vacuum/purging operations are necessary. Finally, the membrane is cleaned and the paint completely removed and evacuated. In addition, the tank tightness will be tested with Helium by inserting it the gaps where the insulation is located and operating a helium leak checker inside the main vessel volume.

The cap was given special attention. The crossing pipes (holding the signal and electrical

feedthroughs) were designed according to their function, and their thermal properties and stress have been studied. Drawings have been produced for the containment system, the cap configuration and the assembly procedure, along with a construction schedule. The total inner volume is $3 \times 4.8 \times 2.4 \text{ m}^3 = 35 \text{ m}^3$. The volume of stored LAr is 17 m^3 with the level of argon at 1.5 m. The residual heat input is 5 W/m^2 for a total BOR of 0.069%. The insulation thickness is 1 m with a density of 70 kg/m^3 (PU Aged HFC245). The temperature of the LAr will be stored between 86.7 and 87.7 K at a pressure of the tank $950 < P < 1050 \text{ mbar}$.

The instrumentation will be suspended by the cap which has therefore to ensure a mechanical requirement as it will have to support the weight of the insulation and of the instrumentation. The entire vessel will also to ensure proper ultra-high vacuum tightness (i.e. He leak rate $< 1e - 9 \text{ mbar lt/s}$). The crossing pipes have been arranged as to provide the optimal path for cables to the readout anode. Three chimneys are in addition used to hang the anode to the top cap. The cap can be opened and closed (welded) about four times in the lifetime of the vessel.

The cap will be welded on its periphery to ensure the tightness. In addition all crossing pipes will be welded to ensure that no pollution of the Argon occurs. Its total weight will be 3.8 tons.

The installation sequence has been studied. It consists of several steps for a total execution time of about 6 weeks. A concrete or a steel structure can be contemplated for supporting tank and must be assembled first. Accurate marking will be performed in order to define the exact anchoring system position (rods). In order to fix the membrane corner elements, rods will be fixed on tank bottom. These rods will be either welded in case of metallic tank, either screwed in insert in case of concrete structure. The bottom insulation will be installed next. Lateral rods will be fixed. Once rods are fixed, vertical insulated panels are installed. As per bottom, insulation is made of 3 layers of insulation. See ???. Steel corners are installed on bottom and vertical corners to anchor the membrane. Securing of these corners steel is ensured by the rods. Then the membrane is positioned and welded. All along corner area membrane will be tighten by means of angle pieces on bottom and vertical area, overlap on the top part of the vertical area, and end cap on the top part of the tank.

4.7 Liquid Argon process

4.7.1 Sources of impurities from outgassing

When pumping a volume from atmospheric pressure, the gas in the volume is removed whereas the speed of evacuation is mainly based on the speed of the vacuum pump. Down to a pressure of $\sim 1 \text{ mbar}$, this is done with a roughing pump and at lower gas pressures, when the air resistance is low enough, with a turbo molecular pump. The pressure drops exponentially with the time as a function

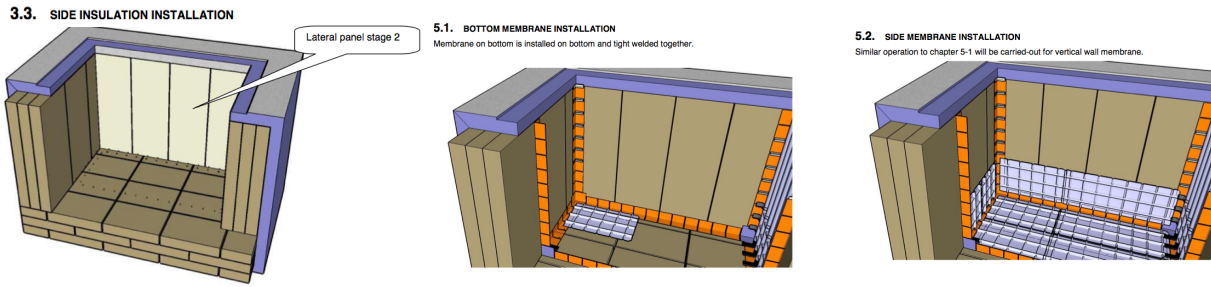


FIG. 95: Some steps of the installation sequence (copyright GTT).

of the pumping speed S and the to be evacuated volume V :

$$p(t) \approx p_0 e^{-\frac{S}{V}t} \quad (4.2)$$

The gas flow while pumping can be assumed to be laminar. This behavior is true down to about 10^{-3} mbar, depending on the used pump. At lower pressures there is no longer any gas flow, but a molecular flow, since single molecules are removed. This is where the turbo molecular pumps become most efficient. In this pressure range, other effects, usually summarized as outgassing, become important. They are complex processes and different mechanisms at different pressure ranges and will be discussed in the following sections:

a) Zero order desorption

A first effect, after most of the gas in a volume is removed, is desorption from the surfaces. When there are multiple layers of material sticking to the surface, (e.g. there is water laying in the chamber) the desorption rate is constant. The rate with which molecules are desorbed depends on the latent heat of vaporization E_v and the temperature T [118]:

$$-\frac{dn}{dt} = \alpha e^{-\frac{E_v}{kT}} \quad (4.3)$$

where α is a constant depending on the initial pressure.

b) First order desorption

When coming to a monolayer of molecules sticking to the surface, the behavior changes. The desorption rate becomes time dependent, according to the molecular density on the surface. To a first approximation it can be assumed that particles are released from the surface, and do not return to it,

with a rate proportional to their surface concentration C [119]. This process can be written as:

$$\frac{dC(t)}{dt} = -K_1 C(t) = \frac{e^{-E_d/N_A kT}}{\tau_0} C(t) \quad (4.4)$$

where the rate constant K_1 , strongly depends on the activation energy of desorption E_d (per mol) and the temperature T . N_A is the Avogadro number and τ_0 the nominal vibration period of an adsorbed molecule; typically of the order of 10^{-13} s.

By integrating Eq. ?? the surface concentration can be written as:

$$C(t) = C_0 e^{-K_1 t} = C_0 e^{-t/\tau_r} \quad (4.5)$$

where τ_r is the average time of a molecule sticking to the surface, i.e. the residence time of a molecule on the surface. It is, using Eq. ??, given by

$$\tau_r = \frac{1}{K_1} = \tau_0 e^{E_d/N_A kT} \quad (4.6)$$

c) Second order desorption

A lot of gas atoms are bound in a diatomic molecular state and they can only be desorbed as a molecule. For example, hydrogen bound to the surface first has to become an H_2 molecule before being able to be desorbed. This process, called second order desorption, is given by a different rate constant K_2 and the concentration can be written as [119]

$$\frac{dC(t)}{dt} = \frac{-K_2 C_0^2}{(1 + C_0 K_2 t)^2} \quad (4.7)$$

K_2 depends on the desorption energy E_d and the temperature. Therefore, it is clear that second order desorption rate, proportional to $1/t^2$ is much smaller than the exponential decay of the first order desorption.

4.7.2 The desorption from real surfaces

In a real vessel, gas is not automatically pumped out when desorbed from the surface. A particle will bounce on the walls several times and can be re-adsorbed. With each re-adsorption, it sticks on average for the time τ_r to the surface before being desorbed again. This leads to an experimentally measured outgassing rate q of

$$q \propto \frac{1}{t^\alpha} \quad (4.8)$$

where α is a coefficient approximately equal to 1 [120]. This coefficient can be time dependent and varies with the composition of the outgassing components. In general the $1/t$ behavior is given for all molecules but for different kind of molecules the time constant of outgassing varies. Therefore, the total desorption is the sum of the desorption of the different molecules.

Since the residence time (Eq. ??) is a function of E_d and T , heating up the walls is increasing the speed of outgassing. For example, for water molecules sticking to a stainless steel surface, the desorption energy E_d is 23 kcal/mol = $96 \cdot 10^3$ J/mol and the residence time is 10^4 seconds at room temperature of 22 °C. Increasing the temperature of the chamber walls, gives a strong decrease of the residence time and for 350 °C it is about 10^{-5} s. It is therefore favorable to bake out the components and the inside walls of the vacuum chamber. But doing so, it has to be taken into account that all the chamber must be heated up and not only one part of it. As mentioned before a molecule released is most likely adsorbed again on another surface. Having now, for example, heated up half of the surface to 350 °C while keeping the other half at 22 °C gives an average residence time of $\frac{1}{2}(10^4 \text{ s} + 10^{-5} \text{ s}) \approx 5 \cdot 10^3$ s corresponding to an average temperature of 27.4 °C. This shows, that always the coldest surface is dictating the outgassing rate. Thus partial heating of one and later another part of the vessel is not having a significant impact on the overall performance of the vacuum.

4.7.3 Diffusion

At a certain pressure most residual gases on the surface of a chamber have been evacuated and diffusion is the major source of gas molecules. This is the transport of molecules inside materials. Gas molecules are moving from inside the detector parts and the walls of the cryostat to the surface where they desorb into the vacuum. Because diffusion is on a much slower time scale than desorption, the residence time for releasing the molecules from the surface can be neglected. The outgassing from diffusion of a solid material for an initial gas concentration C_0 is

$$q = C_0 \left(\frac{D}{t} \right)^{1/2} \left[1 + 2 \sum_0^{\infty} (-1)^n \exp \left(\frac{-n^2 d^2}{Dt} \right) \right] \quad (4.9)$$

where $[D] = \text{m}^2/\text{s}$ is the diffusion coefficient and $2d$ the thickness of the material. The gas concentration C_0 is given as residual pressure in Pascal and the diffusion rate q in $[q] = (\text{Pa} \cdot \text{m}^3)/(\text{m}^2 \text{s})$ [119, 121].

Instead of solving this equation one has a look at its asymptotic solutions. For short times ($t \simeq 0$), only the first term is of importance and Eq. ?? becomes approximately

$$q \approx C_0 \left(\frac{D}{t} \right)^{1/2} \quad (4.10)$$

This shows a decrease in the rate proportional to $t^{-1/2}$, which is much slower than the rate given by desorption. For long times, the infinite sum of Eq. ?? has to be taken into account and, by a translation of the mathematical zero of the summation from the center of the volume, at distance d to one of the surfaces, Eq. ?? reduces to a rapidly converging sum and becomes

$$q = \frac{2DC_0}{d} \exp\left(-\frac{\pi^2 D t}{4d^2}\right) \quad (4.11)$$

This change in slope is a result of the depletion of gas particles inside the outgassing material [119, 121]. The diffusion coefficient D not only depends on the diffusing gas and the material it diffuses from, but it is also a function of the thermal activation energy of the gas in the solid.

$$D = D_0 e^{-E_D/kT} \quad (4.12)$$

Therefore, similar as for desorption, heating up the material leads to a much faster outgassing and is preferred.

4.7.4 Permeation

A surface facing the atmosphere is never completely depleted but also is adsorbing gas molecules of the atmosphere, which then diffuse through the material (walls) and get desorbed into the vacuum. The total motion can be described as an adsorption followed by diffusion and finally a desorption in the vacuum. Having a combination of the above described processes shows that the rate is much smaller than from the individual processes. This is called permeation. Because of the constant supply with new molecules from the atmosphere, permeation cannot be stopped. The only possibility to further reduce the pressure in a vessel is to seal the chamber wall on the outside with another, less permeable material or, more radically, change the chamber to one made of a different material or with thicker walls. For steel surfaces, hydrogen is the main element permeating through. The hydrogen molecule cannot permeate as a molecule but it dissociates on the metal surface into two single atoms that then diffuse through the metal. On the vacuum side of the steel wall the atoms have to recombine to a molecule to be desorbed. The permeation rate is proportional to the square root of the pressure difference [119]. Different from metals, in plastics, ceramics and glass the whole molecules can permeate through. For glass that is mainly the smallest existing molecule, the helium atom. This is of importance since photomultipliers are glass bulbs. Helium atoms diffusing into the tubes ionize in the strong electric field and destroy the photocathode. For this reason, leak testing a chamber, containing PMTs, with a helium leak tester should be omitted. Note, that permeation is only observed in ultra high vacuum

Material	Surface [m ²]	Outgassing rate		Reference
		@ $t = 24$ hr [torr l/s cm ²]	@ $t = 24$ hr [mbar l/s]	
Steel	10.74	$2.00 \cdot 10^{-10}$	$2.86 \cdot 10^{-5}$	[122]
G10	5.60	$1.22 \cdot 10^{-7}$	$9.11 \cdot 10^{-3}$	[123]
Copper	1.25	$3.01 \cdot 10^{-11}$	$5.03 \cdot 10^{-7}$	[124]
Nylon	0.013	$2.50 \cdot 10^{-7}$	$4.20 \cdot 10^{-5}$	[125, 126]
Polyethylene	0.53	$6.00 \cdot 10^{-8}$	$4.25 \cdot 10^{-4}$	[127]
Kapton	0.30	$7.50 \cdot 10^{-8}$	$3.00 \cdot 10^{-4}$	[125]
Polyolefine	1.6	$5.25 \cdot 10^{-8}$	$1.12 \cdot 10^{-3}$	[128]
Teflon	0.02	$8.49 \cdot 10^{-9}$	$2.72 \cdot 10^{-6}$	[125]
Total outgassing after 1 day			$1.1 \cdot 10^{-2}$	

TABLE VIII: Material and calculated outgassing rate of the 40×80 cm² LEM TPC, tested in the ArDM cryostate. All rates are given for $t = 24$ hr from the beginning of the evacuation.

chambers and was never observed in tests performed in smaller LAr TPC by the ETHZ group.

4.7.5 The 40×80 cm² LEM TPC as an example

To give a practical example, the test of the 40×80 cm² LEM TPC is considered [23, 52]. The detector is mainly made from glass epoxy boards (G10). This material has a lot of epoxy resin and therefore solvents in it and a strong outgassing must be expected. Besides the actual detector, there are also cables, electronic components and the support system for hanging the setup inside the ArDM cryostat. All these components are outgassing and possible sources of impurities. ?? gives an overview of the material budget and the corresponding surface areas. The table also gives an expected outgassing rate per square meter after 24 hours of pumping, derived from several sources. These rates are average values to get a feeling, what is contributing how much to the outgassing. If there were several values given for the same material, an average has been taken, normalised to 24 hours by assuming an outgassing rate of $R(t) \propto 1/t$.

To test our model, outgassing measurements were taken several times during the pumping of the volume. The overall pumping time was around 65 days. ?? shows the pressure inside the cryostat as a function of the days since pumping started. The curve is not smooth but has several spikes, above as also below the actual pressure curve.

Values below 10^{-6} mbar are indicating the times when the vacuum gauge was switched off and the spikes above the smooth curve have different origins. There are, for example at ~ 6 days and at ~ 20 days, measurements of the outgassing with the Rate-Of-Rise method. Other spikes, when reaching more than 1 mbar, are from moments when the detector was filled with argon gas for calibrating the PMTs or to do tests with the charge readout. Also, the cryostat was filled with argon gas when a flange or other components on the top flange had to be replaced. At ~ 48 days the detector was completely

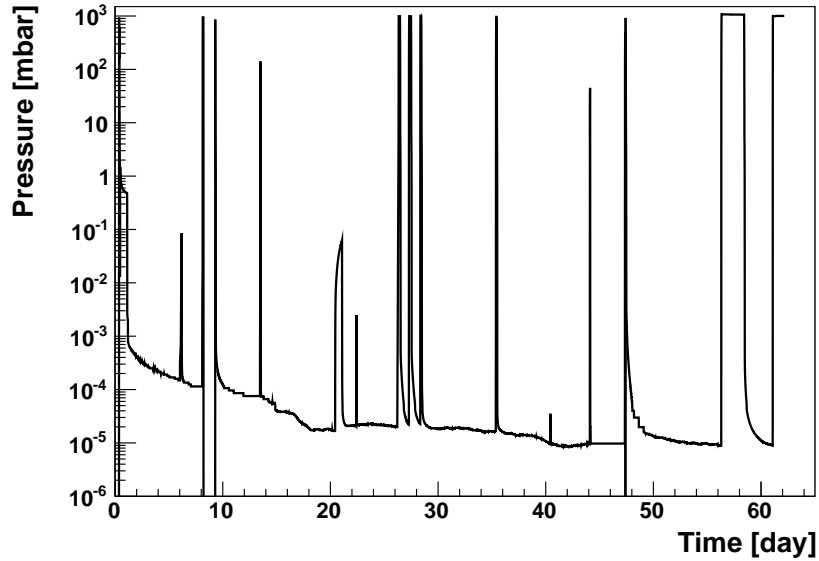


FIG. 96: The pressure as a function of the evacuation time for the $40 \times 80 \text{ cm}^2$ LEM TPC. The pumping started on August 10, 2011 and lasted for 62 days, before starting to fill the detector with argon. The peaks in the curve are coming from tests with pure argon gas and also from venting the vessel. (See text for details)

opened again for a few hours, because of a problem with an electrical contact. It can be seen that it took a while to reach the previous vacuum again because of newly installed PCB parts. In the few hours while the detector was exposed to air some water molecules attached to the detector but the main reason for the slow reaching of the previous vacuum value is presumably the water (and other residual gases) in the new glass epoxy parts.

The reason for showing ?? in the context of outgassing rates is, that every time the detector is filled with gas, there is a short period of a few minutes when the gate valve to the pump is closed but still there is no gas filled in the detector. During these periods the detector is outgassing and, analyzing the outgassing with the Rate-Of-Rise method, the rate as a function of the time can be measured. The values obtained are presented in ?. Also the calculated value of $1.1 \times 10^{-2} \text{ mbar l/s}$, from ?, is drawn (full line), assuming a simple $1/t$ law. The dashed lines are a fit, strictly proportional to $1/t$ as also to a general power law, giving $R = 0.27/t^{1.42}$ with $[t] = \text{hr}$ and $[R] = \text{mbar l/s}$. The theoretical outgassing rate and the measured outgassing rate are different by about one order of magnitude. The actual outgassing is faster than $1/t$. A possible explanation is that, when filling the chamber with argon to atmospheric pressure, water, that is frozen at low pressures, re-liquifies and gets dissolved in the gas. This effect can be seen in ? at about 14 days. After a short period of venting the chamber with argon gas, the pressure drops faster, when the pumps are turned on again, compared to the rate before the venting.

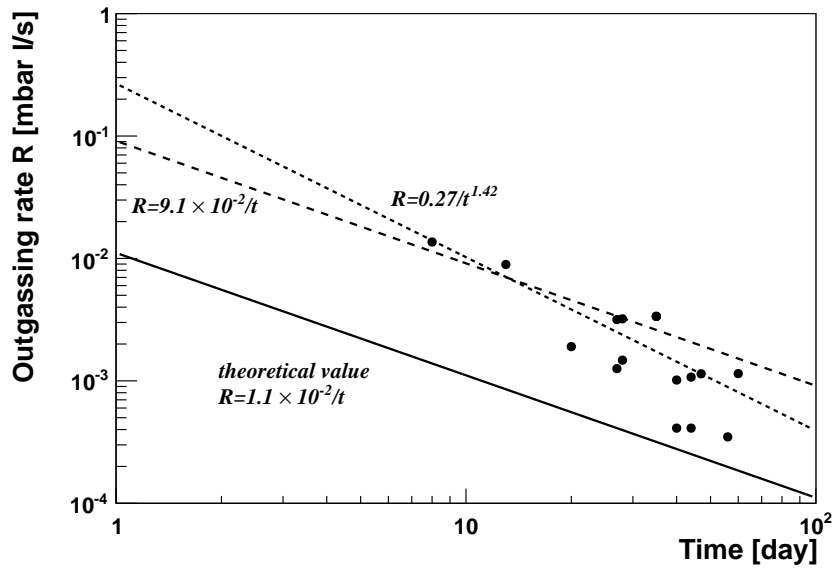


FIG. 97: The outgassing of the $40 \times 80 \text{ cm}^2$ LEM TPC as a function of the pumping time. The full line indicates the calculated value from ?? and the two dashed lines the fit functions for the measured data.

4.7.6 Leaks

Eventually, the outgassing becomes so small that permeation is the main source of impurities. This is the point, where there is no way to improve the vacuum without changing to a bigger, more powerful pump. It is hardly reached with a normal turbo pump and other methods, e.g. using getter pumps, have to be applied. Permeation only gets notable at pressures below 1×10^{-8} mbar. Because of its time independence, the best vacuum reached is

$$p = \frac{Q_{\text{permeation}}}{S} \quad (4.13)$$

here S is the pumping speed.

If this absolute possible vacuum is never reached and the pressure becomes constant, this is an indication for a leak. Leaks behave similar to permeation. Also they are letting a constant, time independent, flux of gas into the vacuum. The leak rate, therefore, is given, similar to Eq. ?? by

$$Q_{\text{leak}} = \frac{\Delta p \cdot V}{\Delta t} = p_{\text{min}} \cdot S \quad (4.14)$$

where p_{min} is the pressure at the best vacuum obtained. [Q_{leak}] = mbar l/s the leak rate of the biggest leak. In general each leak has a different “size” and therefore the largest has most influence on the final pressure and it is the one to be found first.) Fixing smaller ones will not make any major effect and cannot be noted by looking at the pressure. After the main leak is found, the next smaller is the

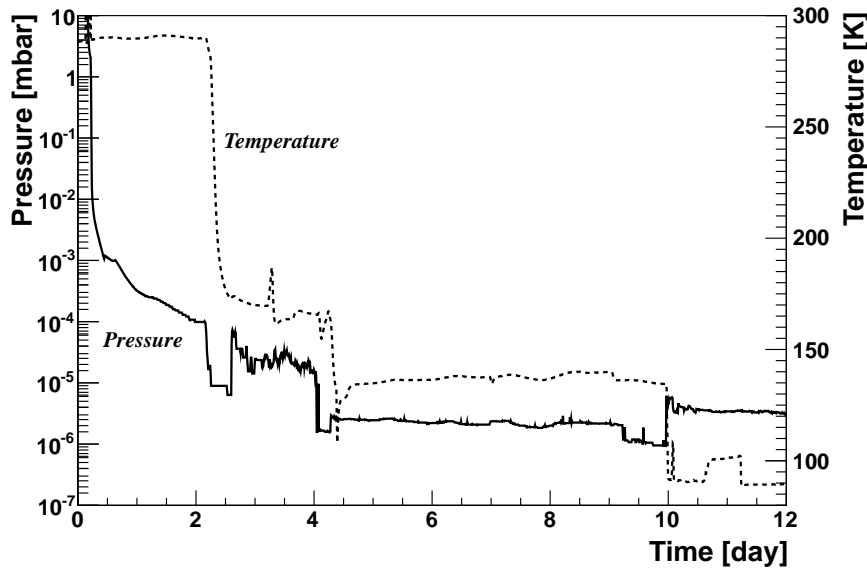


FIG. 98: The correlation between the pressure of the vacuum insulation (full line) and the temperature of a cold line inside it (dotted line) shows the behavior of cold leaks. Most obvious is it at $T = 10$ days where a temperature drop from gaseous to liquid argon immediately gives an increase in the pressure.

leading one to be fixed.

Permanent leaks are actual holes or cracks in the structure, where gas molecules can pass through. Most of the time they occur on connections, where two vacuum parts are flanged together. More rarely they happen to be from production errors like weldings that are not done properly. A third, very critical place, are connections of different materials like for example feed-throughs. In this case there is a material boundary between the stainless steel flange and the insulator and again between insulator and conductor. The vacuum tightness is done with glue, a soft metal like indium or by mechanical force, just pressing together the two parts. This kind of leaks sometimes can be cured by having a very liquid epoxy resin. Having vacuum on one side the epoxy can be put on the insulator and, through the leak it is sucked in and blocks the channel where the molecules went in.

Temporary leaks open and close, under certain conditions. Most of the time a temperature effect is the reason. Having the large gradients from room temperature to cryogenic temperatures in ArDM, the contraction of different materials becomes important. Normally plastics have a thermal contraction of a few percent for a ΔT of ~ 200 °C. Metals on the other hand contract about ten times less. The connection between two different materials can be tight at room temperature but by cooling it down it becomes leaky. ?? shows the correlation between the pressure in the vacuum insulation of ArDM, and the temperature of tubes containing the argon inside it. In the beginning the normal behaviour of evacuation is visible. With the start of cooling down the detector, at $T \sim 2$ days, the vacuum improves because of the cold surfaces. Later, it goes back on its original curve with a lot of fluctuations, which

already indicates the release of a gas from a leaky connection. When cooling down more, to ~ 100 K, the leak seems to close again and the pressure drops again. At $T = 10$ days liquid was filled in the cryostat (what can be seen by the sudden temperature drop to 89 K). In exactly the same moment, the pressure is rising what is a clear indication for a cold leak. This example shows that the cold temperature created a small leak in one of the joints that only opens when the temperature falls below 150 K.

4.7.7 Gas recirculation

The best way to reduce the amount of impurities is to pump the cryostat for a reasonably long time, if possible for several months, before filling with argon. But even after a long evacuation phase there is outgassing. After stopping of the pump the impurities can diffuse into the volume without being pumped away. The argon has to be purified constantly. To make an example, taking the lowest value for outgassing of 3.4×10^{-4} mbar l/s from ?? and the total volume of 1700 l of the system, with a total pressure at the moment when the gate valve is being closed of $\sim 2 \times 10^{-7}$ mbar. 15 minutes later, it is only $\sim 1.8 \times 10^{-4}$ mbar, which corresponds to 180 ppb of impurities when assuming the volume filled with 1 bar of argon gas at room temperature.

One possibility to slow down the outgassing process is to cool down the vessel while still pumping it. The time $t(T)$ for the outgassing of stainless steel at temperature T can be found by fitting the values given in [121], with an exponential function:

$$t(T) = \alpha \cdot e^{-0.0164 \cdot T} \quad (4.15)$$

The 15 minutes at 300 K therefore become ~ 400 min at 100 K. Further, the cold gas is 3 times more dense than the argon at room temperature. Therefore, filling with pure argon and cooling it to ~ 100 K, reduces the ratio of impurities by a factor 3 compared to warm argon gas. When filling with pure liquid argon, it is reduced even by a factor of ~ 800 with respect to argon gas at 20 °C.

This example shows that an initial cool down, with vacuum inside the chamber has a positive effect on the concentration of impurities diffused into the volume as also the ratio is improved. The disadvantage is, that all molecules that did not desorb are still on the surfaces and eventually some are dissolved in the liquid. A constant recirculation and purification of the liquid is needed.

Another approach is, to actually fill the chamber with pure argon gas, while it is still warm. The outgassing in the gas is large but, contrary to cryogenic liquids, purification of the warm gas is not difficult and commercial cartridges can be used. Having a given gas flow S ($[S] = \text{l/s}$) and an outgassing rate R ($[R] = \text{mbar l/s}$) the total amount of impurities $N(t)$ as a function of time can be estimated by

the following idea:

The change of impurities is given by

$$\frac{dN(t)}{dt} = \frac{dN_{in}(t)}{dt} - \frac{dN_{out}(t)}{dt} \quad (4.16)$$

Where the total outgassing rate can be assumed to be constant and the total molecules outgassing into the vessel is given by

$$N_{in} = N_0 + \frac{R}{k \cdot T} \cdot t \quad (4.17)$$

with N_0 being the number of molecules still inside the volume after pumping. They are given by the general gas equation

$$N_0 = \frac{p \cdot V_{tot}}{k \cdot T} \quad (4.18)$$

with p the pressure before closing the gate valve. The differential outgassing rate into the vessel is given by

$$\frac{dN_{in}}{dt} = \frac{R}{k \cdot T} \quad (4.19)$$

The change of impurities filtered out depends on the pump speed and the total impurity concentration inside the vessel. It is given by

$$\frac{N_{out}}{dt} = \frac{S}{V_{tot}} \cdot N(t) \quad (4.20)$$

where the efficiency of the filter has been assumed to be 100%, i.e. all impurities passing through it are filtered out.

Combining the two parts leads to the following differential equation:

$$\frac{N}{dt} = \frac{R}{k \cdot T} - \frac{S}{V_{tot}} \cdot N(t) = A - B \cdot N(t) \quad (4.21)$$

and solved to

$$N(t) = \frac{A}{B} + C \cdot e^{-B \cdot t} = \frac{R \cdot V_{tot}}{k \cdot T \cdot S} + C e^{-\frac{S \cdot t}{V_{tot}}} \quad (4.22)$$

The constant C depends on the initial amount of impurities N_0 in the vessel.

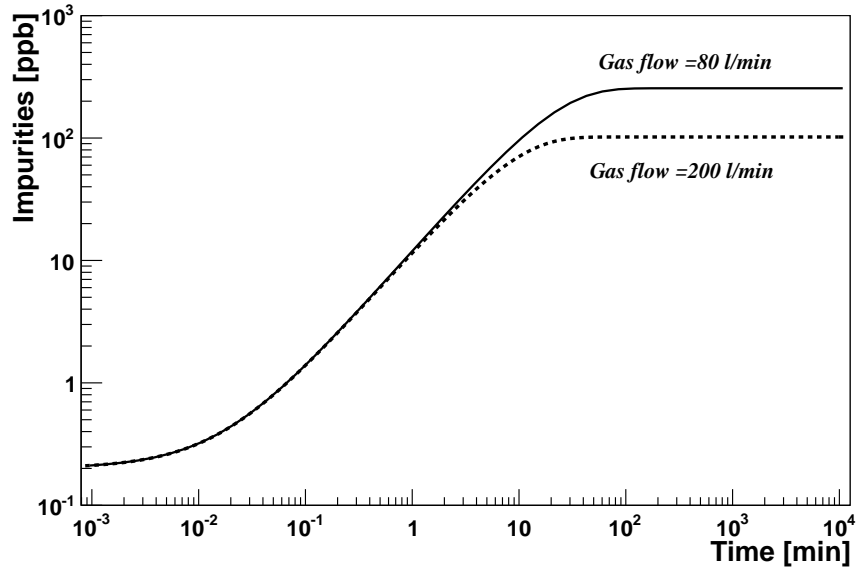


FIG. 99: The contamination of the argon gas at SATP conditions with impurities as a function of the time, from the moment on when the gate valve has been closed and pure argon gas was filled in the system. The curve is calculated according to Eq. ?? for the values discussed in the text for the $40 \times 80 \text{ cm}^2$ LEM TPC in the ArDM dewar.

Taking a total volume $V_{tot} = 1700 \text{ l}$ for the dewar, an outgassing rate of $R = 3.4 \cdot 10^{-4} \text{ mbar l/s}$ and an actual gas flow of $S = 80 \text{ l/min}$ for the gas recirculation, the equilibrium is reached when the rate of impurities, that can be trapped, is equal to the rate of new impurities produced by outgassing, i.e. $N(t \rightarrow \infty)$ in Eq. ??:

$$\begin{aligned}
 N &= \frac{R}{k \cdot T} \cdot \frac{V_{tot}}{S} \\
 &= \frac{3.4 \cdot 10^{-4} \text{ mbar l/s}}{k \cdot 297 \text{ K}} \cdot \frac{1700 \text{ l}}{80 \text{ l/min}} = 1.05 \cdot 10^{19} \text{ particles} \\
 &= \sim 255 \text{ ppb @ SATP}
 \end{aligned} \tag{4.23}$$

Using Eq. ?? the contamination of the argon gas with impurities (in ppb) is plotted as a function of time in ??. For comparison, there is the actual gas flow of the ArDM system of 80 l/min as also an increased gas flow of 200 l/min shown. Analyzing these curves shows that it is most important to reduce the outgassing rate as much as possible. Once stopping to pump pollutes the volume in a few minutes with more than 100 ppb of impurities. Also it can be seen that the maximum contamination with impurities is given by the gas flow through the filter and not the initially reached vacuum.

4.7.8 Liquid argon purification

The initial purity of commercial liquid argon is in the order of ppm of oxygen equivalent impurities. It is not sufficiently clean for the experiment and has to be purified in situ. Different techniques, hereafter discussed, are used to filter out different molecules.

For large setups evacuation is not possible and the majority of the air inside the dewar is removed by flushing the setup with argon gas. A big help is that argon (40 g/mol) is heavier than the other molecules like O₂ (16 g/mol), N₂ (14 g/mol) and H₂O (10 g/mol). Filling up a volume with argon presses out the other gases and after a few exchanges of the whole volume the contamination in a vessel can be reduced to the level of ppm, equivalent to the initial purity of the liquid argon. An example for a large, non evacuatable volume is a dewar of about 6 m³. After ten volume exchanges the oxygen concentration was measured to be ~ 4 ppm [129].

Having reached the initial purity of the liquid argon, the only way of improvement is to actually purify the argon. Depending on the kind of molecule to be removed different filters are used. Also an important role plays the argon state in which the purification takes place, i.e. whether the argon is purified as gas or liquid. In general impurities in the liquid argon are filtered out by binding them to a surface. This can be a cold trap (freezing impurities to a cold surface), physical adsorption (van der Waals force) or chemical adsorption (reaction with other atoms).

4.7.9 Molecular sieve

For filtering out water molecules, in general physical adsorption is used. This can be silica gel, aluminum oxide or a molecular sieve. While the silica gel has the biggest capacity for holding back water, the molecular sieves are the strongest adsorbents. In general the power of adsorption is given at the temperature of the dew-point. For silica gel it is ~ -5 °C and for a molecular sieve up to ~ -100 °C [130]. Assuming a vapor pressure of 1×10^{-4} mbar for water at -100 °C, this gives a ratio of ~ 100 ppb for gaseous argon at room temperature and ~ 0.1 ppb of water for liquid argon. This increase in purity for liquid is due to the 800 times higher density of argon atoms in liquid compared the gas/vapor at room temperature. For the water molecules there is no such increase assumed since the amount is given by the partial pressure of 10^{-4} mbar and independent of the other molecules in the mixture.

Usually a molecular sieve consists of porous aluminosilicates, so called zeolites. They are able to adsorb water and when heated up to release it. For commercial use these kind of crystals are synthetically produced and specially designed to have a uniform and precisely defined pore size. ?? shows the crystalline structure of the two most common types of zeolite. Each “ball” of the structure (in the Zeolite A structure in the eight corners) has a silicon or an aluminum atom in each corner

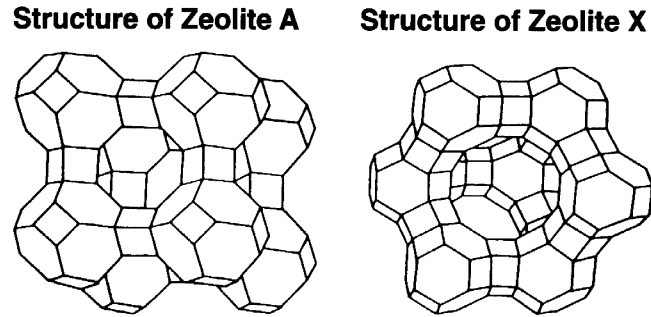


FIG. 100: Molecular structure of the two most common types of zeolites. The pore size in the center depends on the element with which some of the sodium atoms are replaced. It is between $\sim 3 \text{ \AA}$ and $\sim 5 \text{ \AA}$ in diameter for type A and $\sim 10 \text{ \AA}$ for type X.

of the square surfaces, interconnected with oxygen atoms. Because the aluminum atom is trivalent the structure as a whole becomes an anion. To become electrically inert there are sodium, calcium or potassium cations attached to the molecule. Depending on the ratio and the type of these exchangeable cations the properties of the molecule can be influenced.

A crystal with sodium atoms has a pore size of $\sim 4 \text{ \AA}$, while replacing a sodium atom with a potassium atom shrinks the diameter to $\sim 3 \text{ \AA}$. Replacing it with a calcium atom increases the diameter to $\sim 5 \text{ \AA}$. In such a crystal, molecules smaller than the diameter of the pore can enter, larger ones are blocked. Capillary condensation takes place with the molecules entering to a much larger scale than to others since most of the surface of the crystal is inside the structure. So molecules, smaller than a certain size can be attached, while larger ones flow around the crystal. Considering only this property, also the argon atoms should be filtered out and the sieve immediately would saturate. This is not the case since, besides the capillary condensation, there is a second effect. The polarity of the sieve material makes molecules stick to the surface. Because of the crystal structure made out of electrically unbalanced charged parts at fixed positions, the crystal has a polar surface. Therefore, polar molecules like water are attracted and stick to the surface while apolar molecules only are held very weakly. The attachment of argon and nitrogen atoms, can be found in [131]. With this property water can be trapped up to $\sim 28\%$ of the crystal weight and these kind of crystals really act as a “sieve” for filtering out certain molecules. The amount of trapped molecules depends on the temperature of the crystal since at higher temperature molecules are easier detached again. This behavior is also used to regenerate the material. By heating it up to $\sim 250 \text{ }^\circ\text{C}$ and flushing it with dry nitrogen/argon gas the trapped water is released and the zeolite can be used again.

Commercially, there are different molecular sieves available, depending on the diameter of the pore, they are called 3A, 4A or 5A, where “A” stands for Angstrom. Zeolites of type X in general have bigger pores of about 10 \AA .



FIG. 101: Molecular sieve *ZEOCHEM 3A*[®] grains before inserting them in the regeneration cartridge. Each grain has a diameter of about 2 mm.

In ArDM, a molecular sieve is not included in the standard recirculation circuit. Water is removed as much as possible from the detector by evacuating the volume for a long period before filling with argon. The remaining water, if attached to a surface, is sticking to it very strongly due to the low temperatures. If it is dissolved in the liquid argon, it (partly) sticks to the oxygen filter described in ???. Therefore, the only way for water to enter the detector volume is to be already dissolved in the liquid argon, used for filling the detector. For this reason a purification cartridge, partly filled with a 3A molecular sieve is placed before the inlet to the detector. It is filtering out the water from the commercial liquid argon. ??? shows the 3A crystals with a diameter of ~ 2 mm each. In total the cartridge contains 0.7 l of molecular sieve.

4.7.10 Oxygen filters

As mentioned before, the most critical impurity for drifting electrons in liquid argon is oxygen. A constant recirculation and purification of the argon is mandatory to keep the contamination low. Oxygen is entering the detector volume through micro leaks in the detector shell or, more dramatically, through cold leaks, discussed in ???. Also not to be neglected is the outgassing of the detector material. By evacuating the detector, a lot of the residual gases are pumped out but, by lowering the partial pressure of the vessel, impurities might condense or freeze and can no longer be pumped. Breaking the vacuum with pure argon gas and re-pumping it helps to reduce them.

For filtering out oxygen from argon gas or liquid, chemical adsorption is used. More specifically, the argon oxygen mixture is guided over a surface of a reduced material. It oxidizes and only argon is left. The challenge is to find a material with a low reaction potential for an efficient oxidation and a large surface. Elements in question are easy to be oxidized metals. We have successfully developed

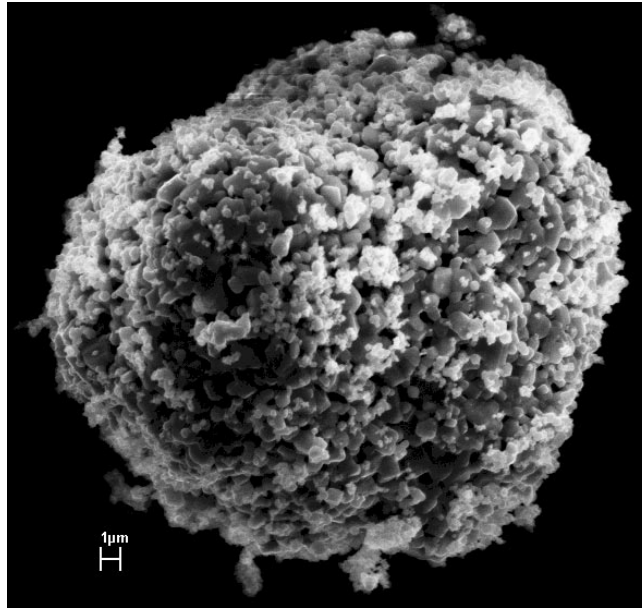


FIG. 102: The copper grains, sintered together from smaller grains, have a diameter of a few $10 \mu\text{m}$. This technique grants a large ratio of surface to volume.

filters containing pure copper powder. Oxidation is an exothermal reaction and takes place according to



The heat of adsorption is ~ 82 kcal/mole on the true oxidation and goes down to ~ 55 kcal/mole for the partly oxidized copper grains [132]. This reaction is a surface process and takes place in a monolayer of the copper. In fact the thickness of the layer is increasing with the temperature. At 87 K it is $\sim 4 \text{ \AA}$ while at 300 K it is $\sim 17 \text{ \AA}$ [133]. Since the temperature is given by the liquid argon, it is important to have a maximum possible surface per volume. It can be reached by the use of sintered copper pellets[170]. Each grain of copper has a diameter of a few $10 \mu\text{m}$. It is not a single junk of copper but sintered together from smaller grains in the nanometer scale. ?? shows an image of such a grain taken with an electron microscope. Because of its exothermal reaction with oxygen, copper is sold already oxidized to copper(II)oxide (CuO), not to be confused with copper(I)oxide (Cu_2O).

Before being used as a filter it has to be regenerated. This happens by another exothermal reaction where the copper(II)oxide is flushed with hydrogen. The oxide is reduced to pure copper and water according to





FIG. 103: Collected water from regeneration of a copper cartridge.

Since the reaction is exothermal, the temperature has to be monitored by measuring the temperature of the exhaust gas from the cartridge in order not to harm the pellets. The temperature is controlled by the amount of hydrogen entering the cartridge. To initiate the reaction, a temperature of $\sim 150\text{ }^{\circ}\text{C}$ of the copper(II)oxide is needed, which is achieved with heating bands wound around the purification cartridge. By the reaction the temperature rises and, as a clear indication of a complete regeneration, the temperature drops back to the value of the heater. Another indication for the cartridge to be regenerated is to see how much water is extracted from the cartridge by cooling the output gas. The water condenses and can be measured as seen in ??.

Hydrogen is a dangerous gas and the concentration must stay below 3% in order not to take the risk of an explosion. For this reason the regeneration does not take place with pure hydrogen but with a mixture of hydrogen and argon. Also at the end, when the copper is regenerated, the cartridge is flushed with pure argon gas, at $\sim 150\text{ }^{\circ}\text{C}$, to clean out all the water vapor trapped in the sintered material. For transporting and storing, the regenerated cartridge is filled with pure argon gas to an overpressure of $\sim 0.5\text{ bar}$.

4.7.11 Design of the ArDM LAr purification system

A schematic view of the cryogenic installation of ArDM is shown in ??. The dewar, hosting the detector can be seen on the right side of the schematic. All cryogenic services, including the purification cartridge and the liquid argon pump are situated on the left of the drawing. On the top left, above

the cartridge the re-condenser unit, with the two cryocoolers, is situated. All these parts are inside two separate vacuum insulations, one around the dewar (*vacuum insulation 1*) and the other for the cryogenic facilities (*vacuum insulation 2*).

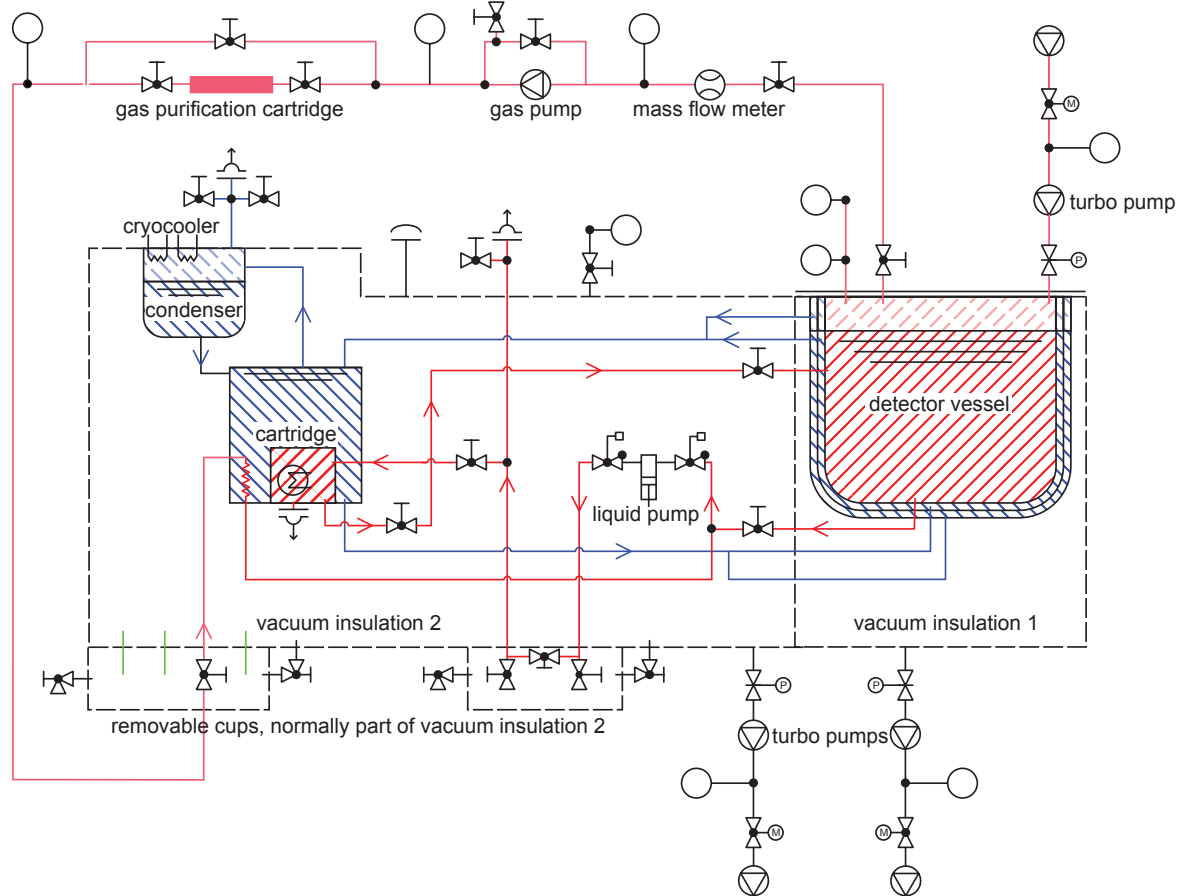


FIG. 104: Schematic view of the cryogenic installation of the ArDM detector. The actual dewar is situated on the right side and all the cryogenic installations containing the re-condensing and the purification of the argon are on the left side.

As indicated by the different colours, there are two independent argon circuits. One containing the highly purified argon used as detector target (red) and a second circuit of argon to cool the primary circuit (blue). The primary argon from the dewar is cleaned from electro negative molecules in a purification cartridge as described in ???. It is pumped by a bellows pump that is completely inside the vacuum insulation.

Besides the liquid purification circuit, also a gas purification system is installed. It is indicated on top in ???. The recirculation of the primary liquid argon circuit is done by extracting the liquid from the bottom of the dewar, pressing it through the filter and then to re-inject it to the detector volume from the top. The recirculation pump, maintaining the constant flow of argon, is situated in the lowest position of the experiment. This gives the maximum *net positive suction head* (NPSH) to press the

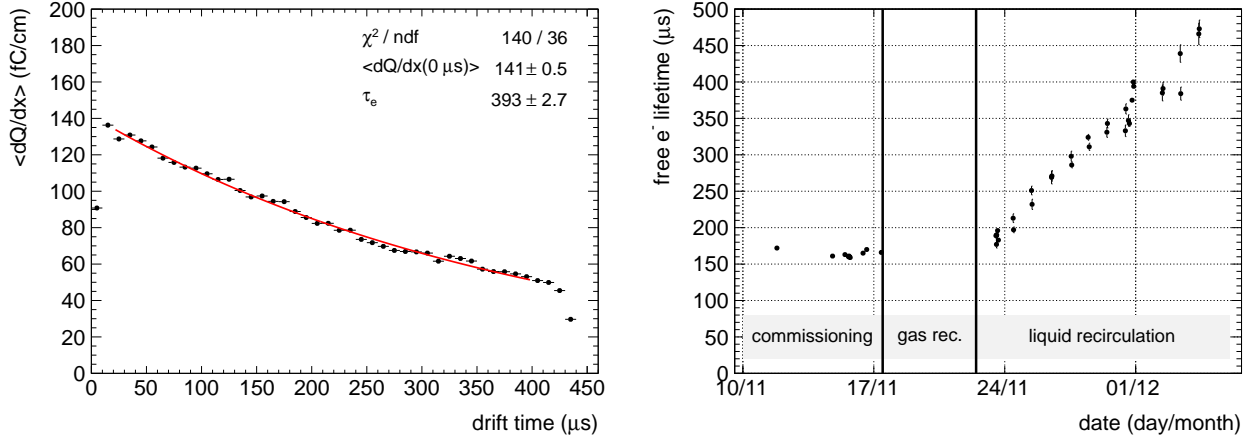


FIG. 105: Left: $\langle dQ/dx \rangle$ as a function of the drift time superimposed with an exponential function with the decay time constant $\tau_e = 393 \pm 3 \mu\text{s}$ fitted to the data points. Right: evolution of the free electron lifetime during the run period.

liquid through the check valve into the pump body. Shortly before the pump, there is a T-connection for the entry of the re-condensed gas, in case the gas recirculation system is used.

Between pump and filter, the liquid argon has to pass through a valve, indicated in the lower middle part of ???. This configuration of valves is normally inside the *vacuum insulation 2* and the central bypass valve is open to let the liquid argon flow from the pump to the purification cartridge. The other two valves are for filling, and for emptying, the dewar. In case of their use, the volume around the valves is separated from the *vacuum insulation 2* and the vacuum is broken. For filling the dewar, the bypass valve from the pump is closed and argon is fed in the system. It first is pressed through the filter to be pure when entering the detector volume. When the dewar is full, the input is closed and the bypass opened again. For emptying the system, the bypass is closed and the other valve is opened. The argon from the dewar now flows through the pump (check valves open automatically by the pressure difference between the dewar and the atmosphere) and leaves the detector. By using the pump, the emptying process can be speeded up. The purification cartridge for the liquid argon is, as indicated in ??, immersed in a bath of liquid argon for keeping it cold and to re-condense possible argon vapor.

4.7.12 Liquid argon purification in the $40 \times 80 \text{ cm}^2$ operation at CERN

As described in the previous section, the cryogenic system of the $40 \times 80 \text{ cm}^2$ [23] developed for ArDM, was equipped with two separate purification systems. During the run period both systems were operated, thus it was important to monitor the liquid argon purity. In order to measure the charge attenuation as a function of the drift time, we have used the reconstructed cosmic muon tracks. The data points in Figure 105 show the mean dQ/dx values of all reconstructed muons for different drift

times. It can be seen that the exponential function e^{-t_{drift}/τ_e} with the free electron lifetime τ_e perfectly fits the obtained distribution. The maximum electron drift time is about $430 \mu\text{s}$. The plot on the right side shows the lifetime evolution during the last three weeks of operation. Starting from a lifetime of about $170 \mu\text{s}$ we first did initial tests with the liquid recirculation. During this commissioning period the free electron lifetime remained constant. In a second phase, the gas recirculation was turned on. Due to changes in pressure and liquid argon level we did not acquire data with the double phase readout. However, after stopping the gas recirculation, the measured free electron lifetime was not significantly improved although was maintained at constant value. During the last phase we have operated the liquid argon recirculation system at a flow rate of about 5 to 7 lt LAr/h. Since we saw a steady increase of the free electron lifetime until we stopped the run, we conclude that the liquid argon recirculation system was efficiently working. When we stopped the run a lifetime of $470 \mu\text{s}$ was measured, but still growing linearly with time. This corresponds to an oxygen equivalent impurity concentration of about 0.64 ppb.

4.7.13 Concept for the gas and liquid purification of the $6 \times 6 \times 6 \text{ m}^3$ prototype

The liquid argon process and the performance of its sub-units are a critical item for the successful operation of the $6 \times 6 \times 6 \text{ m}^3$ prototype. The basic parameters are summarised in ???. The design is based on the extensive experience developed during several years of tests and R&D. As purity requirements are so stringent welded connections or ISO CF flanges with metal seals will be used. The system will be scaled to reach the required purification volume given the size of the $6 \times 6 \times 6 \text{ m}^3$ vessel. The

TABLE IX: Overview of the parameters for the liquid argon process

General properties	
Total inner-vessel volume	600 m^3
Membrane surface in inner-vessel	430 m^2
Liquid level above floor	7 m
Amount of liquid	$\approx 530 \text{ m}^3$
Amount of gas	$\approx 70 \text{ m}^3$
Instrumented volume	$6 \times 6 \times 6 \text{ m}^3 = 216 \text{ m}^3$
Gas purification	
With 2 pumps of 500 l/min each	$\approx 10 \text{ hr/vol. for warm gas (300 K)}$ $\approx 30 \text{ hr/vol. for cold gas (100 K)}$
Boil-off	
Heat input (vessel)	2150 W (5 W/m^2)
Evaporation rate	$450 \text{ l}_{\text{gas}}/\text{min}$
Liquid purification	
Purification speed for $\tau = 1 \text{ day}$	$22 \text{ m}^3/\text{hr} \approx 400 \text{ l/min}$

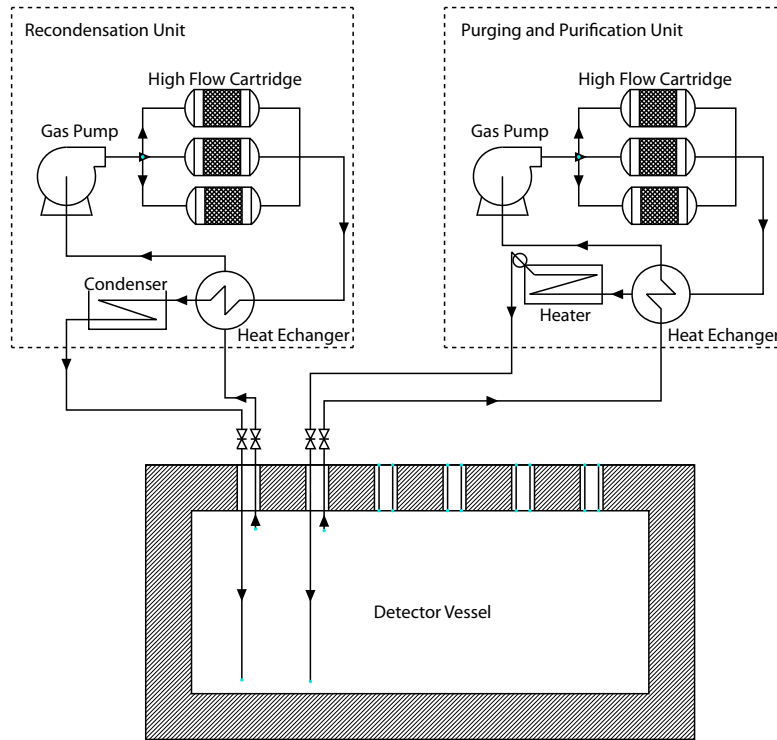


FIG. 106: Schematic diagram for the gas recirculation system.

inner-vessel volume which contains all equipment and the argon is about 600 m^3 . It must be a totally sealed volume with no leaks towards the outside in order to avoid the penetration of any contaminant or the loss of pure argon.

The refrigeration component will be provided by external cryocooler with separate loops, thermally joined with heat exchangers.

During construction and assembly phase, the inner-vessel volume will be maintained in a controlled air environment. Starting from that state, the volume will be first replaced with argon. In [86] we have experimentally demonstrated on a volume of 6 m^3 that the replacement of air with argon gas down to ppm impurities concentration is achievable through flushing.

A fully-submersed centrifugal cryogenic pump (e.g. AC-32 from ACD Cryogenic Industries[171]) will be operated in order to create the liquid argon flow through the purification cartridges. The pump has been chosen at FNAL for the LAPD and 35 ton membrane test [134]. Our pumps will be hanging inside a dedicated chimney and will hang from the top, hence will be lower from the top before usage, or lifted to the top in case of removal when maintenance is required. The pump and the motor are fully flooded with liquid, minimizing start-up and downtime and guaranteeing quick, responsive pumping. The multi-frequency motor provides an efficient and broad range of operation and power, ranging from 15 to 1514 lpm. The pump head is above requirement, and causes no problem. The electrical motor and bearing life is extended being cooled by the cryogen it is pumping, the heat input is minimal and

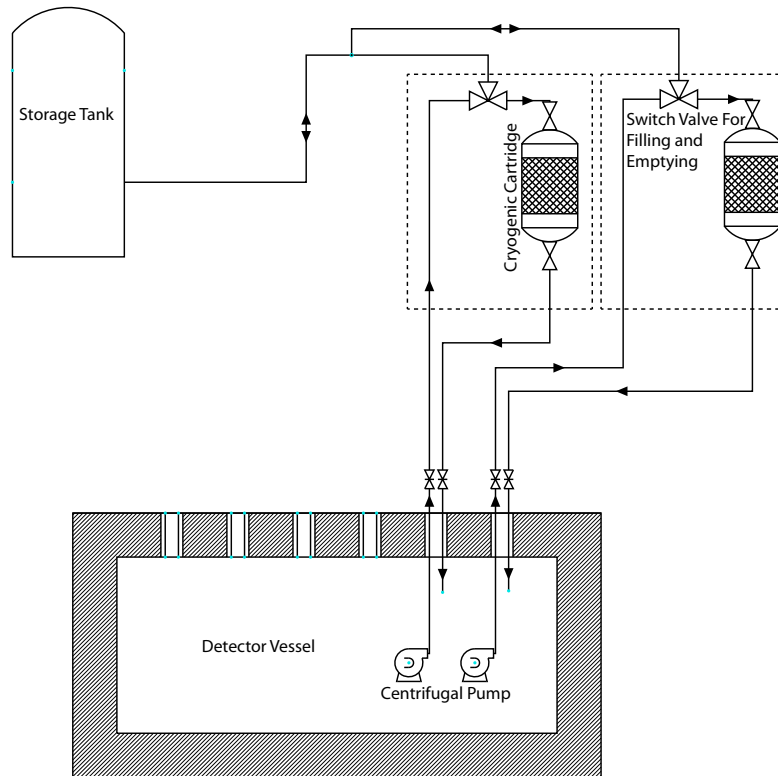


FIG. 107: Schematic diagram for the liquid phase purification system.

carried off by discharging liquid. The power is in the range 2-14 kW.

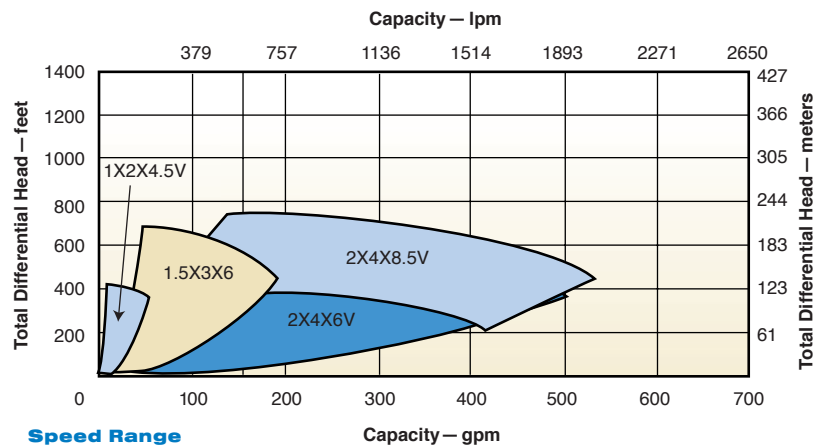


FIG. 108: Specifications of the seless cryogenic pump from ACD Cryogenic industries.

4.8 Process control and monitoring

The main function of the process control and monitoring system is the monitoring of the condition of the prototype and the regulation of the cryogenics and high voltage systems in order to allow a safe operation of the detector. In addition, the control system is a safety monitor that alerts people in case

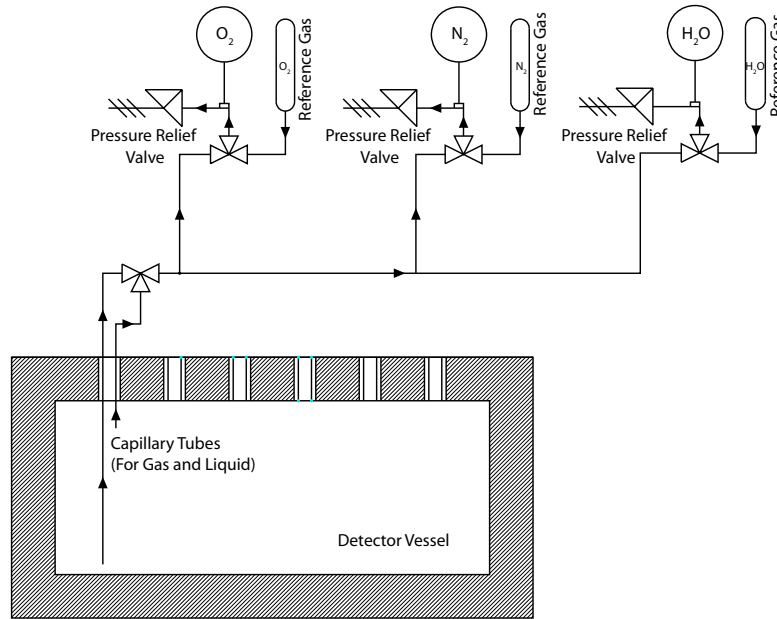


FIG. 109: Schematic diagram for the liquid and gas phase impurity analyser systems.

of an imminent danger, such as oxygen deficiency or fire. The control system allows for process control and is based on a programmable logic controller (PLC). A PLC is a computer specially designed for process automation with a large number of inputs and outputs for sensors and actuators. PLCs possess a high reliability due to specialised hard- and software and therefore the control system serves as a safety system.

The control system developed for the ArDM (RE18) experiment built in Collaboration with the CERN/PH-DT group, is shown in ???. The control system for ArDM is located in seven standard 19 racks next to the detector together with the high voltage supply for the PMTs (HV rack in ??) and the data acquisition system (DAQ rack in ??). The PLC modules are installed in the PLC1 and PLC2 racks. The processor module and the analog input and output modules are in the PLC1 rack, the digital input and output modules are in the PLC2 rack. The INT1 and INT2 racks contain the interfaces for the sensors and actuators and displays for pressure and vacuum sensors whereas the COM rack contains the supervisory computer and its accessories. For safety reasons every rack contains its own power distribution unit that provides the power for the entire rack and allows to cut the power of the complete rack with one single circuit breaker. The main power line of ArDM (three-phase, 400 V, 80 A per phase) arrives to the power distribution unit in the INT1 rack. From there all the power distribution units in the other racks, with the exception of the PLC1 and PLC2 racks, are supplied with single-phase current (230 V, 20 A). The PLC1 and PLC2 racks are supplied with 24 VDC which are delivered by a rectifier in the COM rack. Also all the sensors and actuators installed in the ArDM experiment are powered from the racks of the control system. To protect the control system from short



FIG. 110: The seven standard 19 racks containing the ArDM (CERN RE18) control system (COM, PLC1, PLC2, INT1 and INT2 rack), the high voltage supply of the PMTs (HV rack) and the data acquisition system (DAQ rack). The system was built in Collaboration with the CERN/PH-DT group.

power cuts, all the equipment, with exception of the devices supplied by the INT1 rack, are connected to two UPSs (uninterruptible power supplies), UPS 12 and UPS 23 , with a total power of 6300 W. The two UPSs can cover the power consumption of the connected equipment for about 15 min. In case of a power cut, the UPS 1 supplies the equipment in the INT2, the DAQ and the HV rack, the UPS 2 supplies the COM rack and thus also the PLC1 and PLC2 racks. The control software is based on PVSS (Prozessvisualisierungs- und Steuerungssystem, process visualisation and control system) used by CERN.

Although larger in scale, we expect that the process control and monitoring system for the $6 \times 6 \times 6 \text{m}^3$ prototype will be functionally very similar to the one developed and successfully operated for ArDM. We therefore expect that it will be rather straight-forward to develop and implement a new dedicated process control and monitoring system.

5 DLAr offline requirements and software

5.1 Overview

LAr TPCs record the complete electronic image of an ionizing event. Due to the optimal electron transport properties of the LAr medium (high electron mobility and small diffusion), large volumes can be instrumented with a spacial resolution down to the millimeter-scale. Ionization electrons drift over the distance $z = v \cdot t_{drift}$ towards the charge readout passing from liquid to gas phase, where they induce signals on different sets of readout electrodes, hereafter referred to as *views*. The readout views provide at each sampling time two or more projections of the (x, y) image of the event. In addition to the event topology, the amplitude of the recorded signals give a direct measure of the produced ionization charge along each track, providing calorimetry and particle specific local energy loss information.

Track reconstruction aims at the extraction of the relevant information, such as the types and the momenta of the detected particles. In the simplest case, where particles stop inside the detector, the stopping power along the produced track allows to identify the particle [89, 135]. In case the particle does not stop inside the fiducial volume, an estimation of the momentum can be obtained by measuring the multiple scattering of the traversing particle [136]. Besides the reconstruction of tracks, it is possible to reconstruct showers: in this case, it is not needed to reconstruct each single hit in three dimensions. A strategy is to reconstruct global event parameters like the total charge, the shower direction, the charge profile and the vertex as well as the initial part of the shower. This latter is used to discriminate e^-/e^+ from γ/π^0 showers [137].

5.2 The Qscan software

Qscan is a multipurpose software framework to simulate, reconstruct and visualize events from LAr TPC detectors. It was originally created and developed by the ETHZ group for the ICARUS experiment and was then adapted to other detectors. It was employed for all analyses the ICARUS data collected in Pavia [16–18, 138] as well as to reconstruct quasi-elastic neutrino events in the 50 L ICARUS TPC that was exposed to the CERN West Area Neutrino Facility WANF [135, 139]. Qscan allows to simulate, reconstruct and visualize events for various detectors. It is able to read raw-data of all our hardware setups developed since 1997. Due to the development of several new double phase LAr TPC prototypes, including the 3 L [25], the 120 L at J-PARC and the 200 L detector at CERN [23, 24], a set of new algorithms and a new ROOT[172] [140] based graphical user interface have been implemented.

The Qscan software framework comes along with three main functionalities:

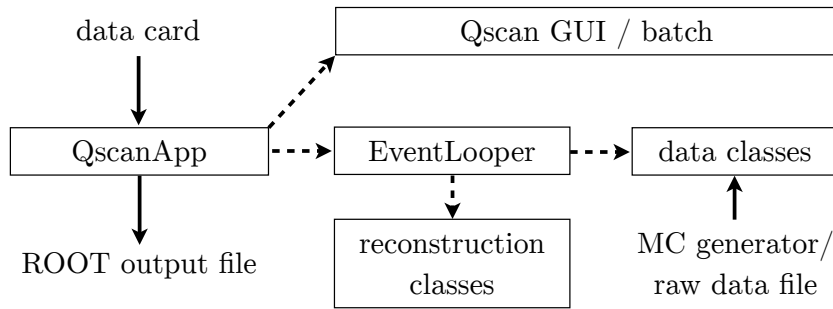


FIG. 111: Basic organisation of the Qscan software: boxes without frame are calibration, in and output files, while framed boxes name different classes.

- It provides a set of tools to decode, store and reconstruct data from all our hardware setups.
- Being interfaced to VMC (and currently GEANT3 and GEANT4) to propagate particles through any detector geometry, it allows to produce fully digitized MC events that can be post-processed similar to real data from a detector.
- A batch-mode
- An interactive mode with graphical user interface that allows to scan raw data online or offline. Moreover, Qscan has a 3D event display to visualize MC truth events as well as the reconstructed event for both real and MC generated data inside the detector geometry.

In order to have a well structured software package that allows to add new detectors with minimal efforts, Qscan is written in the object oriented C++ language. As shown in the diagram in ??, the main program *QscanApp* can either run in batch mode in order to process a large amount of data, or it initiates the graphical user interface of Qscan. Depending on which detector and which kind of reconstruction is asked by the user in the so called *data cards* file, the proper data class with the detector geometry is initialized as well as the reconstruction menu. After the initialization, the *EventLooper* goes from event to event, either reading an external data file or generating artificial events via MC simulation. Once all the signal waveforms are stored in the data class, the event is processed by the reconstruction algorithms. The resulting reconstructed objects are finally written into a file with the common ROOT format that can later be used for a further analysis. More details on the software layout are presented in [141].

5.3 Event simulation

To optimally utilise the fact that LAr TPCs ideally provide a high resolution image of any ionizing event, MC simulations are an important tool to validate reconstruction algorithms and to study the

detector performance. Moreover, a working MC simulation of a detector allows to study different effects like non-uniform drift fields, different noise levels, impurities, *etc.* This is in particular important for physics performance studies of giant LAr detectors for future long baseline neutrino oscillation experiments [1]. All the MC simulation code and in particular the digitization procedures that are presented hereafter, have been validated with both testbeam and cosmic ray data, as reported in [141].

5.3.1 Particle propagation in detector geometries

Qscan uses the Virtual Monte Carlo package VMC[173] (see [142] and references therein) to interface with GEANT4[174], a toolkit for the passage of particles through matter [143]. Since the VMC interface loads the MC libraries at runtime, Qscan is completely independent from the MC simulation code, allowing for instance to use GEANT3 instead of GEANT4. The second advantage is that the ROOT geometry package *TGeo* can be used to define the geometry of the experimental setup. This feature is important since the same geometry definition can be used to track particles in GEANT3 and GEANT4. Moreover, TGeo is also the preferred geometry format to display the detector together with its reconstructed event objects in the three dimensional, ROOT based, event display. An example of a MC simulated muon event in the 200 L detector [23, 24] is displayed in ???. (1) shows the overview of the geometry, consisting of the cylindrical cryostat and the cuboidal detector. The isolated TPC volume with the MC truth tracks are shown in (2) and (3) shows a closeup of the μ^- track in blue with some δ -ray electrons in green.

GEANT4 provides a large set of different physics processes. Depending on the required level of details and physics models, it is possible to enable or disable different electromagnetic and hadronic processes via physics lists. Typically we are using the QGSP_BERT physics list that uses the Quark Gluon String model for simulating high energy hadronic interactions. To provide accuracy at energies below 10 GeV, the list is extended with the Bertini cascade model [144]. Concerning the tracking configuration, depending on the readout pitch of the simulated detector, one usually has to define an upper limit for the stepping size in order not to see any discrete effects. Typically the maximum step length is fixed to about 10% of the readout pitch. Unlike in the case of typical GEANT4 simulations, particle propagation cut-offs are defined as kinetic energies, rather than ranges. In order to properly implement charge quenching effects, one wants to track secondary electrons, being produced along ionizing tracks, down to very low energies. As discussed elsewhere [18, 145], an electron tracking cut-off of 10 keV is a good compromise between microscopic accuracy and computing speed.

A first version of the $6 \times 6 \times 6$ m³ detector geometry has been implemented in Qscan. The geometry is described with the ROOT *TGeo* package and the particle tracking through the detector can be performed with either Geant4 or Geant3 using the Virtual Monte Carlo interface, as discussed above.

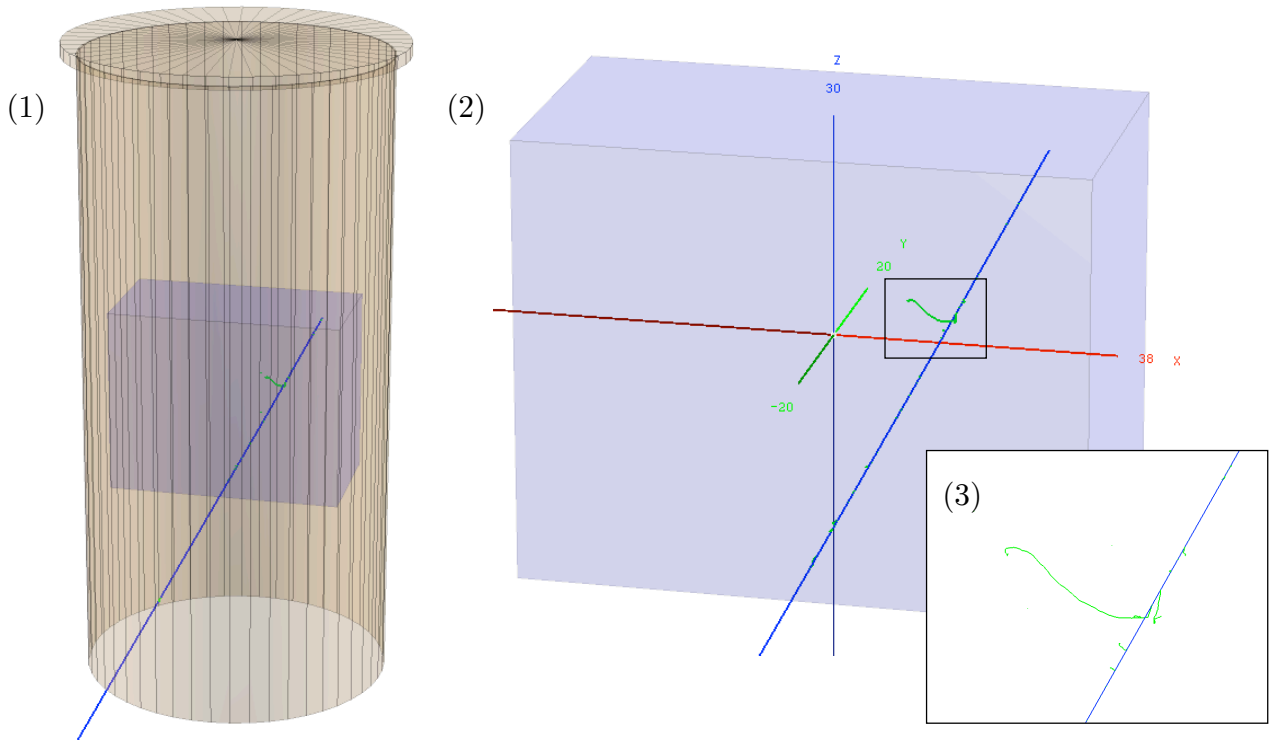


FIG. 112: Three dimensional event display of Qscan, showing the ROOT geometry of the 200 L detector and μ^- , tracked through the geometry by GEANT4. The figure shows an overview of the geometry (1), the extracted fiducial volume together with its local coordinate system (2) and a closeup of the μ^- track with several δ -electrons (3).

The materials and their densities used in the simulation are listed in Table X. Figure 113 shows a simulated event of a 5 GeV/c π^+ shot through (a preliminary version of) the beam pipe and initiating a shower in the LAr fiducial volume. Most parts of the detectors can be seen in the figure: the fiducial (cyan) and LAr (blue) volumes, the corrugated membrane (too thin to be visible), the insulating polyurethane foam (dark gray) the concrete outer vessel (light gray) and the preliminary beam pipe (green). The latter consists of a horizontal vacuum cylinder placed at 1.5 m from the top of the liquid argon level. The beam axis is oriented at 45 degrees with respect to the readout strips of both views.

Detector component	Material	Density[g/cm ³]
tracking medium	liquid argon	1.396
membrane	stainless steel	8.030
thermal insulator	polyurethane foam	0.100
outer vessel	concrete	2.500

TABLE X: Materials and densities for the simulated $6 \times 6 \times 6$ m³ detector.

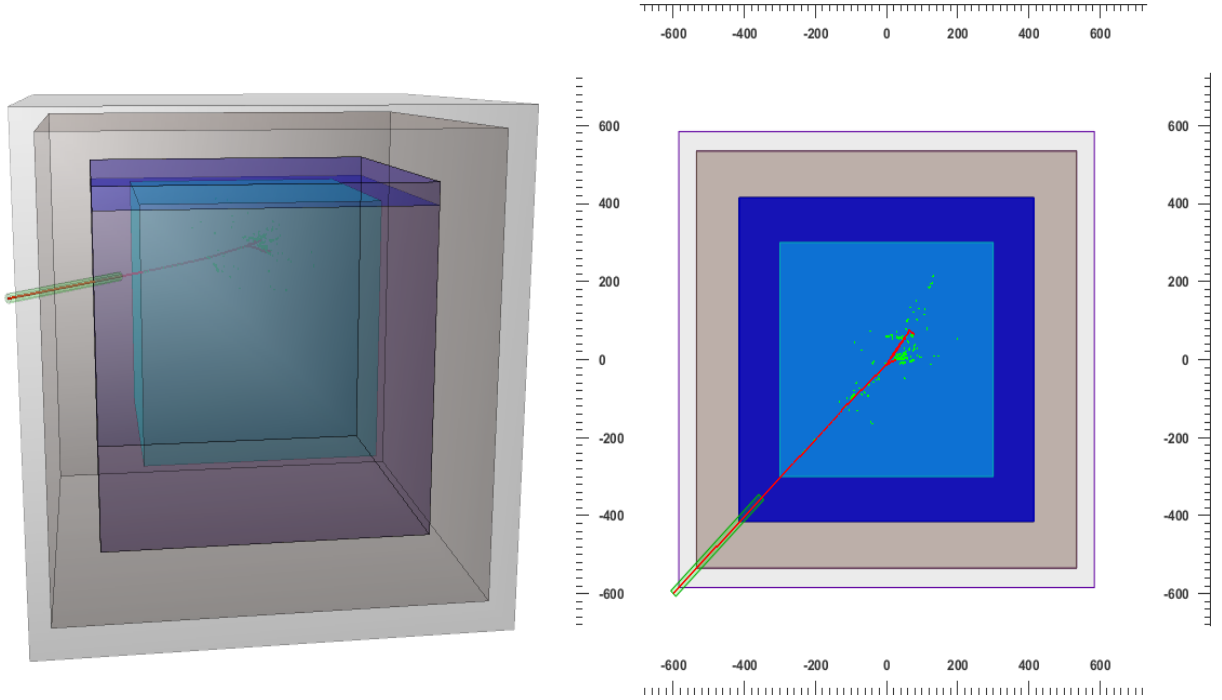


FIG. 113: Simulation of a $5 \text{ GeV}/c \pi^+$ event in the $6 \times 6 \times 6 \text{ m}^3$ detector. 3 dimensional view (left) and top projection of the detector (right).

5.3.2 Waveform generation

The goal of the waveform generation is to convert the MC truth information to LAr TPC data, as it would be recorded in a real experiment. Based on the energy deposit ΔE_{dep} and the length Δx , given at each step of every tracked particle in the MC simulation, the readout signals are produced as explained in the following:

1. The deposited energy ΔE_{dep} is converted into the amount of produced ionization charge $\Delta Q_0 = e(\Delta E_{dep}/W_{ion})$ with the elementary charge e and the ionisation energy of $W_{ion} = 23.6 \text{ eV}$, as given in ???. Due to electron ion recombination, which depends on the ionization density as well as on the applied electric field, a fraction of the produced electrons recombine. Since Birks' approximation gives the best fit to the reconstructed data [18], it is reasonable to implement quenching at MC level by multiplying the charge with $\mathcal{R}_{Birks}(\Delta E_{dep}, \Delta E_{dep}/\Delta x)$. The two parameters of the model $A_{MC} = 0.8$ and $k_{MC} = 0.05 \text{ (kV/cm)} \left(\frac{\text{MeV}}{\text{g/cm}^2} \right)$ provide good agreement with the data.
2. The remaining charge is then transported up to the collection plane. After choosing the coordinate system such that the anode plane is parallel to the (x, y) plane, the charge, being initially produced at (x, y, z) , is drifted along the electric field lines until it leaves the fiducial volume or it reaches the readout plane. In case of a constant field $(0, 0, \mathcal{E})$, the final charge position equals

($x' = x, y' = y, z' = z_{anode}$) and the corresponding drift time is $t_{drift} = (z_{anode} - z)/v_{drift}(\mathcal{E})$. Otherwise, in case of an inhomogeneous electric field, an external look-up table, providing the final coordinate as well as the drift time for any point within the fiducial volume, is used. After including also charge attenuation effects due to an imposed finite free electron lifetime τ_{MC} , the charge is given by

$$\Delta Q = \frac{\Delta E_{dep}}{W_{ion}} \cdot e \cdot \frac{A_{MC}}{1 + k_{MC}/\mathcal{E} \cdot \Delta E_{dep}/\Delta x} \cdot e^{-t_{drift}/\tau_{MC}}. \quad (5.1)$$

Longitudinal diffusion effects are included by convoluting the charge with a Gaussian of width given by Eq. ??.

3. Depending on the arrival position ($x', y', z' = z_{anode}$) of the drift charge ΔQ , currents are induced on the corresponding readout electrodes of the different views. These currents are then further processed by a charge sensitive preamplifier. The finally recorded signal $V_{out}(t)$ is a convolution of the induced current $I(t)$ and the response of the preamplifier $h(t)$:

$$V_{out}(t) = I * h(t) = \int_{t_0}^t I(t') \cdot h(t - t') dt'. \quad (5.2)$$

Obviously both the preamplifier response and the induced currents depend on the readout type and the used electronics. The simplest case is the LEM readout with a 2D anode: due to the fast electron drift in gas and the short induction gap between LEM and 2D anode, the induced current $I(t)$ approaches a δ -function and the signal is directly given by the fast response of the preamplifier.

After finishing this procedure for each step, noise of a given amplitude can be added on top of the signal waveforms. Besides the generation of white noise, it is also possible to use a specific frequency spectrum that has e.g. been taken from real data. The final step is the digitization of the generated waveforms. ?? shows on top the generated waveforms of the MC μ^- from ?? and on the bottom the corresponding event display.

5.4 Event Reconstruction

After recording data from the detector, the data is processed by several reconstruction algorithms. Starting from the local, channel-by-channel signal discrimination, the final goal is to reconstruct physical objects like tracks, showers and event vertices. As there can be large differences among detectors and event types, Qscan provides various methods to reconstruct events. The reconstruction basically

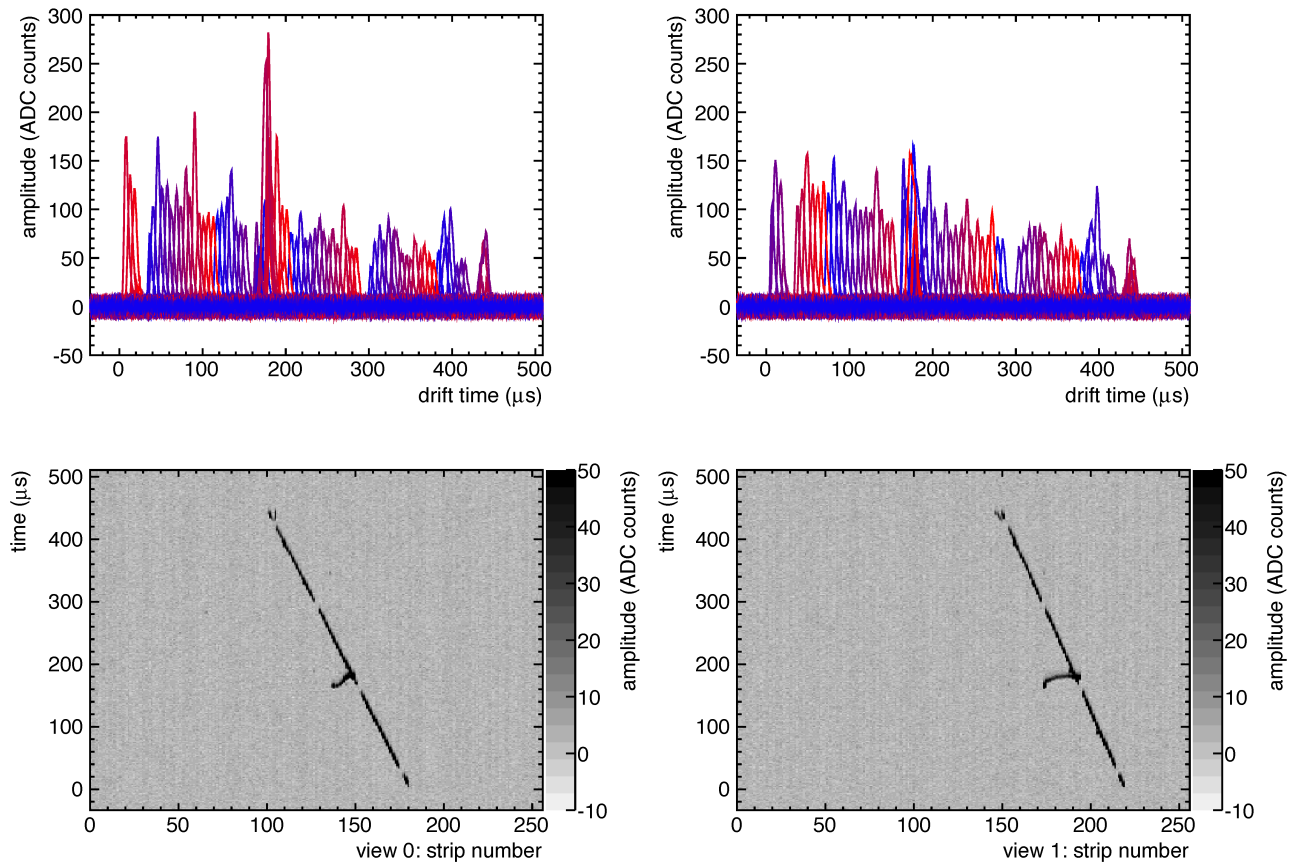


FIG. 114: Example of a fully MC generated μ^- event in the 200 L detector. The MC steps of the same event are shown in ???. The waveforms for the two views (left and right) have been generated, using the known ETHZ preamplifier response, and Gaussian noise with an RMS value of 3 ADC counts. Top: waveforms $V_{out}(t)$ of all the readout channels are shown with different colors. Bottom: typical event display, showing the drift time vs strip number. The greyscale is proportional to the amplitude.

goes through the following steps:

1. The raw waveforms are processed: this involves noise reduction as well as the subtraction of the baseline (see ??).
2. Hits, defined as signals that are discriminated from the noise, are identified and reconstructed (see ??).
3. Clusters are formed by grouping close hits together (see ??).
4. Tracks are identified for each view (see ??).
5. Finally, the three dimensional track reconstruction is done by matching coincident tracks from different views (see ??).

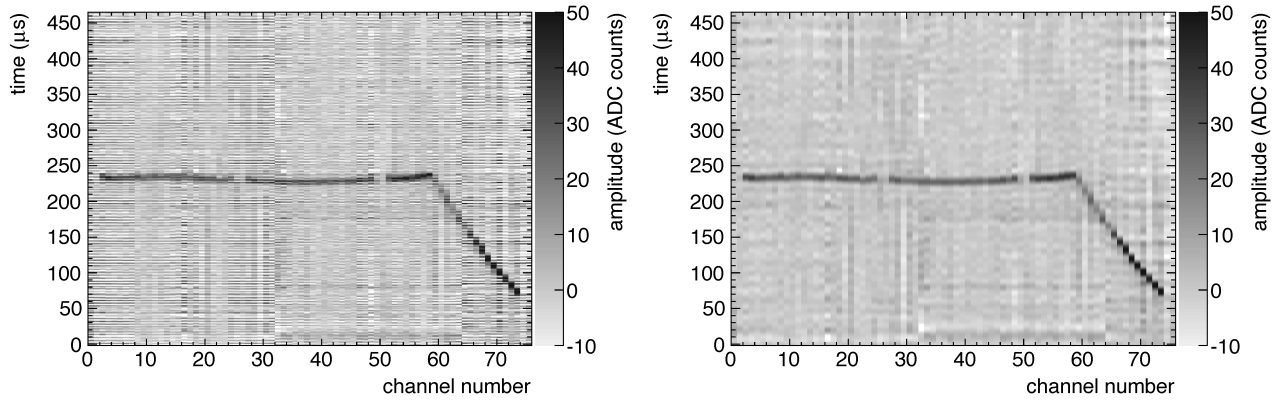


FIG. 115: Raw (left) and FFT filtered (right) stopping K^+ event from the 120 L single phase LAr TPC in a beam test at J-PARC ([145]). The noise pattern, shown on the raw event on the left, is removed by the low pass filtering with a smoothed cut-off at the frequency of 80 kHz.

5.4.1 Signal processing

The data acquisition system records the amplified, shaped and digitized output voltage $V_{out}(t)$ for each electrode with a discrete time sampling. In order to extract physical signals efficiently and accurately, a minimal signal to noise ratio of about 10 is required. Although the electronics is in principle designed to fulfill this requirement, experimental data can be distorted by external noise sources and an imperfect shielding of the detector and the signal lines. In order to suppress noise without affecting the signal component too much, hence improving the signal to noise ratio, two different algorithms are used: the *Fast Fourier Transform (FFT) filter*, and the *coherent noise subtraction* algorithm.

The *FFT filter* makes use of the fact that induced noise, being produced by external sources like switching power supplies, computers, *etc*, is often dominated by a few specific frequencies. After transforming the waveforms $V_{out}(t)$ to the frequency space, the Fourier transformed waveforms $\hat{V}_{out}(\omega)$ are processed in order to reduce the noise components. The final, noise suppressed waveforms $V_{out, filt}(t)$ are then obtained by applying an inverse FFT to $\hat{V}_{out, filt}(\omega)$. Due to the fact that the waveforms are discrete and the total number of samples is an integer power of two, the computing time is minimized by using the FFT implementation from [146].

A concrete example of the FFT algorithm is presented in ???: the K^+ beam event, recorded with the 120 L single phase LAr TPC in the beam test at J-PARC [145], demonstrates the effect of the filter. The high frequency noise, seen in the raw event on the left of ??, is efficiently removed in the filtered event on the right. In this case the best way to improve the signal to noise ratio was to suppress frequencies above 80 kHz. The left plot of ?? shows the amplitude for each channel and frequency. In this plot it can be seen that a continuous background is superimposed with discrete frequency lines.

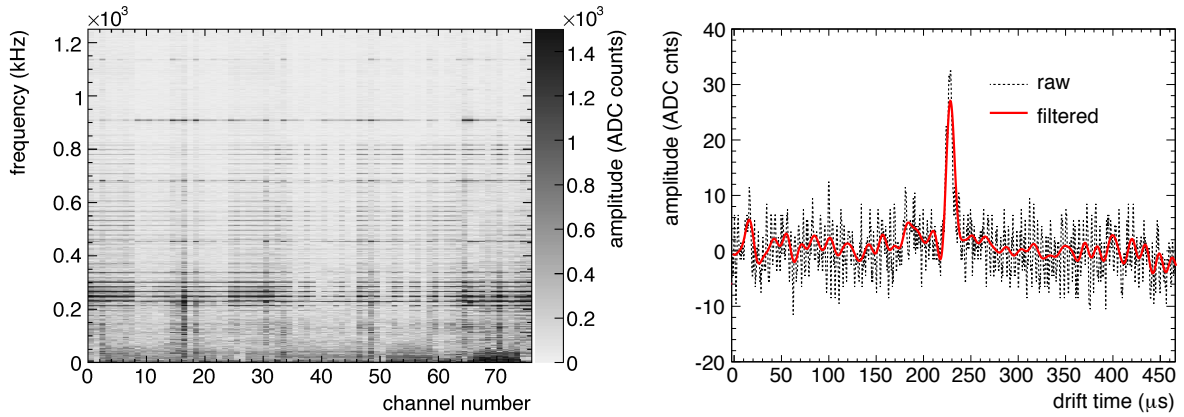


FIG. 116: Left: power spectrum of the raw event from ???. The two dimensional histogram shows the amplitude for each readout channel and frequency bin. Common noise frequency on all the channels are visible well above the 80 kHz cut-off. Right: single readout channel raw (dashed black line) and the filtered waveform (solid red line).

While the continuous component is due to the signals and the intrinsic preamplifier noise, the sharp lines correspond to discrete noise frequencies that are induced by external sources. Due to the fact that most of the noise frequencies are above 100 kHz, a smooth cut-off, implemented with a Fermi potential of width 3 kHz, efficiently suppresses the noise, while keeping the signals, besides a reduction of the bandwidth, unaffected. Unlike a smooth cut-off, a sharp cut in the frequency spectrum introduces artefacts in the time domain. ??? shows the effect on a single waveform before (dashed black line) and after filtering (solid red line).

The *coherent noise filter* is implemented to remove identical noise patterns that are seen on larger sets of readout channels. Unlike in the case of the FFT filter, which directly suppresses the frequencies of single channels and thus reducing the signal bandwidth, the coherent noise filter ideally subtracts only the noise while keeping the signals unchanged. During the operation of detectors it is often observed that all the readout channels, being hosted on the same readout board, have exactly the same noise in terms of frequency, phase and amplitude. An example of such an event, recorded with the 200 L double phase LAr LEM-TPC [23, 24], is given in ???. Since the noise of every channel that belongs to the same acquisition board is almost identical, it can be considered as disturbance of the baseline. This time-dependent baseline first has to be computed for each single time sample, including all the channels on a physical readout board. Finally, similar to the subtraction of a constant pedestal, the baseline is subtracted from each sample. The difficulty of the calculation of the time-varying baseline is to select only the channels without a signal. Since signals are amplitude fluctuations with respect to the baseline, a good way to compute the baseline value for a given time sample is to use only the N channels with the smallest voltage values. Depending on the needs, N can be chosen between

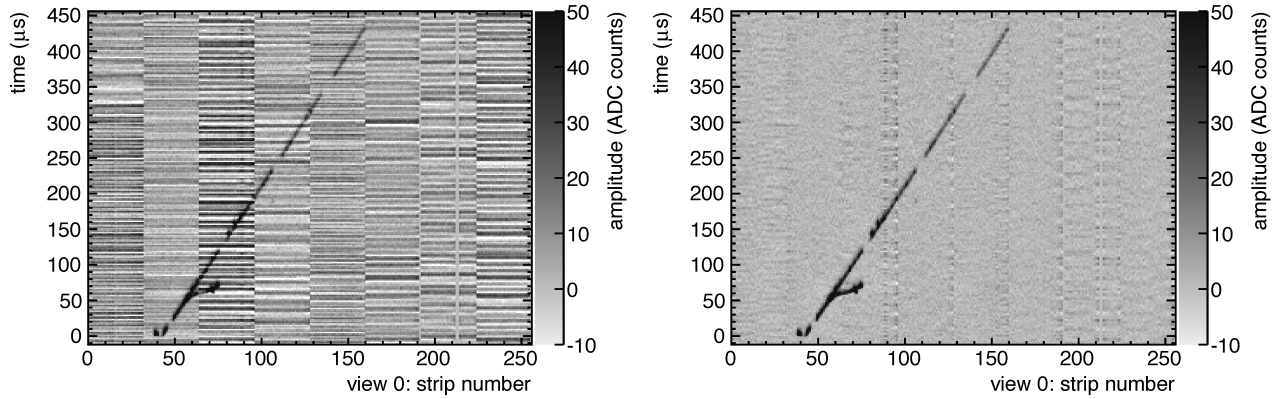


FIG. 117: Cosmic ray event from the $40 \times 80 \text{ cm}^2$ LAr LEM-TPC. Left: raw event that shows a characteristic coherent noise pattern. Right: final event, after applying the coherent noise filter.

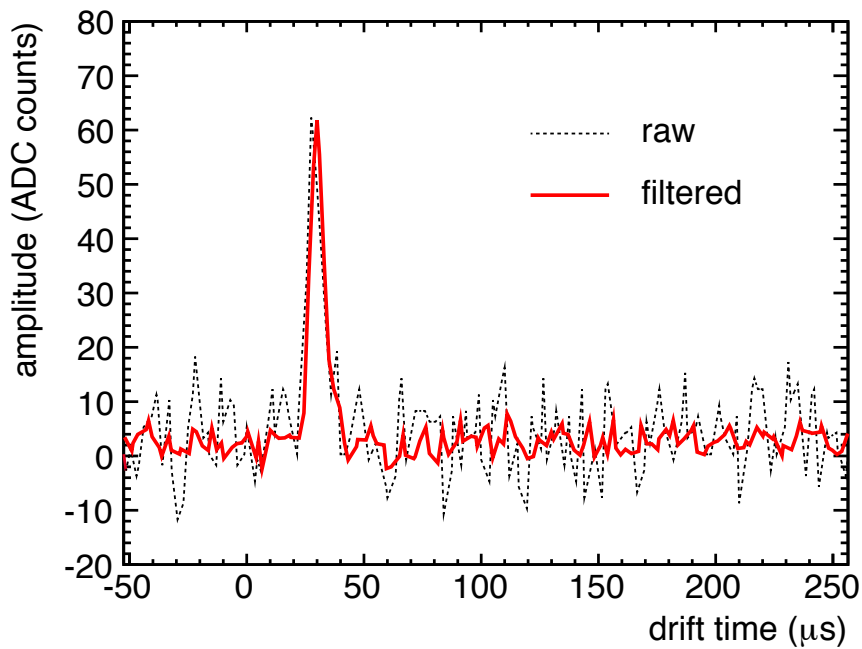


FIG. 118: Single waveform, extracted from the event shown in ???. Both the raw (dashed black line) and coherent noise filtered (solid red line) waveform are shown.

1 and 32: in the case of $N = 1$, the baseline is defined at each time sample t by the minimum Voltage $V_{out}(t)$ of all the 32 readout channels per acquisition board. On the other hand, in the case of $N = 32$, signals are discarded and all the channels are used to calculate the baseline. The choice $N \approx 16$ allows that signals are not affected, even in case they are present in half of the readout channels. ??? shows a single readout channel, taken from the same event that is presented in ???. The noise fluctuations

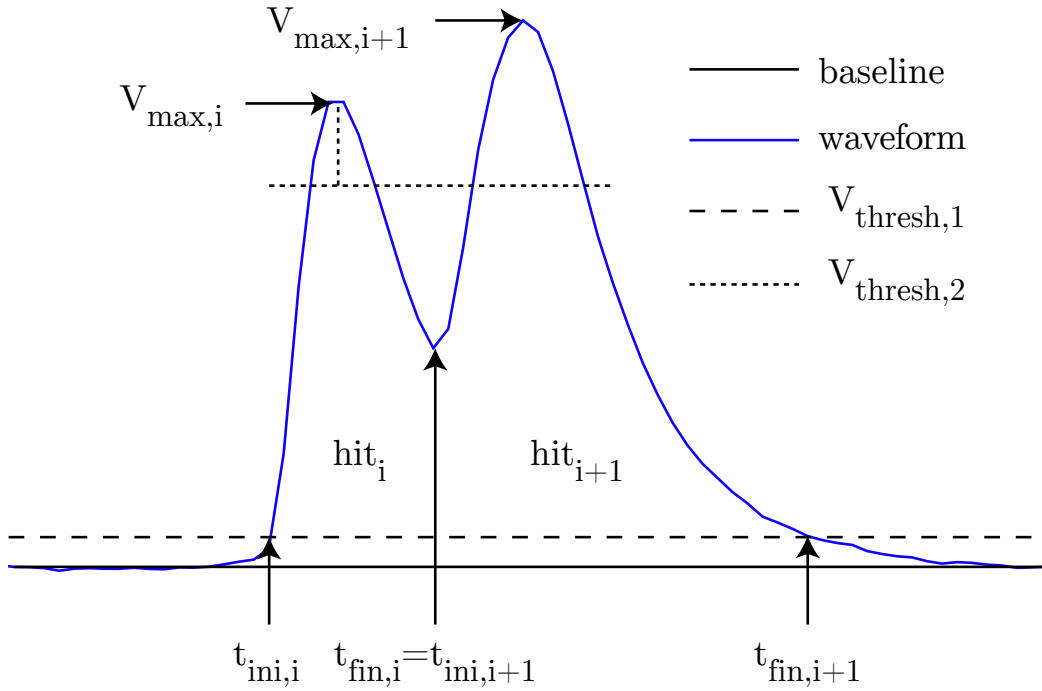


FIG. 119: Waveform (blue line) from a cosmic ray event that was recorded with the 3 L detector, showing a double hit structure (hit_i and hit_{i+1}). It defines the hit variables t_{ini} , t_{fin} and V_{max} as well as the *baseline* (black line) and the two thresholds $V_{thresh,1}$ and $V_{thresh,2}$.

that are present in the unfiltered event (dashed black line) are significantly suppressed after applying the filter (solid red line). It can also be seen that the algorithm does not affect the signals, despite its significant effect on the noise.

After suppressing the noise, the (constant) pedestal of each waveform has to be computed and subtracted from each sample. In order to avoid any bias due to physical signals, only pre-trigger samples are used to compute the mean value. Another possibility is to use the most probable value since it does not depend on tails, which are due to signals.

5.4.2 Hit identification and reconstruction

The smallest sub-unit of the reconstructed event is the *hit*. Physically, a hit corresponds to a track segment below a readout strip. The charge of this segment is then drifted towards the strip, where it induces a signal. The information that is attributed to a hit is the deposited charge ΔQ , the three-dimensional length Δx of the track segment, the drift time, which is equivalent to the drift coordinate z , the readout view and the electrode strip number. Hits have to be extracted from the signal waveforms by means of a standard threshold discrimination. Due to changing noise conditions, the threshold is defined in relation to the measured RMS noise value σ , which is measured for each event and readout strip, using the pre-trigger samples. A typical value for the threshold is $V_{thresh} = 3\sigma$. In the general

case there can be several close, or overlapping tracks per event, producing a superposition of several signals/hits on a single readout strip. The shaping time constants of the preamplifiers are chosen such, that double tracks being separated by a few μs can be resolved. In order to explain the working principle of the *hit-finding* algorithm, ?? shows an example of two subsequent hits in a single readout channel. The waveform was recorded with the $10 \times 10 \text{ cm}^2$ LAr LEM TPC prototype [25] and shows a single waveform from a cosmic ray track with an emitted knock on electron.

Moving from the left to the right, a hit candidate hit_i is initiated in case the signal waveform (blue) exceeds a pre-defined threshold $V_{thres,1}$ (dashed line) and terminated, when it either goes again below the same threshold or in case a new, subsequent hit candidate hit_{i+1} is triggered. The imposed trigger condition for subsequent hits is that the minimum voltage between the two hit candidates goes below the value $\min(V_{max,i}, V_{max,i+1}) - V_{thres,2}$. $V_{thres,2}$ (dotted line) is a secondary pre-defined threshold, responsible for the re-triggering of subsequent hits. Besides increasing the hit finding threshold, the number of fake hits due to noise can be reduced by imposing a minimum time over threshold $t_{fin} - t_{ini} > \Delta T$. Initial and final drift times (t_{ini} and t_{fin}), as well as the hit amplitudes V_{max} are defined as indicated in ?. In order to calculate the integral of each hit, the waveform is integrated from the initial to the final time sample. To reduce any bias, coming from the height of the threshold, the window, in which the integral is computed, can be extended in case there is no other hit attached.

The main parameters of the hits that need to be reconstructed are the *hit time* and the *hit integral*: together with the location of the corresponding readout channel, the hit time directly provides the information of the hit location in the considered view (projection), whereas the hit integral is related to the produced ionization charge and therefore provides the calorimetric information. In order to improve the accuracy of these two evaluated parameters, the signal waveforms can be fitted with a pre-defined function. Two examples of waveform fits are shown in ?: the left plot shows the waveforms of a double hit from a cosmic ray event, recorded with the 3L double phase LAr LEM-TPC [25], whereas the right plot is a beam event, recorded with the 120 L single phase LAr TPC [145]. As the LEM-TPC has a faster signal induction, the used fitting function is a convolution of a constant current ($\theta(t)$ is the step function):

$$I(t) := I_0 \cdot \theta(t - t_0) \cdot \theta(t_0 + \Delta t - t) \quad (5.3)$$

of duration Δt and integral I_0 and the normalised response of the ETHZ preamplifier $h(t)$ [23]:

$$V(t) = I * h(t) = \int_{t_0}^{\infty} I(t') h(t - t') dt'. \quad (5.4)$$

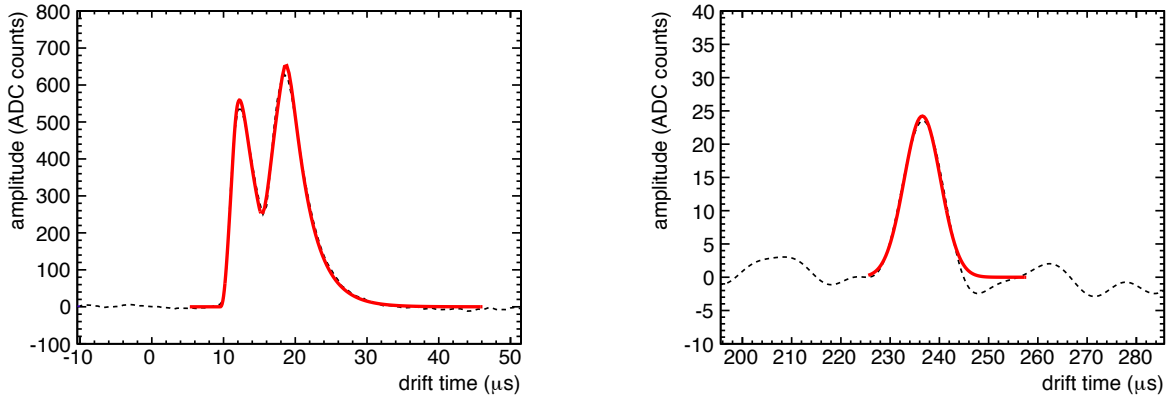


FIG. 120: Waveforms (dashed black line) from two different detectors, superimposed with the fitted functions (solid red line). Left: the cosmic ray event from the 3 L double phase LAr LEM-TPC [25] is, due to the fast response, fitted with a function that is based on the preamplifier response function. Right: beam event from the 120 L single phase LAr TPC [145], due to its slow signals fitted with a Gaussian.

The function is analytically computed and since the response with the integration and differential time constants is already known, the only three fitting parameters are the integral I_0 , the time t_0 and the signal width Δt .

5.4.3 Cluster finding

After a successful hit-finding, adjacent hits of different readout channels are grouped together. Since physical objects like tracks or showers are extended, the *hit clustering* is the first step towards a more global reconstruction of the event. The second advantage of clustering is that single hits can easily be suppressed by applying a cut on the cluster size. Besides the improvement of the purity, also the hit finding efficiency can be increased, since it is possible to search for more hits around the borders of clusters with a lowered threshold. The clustering algorithm is based on the search of directly adjacent hits: starting from a single hit, the *nearest neighbour* algorithm (*NN*) iteratively expands the cluster by adding close hits. Looping over all hits in the cluster, it searches for unclustered hits within a pre-defined time and readout channel range around the current hit. Once a new hit is found, it is added to the cluster. The algorithm continues looping, until no more hits are found in the vicinity of the cluster. Like in the case of the hit-finding algorithm, the parameters of the algorithm depend on the detector as well as on the event type. Since the NN clustering is optimised to reconstruct connected objects, like tracks, it was perfectly suitable for the reconstruction of the 3 L, 120 L and 200 L TPC data. A more detailed description of the implementation of the NN clustering algorithm is presented in [138].

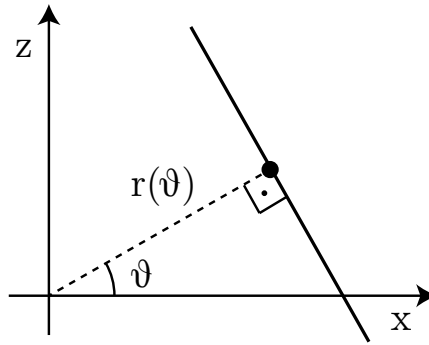


FIG. 121: Straight line parametrization, used for the Hough transformation.

5.4.4 Track reconstruction

Starting from general clusters that can assume any topology, the tracking algorithm, which was used for the reconstruction of the 200 L LAr LEM-TPC data [23, 24], aims at the identification of straight tracks. The straight track assumption is justified, since the multiple scattering is negligible for the maximally 60 cm long cosmic ray tracks. The method being described here can be easily generalized to the case of bent tracks.

In the following, we first describe a Hough-transform based tracking algorithm for the identification of the main, through-going cosmic rays and then a second algorithm to reconstruct knock-on electrons, appearing as secondary tracks. The basic idea of the track identification, being described here, is to convert the problem of finding aligned hits into the trivial problem of finding a maximum. The *Hough Transform (HT)* [147] transforms hits with coordinates (x, z) , where x is given by the readout strip number and z by the drift time, into the parameter space of straight lines, also called *Hough space*. The basic procedure of the HT is to evaluate the parameters of all the straight lines, going through each hit in the (x, z) plane. If a subset of points are aligned, there is a single line going through all of them and its parameter pair (angle θ and offset $r(\theta)$) will appear as a maximum in the two dimensional, binned Hough space. Looping over each cluster, the HT based track identification algorithm goes through the following steps:

1. Each hit coordinate pair (x, z) is transformed via HT to the parameter space. As shown in ??, straight lines are parametrized by an angle θ and the minimal distance to the origin of the coordinate system r . The transformation to the Hough space is then given by

$$r(\theta) = x \cdot \cos \theta + z \cdot \sin \theta. \quad (5.5)$$

After defining the binning of the Hough space with the variables (r, θ) , the algorithm computes

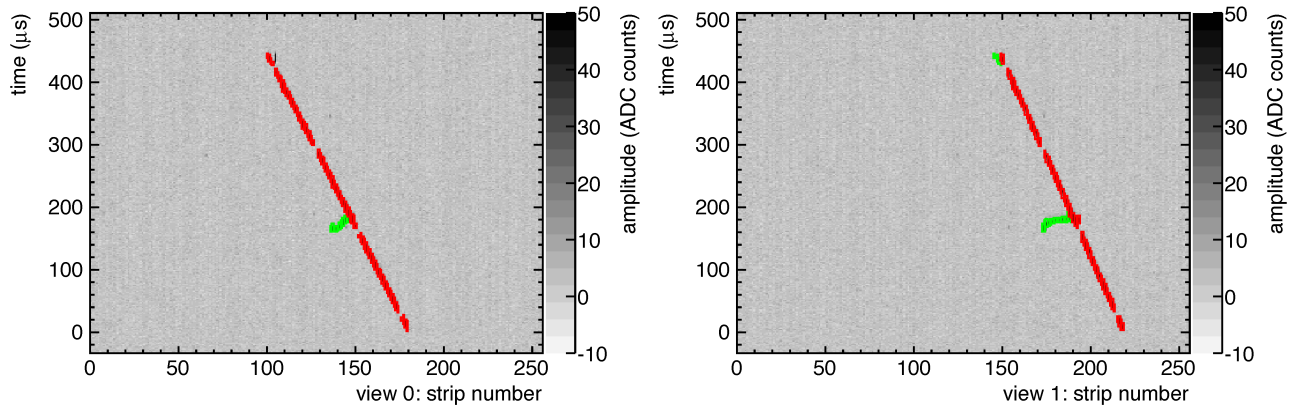


FIG. 122: Two views of a fully reconstructed MC generated muon with a knock-on electron in the TGeo geometry of the 200 L double phase LAr LEM-TPC [23, 24]. Hits belonging to the main track are highlighted in red; hits belonging to secondary tracks that are attached to the main tracks are green.

$r(\theta)$ for each angle θ and adds the point with weight 1 to the two dimensional histogram. This step is then repeated for each hit of the cluster.

2. The bin with the largest number of entries (θ_{max}, r_{max}) gives then directly the parameters of the straight line that crosses most of the hits. In order to avoid fake tracks, a minimum threshold of typically $N_{min} = 4$ hits is required. The two dimensional track is then defined by all the hits that are close to the found straight line.
3. In case it is needed to find other straight tracks, step number 2. can be repeated for the residual hits that belong to the cluster but not to a track, until the number of hits in a track candidate goes below the user-defined threshold N_{min} . Finally, the main track is again fitted with a straight line.
4. After finding the main track, all residual hits that belong to the cluster but not to the track, are tagged as δ -ray hit candidates. Then, the algorithm groups and tags nearby δ -ray hit candidates as δ -rays. Since single hits can easily be produced by noise, δ -rays require at least two consecutive hits. ?? shows the MC generated μ^- with a δ -ray. The event display for both views 0 (left) and 1 (right) show in red the hits that belong to the main track and in green the hits that belong to δ -rays.

5.4.5 Three dimensional track reconstruction

The most important information, obtained from the hits, is the charge ΔQ that is related to the signal integral and the three dimensional track length Δx . The information of the two dimensional tracks from complementary views have to be combined in order to reconstruct Δx as well as the com-

plete three dimensional image of the event. Due to intrinsic ambiguities coming from the projection technique, this task is in general complex. However, the fact that only straight tracks are considered, simplifies the three dimensional reconstruction a lot, since the problem is reduced to the simple matching of two-dimensional tracks: comparing the drift times of the first hits of tracks, an algorithm loops over all two dimensional track candidates until a unique pair of tracks from both views is found. In case of the event shown in ??, the algorithm links the two red tracks, since the first hits from view 0 and 1 both have a similar drift time $t_{drift} \approx 0$ (the μ is entering from the top of the chamber through the anode). To reconstruct the three dimensional hit coordinates (x_0, y_0, z_0) and (x_1, y_1, z_1) for the views 0 and 1, the straight line approximation is used: first, the tracks of both views (view 0 and view 1) are fitted with the linear equation

$$z(x) = a_0 \cdot x + b_0 \quad \text{and} \quad z(y) = a_1 \cdot y + b_1 \quad (5.6)$$

with the slopes $a_{0,1}$, the offsets $b_{0,1}$ and the common drift coordinate $z = t_{drift} \cdot v_{drift}$. Eq. ?? makes use of the fact that the strips of the two readout views are perpendicular and the coordinate system is chosen such that view 0 (1) directly provides the x (y) coordinate. Besides the naturally provided readout coordinate z_0 (z_1) and x_0 (y_1) for view 0 (view 1), inverting Eq. ??, the missing coordinates y_0 (x_1) are given by

$$y_0 = \frac{z_0 - b_1}{a_1} \quad \text{and} \quad x_1 = \frac{z_1 - b_0}{a_0}. \quad (5.7)$$

Besides the absolute position of the hits of view 0 and view 1, the three dimensional track length

$$\Delta r_{0,1} = \sqrt{\Delta x_{0,1}^2 + \Delta y_{0,1}^2 + \Delta z_{0,1}^2} \quad (5.8)$$

has to be computed for both views independently. In the case of view 0 (view 1), Δx_0 (Δy_1) is equal to the readout pitch that is typically for both views equal to 3 mm. Further, Δy_0 and Δx_1 can be computed according to Eq. ?? and $\Delta z_{0,1}$ is given by Eq. ?. As final result for the three dimensional track pitch we get

$$\Delta r_0 = \Delta x_0 \sqrt{1 + a_0^2/a_1^2 + a_0^2} \quad \text{and} \quad \Delta r_1 = \Delta y_1 \sqrt{1 + a_1^2/a_0^2 + a_1^2}. \quad (5.9)$$

Finally, using the proper charge calibration of the readout and $\Delta r_{0,1}$ from Eq. ??, the expression $\Delta Q_{0,1}/\Delta r_{0,1}$ can be computed for both views. For reasons of simplicity, hereafter the same expression is often renamed to $\Delta Q/\Delta x_{0,1}$ or $dQ/dx_{0,1}$.

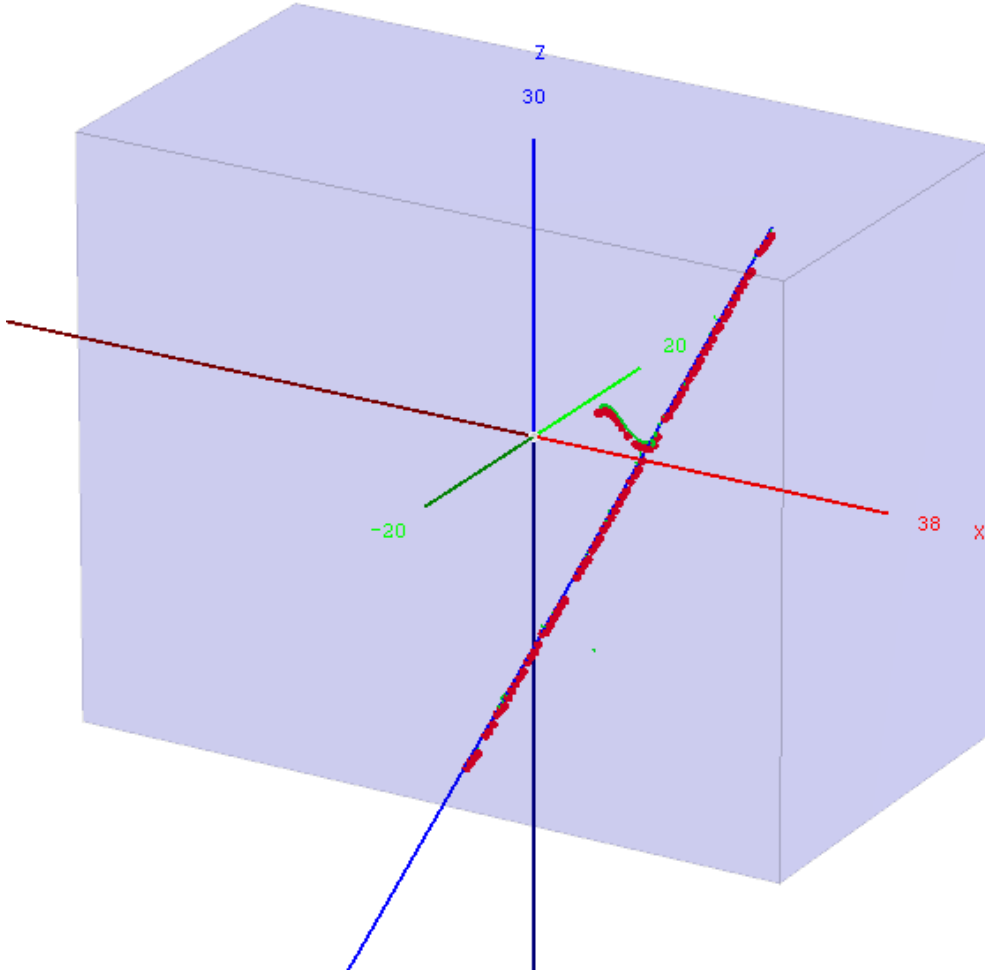


FIG. 123: Full reconstruction of view 0 hits (red dots) of the MC generated cosmic ray event from ??????. The MC truth μ^- track is shown in blue, the emitted δ -ray in green.

The hits that have been tagged as δ -ray hits (see ??), do not necessarily form straight tracks. Therefore, the best way to reconstruct those hits is to find for each δ -ray hit of view 0 a coincident δ -ray hit of view 1. This means, that the resulting coordinate of each hit on view 0 are defined as (x_0, y_1, z_0) , where y_1 is taken from a hit on view 1 with a similar drift time, i.e. $|t_{drift,1} - t_{drift,0}| < \epsilon$. In case no coincident δ -ray hit is found on the other view, it is matched with the main track, since in such a case it can be assumed that δ -ray and μ are superimposed. An example for the final, three dimensionally reconstructed MC generated event from ????? is shown in ??: the coordinates of all reconstructed hits of view 0 are shown in the 3D display, superimposed with the MC tracks. It can be seen that the through-going μ^- , as well as the δ -ray in green match with the reconstructed hits in red.

5.4.6 Particle flow - the PANDORA methodology

Alternative ways of reconstructing events starting from Qscan hits are being developed, in an effort to create a fully-automatic reconstruction package capable of handling all expected neutrino interaction topologies.

The PANDORA framework [148] was originally written for particle flow calorimetry in heterogeneous collider detectors, specifically the ILC and CLIC, by a group at the University of Cambridge led by Mark Thomson. This method of reconstruction attempts to identify all primary final-state particles in an event, and then associate all energy deposits in the detector with a specific primary particle, thus allowing to estimate the energies of all final-state particles through calorimetric methods.

The original PANDORA algorithms are not immediately suitable for reconstruction of neutrino events in LAr TPCs. For example, in a non-collider environment, there is no a priori knowledge of the vertex location from the beam geometry, and so the primary vertex must be reconstructed from event data. In addition, the original algorithms use the fact that different particle species deposit their energy in different parts of a heterogeneous detector (e.g. tracker, ECAL, HCAL, MRD) – this is not the case in a homogeneous LAr detector.

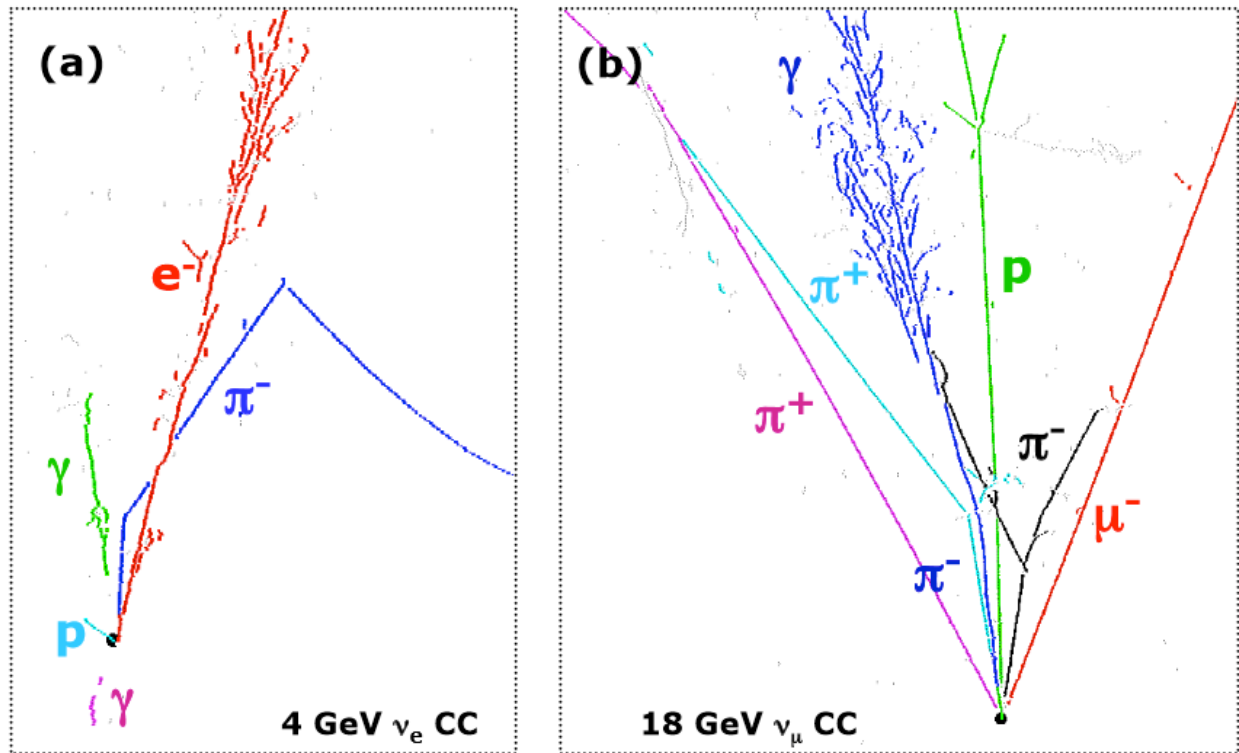
For this reason, the PANDORA developers have produced a suite of algorithms designed specifically for LAr reconstruction [149]. Essentially, the algorithms do the following:

- Split data into separate 2D projections.
- Perform first-pass hit clustering, by
 - clustering individual hits using a nearest-neighbour method; then
 - associating subclusters based on proximity and direction.
- Split clusters using a kink search algorithm.
- Find the primary vertex based on presumed beam direction and cluster positions/directions.
- Identify primary final-state particles (“seed clusters”), based on cluster length and proximity to vertex.
- Association of each remaining, “non-seed” cluster, with “seed” clusters, so that all energy deposits from a single final-state particle are grouped together.

In practice, this process is rather involved and each step is split into several discrete algorithms, each performing a tightly specified operation on the existing list of clusters; the philosophy followed is

that each step should be as conservative as possible, since it is much easier to combine objects later than to separate objects which have already been combined. The present version of the PANDORA reconstruction reconstructs hits in 2D projections rather than in 3D; an algorithm for matching the views to produce a 3D event does not yet exist, but is in development.

Examples of successfully reconstructed Monte Carlo events in liquid argon can be seen in Figure 124.



Coloured lines show reconstructed particles (labelled using MC truth)

FIG. 124: Examples of successfully reconstructed Monte Carlo events in LAr, produced by the PANDORA developers (taken from [149]). Black circles indicate the reconstructed primary vertex.

6 MIND500: North Area MIND

6.1 MIND500 overview

MIND500, a 500 ton Magnetized Iron Neutrino Detector, will operate downstream of the DLar in the North Area. Some characteristics of MIND detectors are poorly known, either because they have not been tested or because the conditions under which tests were carried out were not fully representative of the operational environment (e.g. no B-field). Improvements in technologies and the evolution of software tools such as reconstruction algorithms call for a comparison to experimental data for validation. There is a strong incentive to study in particular:

- Muon charge identification, for wrong sign muon signature of a neutrino oscillation event: golden channel at a neutrino factory: requires correct sign background rejection of 1 in 10^4 , $0.8 \rightarrow 5$ GeV/c.
- Hadronic shower reconstruction for identification of charged current neutrino interactions and rejection of neutral current neutrino interactions. Test beam: protons/pions $0.5 \rightarrow 9$ GeV/c.

Dimensions for the MIND500 are defined by the requirement for having an adequate acceptance for events originating in the DLar.

The three magnetization configurations under study are shown in Figure 125:

- 1-coil configuration;
- 2-coil "Helmholtz" configuration generating a dipole field, with a much smaller B_y component compared to the 1-coil configuration;
- 8-coil configuration generating a toroidal field.

The toroidal field option is the one which is currently favoured. A MIND with a toroidal field configuration has been studied for the Neutrino Factory, showing equivalent δ_{CP} reach to a MIND with a dipole field [8]. The 100 kTon Neutrino Factory MIND has an octagonal cross-section of $14 \text{ m} \times 14 \text{ m}$, and consists of 3 cm plates of iron interleaved with a 2 cm-thick XY lattice of plastic scintillator bars. Another MIND with a toroidal field, the Super B Iron Neutrino Detector (SuperBIND), has been proposed for nuSTORM. SuperBIND has a circular cross-section of diameter 6 m, a length of 16 m, and consists of 1.5 cm plates of iron interleaved with a 2.0 cm-thick XY lattice of plastic scintillator bars.

TABLE XI: MIND500 parameters.

Parameter	Symbol	Unit	Nominal value	Range Min.	Range Max.
Detector global dimensions					
Detector width	w_{det}	m	5.0	2.5	6.0
Detector height	h_{det}	m	5.0	2.5	6.0
Detector depth	d_{det}	m	3.2	2.0	5.0
Iron plates					
Material grade	-	-	AISI1010	-	ARMCO
Number of plates	n_{iron}	-	70	-	-
Iron width	w_{iron}	m	5.0	2.5	6.0
Iron height	h_{iron}	m	5.0	2.5	6.0
Iron thickness	t_{iron}	cm	3.0	1.0	5.0
Total iron mass	m_{iron}	tons	412	-	-
Total iron area	a_{iron}	m ²	1750	-	-
Number of slots for coil	n_{slots}	-	2	2	4
Slot for coil: width	w_{slot}	cm	10.0	-	-
Slot for coil: height	h_{slot}	cm	20.0	-	-
Support structure	-	-	TBD	-	-
Gap between iron plates					
Number of gaps	n_{gaps}	-	70	-	-
Gap thickness	t_{gap}	cm	1.5	1.5	2.0
Material	-	-	air + plastic	-	-
Plastic scintillator					
Material	-	-	Polysterene	-	-
Number of planes per module (xy or uv)	n_{module}	-	2.0	-	-
Gap between planes within module	-	cm	0	0	0.05
Module envelope thickness	t_{env}	cm	0.05	0	0.05
Scintillator bar length	l_{sci}	cm	500.0	100.0	500.0
Scintillator bar width	w_{sci}	cm	3.0	1.0	5.0
Scintillator bar height	h_{sci}	cm	0.7	0.6	1.0
Bars per plane	$n_{bars,pla}$	-	167	-	-
Bars per module	$n_{bars,mod}$	-	334	-	-
Total number of bars	$n_{bars,tot}$	-	23380	-	-
Light readout and conversion					
Light readout optical fibres	-	-	WLS	C.F.	-
Total length of fibre	fibre	m	120000	-	-
Readout device	-	-	SiPM	-	-
Readout channels per bar	-	-	2	1	2

6.2 MIND reconstruction efficiencies

Preliminary simulations in Geant4 of a MIND prototype are reported here. Further optimisation is ongoing, particularly concerning the geometry, definition of the magnetic field and reconstruction algorithms for pions. Assumptions taken for the geometry are octagonal plates 2 m × 1 m, two transmission lines, with a 2.8 m detector depth (along the beam axis). Four different scenarios were tested to validate the steel thickness and for an indication of whether the choice of scintillator geometry

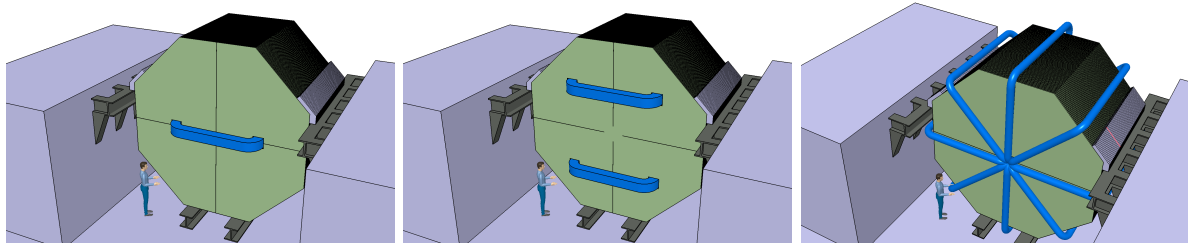


FIG. 125: Three different magnetization schemes for the iron are being considered. The scheme on the left depicts a 1-coil configuration which would provide a dipole magnetic field. The scheme in the center is a 2-coil configuration that leads to a reduction of the B_y component of the field in the central zone of the detector. The scheme on the right leads to a toroidal magnetic field. The cradle support structure is not shown here.

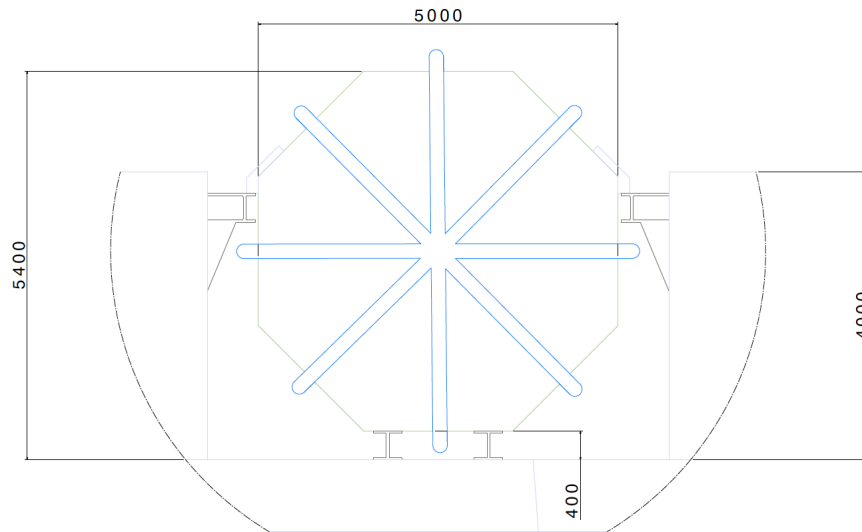


FIG. 126: Dimensions of the North Area MIND.

is acceptable (0.7 cm high rectangular bars vs 1.7 cm high triangular bars), scintillator pitch = 1.0 cm in all scenarios:

- 3 cm steel plate, 1.5 cm scintillator module (i.e. 0.75 cm X plane + 0.75 cm Y plane),
- 2 cm steel plate, 1.5 cm scintillator module,
- 3 cm steel plate, 3.5 cm scintillator module,
- 2 cm steel plate, 3.5 cm scintillator module.

In assessing the various efficiencies from simulations for a small MIND prototype exposed to a charged particle beam, the following were taken into consideration:

- a) The total number of tracks (or simulated particles in the detector);
- b) The number of tracks reconstructed (using the Kalman filter);

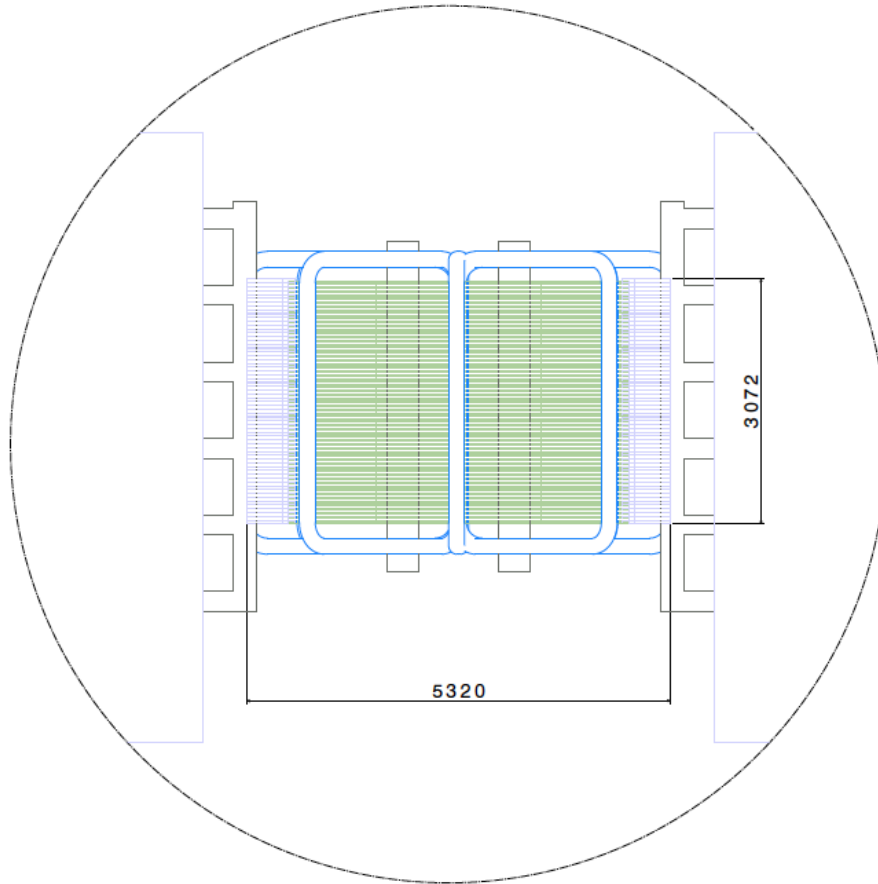


FIG. 127: Top view of the coil configuration generating a toroidal magnetic field in the North Area MIND.

- c) The number of successful tracks (where successful means that the correct charge is identified).

The efficiencies are then defined as:

- 1) The reconstruction efficiency is b/a .
- 2) The charge identification efficiency is c/a .

6.2.1 Muon reconstruction efficiencies

Muon reconstruction efficiencies are shown in Figure 128. All four combinations of steel and scintillator thicknesses show good efficiencies at low momenta <2 GeV/c. Above 1 GeV/c, the combination showing the best performance over the widest momentum range is 3.0 cm of steel and 1.5 cm of scintillator, with efficiencies close to 100% up to 6 GeV/c, staying above 99% up to 10 GeV/c. These efficiencies remain good for the other scenarios, dropping to 97% at high momenta.

A small fraction of events are not successfully reconstructed for the small MIND50 prototype. Track reconstruction using the Kalman filter from RecPack is based on a number of criteria, the most important being the number of hits along the track and the apparent curvature of the track (i.e. is

the curvature well enough defined as to determine the momentum). The Kalman filter algorithm allows for the propagation of track parameters back through successive detector planes using a helix model that considers multiple scattering and energy loss. In a neutrino detector where a ν_μ charged current interaction leads to hadronic activity at the interaction vertex in addition to an outgoing muon, the filter works well when the muon travels much further than particles related to the hadronic interactions. By ranking hits as a function of distance from the interaction vertex, it is possible to distinguish hits furthest away from this vertex as due only to a muon. Those hits then act as a seed for the Kalman filter. A typical reconstruction analysis will consider a number of planes (e.g. five) furthest downstream where hits are due to muons only. At high momenta, the technique works well. It has however limitations at high Q^2 or low neutrino energy, when the muon range is comparable to the range of the hadronic activity and identification of the muon becomes more challenging. When the Kalman filter fails, a cellular automaton method can be applied. It forms possible trajectories from a ranking of hits using a neighbourhood function.

In a charged particle beam scenario with a reduced detector depth along the charged particle beam axis, the Kalman filter can fail to reconstruct a track at low momentum if the number of hits is insufficient, or at high momentum if the curvature of the track is insufficient. Analyses for the much larger Neutrino Factory MIND or nuSTORM SuperBIND with true neutrino interactions yield efficiencies which are much closer to 100%, with a few events ($\ll 1\%$) failing reconstruction due to significant scattering affecting track curvature. For these detectors, pattern recognition and event reconstruction are more complex, and merit some comparison with test beam data.

Charge identification efficiencies are similar for all scenarios, close to 100 % for all momenta above 1 GeV/c, Figure 129. Detailed simulations were not carried out below 1 GeV/c. It is to be expected that the thickness of steel and scintillator start playing a role because of multiple scattering. A hint of the fall in charge identification efficiencies can be seen in Figure 129 with a couple of data points below 1 GeV/c where the thinnest steel and plastic scintillator combination has marginally better efficiency.

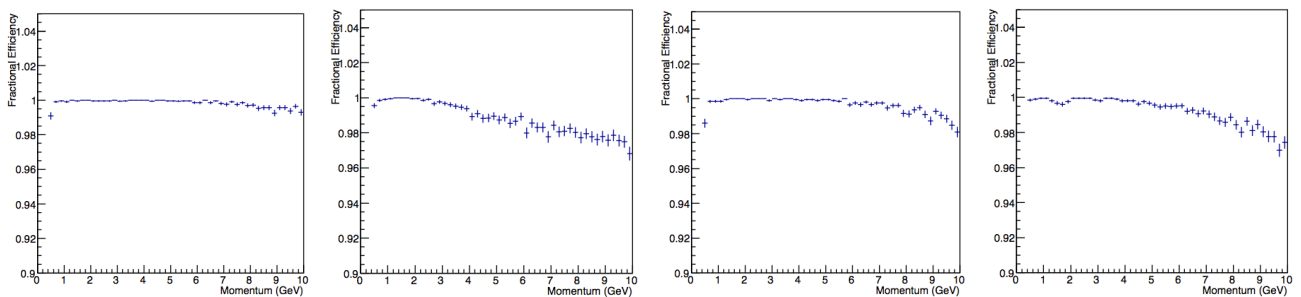


FIG. 128: Reconstruction efficiencies for μ^+ for different steel and scintillator combinations, clockwise from top left: a) 3 cm steel, 1.5 cm scintillator. b) 2 cm steel, 1.5 cm scintillator. c) 3 cm steel, 3.5 cm scintillator. d) 2 cm steel, 3.5 cm scintillator.

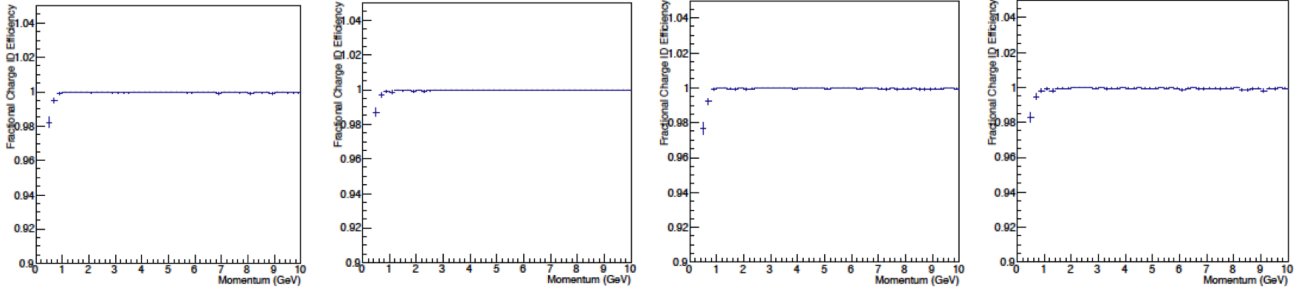


FIG. 129: Charge identification efficiencies for μ^+ for different steel and scintillator combinations, clockwise from top left: a) 3 cm steel, 1.5 cm scintillator. b) 2 cm steel, 1.5 cm scintillator. c) 3 cm steel, 3.5 cm scintillator. d) 2 cm steel, 3.5 cm scintillator.

6.2.2 Pion reconstruction efficiencies

Pion track reconstruction is more challenging because of the hadronic shower development. The pion reconstructed momenta show that individual tracks are poorly reconstructed, Figure 130. The input momentum distribution was uniform in p_z between 0.3 GeV/ c and 10 GeV/ c . The reconstructed momentum distribution is peaked at low momenta. Comparison of π^+ and π^- shows some discrimination of charge although further analysis is required. Charge identification efficiencies are poor for pions, Figure 131. Single track charge identification is unreliable and requires further work.

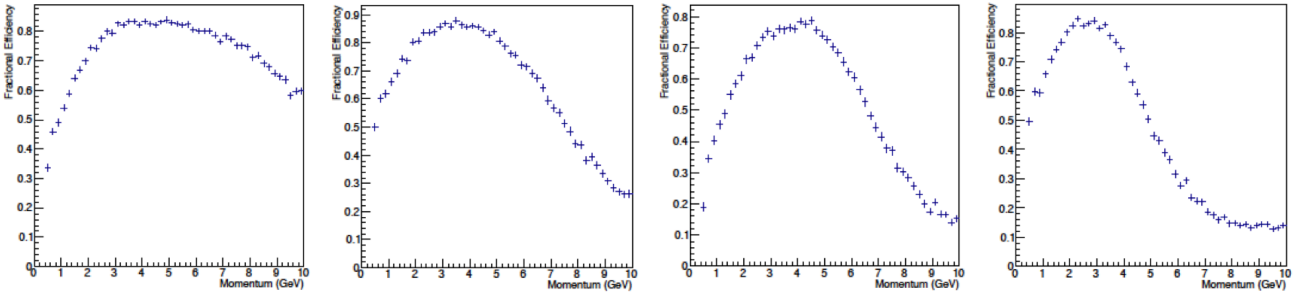


FIG. 130: Reconstruction efficiencies for π^+ , clockwise from top left: a) 3 cm steel, 1.5 cm scintillator. b) 2 cm steel, 1.5 cm scintillator. c) 3 cm steel, 3.5 cm scintillator. d) 2 cm steel, 3.5 cm scintillator.

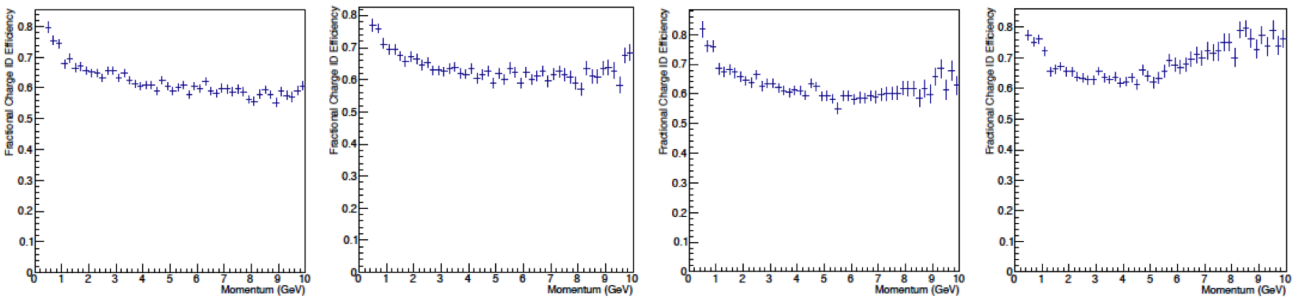


FIG. 131: Charge identification efficiencies for π^+ , clockwise from top left: a) 3 cm steel, 1.5 cm scintillator. b) 2 cm steel, 1.5 cm scintillator. c) 3 cm steel, 3.5 cm scintillator. d) 2 cm steel, 3.5 cm scintillator.

6.3 Detector modules

MIND500 detector module design will be based on developments carried out for the MICE-EMR and MIND50 detectors. The major difference compared to those detectors where scintillator slabs were typically ~ 1 m long, comes from the factor $\times 5$ greater length with associated significant attenuation losses for the light.

The detector modules consist of bars of plastic scintillators with wavelength shifting fibers and silicon photo-multipliers as light sensors. Considerable experience has been gained at the University of Geneva with all stages of the realization of such detectors. Recently, the MICE-EMR detector with similar modules was designed and constructed. It was commissioned in summer 2013, and shipped to the Rutherford Appleton Laboratory (RAL) in the UK where it was installed at the end of the Muon Ionization Cooling Experiment (MICE) beamline on 27th September 2013, Figure 132. First online test beam runs were carried out in October 2013, showing excellent particle identification capabilities of the TASD for low momentum (< 400 MeV/c) muons, pions and electrons. Data analysis is ongoing, an event display is shown in Figure 133.



FIG. 132: Commissioning of the MICE Electron Muon Ranger (EMR) in 2013: left) Assembly of the MICE-EMR detector at the University of Geneva, photo taken in June 2013, middle) Completed MICE-EMR, photo taken mid-September 2013, right) The MICE-EMR installed at the end of the MICE beamline at the Rutherford Appleton Laboratory (RAL) in the UK, photo taken 27th September 2013.

6.3.1 Detector module mechanics

The detector module mechanics proposal is shown in Figure 134. The concept is to have independent modules that can be inserted as cassettes between the steel plates in a MIND.

A module consists of one X plane with a number of scintillator bars glued at either end onto an aluminium support bar and positioned onto one Y plane with an equivalent number of scintillator bars also glued at either end onto a second pair of aluminium support bars. The X and Y planes are sandwiched between two carbon or kapton sheets, of thickness $200 \mu\text{m}$. These sheets provide mechanical support, reinforcing the planar alignment of the scintillator bars, and also provide some degree of light tightness. The carbon sheets will not affect the physics capabilities of the MIND500 detector, since

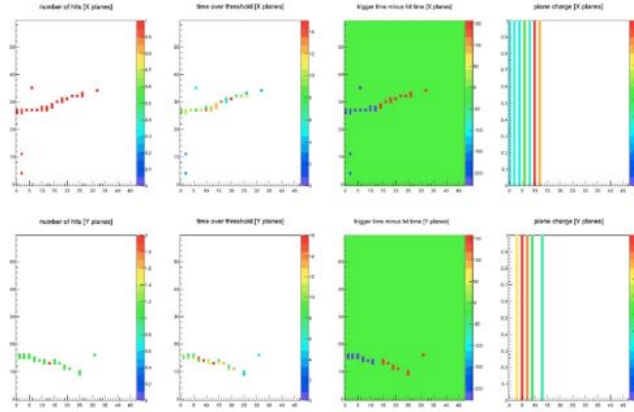


FIG. 133: MICE-EMR event display showing a 140 MeV/c negative muon entering the detector from the left, recorded during test beams on the MICE beamline in October 2013.

their thickness is negligible with respect to that of the steel plates.

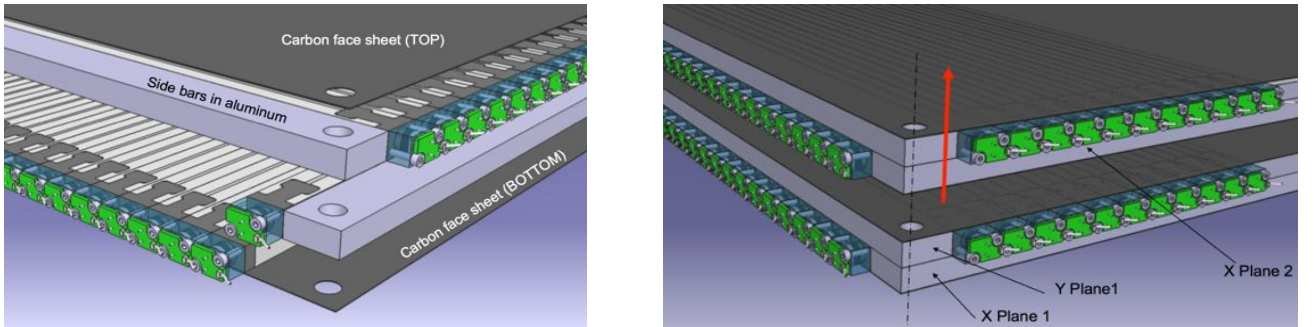


FIG. 134: MIND detector module: assembly.

6.3.2 Scintillators

The plastic scintillator bars will be supplied by the Institute for Nuclear Research (INR) of the Russian Academy of Sciences. The nominal parameters for the geometry are bars of 90 cm long, 0.7 cm in height and 1.0 cm in width, examples are shown in Figure 135. A small batch of prototypes has been manufactured by Uniplast based in Vladimir (Russia). These extruded scintillator slabs are polystyrene-based with 1.5% of paraterphenyl (PTP) and 0.01% of POPOP, similar to the plastics used for the T2K SMRD detector counters. The surface is etched with a chemical agent (Uniplast) to create a 30-100 μm layer acting as a diffusive reflector. Slabs of three different sizes have been manufactured ($895 \times 7 \times 10 \text{ mm}^3$, $895 \times 7 \times 20 \text{ mm}^3$, $895 \times 7 \times 30 \text{ mm}^3$) with 2 mm deep grooves of different widths (1.1 mm, 1.3 mm or 1.7 mm) to embed optical fibres of different diameters.

Tests were carried out at INR to determine basic light yield and timing properties. A wavelength shifting fiber (WLS) from Kuraray (200 ppm, S-type) of $d = 1.0 \text{ mm}$ was embedded into the 1.1 mm wide groove with a silicon grease (TSF451-50M) to improve optical contact between the scintillator

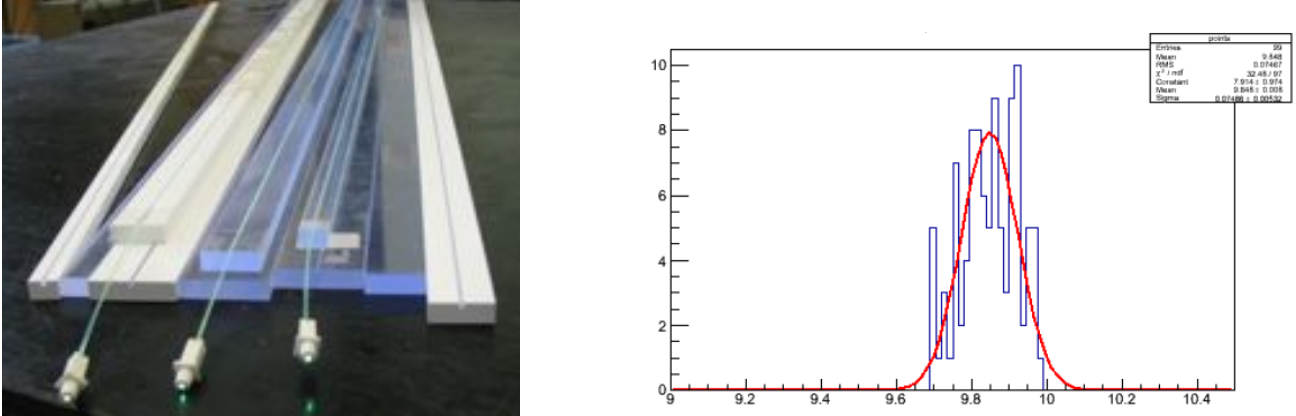


FIG. 135: Left: Prototype plastic scintillators of different dimensions produced by Uniplast. Right: Distribution of measured width for 100 randomly selected plastic scintillator bars for the chosen width of 10 mm, the X scale is [mm].

groove surface and the fiber. Hamamatsu MPPC photosensors ($1.3 \times 1.3 \text{ mm}^2$, 667 pixels, $50 \times 50 \mu\text{m}^2$, gain = 7.5×10^5 @25 °C) were connected to both ends of the ~1m long WLS fibers. A cosmic telescope was set up with two trigger counters. Measurements were made at the center of the scintillator slabs. The temperature during testing was 25-28 °C. Results are summarised in Table XII. Typical response to a minimum ionising particle is shown in Figure 136. Results show good light yield for all bar thicknesses, the highest light yield was obtained with the narrowest 10 mm width with 83 p.e. Comparisons with/without chemical reflector show an increase of light yield of a factor 2.5 when the chemical reflector is present. The effect of the silicon grease is close to 60%. For the final assembly, the silicon grease would be replaced by glue, which is expected to have roughly the same effect. An additional Tyvek reflector provides a 20% increase in light yield, though this reflector is not currently planned for the prototype detectors. The light yield was measured to be 50 p.e./MIP on average for one photosensor, Figure 137, in the case of the previous generation Hamamatsu MPPC $1.3 \times 1.3 \text{ mm}^2$. Very preliminary results of the latest generation process from Hamamatsu show an average of 58.5 p.e./MIP for smaller $1.0 \times 1.0 \text{ mm}^2$ MPPC. Timing properties were studied for the two-sided readout, combining both ends with the result: $\sigma((t_1 - t_2)/2) = 0.5 \text{ ns}$. The timing is mostly determined by the fiber decay constant, $\tau_{fiber} \sim 12 \text{ ns}$.

6.3.3 Scintillator and fiber connectors

A good geometrical interface between the SiPM sensitive area and the fiber is a crucial step in achieving good signal transmission efficiency and signal quality. Experience gained with the design of the MICE EMR optical connectors at the University of Geneva has proved valuable in designing the photosensor connectors. Connector prototypes were manufactured with 3D lithography. The final

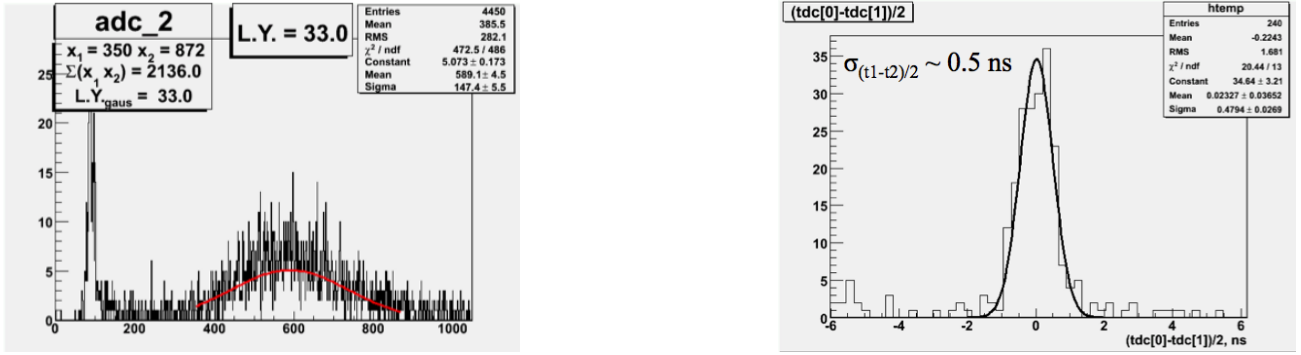


FIG. 136: Response of a scintillator slab and silicon photomultiplier to a minimum ionising particle: a) light yield and b) timing properties.

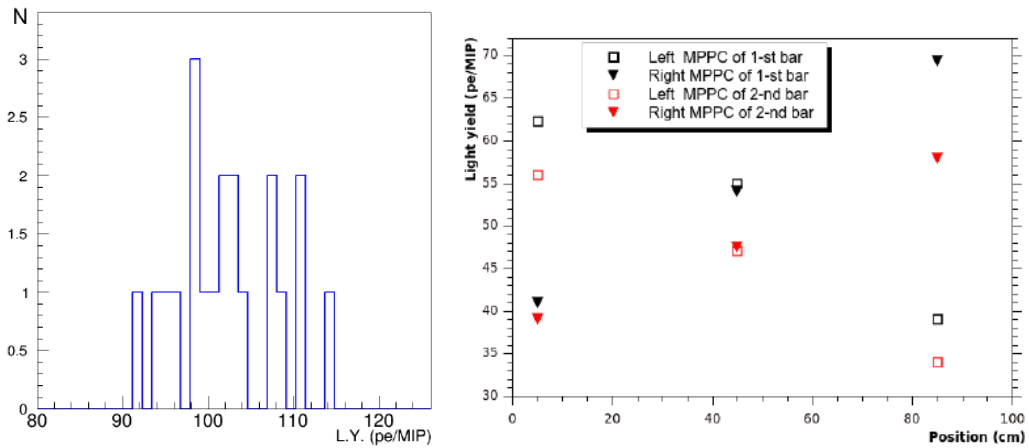


FIG. 137: Light yield from a 0.7 cm-thick plastic scintillator bar, readout from both ends. The plot on the left shows the sum of the two photosensors. The plot on the right shows the individual contribution of each of the two photosensors to the light yield as a function of position along the bar. The photosensors used for these tests were of the T2K-type, $1.3 \times 1.3 \text{ mm}^2$ sensitive area.

connector design and mass production using plastic injection moulding is to be carried out by the INR. Particular attention will be paid to fiber polishing and assembly stages, where quality assurance must be guaranteed and costs and schedule controlled.

The concept for a connector system to ensure optimal coupling between the wavelength shifting fibre and photosensor surface is shown in Figure 138. It consists of the following main components:

- The plastic scintillator slab;
- The wavelength shifting fibre;
- Connector A, which ensures the WLS fibre is centered with respect to the plastic scintillator slab;
- The photosensor (MPPC);

TABLE XII: Light yields from cosmic tests with prototype scintillator bars of different widths, unit is the photoelectron.

Bar width [mm]	MPPC 1 [p.e.]	MPPC 2 [p.e.]	Sum [p.e.]
Bar with no chemical reflector			
10	15.7	15.8	31.5
20	15.5	13.6	29.1
30	12.8	11.5	24.3
20 + Tyvek reflector 100-200 μm			
	41.8	34.8	76.6
Bar with chemical reflector			
10	46.0	36.8	82.8
20 (1) w/o grease	25.7	22.1	47.8
20 (1)	39.7	35.7	75.4
20 (1) + Tyvek reflector	49.3	44.0	93.3
20 (2)	32.6	28.2	60.8
30	31.2	26.6	57.8

- A component with a spring effect (sponge);
- Connector B, which holds the photosensor in place;
- A miniature pcb, which couples to the photosensor pins.

The first connector A once glued onto the plastic scintillator bar provides a support enabling the polishing of the fiber ends. The second connector B is designed to house the photosensor. Some parameters for the above components have been fixed, some choices are still possible. The production of plastic scintillator slabs has started, and in this context, the connector concept was designed to allow for production to proceed on the elements that affect the plastic scintillator production (the WLS, connector A).

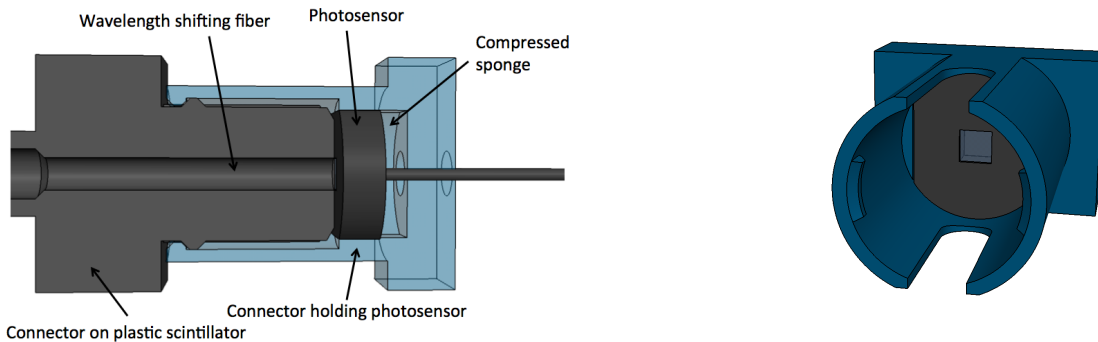


FIG. 138: Photosensor connector concept. The design has evolved from these initial sketches, to include constraints imposed by the plastic injection moulding process.

The connector concept proposed here is based on a connector for the Hamamatsu MPPC devised for the T2K experiment. It is therefore based on the dimensions of physical objects, such as the

MPPC, the pcb for electrical connections which hosts a mini-coaxial connector etc... Many of the geometrical constraints are very similar, modifications were brought to the design to account for the smaller dimensions of the connector.

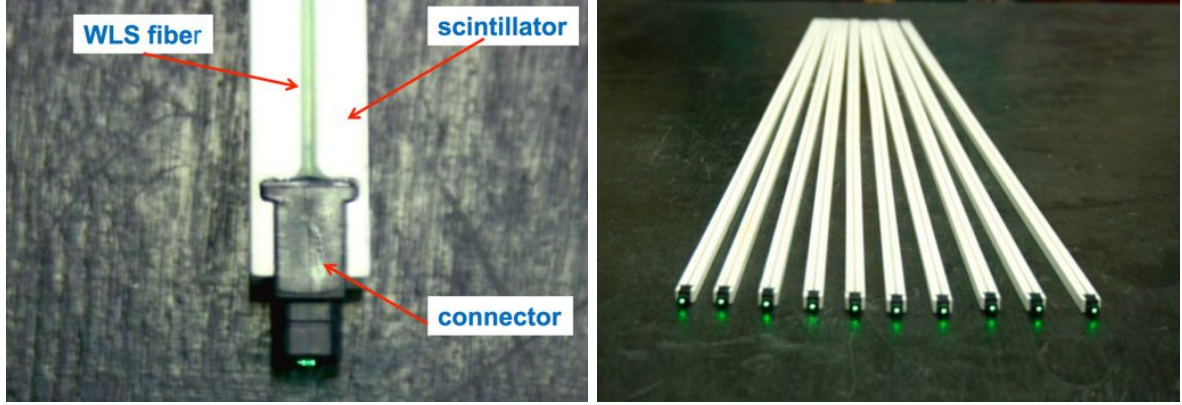


FIG. 139: Plastic scintillator bars with their connectors, as planned for the MIND modules.

6.3.4 Choice of photosensor

The first silicon photomultiplier device used on a large scale in a physics experiment is the Hamamatsu MPPC S10362-13-050C instrumenting all scintillator detectors at the ND280 near detector complex of the T2K experiment, [150]. It was derived from a commercial device, with the sensitive area increased from $1 \times 1 \text{ mm}^2$ to $1.3 \times 1.3 \text{ mm}^2$ to provide better acceptance for the light emitted from the 1.0 mm diameter wavelength shifting fiber from Kuraray. This MPPC consists of 667 pixels, each working in limited Geiger mode with an applied voltage slightly above the breakdown voltage ($V_{bd} = 70V$). With the production of a photo-electron in a pixel, a Geiger avalanche is generated, which is then passively quenched by a built-in resistor in each pixel. The induced charge is independent of the number of photo-electrons produced, and is directly proportional to the over voltage which is therefore a crucial parameter: $Q = C(V - V_{bd})$ or $Q = C\delta V$. In order to operate in the linear regime, where the MPPC output charge is directly proportional to the incoming photons, it is crucial that the total number of photo-electrons remains below the number of pixels in the device.

The thorough work done in the selection and characterization of photosensors for the T2K experiment serves as a very good basis for the selection of photosensors for the AIDA prototypes. Photosensor design is a fast evolving field. Several manufacturers offer a variety of products. Table XIII lists characteristics and measured performance for a selection of devices from different manufacturers tested at the INR in Russia in 2013.

Further tests are planned of the latest generation devices from Hamamatsu. Specifications from this manufacturer indicate improved dark noise, lower after pulse and higher PDE. Smaller cell sizes are

also available, increasing the dynamic range for our application. Hamamatsu will also make available so-called precision measurement devices with significantly less cross-talk between adjacent pixels which is achieved by surrounding each pixel by a trench. These devices will be available from April 2014.

The full electronics chain must be taken into consideration before deciding on the photosensor. In order to determine several of the key operational parameters, a test stand was setup with the final configuration of the plastic scintillator bar, a photosensor connector allowing for tests of various photosensors and an evaluation board for the EASIROC chip designed by Omega micro electronics. The test board is described in more detail in another section. Charge information for the photosensors is shown in Figure... The exact working point for the photosensors, which can be resumed to the applied overvoltage, is still to be determined from more detailed studies. A large overvoltage leads to a large signal from the photosensor, which in turn leads to high ADC counts per photo-electron once the charge information is digitized by the 12-bit ADCs which are external to the chip. It also leads to a higher signal-to-noise ratio. The disadvantages of a large over voltage are the significantly higher cross-talk, and the smaller dynamic range, which is ultimately limited by the ADC. The dynamic range can be extended to some extent by using the low gain analogue signal path, though it is less straightforward to calibrate, due to the much lower gain, which limits the resolution of single photo-electron peaks.

The following points are therefore relevant in setting the operating point of the photosensors and EASIROC chip, from the perspective of the readout electronics; i.e. the over voltage of the photosensor, and the pre-amp and shaper settings of the EASIROC chip:

- Calibration of signals: peak-to-peak resolution:
 - should be able to calibrate high gain signal path;
 - should be able to calibrate low gain signal path;
 - this puts stringent requirements on the cross-talk;
 - calibration can be performed at higher pre-amp gain if linear.
- ADC counts per photo-electron peak:
 - high enough to resolve individual photo-electron peaks;
 - high enough to provide good signal/noise: noise $\sigma = 5ADC$;
 - required noise level is 0.2 p.e. Pk-to-pk should be $> 25ADCcounts$.

As an example, setting the chain to obtain 25 ADC/p.e. on the high gain path, with a 12-bit ADC giving a range of 4096 ADC and a baseline around 1000 ADC (could be improved), the full range of

the high gain path would be 120 p.e. Using the same assumptions for the low gain signal path but this time with 5 ADC/p.e., the full range of the low gain path would be 620 p.e. This example shows that the system can be optimized for both:

- the most likely events with the high gain signal path (one MIP would yield 100 p.e.);
- events with high energy deposition such as stopping particles (estimated at 500 p.e.).

TABLE XIII: Comparison of specifications and performance of different photosensors from a range of manufacturers, measured under conditions representative of the AIDA detector modules.

Parameter	Unit	MPPC-T2K	ASD-40	KETEK	SensL
Manufacturer reported specifications					
Pixel size	μm	50	40	50	20
Number of pixels		667	600	400	848
Sensitive area	mm^2	1.3×1.3	dia 1.2	1.0×1.0	1.0×1.0
Gain		7.5×10^5	1.6×10^6	-	-
Dark rate	MHz	≤ 1	~ 3	≤ 2	≤ 2
Bias voltage	V	~ 70	30-50	33-50	30
Performance					
Overvoltage	V	~ 1.4	3.6	4.5	2.7
Dark rate	kHz	900	3630	1250	1960
Crosstalk	%	10	13.4	35	9.7
Pulse shape	-	good	good	long tails	good
Peak separation	-	good	good	bad	bad
PDE	%	25.6	11	26.4	14.2

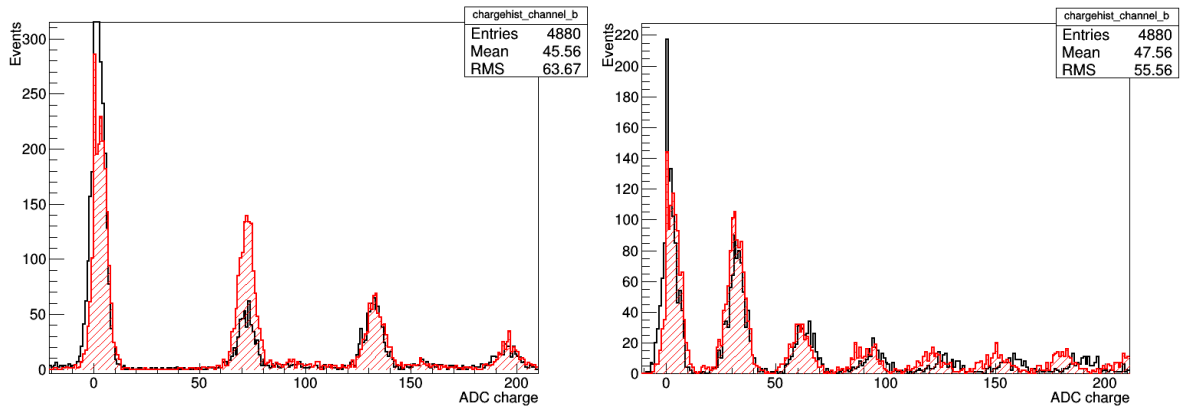


FIG. 140: Charge spectra for the MPPC S12571-050C, a 50-micron cell size, $1 \times 1 \text{ mm}^2$ device. Analogue data from the high gain signal path from the EASIROC chip, digitized with a 12-bit ADC, demonstrates the excellent photo-electron peak-to-peak separation. The EASIROC pre-amp feedback capacitance is set to 100fF, the shaper time constant is set to 50ns. Left) high over voltage leading to $\sim 65 \text{ ADC/p.e.}$ Right) low over voltage leading to $\sim 30 \text{ ADC/p.e.}$ Difference in over voltage between left and right acquisitions is 1.75 V.

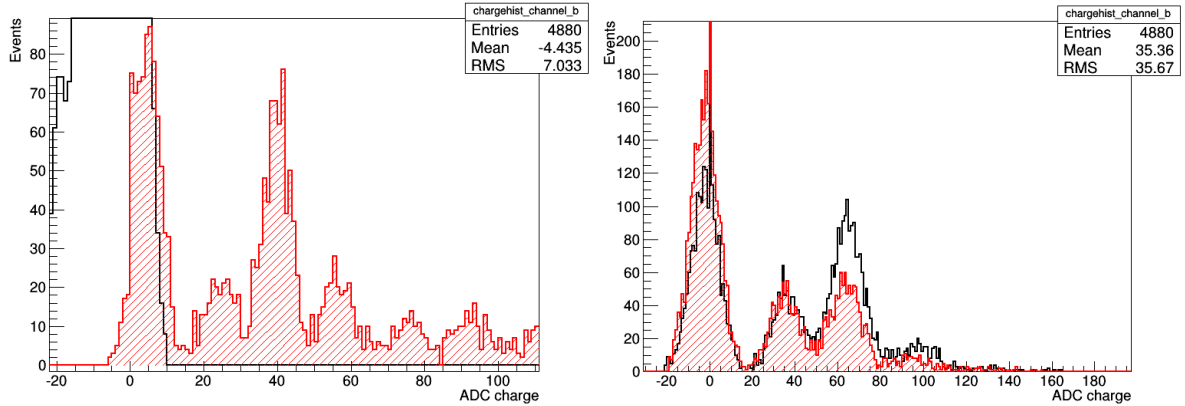


FIG. 141: Charge spectra for the MPPC S12571-025C, a 25-micron cell size, $1 \times 1 \text{ mm}^2$ device. Analogue data from the high gain signal path from the EASIROC chip, digitized with a 12-bit ADC. The EASIROC pre-amp feedback capacitance is set to 100fF for the left plot, and 0fF for the right plot. The shaper time constant is set to 50ns. A relatively low over voltage was used here, it could be increased to provide higher gain.

6.4 Electronics and DAQ

Emphasis will be placed on the electronics options which offer the best opportunity for further development to cover medium-term foreseeable requirements for neutrino detectors and related applications. The following options have been studied:

- DRS4: potential with long term perspectives but currently expensive,
- EASIROC: 3kHz readout rate demonstrated, architecture close to the MICE EMR,
- T2K ND280 TRIP-t option: will not be considered for this test beam.

The data acquisition system will be adapted from the MICE EMR DAQ. The EASIROC readout chip is the baseline solution. R&D on the DRS4 chip is ongoing at the University of Geneva within the framework of upgrades to the NA61 experiment. Depending on progress, a few modules could be equipped with DRS4 readout boards.

We plan to adopt a readout system where we readout separately the slower low and high gain analogue signal paths at 1 kHz providing charge information, and the faster hit-only digital triggers representing 4000 samples for every particle trigger running at 400 MHz, covering $10 \mu\text{s}$ after each event, with an average readout rate of 100 kHz. The faster digital triggers should allow tagging of delayed signals related to each event (e.g. muon decay to electron).

6.4.1 Outline of electronics chain

The planned electronics chain is based on the electronics chain developed for the MICE-EMR detector, installed on the MICE beamline at the Rutherford Appleton Laboratory in September 2013.

It is to be adapted taking into consideration:

- the beam characteristics of the beamline at CERN;
- the different photosensors, going from PMTs to silicon photomultipliers;
- the different readout chip, from MAROC to EASIROC.

In particular, a new front-end board must be designed. Coupling of the photosensors to the EASIROC chip can be done using the scheme implemented on the EASIROC evaluation board.

Concepts to be re-used from the MICE-EMR detector include the use of a Digitizer Buffer that acts as a TDC, assigning a time stamp to every event. The VME Readout Board (VRB) will also be re-used. It collects information from the front-end memory buffers and transmits it to the PC.

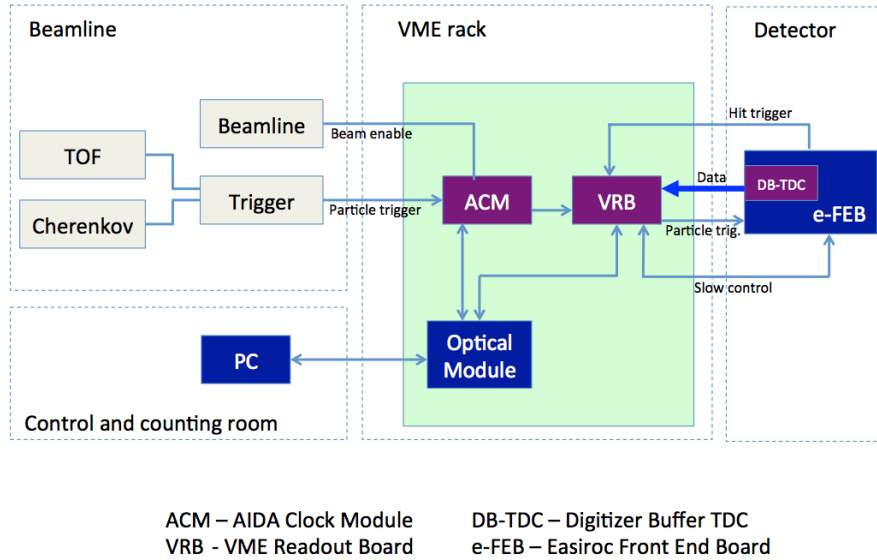


FIG. 142: Overview of the electronics chain for the AIDA neutrino detector prototypes.

6.4.2 Beam considerations for electronics

The planned set of runs in the North Area foresees the implementation of a very low energy beam line, delivering protons, pions, electrons, muons in the energy range 0.5 to 9 GeV/c, Table XIX. The beam is a slow extracted beam with a pulse length of up to 10 s, delivering particles at a rate of 1 kHz or so, Figure 143. The pulse repetition frequency is maximum 0.03 Hz.

The background is expected to be mainly from high energy muons created from the interaction of the primary beam with the first target. It should be low enough that triggering on interesting events will be achievable with high efficiencies.

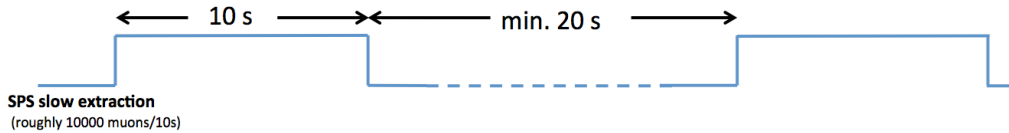


FIG. 143: SPS slow extraction beam time structure. These assumptions are taken in the design of the AIDA neutrino detector electronics.

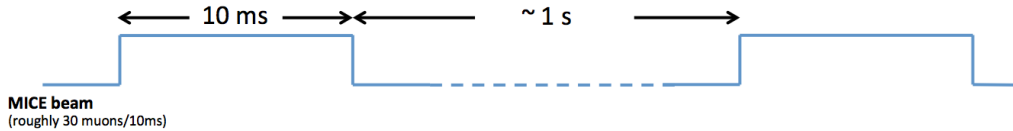


FIG. 144: MICE beam structure. The downstream components of the MICE electronics chain will be adapted for use in the AIDA readout electronics chain.

6.4.3 EASIROC chip

The EASIROC (Extended Analogue SI-pm ReadOut Chip) chip is designed in $0.35 \mu\text{m}$ SiGe technology, with first versions available since 2010 and used in a variety of experiments such as PEBS, MuRAY, at JPARC and in medical imaging. It is a 32 channel fully analogue front-end ASIC dedicated to readout of SiPM photosensors. It is derived from the SPIROC chip which was developed for hadron calorimetry foreseen for the International Linear Collider.

The chip integrates a 4.5 V (2.5 V) range 8-bit DAC for individual SiPM gain adjustment. A multiplexed charge measurement is available from 160 fC to 320 pC with 2 analogue outputs. These charge paths are made of 2 variable gain preamplifiers followed by 2 tunable shapers and a track and hold.

The analogue core is sensitive to positive SiPM signals. For each channel, two parallel AC coupled voltage preamplifiers ensure the read out of the charge from 160 fC to 320 pC (ie. 1 to 2000 photoelectrons with SiPM Gain = 10^6 , with a photoelectron to noise ratio of 10). Two variable shapers are used to reduce noise; each of them has an adjustable peaking time from 25 to 175 ns to allow the user to minimize the noise depending on the final application. A trigger line is available from the high gain preamplifier. It is composed of a 15 ns peaking time fast shaper followed by a discriminator. The threshold is set by an internal 10-bit DAC and is common to the 32 channels. The 32 triggers are

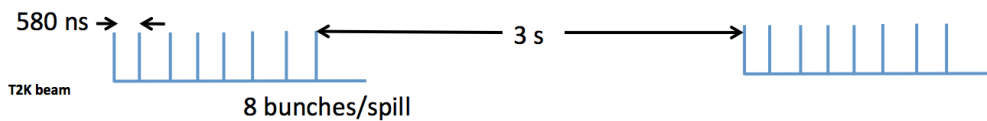


FIG. 145: T2K beam structure. The Trip-t electronics for T2K were initially chosen as the baseline but are no longer being considered for AIDA.

available as a 32-bit output bus and can be either latched or directly outputted.

In addition to the charge output, timing measurements are possible via a trigger path, that integrates a fast shaper followed by a discriminator. Its threshold can be set via a common 10-bit DAC. The 32 trigger outputs are complemented by an OR32 output.

Power consumption is 5 mW/channel and unused features can be powered OFF.

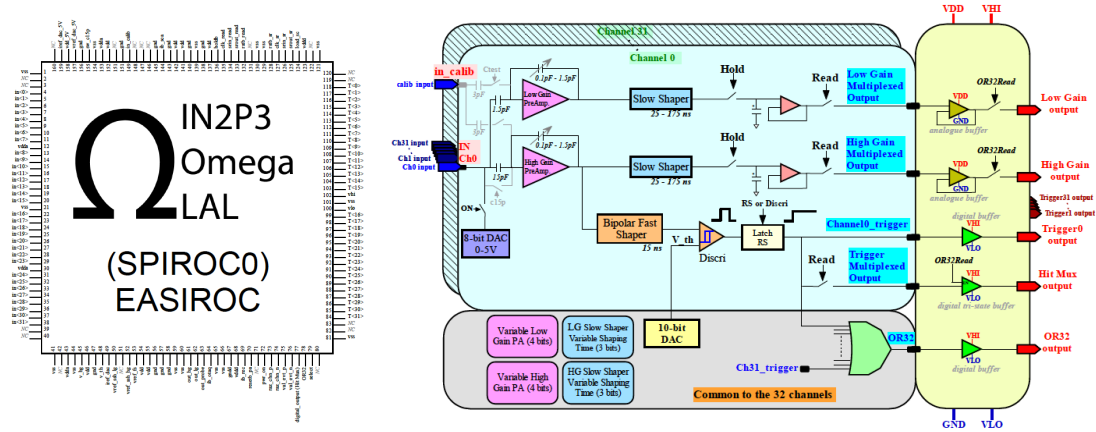


FIG. 146: Pinout and schematic of the EASIROC chip.

6.4.4 Readout modes

As described above, two readout modes from the EASIROC are possible:

- Mode A: slow readout of the analogue multiplexed signals;
- Mode B: Fast readout of the 32 triggers.

Used in combination, it is planned to operate with an external particle trigger provided by a system upstream, for example a Time of Flight detector, at rates of few \sim kHz. Mode A would then provide one charge sample per particle trigger. Mode B can be operated at 400 MHz, recording 10 μ s-worth of digital hits occurring immediately after the primary event, such as decay products, i.e. 4000 samples per particle trigger, see Figure 147.

The Front-End Board will be designed with sufficient memory buffers to record all data within a spill, lasting 10s in the case of a slow extracted beam at the SPS. The stored data will be transmitted between spills to the VME Readout Board (VRB), and then onto a PC. The minimum length between spills is 20s.

6.4.5 Data stream

It is planned to have one Front End Board per plane, i.e. 90 ch/FEB. However, detailed studies are required, including costing, before committing to a 1 FEB/plane scheme. Another possibility is to

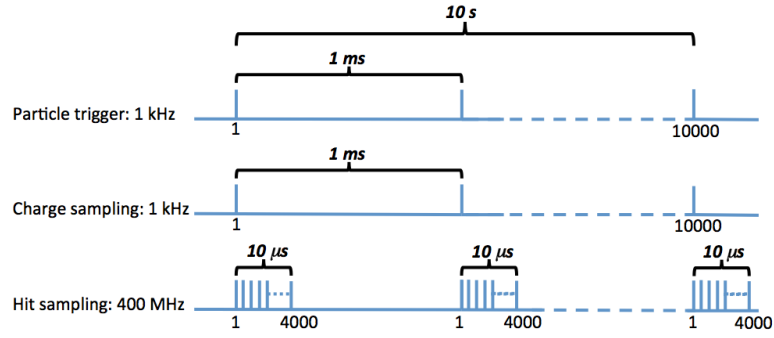


FIG. 147: Particle triggers, charge sampling and hit sampling within a 10s slow extraction spill from the SPS.

have one FEB/EASIROC chip, i.e. 30 ch/FEB, 3 FEB/plane. Since only roughly 1/3 of channels will be instrumented in phase 1, it is to be decided whether the corresponding fraction of each module will be instrumented, or whether full modules will be instrumented, but only 1/3 of the total number of modules will be used.

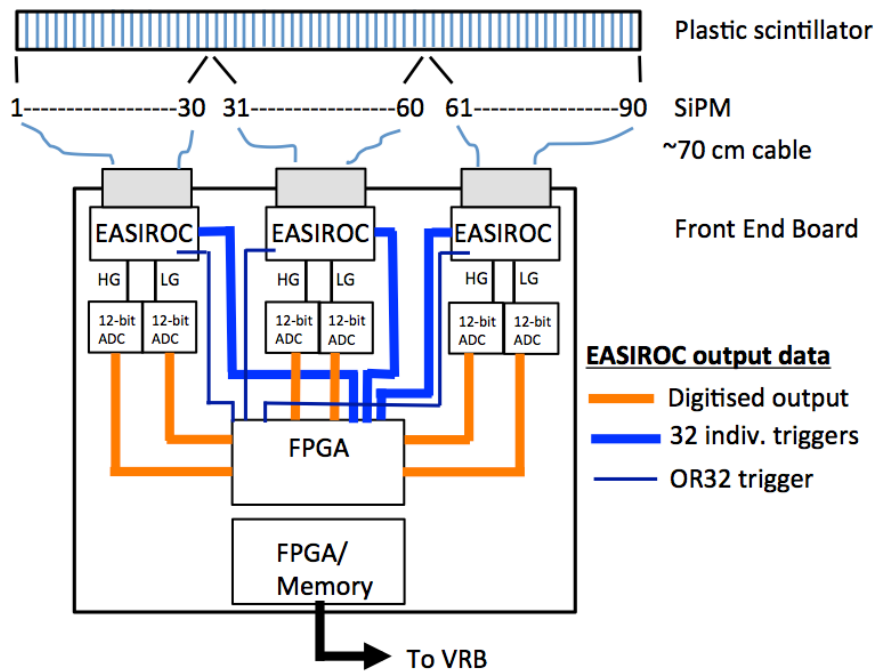


FIG. 148: Readout scheme for one plane.

The bit allocation scheme is reported in Table XIV. The scheme was devised to allow flexibility in the recording of time, with several configurations possible by combining the 16-bit **Hit time measurement** with the 20-bit **Event time tag**.

For timing under normal operation at the SPS with a slow extraction spill, the hit time measurement should cover 10 μs with sampling every 2.5 ns: 12 bits are sufficient. The event time tag should reset every 10 μs, a rate of 100 kHz, and cover 10s which is the spill length: 20 bits are required.

TABLE XIV: Allocated bits for different parameters in the recorded data.

Parameter	Allocated bits	Full range	Requirement
Word type	4	16	-
Board ID	10	1024	100
Spill number	16	65536	-
Event count (Ext. particle trigger)	28	268435456	1e8
Event ID (TBC)	-	-	-
Channel ID	7	128	90
Hit ID	5	32	-
Hit time measurement	16	65536	4000
Amplitude status	4	16	2
Hit amplitude measurement	12	4096	4096
Hit count within event	6	64	-
Event time tag	20	1048576	1e6
Spill width (TBC)	22	4194304	-

Spill header

31	30	29	28	27	26	25	24	23	22	21	20	19	18	17	16	15	14	13	12	11	10	9	8	7	6	5	4	3	2	1	0								
Spill header type														Board ID										0	0	Spill Number													
Spill header type 2														Event count (Trigger)																									

Event header: Event #1

31	30	29	28	27	26	25	24	23	22	21	20	19	18	17	16	15	14	13	12	11	10	9	8	7	6	5	4	3	2	1	0
Event header type				Board ID										0	0	Event ID (Ext. trig.)															

Event Data: Hit #1

31	30	29	28	27	26	25	24	23	22	21	20	19	18	17	16	15	14	13	12	11	10	9	8	7	6	5	4	3	2	1	0
Hit time type				Channel ID								Hit ID				Hit time measurement															

31	30	29	28	27	26	25	24	23	22	21	20	19	18	17	16	15	14	13	12	11	10	9	8	7	6	5	4	3	2	1	0		
Hit ampl type				Channel ID								Hit ID				Amplitude Status				Hit amplitude measurement: High Gain OR Low Gain													

Event Data: Hit #n

31	30	29	28	27	26	25	24	23	22	21	20	19	18	17	16	15	14	13	12	11	10	9	8	7	6	5	4	3	2	1	0
Hit time type				Channel ID								Hit ID				Hit time measurement															

31	30	29	28	27	26	25	24	23	22	21	20	19	18	17	16	15	14	13	12	11	10	9	8	7	6	5	4	3	2	1	0		
Hit ampl type				Channel ID								Hit ID				Amplitude Status				Hit amplitude measurement: High Gain OR Low Gain													

Event Trailer

31	30	29	28	27	26	25	24	23	22	21	20	19	18	17	16	15	14	13	12	11	10	9	8	7	6	5	4	3	2	1	0				
Event Trailer Type				Board ID										0	0	Event ID (Ext. trig.)																			
Hit count within Event														0	0	0	0	0	0	0	0	Event time tag													

Spill trailer

31	30	29	28	27	26	25	24	23	22	21	20	19	18	17	16	15	14	13	12	11	10	9	8	7	6	5	4	3	2	1	0				
Trailer Type 1				Board ID										0	0	Spill Number																			
Trailer Type 2														0	0	0	0	0	0	0	0	Spill width													

FIG. 149: Data structure for the MIND neutrino detector prototypes.

The estimation of data rate is critical in defining the buffer size for memory on the Front End Board. Several assumptions are made, these are usually conservative. Experience with the MICE detector would suggest that during normal data taking, the buffers are over-dimensioned by a large

factor. However, some events, such as electromagnetic or hadronic showers, lead to a large number of hits, which must be recorded.

Table XV lists the expected data rates for runs under the assumptions of a slow extracted beam at the SPS outlined previously. In summary, we expect **1 MB/plane/spill**, where a spill is 10s. The VRB memory buffer of the existing MICE-EMR detector is 8 MB. With one FEB/plane, it is relatively straightforward to reconfigure the firmware of the VRBs so that each VRB serves 8 planes, or 4 modules. A fraction of the 9000 plastic scintillator bars will be instrumented in the first phase. 3000 channels will be instrumented, we would therefore need 34 FEBs, 5 VRBs, 1 VME crate. The transfer rate from VRB to PC was measured to be $80 \mu\text{s}$ per kB, it should be re-measured with the configuration described here. It would lead to transfer times of 2.5s/event for the instrumented part of the detector, i.e. 3000 channels.

TABLE XV: Data rates estimated during operation of the AIDA neutrino detector prototypes. Note that in the first phase, only a fraction of the whole detector, 3000 of 9000 bars, will be instrumented.

Parameter	Per plane Instrumented detector (Whole)	
Items per plane		
# channels	90	3000 (9000)
# FEB	1	34 (100)
# EASIROC	3	102 (300)
Charge and hits per particle trigger(event)		
# Charge output/Particle trig/plane	10	-
# Hit output/Particle trig/plane	10	-
Stored information		
Stored Bytes/event	92.0	
Particle triggers/spill	10000	
Stored Bytes/spill [MB]	0.920	31.28

6.4.6 Slow control

It is planned to implement the slow control via the VRB chain, i.e. one link for both data and control.

6.5 Iron plates

6.5.1 Plate dimensions

The iron plates for the MIND500 will be octagonal, with a height of 5 m and a width of 5 m. Their thickness is currently set to 3 cm, with a potential range of 1.5 - 5 cm. Whether the iron thickness between detector modules is made up of 1 or 2 layers of iron will be determined from optimization of the mechanical engineering of the MIND. A cradle configuration is being explored, adapted from

MINOS, where the iron plates are hung on ears. The main advantage of a cradle configuration is that detector positioning and alignment are independent of the building, particularly important given that it is planned to move the MIND500 within the North Area building onto several beamlines. The displacement of the MIND will have to be studied in detail, since it is unlikely that modularity will be possible, given that the 8 superconducting coils will have to be spliced together once the detector is assembled. A system on rails might be possible, though the floor levels for different beam lines in the extension to the North Area building are planned to be different.

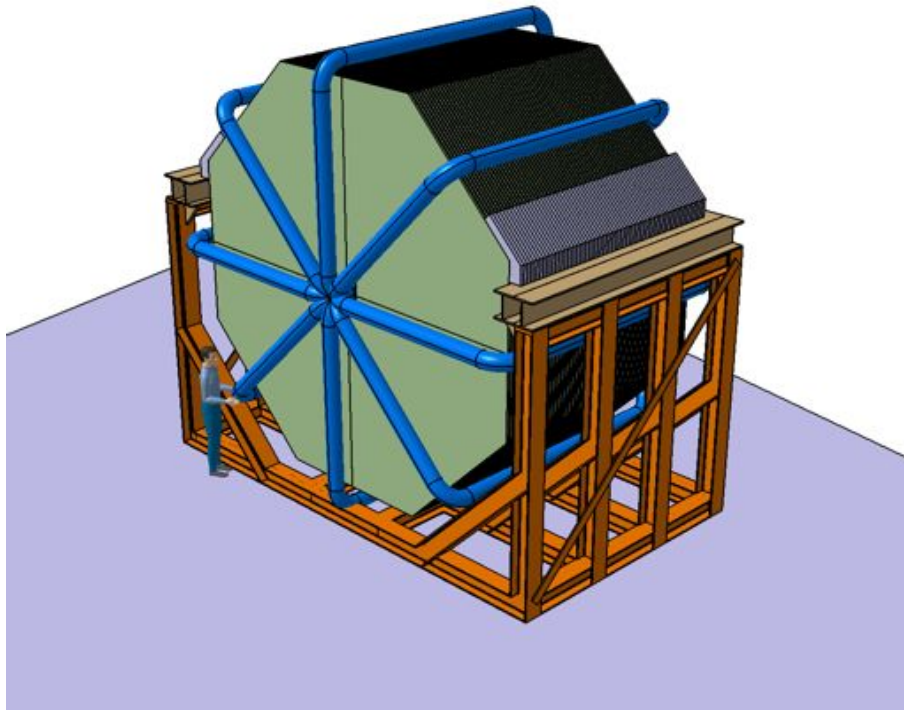


FIG. 150: The 8-coil configuration for the MIND500 with supporting cradle.

Each plate is fabricated from 2 half-octagons which are skip-welded together. The 2.5 m high by 5 m wide half-plates are transportable via standard means from the point of fabrication. The ears on the side would be welded and screwed onto one of the two half-octagons. They serve the purpose of supporting the load from the weight of the fully assembled plate, and will be used for alignment and to block the plates in position on the cradle.

6.5.2 Material selection

Selection of the iron is a compromise between adequate mechanical properties (tensile strength), and good magnetic properties (high magnetic permeability). Given the cost of pure iron such as ARMCO, we plan to select a more affordable construction steel with low carbon content such as the construction steel AISI1006. Our specifications are derived from previous experience with the MINOS

and BaBar magnet steels. Both those experiments used AISI1006. Similar construction steels such as AISI1010 (DIN CK10, 1.1121) could also be considered. An example specification is the American Society of Testing and Materials (ASTM) "Standard Specification for General Requirements for Rolled Steel Plates, Shapes, Sheet Piling and Bars for structural use." ASTM Designation A6.

Table XVI shows the flatness tolerances which are critical for this type of detector. The flatness is taken to be for steel plates lying on a perfectly flat horizontal surface such as a large marble slab. The ASTM specifications for flatness for these steel plate dimensions are a flatness of 18 mm. This is too large a value for the MIND steel plates, where we request a flatness of 1.0 mm.

Tolerances for plate thickness are taken from the standard ASTM Designation A6. The thickness is measured 10.0 to 20.0 mm from the longitudinal edge of the plates.

TABLE XVI: *Dimensions and tolerances for the MIND steel plates.*

Dimension	Value [mm]
Plate thickness	30.0
Thickness tolerance	+1.5, -0.3
Plate length	5000.0
Length tolerance	25.0
Plate width	2500.0
Width tolerance	16.0
Flatness tolerance over 5.0 m	±1.0

6.5.3 Chemical and mechanical properties

The plate manufacturer will be requested to demonstrate that analysis of the chemical composition can be made for each heat used in the production of all steel plates. The chemical composition of AISI1006 is given in Table XVII as an example. The most important element to control is Carbon, since it affects the magnetic properties. Other elements should be monitored in case reported values could lead to significant differences with respect to the mechanical properties.

The mechanical requirements in Table XVIII are given as an indication. Full finite element analysis for the particular design of the MIND detector prototype could call for a revision of these numbers.

6.6 Magnetization of MIND500

6.6.1 The Superconducting Transmission Line

Concerning the magnetization of the MIND prototype, a low carbon steel will be selected. There are no particular radiation or environmental constraints (corrosion/humidity). The magnetization will be set by passing a current through one or more conductor coils. Specifications for the field are the following:

TABLE XVII: *Chemical composition (% by weight) for the MIND steel plates (from MINOS TDR).*

Property	Specification
Carbon	0.04% to 0.06%
Manganese	0.40% (Max.)
Silicon	0.40% (Max.)
Sulfur	0.01% (Max)
Phosphorus	0.07% (Max)
Nitrogen	0.008% (Max)
Aluminium	0.05% (Max)
Chromium	0.05% (Max)
Copper	0.06% (Max)
Nickel	0.06% (Max)
Molybdenum	0.01% (Max)
Vanadium	0.01% (Max)
Niobium	0.01% (Max)

TABLE XVIII: *Mechanical specifications for tensile properties of the MIND steel plates (from MINOS TDR).*

Property	Specification
Ultimate tensile strength	275 MPa minimum
Yield strength	140 MPa minimum
Elongation of 5 cm	22% minimum

- field value: 1.5 T \pm 20%,
- knowledge of field in volume of interest to a precision of 10^{-4} , especially B_x and B_y components,
- field uniformity within steel along projection of plastic scintillator volume: 10%,
- field value outside MIND volume: maximum = 10 mT.

The assumption made concerning power supplies is that one can be provided by CERN. The coil design will therefore be made as a function of available power supplies. Initial studies were carried out to optimise the uniformity of the B_y component of the field whilst minimising the B_x component. Although this does not represent the current consensus on MIND-type detector design, this approach was meant to minimise uncertainties in the knowledge of the B-field. The resulting geometry led to a considerable height increase for the steel plates (factor $\times 2$), in order to have a return path for the field lines well away from the detector plane area. The results of the optimisation of field lines is an impressive constraining of the B_x component of the field, 115 Gauss (0.7% of B_y) for the two coil configuration, compared to 8210 Gauss (110% of B_y) for the one coil configuration. However, the doubling of the cost of steel and the introduction of large "empty" slots are disadvantages which drive the adoption of the more affordable and adequate one coil configuration in the case of the MIND50.

Having chosen the one-coil configuration, attention is now turning to the challenge of determining with accuracy the value of the field, not simply the total field but separate knowledge of the B_x and B_y components of the field. One solution that has been proposed and which is currently being investigated is to create a slot away from the detector planes from the coil to the outer edge of the steel plate, into which a non-magnetised material such as a stainless steel or aluminium is inserted with an embedded magnetic field sensor. By displacing this sensor along the entire length of the gap, it is possible to create a map of the field in the gap and thus infer the field lines in the area of the detector planes, Figure 151. This technique could have relevance for the much larger MIND-type detectors planned for future facilities. Further optimisation work is required to produce a design for the MIND that includes detailed maps of the B- field, thorough mechanical design and integration of a B-field measurement system.

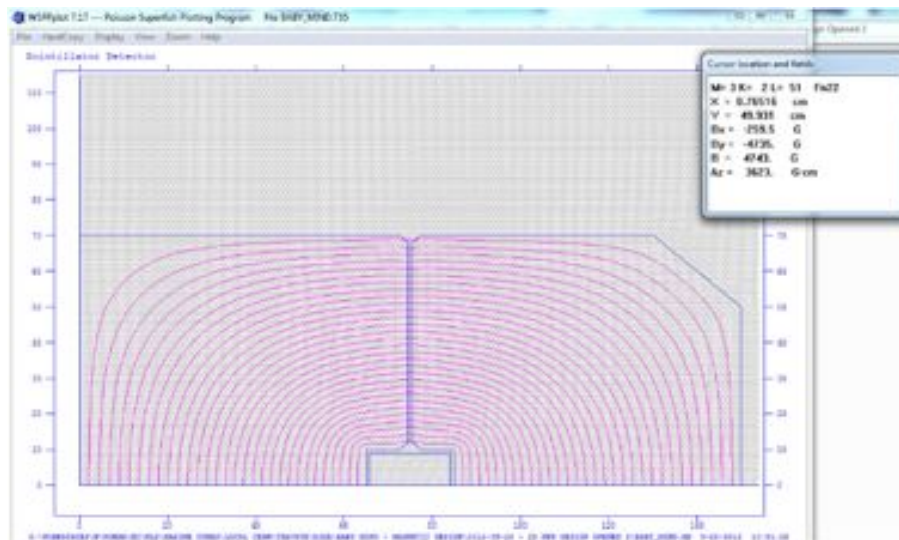


FIG. 151: Simulation of the magnetic field lines for the MIND50 prototype with a vertical gap for the insertion of a measuring device. This gap can be seen at ~ 75 cm on the horizontal axis. One possible method of measuring the B field is to insert a probe embedded in a non-magnetisable material into this vertical gap. Field lines in the detector module area between 0 and +45cm on both vertical and horizontal axes can be inferred from measurements made with the probe along the gap length.

The excitation of the MIND iron plates can be achieved with the Superconducting Transmission Line concept (STL) developed during the design study for a Staged Very Large Hadron Collider, see ???. The excitation current required is likely to be higher than the 40 kA-turns of the MINOS near detector. This is definitely the case if the concept for in-situ measurement of the B-field is adopted, where a much higher excitation current is required to establish a homogeneous field through the gap in the iron plate.

The STL is based on a NbTi superconductor cooled by forced flow of LHe. This approach proposed by G. W. Foster was successfully tested for the VLHC, carrying up to 100 kA and generating up to 2

T in the double aperture dipole magnet of the VLHC [151, 152]. The compactness of the line (80 mm OD) is cost effective since it eliminates the requirement for a large and expensive cryostat. The total current required for the magnetization of the MIND will be split evenly between the 8 coils, keeping the maximum current in each coil at an acceptable level to reduce Lorentz forces on the superconductor.



FIG. 152: The Superconducting Transmission Line (STL) developed for the VLHC.

6.6.2 Dimensioning the STL for MIND500

The nuSTORM proposal outlines in detail characteristics of the STL for SuperBIND, reported here [153]. The peak effective magnetic field in the iron is 2.5 T which drops to 1.87 T at a radius of 2.5 m. The peak field on the superconductor is 0.83 T on the coil inner radius. For SuperBIND, 30 kA of current in each of the 8 coils is required to generate those magnetic fields, with a total coil length of 320 m. The total coil length for the MIND500 is 104 m. The total current is likely just as high in the MIND500, though the total stored energy will scale with the coil length. Radial Lorentz forces on the inner and outer conductor for SuperBIND are -271 kN and 40 kN on inner and outer conductors respectively. The longitudinal force component is 2.4 kN. These loads are within the capability of the VLHC STL design where critical elements are the Ultem rings supporting the cold cable mass within the vacuum shell. A stainless steel slotted tube is required in the center to sustain the large radial forces directed to the center experienced by the inner coil.

The inner coil assembly cold mass has a diameter of 120 mm and is cooled by forced helium flow through a 40 mm-diameter central hole. Eight straight NbTi bars are mounted with epoxy

resin between the central tube and the outer aluminium tube. During cool down, the aluminium shell provides a pre-stress for the coil, which increases the superconducting coil mechanical stability. Aluminized Mylar super insulation is wrapped around the cold mass and the nitrogen shield. The cold mass is mounted inside a stainless steel vacuum vessel of 200 mm diameter and includes a nitrogen shield.

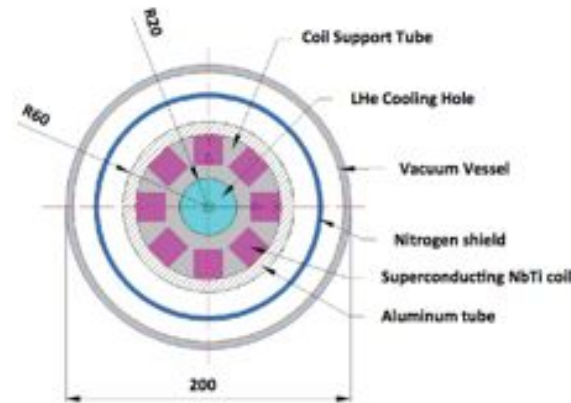


FIG. 153: Cross-section of the STL coil inner assembly.

6.6.3 The STL superconducting coil

A couple of options are available for the assembly of the NbTi superconducting coil:

- the SSC-type Rutherford cables used in the original STL [151, 152];
- the ITER-type Cable in a Conduit Conductor (CICC) [154].

The latter option is widely used for ITER correction coils, poloidal coils, buses and manifold cables. Production technology and facilities are developed and these cables have been tested in Europe, Russia and China. CICC has direct cooling through the cooling hole for large currents, or cooling between cable strands. The transmission line is one of the cost drivers for large superconducting magnet systems. The STL for the VLHC was estimated at \$500/m including cost of vacuum and shield tubes, Ultem spacers and super-insulation. The ITER project evaluated correction coil costs at \$220/m. For nuSTORM, the STL VLHC estimate runs at \$160k for 320 m. Scaling for the MIND500 leads to an estimate of \$52k.

7 Overall layout and space requirements

7.1 General Requirements

The Experimental Hall EHN1, being at present largely occupied by other fixed target experiments, must be extended to host the LAGUNA/LBNO prototypes. This choice allows not perturbing the existing experimental program in EHN1. Services (i.e. crane, electricity, water, etc...) could still be derived from the existing area, provided that the experiment does not suffer or generates perturbations related to the operation of other experiments or activities in the Hall.

The space requirements can be summarised as such:

- $>256 \text{ m}^2$ recessed floor space: The DLAr prototype is located in a recessed floor region (a pit of $\geq 16\text{m}$ large, $\geq 16\text{m}$ long, $\sim 7\text{m}$ deep) of the extension of the EHN1 experimental hall (EHN1-X).
- $5\text{m} \times 16\text{m} = 80\text{m}^2$ clean assembly + control room
- $5\text{m} \times 16\text{m} = 80\text{m}^2$ unloading area
- $10\text{m} \times 10\text{m}$ should be left open for installing the MIND.

In the baseline option, the detectors are located in a recessed floor region ($\geq 16\text{m}$ large, $\geq 16\text{m}$ long, $\sim 7\text{m}$ deep) of the EHN1 extension, as illustrated in ??.

The pit can house the detectors in such a way that they can receive a beam of charged particles. The geometry and tolerance for the direction of the incoming charge particles are presented in ?. The floor of the pit should be designed to support a weight of 800 tons. The detector should be standing on pillars whose number and size must be appropriately chosen. The supporting pillars act as thermal insulation (to avoid freezing of the floor) and as anti-seismic shock absorbers.

The requirements for the MIND detector will be defined at a later stage.

7.2 Control room

The control room hosts the computers responsible for the data acquisition and the local storage. The control room hosts several screens to monitor the various functions and statuses of the experiment. The control room is the location where physicists take shifts (24 hours per day, 7 days per week during beam time). The noise level should be, according to safety rules, such that extended period of stays are possible by staff. The ventilation of the control room should be dimensioned to dissipate up to 50 kW.

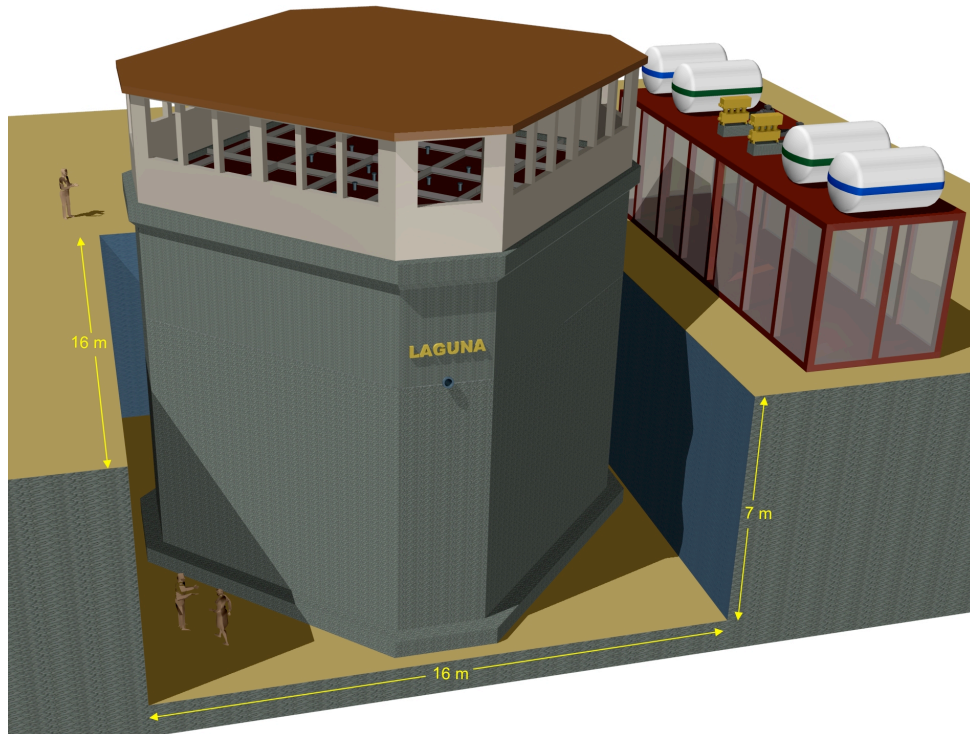


FIG. 154: Illustration of the $6 \times 6 \times 6\text{m}^3$ DLA demonstrator in the trench.

7.3 Clean-room

During assembly of the inner detector, the inner vessel shall become a clean room and be connected to an external clean room. The external clean room shall have a section with an external door to bring in preassembled and sealed components. The external clean room is used to open the shipped sealed packages and install individual components inside the inner vessel by means of a 10T crane (see ??). The environment in these volumes should be a class 1:100'000 (ISO Class 8).

7.4 Access to EHN1-X area

Equipment needed during the various phases of the installation and assembly will be transported by truck, truck-containers or with internal CERN vehicles (likely from the Meyrin site e.g. Blg 182). Unloading from the trucks will be done with the cranes or with forklifts. A convenient and unobstructed road access and a truck-unloading zone accessible from the cranes and with the forklifts should be available. During the initial construction phase of the vessel and the installation of the cryogenic facilities (see ??????), the 40T crane will be used. During the inner detector construction within the clean room, trucks will be unloaded with a forklift. The 10T crane to be located within the clean tent will be used to insert elements into the vessel from the top roof openings.

7.5 Liquid Argon filling and emptying

A liquid argon receiving and transmitting station will be used. The total liquid argon volume is $\sim 500 \text{ m}^3$ or approximately the equivalent amount transported by 25-30 trucks, with a maximum rate of several trucks per day giving a filling or emptying time of ~ 10 days. The delivered Liquid Argon shall be of the Welding Grade with following maximum contaminants at the arrival (contaminants at departure + contamination during loading and by truck itself):

- Purity > 99.99% molar
- Oxygen < 4 ppm molar
- Nitrogen < 2 ppm molar
- Water < 1 ppm molar
- Hydrocarbons < 0.5 ppm molar

In order to reduce nuisance and interference caused by the many trucks in the experimental hall, the LAr receiving and transmitting zone should be located externally, outside the experimental hall, and connected with the prototype cryogenic facilities via appropriate vacuum-insulated cryogenic transfer lines. An immersed LAr pump is necessary to empty the vessel (See Section ??). Heaters will be located inside the vessel to warm up the detector after emptying the liquid argon. Alternatively purging warm argon gas inside the tank can be considered to warm up the inner detector (See ??). In order to test the aging of the membrane weldings and the potential creation of micro-leaks, which would deteriorate the liquid argon purity even after complete outgassing of the inner detector materials, the vessel will be purposely cycled by filling and emptying several times. For an efficient filling and emptying, a local external storage with a capacity of 500 m^3 LAr should be available, using e.g. nr. 10 cryogenic standard tanks Linde LITS 2 of net capacity 58,500 lt / each[175].

7.6 Liquid argon boiloff recondensation

See ??. With the insulation thickness chosen, the average heat input is $\sim 5 \text{ W/m}^2$ and the total heat input (including also the roof input) is about $\sim 4 \text{ kW}$ at LAr temperature. The corresponding boiloff rate is $\sim 2 \text{ ton LAr/day}$ ($\sim 0.3\%/day$). A cryogenic plant must re-condense the boiloff rate in order to keep the pressure and the level of liquid argon constant. The absolute pressure of the argon remains constant $\pm 1 \text{ mbar}$, and can differ $\pm 75 \text{ mbar}$ relative to the atmospheric pressure. In order to avoid contamination of the pure liquid argon, the boiloff will be re-condensed via heat exchangers connected

to a nitrogen loop. The re-condensed argon will be purified (see next section) before it is returned to the main vessel. The LAr condensation can be made using liquid nitrogen at 1.5 barg and -187.1°C in a cross current heat exchanger. Liquid nitrogen is introduced at bottom of exchanger and exits on top in gaseous state. Gaseous argon goes at top of exchanger and exits at bottom in liquid form. Gaseous nitrogen is compressed and expanded in the thermodynamic cycle. Preliminary calculations indicate a thermodynamic efficiency of about 10%, so an electrical power of 40kW is needed to re-condense the boiloff argon.

7.7 Gas phase argon purging and purification

See ???. Gas purging in warm phase has been shown to be a very effective method to remove air from the vessel and to reduce the impurities to *ppm* level [86]. A forced gas recirculation and filtration is implemented to remove molecules (mostly water) outgassed from materials at warm temperature, before the detector is cooled down. Flushing gaseous argon at a temperature of $\sim 40\text{-}50^{\circ}\text{C}$ improves the outgassing, by warming up the surfaces of the detector components.

7.8 Liquid Argon filtration

See ???. The free-electron lifetime in liquid must be more than 10 ms in order to drift over 6 m without significant charge amplitude degradation. The impurities in the liquid argon should be less than 0.030 ppb = 30 ppt O_2 equivalent. A filtration system removes the impurities from the commercially delivered bulk argon (see Section ??) to the required level. Filtration is done by flowing liquid argon through custom-made purification cartridges, made of sections of molecular sieves followed by oxygen-reduced copper oxide powder, such as e.g. those successfully operated in CERN Blg182 in the context of ArDM (CERN RE18). The total volume of liquid argon in the vessel is continuously extracted by an immersed pump, and forced to flow through purification cartridges to filtrate residual impurities and those arising from outgassing materials inside the vessel. The flow of recirculation is at least 20 m^3 LAr/hr. The heat input into the LAr caused by the liquid argon filtration is about 4 kW.

7.9 Cranes

A 40T crane to be used during the initial phases of construction (e.g. tank assembly) and to install the cryogenic and liquid argon filtration plants. A dedicated 10T crane is located within the clean room tent (see ??) and is used during the phase of installation of the inner detector.

7.10 Ventilation requirements

The temperature and humidity in the hall are controlled by the ventilation and air conditioning system. An exhaust pipe from the recessed floor region is necessary. Dimension and location will be specified in agreement with the safety review. An exchange of the air volume in the recessed pit in which the LBNO LAr prototype is mandatory in order to mitigate the risk of accumulation of argon at the bottom of the recessed pit. The flow is to be defined in agreement with safety regulations. An increased air flow (two- or three-fold) which should be activated in case of emergency, might be required by safety regulations.

7.11 Cryorefrigeration requirements

The cryorefrigerator has a total of 10 kW cooling power at the LAr temperature. The operation at the full capacity dissipates about 100-150 kW. A totally redundant system (i.e. 20 kW) might be required to satisfy safety regulations. External buffers of LN₂ (~30 m³ LN₂/each) are used as cold source to ensure boil-off re-condensation in case of major event on the cryorefrigerator system. The total storage volume of the external buffers will be defined after the safety review. An area of 10x10 m² must be foreseen to install the cryo-refrigerators.

7.12 HVAC requirements

The total heat dissipation is dominated by the cryo-refrigerators. The heat generated by the cryo-compressors is evacuated via water-cooling (see ??). The heat dissipated by the rest of the equipment (electronics, power supplies, pumps, control systems, computers, ...) can be removed by air-cooling via an appropriate air conditioning system. The temperature and humidity of the hall should be controlled and stable. The dew point in the hall should be ~10° C.

7.13 Cooling water requirements

The heat generated by the cryo-compressors is evacuated via water-cooling, using a flow of fresh demineralised water is foreseen with standard CERN pressure (4-6 bar) and modest flow (~1m³/h). The temperature of the inflow water is in the range 6~10°C.

7.14 Electrical requirements

The area should be equipped with an arrival and a switchboard with protected lines dedicated. In the first phase, the electrical power consumptions are:

- 200 kW 400V/3P for the cryocoolers
- 100 kW 400V/3P for the cryogenic system, pumps, etc.
- 100 kW 400V/3P, 220V/1P for the detector electronics, power supplies, slow control, computers, etc.
- power for the magnetisation of MIND (tbd).

The available electric power might be upgraded to accommodate the MIND magnetised detector.

7.15 Additional laboratory space at CERN

The chain for the assembly, Q&A and test area to assemble the 36 m² for the charge readout components requires 30×20 m² laboratory space. The amount of space and the already existing infrastructure used by CERN RE18 (ArDM experiment) is adequate and can be in large part reused/upgraded.

7.16 Data storage and computing requirements

Gigabit Ethernet connections to the CERN backbone are expected. The needed storage of raw data in CASTOR of the order of 100TB per year of running.

8 Test beam requirements

In order to characterise the response of the detectors in terms of tracking, electromagnetic and hadronic calorimetry, and the physics of secondary interactions the detectors will be exposed to charged particle beams. The charged particles momentum should be selectable and cover the range 0.5-20 GeV/c with a bite of $\Delta p/p \approx 5\%$. The beam composition should be pions, muons, electrons, . . . and sign selected. Its composition is being studied with beam line simulations that takes into account the geometry of the various magnet elements. The rate of particles should be in the range 200-1000 Hz. Preliminary calculations assuming primary pion beam in the 60-80 GeV/c range show that this is feasible down to the desired momenta below 1 GeV/c. At 1 GeV/c the pion-to-muon ratio is estimated to be about 10:1. Below 1 GeV/c the fraction of muons increases due to upstream decays. Above 1 GeV/c, the fraction of muons decreases and reaches about 100:1 at 10 GeV/c. External instrumentation should include counters and chambers and early trigger signals.

Several configuration will be considered: (1) DLAr only, (2) MIND only, and (3) DLAr+MIND where the MIND500 measures particles exiting the DLAr. One of the more significant elements to be checked in the simulations will be the digitisation, which requires hardware efficiencies that are measured online.

A close collaboration between detector and beam group is required because a number of parameters such as particle rate, beam size and angle of incidence on the detector affects the detector design, e.g. readout electronics buffers. For the DLAr, the incoming direction should be at $45 \pm 15^\circ$ w.r.t. the two perpendicular readout views orientations of the TPC, and vertically point to the center of the active volume $\pm 15^\circ$. A beam window is foreseen in order not to spoil the momentum of the incoming particles and to minimise interactions upstream of the active volume. The top view of the present layout is shown in ??, and the side view in ?. Because of the recessed floor, the H2 line will be bent towards in order to hit the center of the DLAr detector.

Particle rates presented in Table XIX are given as an indication, in order to have a rough idea of the estimated beam time for sufficient statistics. The rate assumed is in the range of 100 Hz – 1 kHz of particles per spill. With a sample of 2×10^6 particles for each momentum bin and configuration, same overall test beam time online, estimated to be 6 weeks if we make the assumption of 175×10^6 triggers in total at 100 Hz with 50% running efficiency.

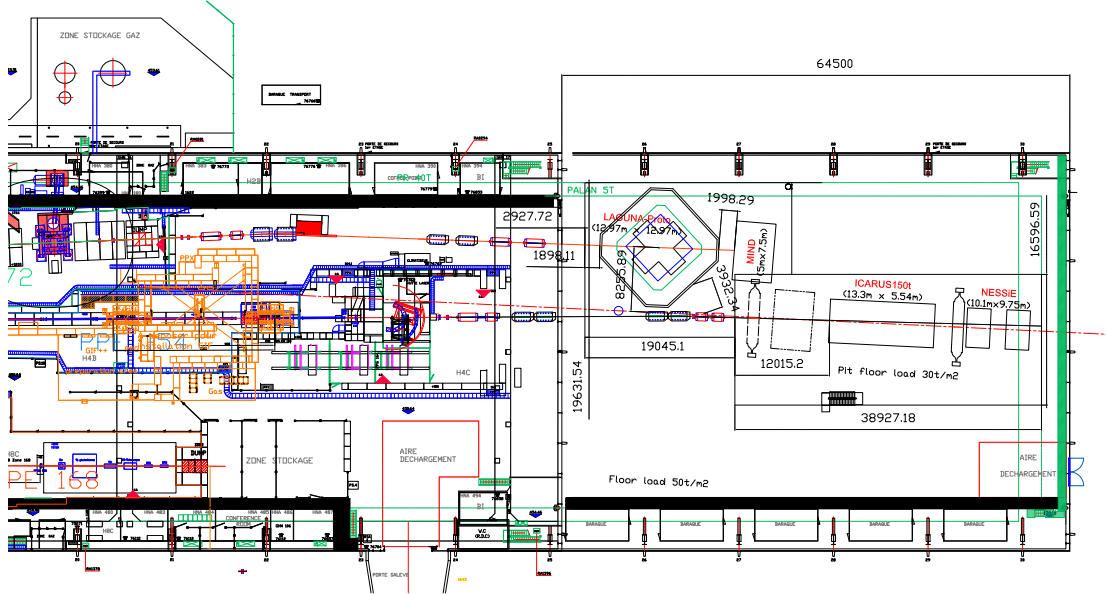


FIG. 155: Top view of the layout of LBNO-DEMO (LAGUNA-Proto and MIND) in the EHN1 building and its extension.

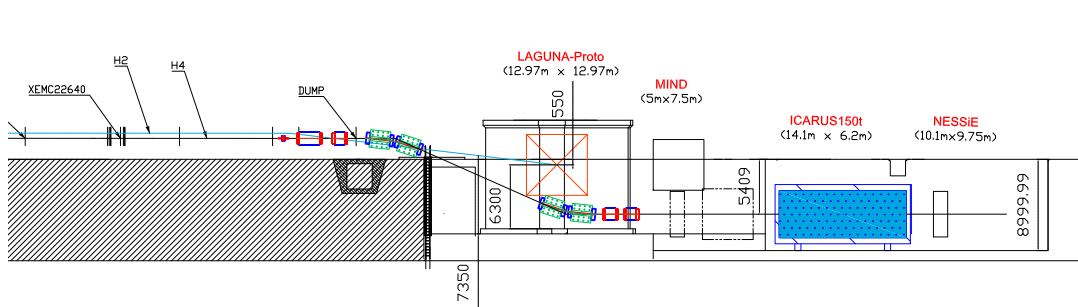


FIG. 156: Side view of the layout of the LBNO-DEMO (LAGUNA-Proto and MIND) in the EHN1 building and its extension.

TABLE XIX: Requirements for particles and their momenta. The particle rate here is the rate within a spill, regardless of the spill length, slow extraction is assumed.

Type	Momentum [GeV/c]	Rate [kHz]	Total	Time est. [hrs]
Muon tracks				
$\mu^{+/-}$	0.8, 1.0, 1.5, 2.0, 5.0, 10.0, 20.0	0.1	$5 \times 10^6 \times 14$	200
Shower reconstruction				
$\pi^{+/-}$	0.5, 0.7, 1.0, 2.0, 5.0, 10.0, 20.0	0.1	$5 \times 10^6 \times 14$	200
e	0.5, 0.7, 1.0, 2.0, 5.0, 10., 20.0	0.1	$5 \times 10^6 \times 7$	100

9 Organization, cost estimate, schedule and risk assessment

9.1 Organisation

The tentative organisation of the Collaboration (see ??) is based on typical schemes commonly successfully adopted in high-energy experiments. It will be finalised and formally voted in the coming months.

The Collaboration Board (CB) is the top-level decision-making and arbitration body. It has one representative with voting rights from institution involved in the project. It will review the progress of the project at the annual meetings, and, where necessary, will decide on changes in the work plan and budget allocation for the next period.

The Executive Board (EB) assures the day-to-day follow-up of the program and it is formed by the spokesperson, the deputy-spokesperson, the technical and scientific board leaders plus the administration responsible members. It will be responsible for the co-ordination and harmonization of all WA105 actions and particularly for the administrative and co-operative support of all transnational research activities. It will follow up all important horizontal issues and will prepare the IB meetings of the Collaboration. It will also be responsible for the official contact to CERN and its various committees, for public relation issues and for the contents of the WA105 websites. It will meet at least every two months, and decisions will be taken on a unanimity basis. On exceptional cases differences may be resolved by qualified majority rule (2/3 of the members) or can be directed to an exceptional CB meeting.

The Technical Board (TB), coordinated by the Technical Coordinator, manages the technical follow-up of the project.

The Scientific board (SB), coordinated by the Scientific Chair, manages the scientific follow-up of the project.

The Finance Review Committee will be composed of representatives from the various national and international funding agencies and research entities and will be setup to provide recommendations to the Project and guidance to the IB from the point of view of the Funding Agencies. The FRC shall usually meet every year. It will make recommendations on the use of resources and financing for the various implementation phases of the project.

The definition of the Work breakdown structure (WBS) down to level 3 with the contributing institutes is shown in ??.

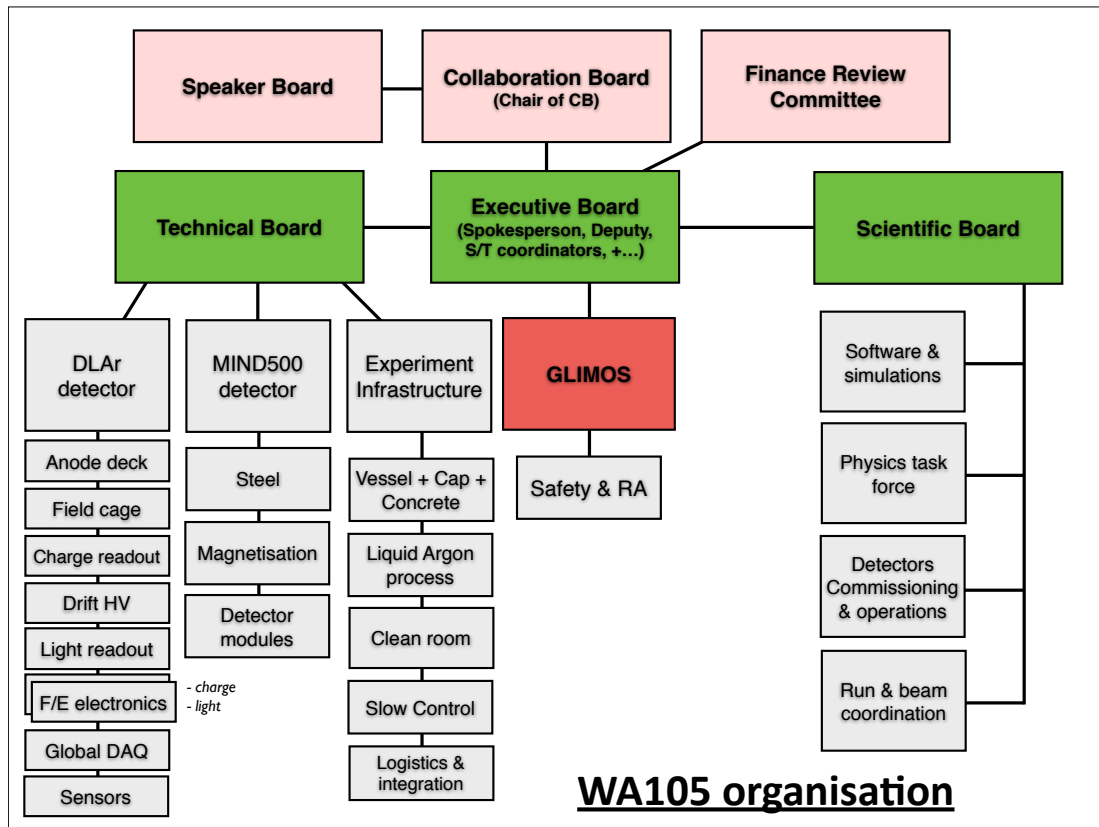


FIG. 157: Tentative organisation of the Collaboration.

9.2 Cost estimate

The total estimated cost of the LAGUNA $6 \times 6 \times 6$ m³ LAr demonstrator is presented and detailed in Table XXI. The figures based on preliminary discussion with industrial partners and on extensive experience of the groups on smaller scale prototypes are assumed to have an error at the level of 20-30%.

9.3 Schedule and milestones

Pending a prompt approval of the activities presented in this document, the schedule and milestones are summarised below:

- Beneficial occupancy EHN1: September 2015
- Vessel constructed: March 2016
- Inner-detector constructed: Jan 2017
- Detector start commissioning: Mar 2017

	Work package	Contributing institutes
WBS 1	Management	–
WBS 2	Technical Board	
WBS 2.1	DLAr detector	
WBS 2.1.1	Anode deck	LAPP
WBS 2.1.2	Field cage	CEA, ETHZ
WBS 2.1.3	Charge readout	CEA, ETHZ, UCL
WBS 2.1.4	Drift HV	LPNHE, ETHZ
WBS 2.1.4	Light readout	APC, Barcelona, CIEMAT, KEK
WBS 2.1.5	F/E readout (charge)	IPNL, ETHZ
WBS 2.1.6	F/E readout (light)	APC, LAPP, KEK
WBS 2.1.7	Global DAQ and trigger	UCL, IPNL, APC, KEK, Jyväskylä
WBS 2.1.8	Sensors	KEK, ETHZ, Oulu, IFIN-HH
WBS 2.2	MIND500 detector	
WBS 2.2.1	Steel	INR, UniGE
WBS 2.2.2	Magnetisation	Glasgow, INR, UniGE
WBS 2.2.3	Detector modules	Glasgow, INR, Sofia, UniGE
WBS 2.3	Experiment infrastructure	
WBS 2.3.1	Vessel + cap + concrete	CERN, ETHZ
WBS 2.3.2	Liquid Argon process	CERN, ETHZ
WBS 2.3.3	Clean room	CERN, ETHZ
WBS 2.3.4	Slow control (DCS)	CERN, ETHZ
WBS 2.3.5	Logistics and integration	CERN, ETHZ
WBS 3	Safety & GLIMOS	
WBS 4	Scientific Board	
WBS 4.1	Software & simulations	all
WBS 4.2	Physics task force	all
WBS 4.3	Detector commissioning & operations	all
WBS 4.4	Run & beam coordination	all

TABLE XX: Definition of the Work breakdown structure (WBS) down to level 3.

TABLE XXI: Total estimated cost of the DLAr demonstrator

Nr.	Item	Cost (kCHF)	Remark
1	Anode charge readout	800	
2	Hanging anode frame + movement	100	
3	Drift cage	500	
4	Light readout	300	
5	Power supplies	300	
6	Drift field supply	300	
7	F/E electronics	350	
8	DAQ	300	
9	Supporting infrastructure	100	
10	Cryogenic vessel	2300	(market survey)
11	Cryogenic plant	1400	(market survey)
12	Detector DCS	360	
13	Clean room	430	
14	Logistics	450	
	Total	7'990	preliminary

TABLE XXII: Preliminary cost estimate of the MIND500 detector

Nr.	Item	Cost (kCHF)	Remark
1	Steel	800	
2	Mechanics + coils	200	
3	Power supply	300	
4	Plastic scintillator	500	
5	WLS fiber	400	
6	Optical connectors	137	
7	Photosensors	480	
8	Mechanics	100	
9	Electronics + DAQ	720	
	Total	3'637	preliminary

- Beginning test-beam data-taking: Spring 2017

The construction of the infrastructure and vessel for the DLAr must be done on site. At this stage, it therefore appears that the readiness of the EHN1 extension is on the critical path. Once the vessel is constructed, the inner detector will be assembled inside, using a side opening defined as the TCO (Temporary Construction Opening). The assembly sequence will follow as closely as possible the one developed with industrial support for the LAGUNA/LBNO 20 and 50 kton detectors.

9.4 Risk assessment

A set of measures will be implemented to ensure H&S of people, protect equipment, and to mitigate risks associated to the storage and process of large amounts of cryogenic liquids. Additional equipment might be necessary as the results of detailed risk analyses and CERN specific safety regulations. Fire hazards are expected to be predominantly located in specific areas of the facility such as (1) the electronic racks located on top of the detector and (2) the high current cryogenic facilities. Measures to limit fire propagation from those areas might be required. The cryogenic infrastructure should be separated and protected from the regions of potential fire hazard. CERN is expected to contribute to the infrastructure resulting from the CERN safety rules (see e.g. CERN Safety Instruction IS 47 - The use of cryogenics fluids, http://edms.cern.ch/file/335812/LAST_RELEASED/IS47_E.pdf). CERN provides and installs remote cabinets, which are connected to appropriately located ODH and fire detectors, and which the CERN fire brigade remotely monitors. The building extension is equipped with fire detectors and evacuation alarms. CERN takes the responsibility for the measures needed to mitigate risk interference between the LBNO prototypes and potential other experiments or equipment to be installed in the EHN1 extension hall. The present design concept might be affected by so-far unforeseen and additional requirements set by safety regulations and identified by safety reviews. CERN will take possible measures to implement these additional requirements.

10 Conclusions

For over a decade (some) members of this collaboration have worked towards the realisation of a giant underground detector for next-generation long-baseline experiments, neutrino astrophysics and proton decay. Such experiments require concrete and large-scale prototyping for their far detectors – best realised on surface in laboratories with extensive expertise and competence such as CERN – as well as an accompanying campaign of measurements in precisely-defined charged particle beams aimed at assessing the tracking and calorimetric response of the detectors, the sophisticated energy-flow and other reconstruction algorithms, and the phenomenology of secondary hadronic interactions. All these parameters and their systematic errors will crucially affect the sensitivity of future long-baseline physics programmes, in particular for what concerns their ability to discover CP-violation in the leptonic sector.

In this context, following our submission of an Expression of Interest for a long-baseline experiment (LBNO), and the SPS Committee having reviewed positively the technology choices, it was requested to submit a technical proposal describing the R&D programme to be led at CERN. We have defined as priority the construction and operation of a $6 \times 6 \times 6\text{m}^3$ (active volume) double-phase liquid argon demonstrator (DLAr) and in parallel the development of the technologies necessary for large magnetised MIND detectors.

Successful operation of these detectors will provide very important feedback and will represent in many areas milestones that have so far never been achieved. The detectors concepts symbolise concrete steps towards the extrapolation of the technologies to very large masses, with the goal to reach tens of kilotons in underground environments. The proven technical choices deployed for the demonstrators will be directly scalable and their components mass-produceable in view of a potential large-scale implementation.

The programme and the results that will be obtained will be quite general and be useful for several neutrino programmes being presently contemplated by the community. Specifically, the detectors described in this document and their successful operation could, if performed in a timely fashion, have an important impact on the design of LBNE and be the seed for a significant European contribution to the US project. Similarly, the technologies could be considered in the context of the near detectors of the Japanese HyperKamiokande project.

Last but not least, the deployment and successful operation of these detectors at CERN could naturally be revisited in the context of a short baseline neutrino programme, based either on the CENF conventional neutrino beam, the NUSTORM beam from a muon storage ring, or on the SHIP beam dump for which prompt neutrinos would need to be studied. The goal of these programmes (in

particular the first two) would be to complement the long-baseline efforts, with measurements aimed at improving significantly our knowledge on neutrino and antineutrino cross-sections and reducing their systematic errors to the required level for discovery of CP-violation in the leptonic sector.

Hence, in the coming years, we intend to focus on the realisation and operation of the demonstrators, whose technical designs were presented in this document. We will reconsider potential future steps after that milestone has been reached.

We look forward to a prompt support of the SPSC towards ensuring a timely implementation of the North Area facility and the exposure to charged particle beams before the second LHC long shutdown (LS2).

Acknowledgements

We acknowledge the support from the FP7 Research Infrastructure Design Studies LAGUNA (Grant Agreement No. 212343 FP7-INFRA-2007-1), LAGUNA-LBNO (Grant Agreement No. 284518 FP7-INFRA-2011-1), and project AIDA (Grant Agreement No. 262025).

We are also grateful to the CERN Management for their encouragements, recognising the importance of CERN in the coherent definition of a potential future program for the European neutrino community.

A Appendix: Event rates with neutrino beams

The proposed prototype will collect a large number of neutrino interactions if a neutrino beam will be built in the North Area.

These interactions will be used to measure neutrino cross section on Argon in the GeV region. The lack of a precise knowledge of the neutrino-nucleus interactions at this energy region is one of the main sources of systematic uncertainties in long baseline neutrino oscillation experiments. The measurements of ν_μ cross section still have large uncertainties while no measurements exist of ν_e cross section at this energy. The situation is even worse for antineutrinos, where cross-sections presently have uncertainties above 10-20%. This is an issue for experiments relying on the ratio of neutrinos to antineutrinos to measure the CP violation phase.

LBNO presently assumed systematic errors for its MH and CPV sensitivity studies at the level of 5% for the signal [1]. The predicted sensitivities of LBNO could be improved if one could show that these systematic errors could be reduced [155]. Other future experiments, looking for CP violation in the leptonic sector, aim for systematic uncertainties of the order of (1-2)% and this will only be possible if precise measurements of electron and muon flavours cross sections for both neutrinos and antineutrinos will be available.

In this appendix we have computed the expected event rates in the LBNO prototype for two different beams: a conventional neutrino beam (CENF) [156] in which mainly ν_μ are produced by the decay of pions and kaons with a small intrinsic component of ν_e and the NuSTORM beam [6] in which $\bar{\nu}_e$ and ν_μ (ν_e and $\bar{\nu}_\mu$) are produced from the decay of μ^- (μ^+). The event rates are obtained with the GENIE neutrino simulation program [157] in which we simulated the proposed prototype and the two different beam configurations.

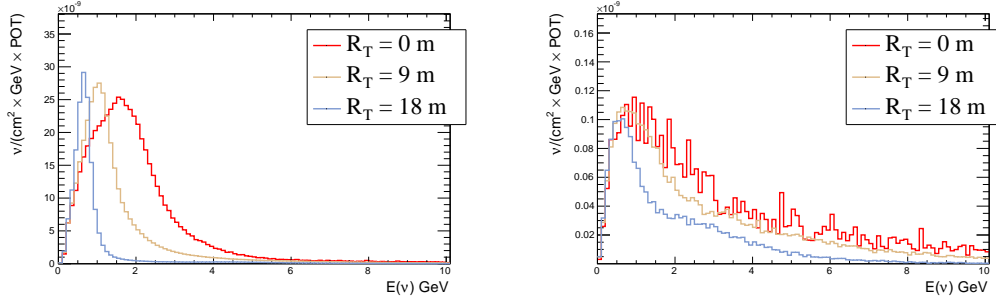
1 CENF conventional beam

For the conventional neutrino beam we used the CENF fluxes that are produced by the SPS accelerating protons to 100 GeV/c [158]. To avoid large pile-up the beam is produced off-axis with respect to the detector. The center of the prototype is at a radial distance from the axis of the beam of ~ 9 m.

The detector is rotated by 45 degrees with respect to the beam direction to maximize the sharing on the two readout views of the ionization produced by particles coming from neutrino interactions.

The CENF neutrino fluxes are available for ν_μ and ν_e for the positive and negative horn polarities and for different radial bins R_T with R_T going from 0 to 25 meters. An example of the fluxes with the positive horn polarity is shown in ??.

The neutrino fluxes are used to obtain the event rates with the GENIE neutrino event generator.

FIG. 158: Expected CENF fluxes for ν_μ (left) and ν_e (right) for different off-axis distances.

Int. Type	N_{exp} ν_μ	Fraction (%)	Mean $E(\nu_\mu)$ (GeV)	N_{exp} ν_e	Fraction (%)	Mean $E(\nu_e)$ (GeV)
Inclusive	559168	100	2.44	9734	100	3.86
CC	411004	73.5	2.47	7312	75.1	3.87
CCQE	235786	42.2	1.37	2448	25.1	2.44

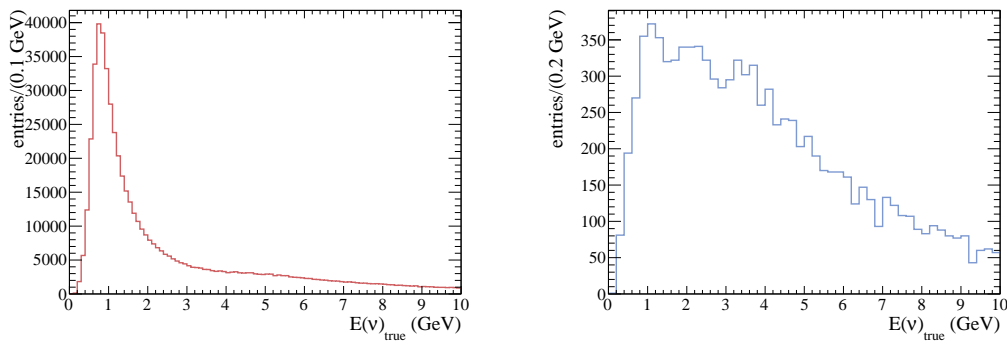
TABLE XXIII: Expected ν_μ and ν_e event rates and mean neutrino energy for different neutrino interaction types, in the Liquid Argon active volume, for an exposure of 10^{19} POT and for $E(\nu) < 10$ GeV.

The geometry of the prototype is simulated and the neutrino cross section for the different materials that compose the detector are computed according to the predefined models included in GENIE.

We computed the event rate for an exposure of 10^{19} POT. We only counted neutrino interactions occurring inside the active volume of the prototype corresponding to 300 tons of Liquid Argon.

The number of neutrino interactions inside the active volume is shown in ?? for ν_μ and ν_e . The energy spectrum of the interacting neutrinos is shown in ??.

This large data sample will allow to perform precise measurements of ν_μ cross sections on Argon in different exclusive channels. As far as the ν_e cross section are concerned, the expected fraction of ν_e interactions inside the active volume is 1.7% but the large mass of the prototype will allow to select a sizable data sample to measure also ν_e cross section.

FIG. 159: True neutrino energy for the inclusive sample of neutrino interactions occurring inside the prototype active volume for 10^{19} POT for ν_μ (left) and ν_e (right) interactions.

Int. Type	N_{exp} $\bar{\nu}_\mu$	Fraction (%)	Mean $E(\bar{\nu}_\mu)$ (GeV)	N_{exp} $\bar{\nu}_e$	Fraction (%)	Mean $E(\bar{\nu}_e)$ (GeV)
Inclusive	167837	100	2.47	2999	100	3.96
CC	108831	64.8	2.59	2059	68.7	4.04
CCQE	74339	44.3	1.59	887	29.6	2.79

TABLE XXIV: Expected $\bar{\nu}_\mu$ and $\bar{\nu}_e$ event rates and mean neutrino energy for different neutrino interaction types, in the Liquid Argon active volume, for an exposure of 10^{19} POT and for $E(\nu) < 10$ GeV.

For this off-axis configuration the event pile-up is expected to be small: by assuming that in each spill there will be 10^{13} protons, we expect ~ 0.6 neutrino interactions per spill in the active volume.

We have also performed the simulation in the case of horns' opposite polarity in which mainly $\bar{\nu}_\mu$ and $\bar{\nu}_e$ are produced. The expected event rates for $\bar{\nu}_\mu$ and $\bar{\nu}_e$ in the active volume of the prototype for an exposure of 10^{19} POT is shown in ??.

2 Muon storage ring - NuSTORM

We have also computed the expected event rates using neutrinos produced by the decays of stored muons (NuSTORM proposal). In this case we have assumed muon decays in a straight line of 226 m with the end point of the straight line at a distance of 55 m from the center of the detector. The neutrino fluxes have been simulated using a software developed by the NuSTORM collaboration.

We have simulated 10^{16} muon decays that, assuming a 1/1000 ratio between the number of useful muons and the number of protons would roughly correspond to an exposure of 10^{19} POT (the same exposure used for the event rates with the CENF). The spectrum of ν_μ and ν_e produced by muons decays in NuSTORM and arriving to a disk with a 3 m radius at a distance of 50 m from the end of the straight line is shown in ??.

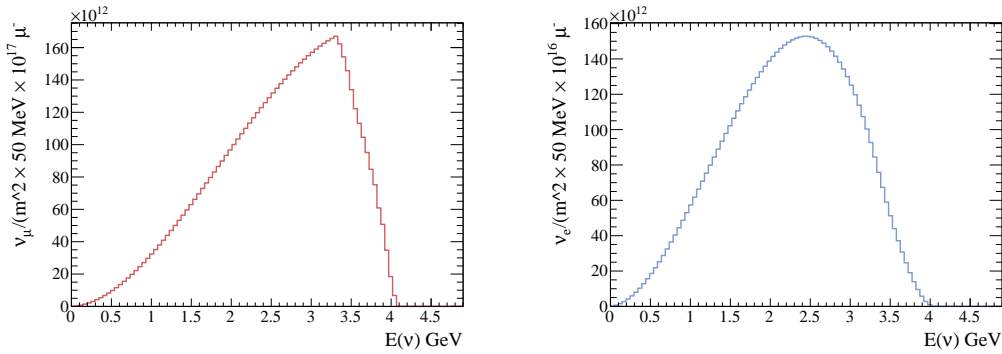


FIG. 160: Expected NuSTORM fluxes for ν_μ (left) and $\bar{\nu}_e$ (right) ($\bar{\nu}_\mu$ and ν_e) produced in μ^- (μ^+) decays.

The expected number of events in the active volume of the prototype for the neutrino fluxes of ?? are shown in ???? for the μ^- and μ^+ decays respectively. The energy spectra of the interacting

neutrinos for the inclusive samples are shown in ????.

Int. Type	N_{exp} ν_μ	Fraction (%)	Mean $E(\nu_\mu)$ (GeV)	N_{exp} $\bar{\nu}_e$	Fraction (%)	Mean $E(\bar{\nu}_e)$ (GeV)
Inclusive	97251	100	2.82	34794	100	2.51
CC	72213	74.2	2.82	23645	67.9	2.52
CCQE	23284	24.0	2.60	11123	32.0	2.36

TABLE XXV: Expected ν_μ and $\bar{\nu}_e$ event rates and mean neutrino energy for different neutrino interaction types and for 10^{16} μ^- decays.

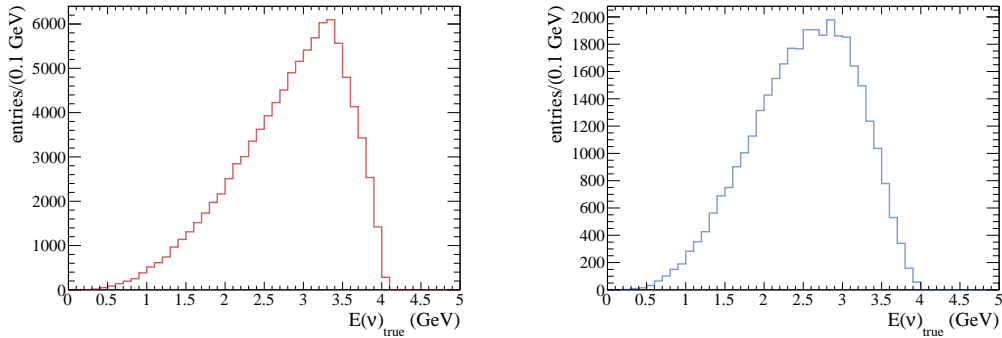


FIG. 161: True neutrino energy for the inclusive sample of neutrino interactions occurring inside the prototype active volume for 10^{16} μ^- decays for ν_μ (left) and $\bar{\nu}_e$ (right) interactions.

Int. Type	N_{exp} $\bar{\nu}_\mu$	Fraction (%)	Mean $E(\bar{\nu}_\mu)$ (GeV)	N_{exp} ν_e	Fraction (%)	Mean $E(\nu_e)$ (GeV)
Inclusive	40328	100	2.86	86074	100	2.46
CC	27538	68.3	2.87	64071	74.4	2.46
CCQE	11991	29.7	2.73	23288	27.1	2.25

TABLE XXVI: Expected $\bar{\nu}_\mu$ and ν_e event rates and mean neutrino energy for different neutrino interaction types and for 10^{16} μ^+ decays.

One of main advantage of the NuSTORM beam with respect to the CENF one will be to produce a large statistical sample of ν_e and $\bar{\nu}_e$ interactions, while in the CENF beam, ν_e are expected to be only 1.7% of the total flux. This will allow to perform precise measurements of ν_e cross section that are currently completed unknown. The systematic error on the absolute flux is also expected to be much smaller for NuSTORM compared to CENF, since neutrinos are produced in very well-defined muon decay processes. One should also stress that the ratio of neutrinos to antineutrinos is very well defined. The energy of the beam is very well defined by the ring energy and could in principle be changed to study systematics associated to the energy scale.

With this data sample it will be possible to precisely investigate cross section differences between ν_e and ν_μ and this will be of fundamental importance for future experiments looking for CP violation

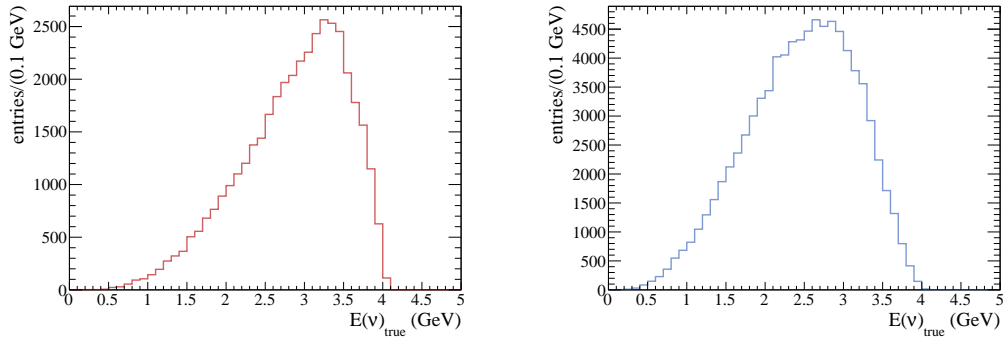


FIG. 162: True neutrino energy for the inclusive sample of neutrino interactions occurring inside the prototype active volume for 10^{16} μ^+ decays for $\bar{\nu}_\mu$ (left) and ν_e (right) interactions.

and the mass hierarchy in the leptonic sector. All these experiments aim to measure CP and the mass hierarchy by observing ν_e ($\bar{\nu}_e$) appearance in ν_μ ($\bar{\nu}_\mu$) beams. In such experiments, systematic uncertainties are constrained mainly by observing the unoscillated ν_μ flux at the Near Detector, while after the oscillation ν_e interactions are observed at the Far Detector. As a consequence, if ν_e/ν_μ cross section differences will not be precisely measured, they will have a large impact on the systematic uncertainties and on the discovery potential of the experiments.

B Appendix: Test of full-scale APA's for LBNE

In Collaboration with LBNE colleagues, we have started to investigate the possibility to insert in the cryostat for the $6 \times 6 \times 6\text{m}^3$ (see ??) the APA prototype detector developed at FNAL for the LBNE project. This prototype instruments a parallelepiped volume of $\sim 267\text{ m}^3$ (374 ton LAr), with dimensions $H = 7.20\text{m}$, $W = 7.48\text{m}$, $L = 5.16\text{ m}$, vertically split into two drift volumes by a double face vertical wire chamber (APA) positioned at half-width, with 2 vertical cathode planes on its right and on its left. The drift length results of 3.74m , requiring a negative high voltage in the range $150\text{ kV} - 380\text{ kV}$ on the 2 cathodes.

It appears possible to insert the LBNE APA detector in the LAGUNA/LBNO DLAr cryostat, although the dimensions of the vessel will likely have to be increased slightly compared to the ones presented in this document. To cope with its vertical dimension and with the position of the signal, HV and suspension feedthroughs, a dedicated top thermal insulation/support cap will be required (see ????, with adjustable dimensions). This poses no issue as the cap will be welded and removable without interference with the overall structure of the storage vessel. A detailed design is being developed and will be ready by the time the vessel needs to be procured.

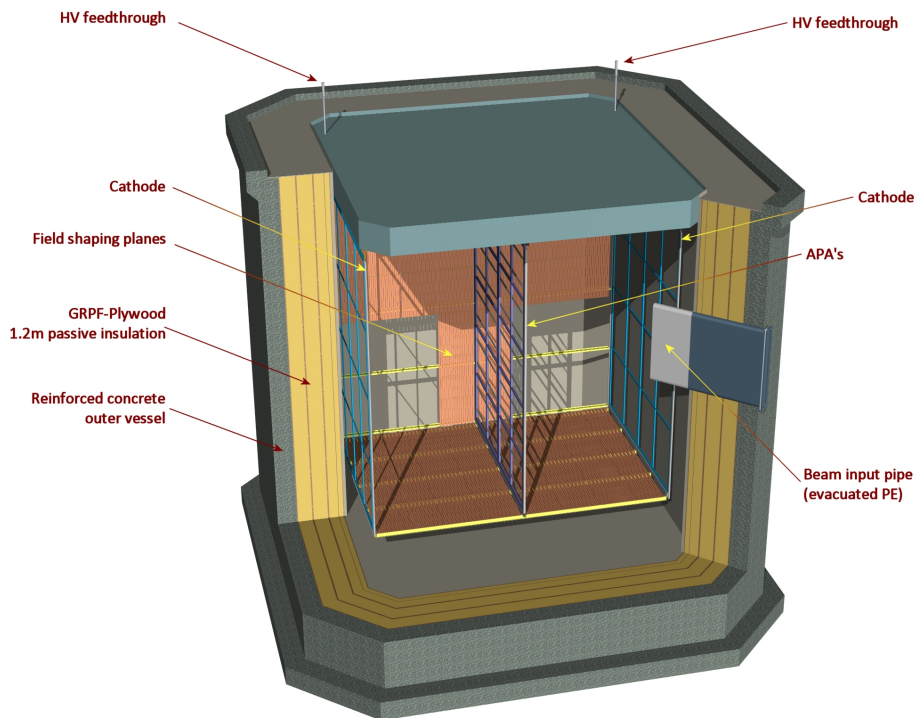


FIG. 163: Perspective view of the $6 \times 6 \times 6\text{m}^3$ vessel and the inserted APA + cathode chamber based on the LBNE design.

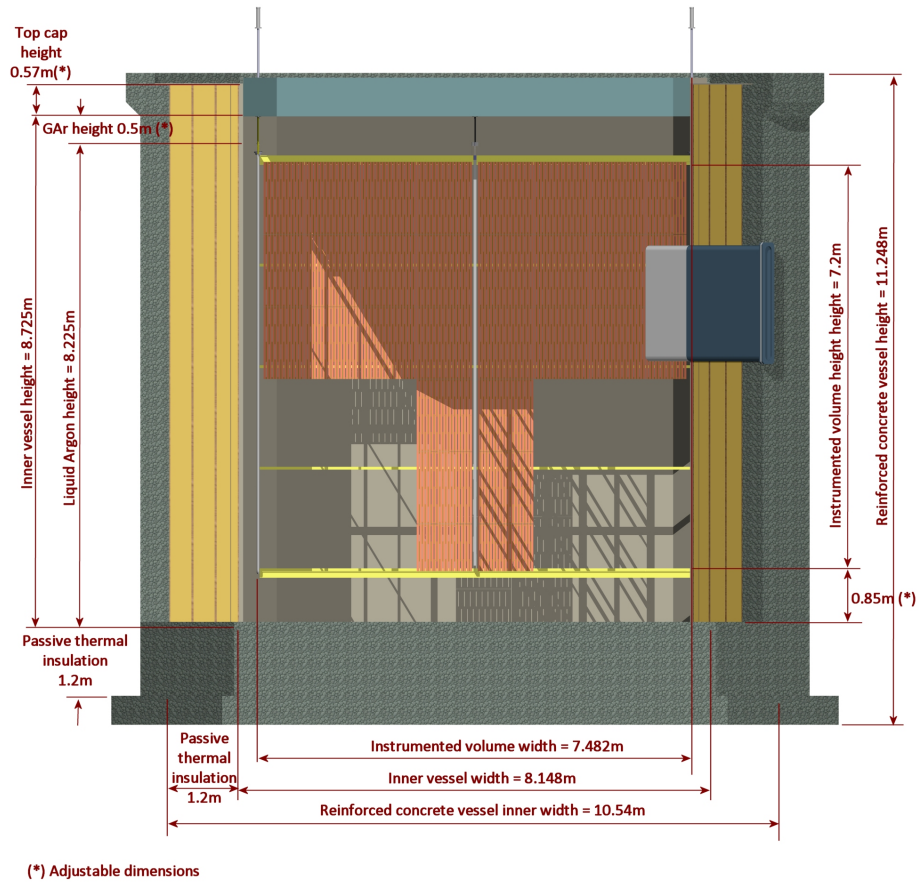


FIG. 164: Side view of the $6 \times 6 \times 6\text{m}^3$ vessel and the inserted APA + cathode chamber based on the LBNE design.

-
- [1] A. Stahl, C. Wiebusch, A. Guler, M. Kamiscioglu, R. Sever, *et al.*, “Expression of Interest for a very long baseline neutrino oscillation experiment (LBNO), CERN-SPSC-2012-021, SPSC-EOI-007,” tech. rep., CERN, 2012.
- [2] A. Rubbia, “Experiments for CP violation: A Giant liquid argon scintillation, Cerenkov and charge imaging experiment?,” pp. 321–350, 2004, hep-ph/0402110.
- [3] C. Adams *et al.*, “Scientific Opportunities with the Long-Baseline Neutrino Experiment,” 2013, 1307.7335.
- [4] K. Abe, T. Abe, H. Aihara, Y. Fukuda, Y. Hayato, *et al.*, “Letter of Intent: The Hyper-Kamiokande Experiment — Detector Design and Physics Potential —,” 2011, 1109.3262.
- [5] M. Antonello, D. Bagliani, B. Baibussinov, H. Bilokon, F. Boffelli, *et al.*, “Search for ‘anomalies’ from neutrino and anti-neutrino oscillations at $\Delta_m^2 \sim 1eV^2$ with muon spectrometers and large LAr-TPC imaging detectors,” 2012, 1203.3432.
- [6] P. Kyberd *et al.*, “nuSTORM - Neutrinos from STORed Muons: Letter of Intent to the Fermilab Physics Advisory Committee,” 2012, 1206.0294.
- [7] W. Bonivento, A. Boyarsky, H. Dijkstra, U. Egede, M. Ferro-Luzzi, *et al.*, “Proposal to Search for Heavy Neutral Leptons at the SPS,” 2013, 1310.1762.
- [8] A. Bross, R. Wands, R. Bayes, A. Laing, F. Soler, *et al.*, “A Toroidal Magnetised Iron Neutrino Detector (MIND) for a Neutrino Factory,” *Phys.Rev.ST Accel.Beams*, vol. 16, p. 081002, 2013, 1306.5327.
- [9] C. Rubbia, “The Liquid Argon Time Projection Chamber: A New Concept for Neutrino Detectors,” 1977.
- [10] E. Aprile, K. Giboni, and C. Rubbia, “A STUDY OF IONIZATION ELECTRONS DRIFTING LARGE DISTANCES IN LIQUID AND SOLID ARGON,” *Nucl.Instrum.Meth.*, vol. A241, p. 62, 1985.
- [11] F. Arneodo *et al.*, “Performance Of A Liquid Argon Time Projection Chamber Exposed To The WANF Neutrino Beam,” *Phys.Rev.*, vol. D74, p. 112001, 2006, physics/0609205.
- [12] P. Cennini, S. Cittolin, J. Revol, C. Rubbia, W. Tian, *et al.*, “Performance of a 3-ton liquid argon time projection chamber,” *Nucl.Instrum.Meth.*, vol. A345, pp. 230–243, 1994.
- [13] F. Arneodo, A. Badertscher, B. Baibusinov, G. Battistoni, P. Benetti, *et al.*, “Performance of the 10-m**3 ICARUS liquid argon prototype,” *Nucl.Instrum.Meth.*, vol. A498, pp. 292–311, 2003.
- [14] S. Amerio *et al.*, “Design, construction and tests of the ICARUS T600 detector,” *Nucl.Instrum.Meth.*, vol. A527, pp. 329–410, 2004.
- [15] F. Arneodo, B. Badelek, A. Badertscher, B. Baibusinov, M. Baldo-Ceolin, *et al.*, “Observation of long ionizing tracks with the ICARUS T600 first half-module,” *Nucl.Instrum.Meth.*, vol. A508, pp. 287–294, 2003.
- [16] S. Amoruso *et al.*, “Measurement of the mu decay spectrum with the ICARUS liquid argon TPC,” *Eur.Phys.J.*, vol. C33, pp. 233–241, 2004, hep-ex/0311040.
- [17] S. Amoruso, M. Antonello, P. Aprili, F. Arneodo, A. Badertscher, *et al.*, “Analysis of the liquid argon purity in the ICARUS T600 TPC,” *Nucl.Instrum.Meth.*, vol. A516, pp. 68–79, 2004.
- [18] S. Amoruso *et al.*, “Study of electron recombination in liquid argon with the ICARUS TPC,”

- Nucl.Instrum.Meth.*, vol. A523, pp. 275–286, 2004.
- [19] A. Ankowski *et al.*, “Measurement of through-going particle momentum by means of multiple scattering with the ICARUS T600 TPC,” *Eur.Phys.J.*, vol. C48, pp. 667–676, 2006, hep-ex/0606006.
- [20] A. Ankowski *et al.*, “Energy reconstruction of electromagnetic showers from pi0 decays with the ICARUS T600 Liquid Argon TPC,” *Acta Phys.Polon.*, vol. B41, pp. 103–125, 2010, 0812.2373.
- [21] C. Rubbia, M. Antonello, P. Aprili, B. Baibussinov, M. B. Ceolin, *et al.*, “Underground operation of the ICARUS T600 LAr-TPC: first results,” *JINST*, vol. 6, p. P07011, 2011, 1106.0975.
- [22] A. Rubbia, “Underground Neutrino Detectors for Particle and Astroparticle Science: The Giant Liquid Argon Charge Imaging Experiment (GLACIER),” *J.Phys.Conf.Ser.*, vol. 171, p. 012020, 2009, 0908.1286.
- [23] A. Badertscher *et al.*, “First operation and performance of a 200 lt double phase LAr LEM-TPC with a 40×76 cm² readout,” *JINST*, vol. 8, p. P04012, 2013, 1301.4817.
- [24] A. Badertscher, A. Curioni, U. Degunda, L. Epprecht, A. Gendotti, *et al.*, “First operation and drift field performance of a large area double phase LAr Electron Multiplier Time Projection Chamber with an immersed Greinacher high-voltage multiplier,” *JINST*, vol. 7, p. P08026, 2012, 1204.3530.
- [25] A. Badertscher, A. Curioni, L. Knecht, D. Lussi, A. Marchionni, *et al.*, “First operation of a double phase LAr Large Electron Multiplier Time Projection Chamber with a two-dimensional projective readout anode,” *Nucl.Instrum.Meth.*, vol. A641, pp. 48–57, 2011, 1012.0483.
- [26] A. Badertscher, L. Knecht, M. Laffranchi, D. Lussi, A. Marchionni, *et al.*, “Operation of a double-phase pure argon Large Electron Multiplier Time Projection Chamber: Comparison of single and double phase operation,” *Nucl.Instrum.Meth.*, vol. A617, pp. 188–192, 2010, 0907.2944.
- [27] M. Chefdeville, “RD51, a world-wide collaboration for the development of micro pattern gaseous detectors,” *J.Phys.Conf.Ser.*, vol. 309, p. 012017, 2011.
- [28] F. Sauli, “GEM: A new concept for electron amplification in gas detectors,” *Nucl.Instrum.Meth.*, vol. A386, pp. 531–534, 1997.
- [29] Y. Giomataris, P. Rebourgeard, J. Robert, and G. Charpak, “MICROMEGAS: A High granularity position sensitive gaseous detector for high particle flux environments,” *Nucl.Instrum.Meth.*, vol. A376, pp. 29–35, 1996.
- [30] A. Breskin, R. Alon, M. Cortesi, R. Chechik, J. Miyamoto, *et al.*, “A Concise review on THGEM detectors,” *Nucl.Instrum.Meth.*, vol. A598, pp. 107–111, 2009, 0807.2026.
- [31] A. Rubbia, “Future liquid Argon detectors,” *Nucl.Phys.Proc.Suppl.*, vol. 235-236, pp. 190–197, 2013, 1304.0127.
- [32] A. Cervera, A. Laing, J. Martin-Albo, and F. J. P. Soler, “Performance of the MIND detector at a Neutrino Factory using realistic muon reconstruction,” *Nucl. Instrum. Meth.*, vol. A624, pp. 601–614, 2010, 1004.0358.
- [33] W. Willis and V. Radeka, “Liquid Argon Ionization Chambers as Total Absorption Detectors,” *Nucl.Instrum.Meth.*, vol. 120, p. 221, 1974.
- [34] S. Schuwalow, “Calorimetry at the ILC detectors,” *Nucl.Instrum.Meth.*, vol. A598, pp. 258–263, 2009.
- [35] F. Simon, “Particle Showers in a Highly Granular Hadron Calorimeter,” *J.Phys.Conf.Ser.*, vol. 293,

- p. 012073, 2011, 1008.2318.
- [36] D. Lussi, *Study of the response of the novel LAr LEM-TPC detector exposed to cosmic rays and a charged particle beam*. PhD thesis, ETH Zurich, 2013.
 - [37] C. Andreopoulos, “The GENIE neutrino Monte Carlo generator,” *Acta Phys. Polon.*, vol. B40, pp. 2461–2475, 2009.
 - [38] D. Rowntree *et al.*, “ π^+ absorption on N and Ar,” *Phys.Rev.*, vol. C60, p. 054610, 1999.
 - [39] B. A. Younglove and H. J. M. Hanley, “The Viscosity and Thermal Conductivity Coefficients of Gaseous and Liquid Argon,” *J. Phys. Chem. Ref. Data*, vol. 15, p. 1323, 1986.
 - [40] C. Ramsauer, “Über den wirkungsquerschnitt der gasmoleküle gegenüber langsamen elektronen,” *Ann. Phys.*, vol. 369, no. 6, pp. 513–540, 1921.
 - [41] H. N. Kucukarpaci and J. Lucas, “Electron swarm parameters in argon and krypton,” *J. Phys. D*, vol. 14, p. 2001, 1981.
 - [42] S. Biagi, “A multiterm boltzmann analysis of drift velocity, diffusion, gain and magnetic-field effects in argon-methane-water-vapour mixtures,” *Nucl. Instr. and Meth. A*, vol. 283, p. 716, 1989.
 - [43] F. Sauli, “Principles of operation of multiwire proportional and drift chambers,” *CERN 77-09; Academic lecture*, 1977.
 - [44] Y. Nakamura and M. Kurachi, “Electron transport paramters in argon and its momentum transfer cross section,” *J. Phys. D*, vol. 21, p. 718, 1988.
 - [45] M. Suzuki, T. Taniguchi, and H. Tagashira, “Momentum transfer cross section of argon deduced from electron drift velocity data,” *J. Phys. D*, vol. 23, p. 842, 1990.
 - [46] J. Lekner, “Motion of Electrons in Liquid Argon,” *Phys. Rev.*, vol. 158, p. 130, 1967.
 - [47] W. Walkowiak, “Drift velocity of free electrons in liquid argon,” *Nucl. Instr. and Meth. A*, vol. 449, p. 288, 2000.
 - [48] A. Badertscher *et al.*, “Construction and operation of a Double Phase LAr Large Electron Multiplier Time Projection Chamber,” *arXiv:0811.3384v1 [physics.ins-det]*, 2008.
 - [49] S. Amoruso *et al.*, “Analysis of the liquid argon purity in the ICARUS T600 TPC,” *Nucl. Instr. and Meth. A*, no. 516, p. 68, 2004.
 - [50] E. Buckley *et al.*, “A study of ionization electrons drifting over large distances in liquid argon,” *Nucl. Instr. and Meth. A*, vol. 275, no. 2, pp. 364 – 372, 1989.
 - [51] L. S. Miller, S. Howe, and W. E. Spear, “Charge Transport in Solid and Liquid Ar, Kr, and Xe,” *Phys. Rev.*, vol. 166, p. 871, 1967.
 - [52] A. Badertscher, A. Curioni, U. Degunda, L. Epprecht, A. Gendotti, S. Horikawa, L. Knecht, D. Lussi, A. Marchionni, G. Natterer, K. Nguyen, F. Resnati, A. Rubbia, and T. Viant, “First operation and drift field performance of a large area double phase LAr Electron Multiplier Time Projection Chamber with an immersed Greinacher high-voltage multiplier,” *JINST*, vol. 7, p. P08026, 2012.
 - [53] D. W. Swan, “Drift velocity of electrons in liquid argon, and the influence of moecular impurities,” *Proc. Phys. Soc.*, vol. 83, p. 659, 1964.
 - [54] E. Shibamura, T. Takahashi, S. Kubota, and T. Doke, “Ratio of diffusion coefficient to mobility for

- electrons in liquid argon,” *Phys. Rev. A*, vol. 20, p. 2547, 1979.
- [55] A. Einstein, “Über die von der molekularkinetischen theorie der wärme geforderte bewegung von in ruhenden flüssigkeiten suspendierten teilchen,” *Ann. Phys.*, vol. 322, no. 8, p. 549, 1905.
- [56] B. A. Dolgoshein *et al.*, “New method of registration of ionizing-particle tracks in condensed matter,” *JETP Lett.*, vol. 11, pp. 351–353, 1970.
- [57] E. M. Gushchin *et al.*, “Emission of hot electrons from liquid and solid argon and xenon,” *Sov. Phys. JETP*, vol. 55, pp. 860–862, 1982.
- [58] A. Borghesani *et al.*, “Electron transmission through the Ar liquid-vapor interface,” *Phys. Lett.*, vol. 149, pp. 481–484, 1990.
- [59] E. L. Murphy and R. H. Good, Jr, “Thermionic emission, field emission, and the transition region,” *Phys. Rev.*, vol. 102, pp. 1464–1473, 1956.
- [60] T. Sometani and K. Hasebe, “Method for solving electrostatic problems having a simple dielectric boundary,” *Am. J. Phys.*, vol. 45, pp. 918–921, 1977.
- [61] A. I. Bolozdynya, “Two-phase emission detectors and their applications,” *Nucl. Instr. Meth.*, vol. A422, pp. 314–320, 1999.
- [62] R. Lagushenko and J. Maya, “Electron swarm parameters in rare gases and mixtures,” *J. Appl. Phys.*, vol. 55, pp. 3293–3300, 1984.
- [63] T. H. V. T. Dias *et al.*, “A unidimensional Monte Carlo simulation of electron drift velocities and electroluminescence in argon, krypton and xenon,” *J. Phys. D: Appl. Phys.*, vol. 19, pp. 527–545, 1986.
- [64] C. Monteiro, J. Lopes, J. Veloso, and J. dos Santos, “Secondary scintillation yield in pure argon,” *Phys. Lett. B*, vol. 668, p. 167, 2008.
- [65] E. M. Gushchin *et al.*, “Electron dynamics in condensed argon and xenon,” *Sov. Phys. JETP*, vol. 55, pp. 650–655, 1982.
- [66] T. Doke, K. Masuda, and E. Shibamura, “Estimation of absolute photon yields in liquid argon and xenon for relativistic (1 mev) electrons,” *Nuclear Instruments and Methods in Physics Research Section A: Accelerators, Spectrometers, Detectors and Associated Equipment*, vol. 291, no. 3, pp. 617 – 620, 1990.
- [67] S. Kubota, M. Hishida, and J. Raun, “Evidence for a triplet state of the self-trapped exciton states in liquid argon, krypton and xenon,” *Journal of Physics C: Solid State Physics*, vol. 11, no. 12, p. 2645, 1978.
- [68] T. Strickler and E.T.Arakawa, “Optical emission from argon excited by alpha particles: Quenching studies,” *J. Chem. Phys.*, vol. 41, p. 1783, 1964.
- [69] C. M. B. Monteiro *et al.*, “An Argon Gas Proportional Scintillation Counter With UV Avalanche Photodiode Scintillation Readout,” *IEEE Trans. Nucl. Sci.*, vol. 48, pp. 1081–1086, 2001.
- [70] E. Aprile *et al.*, “Dark Matter Results from 100 Live Days of XENON100 Data,” *arXiv:1104.2549v1 [astro-ph.CO]*, 2010.
- [71] P. Benetti, R. Acciarri, F. Adamo, B. Baibussinov, M. Baldo-Ceolin, M. Belluco, F. Calaprice, E. Calligarich, M. Cambiaghi, F. Carbonara, F. Cavanna, S. Centro, A. Cocco, F. D. Pompeo, N. Ferrari, G. Fiorillo, C. Galbiati, V. Gallo, L. Grandi, A. Ianni, G. Mangano, G. Meng, C. Montanari, O. Palamara, L. Pandola, F. Pietropaolo, G. Raselli, M. Rossella, C. Rubbia, A. Szec, S. Ventura, and C. Vignoli,

- “First results from a dark matter search with liquid argon at 87 K in the Gran Sasso underground laboratory,” *Astroparticle Physics*, vol. 28, no. 6, pp. 495 – 507, 2008.
- [72] A. Rubbia, “ArDM: A Ton-scale liquid Argon experiment for direct detection of dark matter in the universe,” *J.Phys.Conf.Ser.*, vol. 39, pp. 129–132, 2006, hep-ph/0510320.
- [73] Y. P. Raizer, *Gas Discharge Physics*. Springer-Verlag, 1991.
- [74] S. F. Biagi, “Monte Carlo simulation of electron drift and diffusion in counting gases under the influence of electric and magnetic fields,” *Nucl. Instr. Meth.*, vol. A421, pp. 234–240, 1999.
- [75] R. Veenhof. <http://garfield.web.cern.ch/garfield> [11/2011].
- [76] I. Velchev, W. Hogervorst, and W. Ubachs, “Precision VUV spectroscopy of Ar I at 105 nm,” *J. Phys. B: At. Mol. Phys.*, vol. 32, p. L511, 1999.
- [77] T. Ficker, “Statistics of Electron Avalanches and Streamers,” *Acta Polytechnica*, vol. 47, p. 31, 2007.
- [78] W. H. Furry, “On Fluctuation Phenomena in the Passage of High Energy Electrons through Lead,” *Phys. Rev.*, vol. 52, pp. 569–581, 1937.
- [79] D. W. Swan, “Electron Attachment Processes in Liquid Argon containing Oxygen or Nitrogen Impurity,” *Proc. Phys. Soc.*, vol. 82, p. 74, 1963.
- [80] G. Bakale, U. Sowada, and W. Schmidt, “Effects of an Electric Field on Electron Attachment to SF₆, N₂O and O₂ in Liquid Argon and Xenon,” *J. Phys. Chem.*, vol. 80, no. 23, p. 2556, 1976.
- [81] S. Suzuki, “Liquid Argon Purification for ICARUS,” in *Proceeding of the 4th Miniworkshop on Low Level Counting and Space-Based use of Liquid Argon and Xenon Detectors*, Waseda University, April 1990.
- [82] R. Andrews, W. Jaskierny, H. Jöstlein, C. Kendziora, S. Pordes, and T. Tope, “A system to test the effect of materials on electron drift lifetime in liquid argon and the effect of water,” *Nucl. Instr. and Meth. A*, vol. 608, p. 251, 2009.
- [83] H. Chen *et al.*, “Proposal for a New Experiment Using the Booster and NuMI Neutrino Beamlines: MicroBooNE,” 2007.
- [84] T. Akiri *et al.*, “The 2010 Interim Report of the Long-Baseline Neutrino Experiment Collaboration Physics Working Groups,” *arXiv*, 2011, 1110.6249.
- [85] A. Rubbia, “The LAGUNA design study: Towards giant liquid based underground detectors for neutrino physics and astrophysics and proton decay searches,” *Acta Phys.Polon.*, vol. B41, pp. 1727–1732, 2010.
- [86] A. Curioni, L. Epprecht, A. Gendotti, L. Knecht, D. Lussi, *et al.*, “Towards a liquid Argon TPC without evacuation: filling of a 6 m³ vessel with argon gas from air to ppm impurities concentration through flushing,” *J.Phys.Conf.Ser.*, vol. 308, p. 012024, 2011, 1009.4073.
- [87] R. Acciarri, M. Antonello, B. Baibussinov, M. Baldo-Ceolin, P. Benetti, F. Calaprice, E. Calligarich, M. Cambiaghi, N. Canci, F. Carbonara, F. Cavanna, S. Centro, A. Cocco, F. D. Pompeo, G. Fiorillo, C. Galbiati, V. Gallo, L. Grandi, G. Meng, I. Modena, C. Montanari, O. Palamara, L. Pandola, F. Pietropaolo, G. Raselli, M. Roncadelli, M. Rossella, C. Rubbia, E. Segreto, A. Szelc, F. Tortorici, S. Ventura, and C. Vignoli, “Effects of Nitrogen and Oxygen contamination in liquid Argon,” *Nucl. Phys. Proc. Suppl.*, vol. 197, no. 1, p. 70, 2009.
- [88] T. H. Dey and T. J. Lewis, “Ion mobility and liquid motion in liquefied argon,” *Journal of Physics D:*

- Applied Physics*, vol. 1, no. 8, p. 1019, 1968.
- [89] A. Bueno, Z. Dai, Y. Ge, M. Laffranchi, A. Melgarejo, *et al.*, “Nucleon decay searches with large liquid argon TPC detectors at shallow depths: Atmospheric neutrinos and cosmogenic backgrounds,” *JHEP*, vol. 0704, p. 041, 2007, hep-ph/0701101.
- [90] V. Ushakov, “Behavior of liquids in strong electric fields,” in *Impulse Breakdown of Liquids*, Power Systems, pp. 1–51, Springer Berlin Heidelberg, 2007.
- [91] F. Bay, C. Cantini, S. Murphy, F. Resnati, A. Rubbia, *et al.*, “Evidence of electric breakdown induced by bubbles in liquid argon,” 2014, 1401.2777.
- [92] W. Rogowski, “Die elektrische festigkeit am rande des plattenkondensators,” *Archiv für Elektrotechnik*, vol. 12, no. 1, pp. 1–15, 1923.
- [93] A. Blatter, A. Ereditato, C. C. Hsu, S. Janos, I. Kreslo, *et al.*, “Experimental study of electric breakdowns in liquid argon at centimeter scale,” 2014, 1401.6693.
- [94] A. Breskin *et al.*, “A concise review on THGEM detectors,” *Nucl. Instrum. Meth. A*, vol. 598, no. 1, pp. 107–111, 2009.
- [95] F. Resnati, *Modeling, design and first operation of the novel double phase LAr LEM-TPC detector*. PhD thesis, ETH Zurich, 2012.
- [96] C. Monteiro, J. Lopes, J. Veloso, and J. dos Santos, “Secondary scintillation yield in pure argon,” *Phys.Lett.*, vol. B668, pp. 167–170, 2008.
- [97] R. Acciarri, M. Antonello, F. Boffelli, M. Cambiaghi, N. Canci, *et al.*, “Demonstration and Comparison of Operation of Photomultiplier Tubes at Liquid Argon Temperature,” *JINST*, vol. 7, p. P01016, 2012, 1108.5584.
- [98] V. Boccone *et al.*, “Development of wavelength shifter coated reflectors for the ArDM argon dark matter detector,” *JINST*, vol. 4, p. P06001, 2009, 0904.0246.
- [99] A. Bressan *et al.*, “Two-dimensional readout of GEM detectors,” *Nucl. Instrum. Meth. A*, vol. 425, no. 1-2, pp. 254–261, 1999.
- [100] W. Shockley, “Currents to Conductors Induced by a Moving Point Charge,” *J. Appl. Phys.*, vol. 9, no. 10, pp. 635–636, 1938.
- [101] S. Ramo, “Currents Induced by Electron Motion,” *Proc. of the IRE*, vol. 27, no. 9, pp. 584–585, 1939.
- [102] C. Cantini, L. Epprecht, A. Gendotti, S. Horikawa, S. Murphy, *et al.*, “Long-term operation of a double phase LAr LEM Time Projection Chamber with a simplified anode and extraction-grid design,” 2013, 1312.6487.
- [103] Y. Giomataris, P. Rebourgeard, J. Robert, and G. Charpak, “Micromegas: a high-granularity position-sensitive gaseous detector for high particle-flux environments,” *Nuclear Instruments and Methods in Physics Research Section A: Accelerators, Spectrometers, Detectors and Associated Equipment*, vol. 376, no. 1, pp. 29 – 35, 1996.
- [104] I. Giomataris, R. D. Oliveira, S. Andriamonje, S. Aune, G. Charpak, P. Colas, G. Fanourakis, E. Ferrer, A. Giganon, P. Rebourgeard, and P. Salin, “Micromegas in a bulk,” *Nuclear Instruments and Methods in Physics Research Section A: Accelerators, Spectrometers, Detectors and Associated Equipment*, vol. 560,

- no. 2, pp. 405 – 408, 2006.
- [105] A. Delbart, “Production and calibration of 9m2 of bulk-micromegas detectors for the readout of the nd280/tpcs of the {T2K} experiment,” *Nuclear Instruments and Methods in Physics Research Section A: Accelerators, Spectrometers, Detectors and Associated Equipment*, vol. 623, no. 1, pp. 105 – 107, 2010.
- [106] A. Delbart, D. Attie, J. Beucher, O. Besida, E. Ferrer-Ribas, *et al.*, “Micromegas for charge readout of double phase Liquid Argon TPCs,” *J.Phys.Conf.Ser.*, vol. 308, p. 012017, 2011.
- [107] K. Mavrokoridis, F. Ball, J. Carroll, M. Lazos, K. McCormick, *et al.*, “Optical Readout of a Two Phase Liquid Argon TPC using CCD Camera and THGEMs,” 2014, 1401.0525.
- [108] W. Walkowiak, “Drift velocity of free electrons in liquid argon,” *Nucl.Instrum.Meth.*, vol. A449, pp. 288–294, 2000.
- [109] S. Horikawa, A. Badertscher, L. Kaufmann, M. Laffranchi, A. Marchionni, *et al.*, “Feasibility of high-voltage systems for a very long drift in liquid argon TPCs,” *J.Phys.Conf.Ser.*, vol. 308, p. 012027, 2011, 1009.4908.
- [110] E. Bechetoille and H. Mathez, “CMOS Charge amplifier for liquid argon Time Projection Chamber detectors,” *WOLTE 8, Workshop On Low Temperature Electronics*, [in2p3-00339737], 2008.
- [111] C. Girerd, D. Autiero, B. Carlus, S. Gardien, J. Marteau, and W. Tromeur, “MicroTCA implementation of synchronous Ethernet-Based DAQ systems for large scale experiments,” *arXiv:0906.2325 [physics.ins-det]*, 2009.
- [112] P. group, “PICMG Advanced Mezzanine Card AMC.0 Specification R2.0,” 2006.
- [113] C. Amsler *et al.*, “First results on light readout from the 1-ton ArDM liquid argon detector for dark matter searches,” *JINST*, vol. 5, p. P11003, 2010, 1009.3641.
- [114] A. Marchionni *et al.*, “ArDM: a ton-scale LAr detector for direct Dark Matter searches,” *J. Phys. Conf. Ser.*, vol. 308, p. 012006, 2011, 1012.5967.
- [115] J. E. Campagne, S. C. D. Lorenzo, S. Drouet, D. Duchesneau, F. Dulucq, N. Dumont-Dayot, A. E. Berni, J. Favier, A. Gallas, B. Genolini, K. Hanson, N. Hauchecorne, R. Hermel, M. Imre, B. Ky, C. de La Taille, J. Maltese, A. Maroni, G. Martin-Chassard, T. N. Trung, J. Peyr, J. Pouthas, E. Rindel, P. Rosier, L. Sminor, J. Tassan, C. Thneau, E. Wanlin, and A. Zghiche, “Pmm 2 : R&d on triggerless acquisition for next generation neutrino experiments,” *Journal of Instrumentation*, vol. 6, no. 01, p. C01081, 2011.
- [116] S. C. Di Lorenzo, J. Campagne, F. Dulucq, C. De La Taille, G. Martin-Chassard, *et al.*, “PARISROC, a Photomultiplier Array Integrated Read Out Chip,” 2009, 0912.1269.
- [117] B. Genolini, P. Barrillon, S. Blin, J.-E. Campagne, B. Combettes, S. Conforti, A.-G. Dehaine, D. Duchesneau, F. Dulucq, N. Dumont-Dayot, J. Favier, F. Fouch, R. Hermel, C. de La Taille, G. Martin-Chassard, T. N. Trung, C. Prinnet, J. Peyr, J. Pouthas, L. Raux, E. Rindel, P. Rosier, J. Tassan-Viol, W. Wei, and A. Zghiche, “Pmm2: Large photomultipliers and innovative electronics for the next-generation neutrino experiment,” *Nuclear Instruments and Methods in Physics Research Section A: Accelerators, Spectrometers, Detectors and Associated Equipment*, vol. 610, no. 1, pp. 249 – 252, 2009.
- [118] P. Redhead, “Modeling the pump-down of a reversible adsorbed phase. ii. multilayer coverage,” *J. Vac.*

- Sci. Technol. A*, vol. 13, p. 2791, 1995.
- [119] J. F. O'Hanlon, *A User's Guide to Vacuum Technology*. John Wiley & Sons Inc., 3 ed., 2003.
- [120] P. Redhead, "Modeling the pump-down of a reversible adsorbed phase. i. monolayer and submonolayer initial coverage," *J. Vac. Sci. Technol. A*, vol. 13, p. 467, 1995.
- [121] R. Calder and G. Lewin, "Reduction of stainless-steel outgassing in ultra-high vacuum," *British Journal of Applied Physics*, vol. 18, no. 10, p. 1459, 1967.
- [122] D. Edwards, "An upper bound to the outgassing rate of metal surfaces," *J. Vac. Sci. Technol.*, vol. 14, p. 1030, 1977.
- [123] R. M. Yamamoto and J. Harvey, "Outgassing measurements and results used in designing the DOUBLET III neutral beam injector system," LBNL Paper LBL-9997, Lawrence Berkeley National Laboratory, 1979.
- [124] Y. Koyatsu, H. Miki, and F. Watanabe, "Measurements of outgassing rate from copper and copper alloy chambers," *Vacuum*, vol. 47, no. 6–8, pp. 709 – 711, 1996.
- [125] M. Wong, "Review of papers regarding vacuum system and materials," http://home.fnal.gov/~mlwong/outgas_rev.htm, March 2002 last checked: July 2012.
- [126] R. S. Barton and R. P. Govier, "A mass spectrometric study of the outgassing of some elastomers and plastics," *J. Vac. Sci. Technol.*, vol. 2, no. 3, pp. 113–122, 1965.
- [127] E. D. Erikson, T. G. Beat, D. D. Berger, and B. A. Frazier, "Vacuum outgassing of various materials," *J. Vac. Sci. Technol. A*, vol. 2, no. 2, pp. 206–210, 1984.
- [128] C. Montanari, M. Rossella, and C. Vignoli, "Measurement of outgassing rates of signal cables," tech. rep., ICARUS-TM-98/14, 1998.
- [129] A. Curioni, L. Epprecht, A. Gendotti, L. Knecht, D. Lussi, A. Marchionni, G. Natterer, F. Resnati, A. Rubbia, J. Coleman, M. Lewis, K. Mavrokoridis, K. McCormick, and C. Touramanis, "Towards a liquid Argon TPC without evacuation: filling of a 6 m³ vessel with argon gas from air to ppm impurities concentration through flushing," *J. Phys. Conf. Ser.*, vol. 308, p. 012024, July 2011, 1009.4073.
- [130] R. E. Trent, "Fundamentals of Molecular Sieve Design," in *Presented at the American Institute of Chemical Engineers Spring National Meeting*, Huston, Texas, April 19 1992.
- [131] R. M. Barrer and W. I. Stuart, "Ion Exchange and the Thermodynamics of Intracrystalline Sorption. I. Energetics of Occlusion of Argon and Nitrogen by Faujasite-Type Crystals," *Proc. R. Soc. Lond. A*, vol. 249, p. 464, 1959.
- [132] R. M. Dell, F. S. Stone, and P. F. Tiley, "The adsorption of oxygen and other gases on copper," *Trans. Faraday Soc.*, vol. 49, pp. 195–201, 1953.
- [133] T. N. Rhodin, "Low temperature oxidation of copper. i. physical mechanism1a," *Journal of the American Chemical Society*, vol. 72, no. 11, pp. 5102–5106, 1950, <http://pubs.acs.org/doi/pdf/10.1021/ja01167a079>.
- [134] D. Montanari *et al.*, "First scientific application of the membrane cryostat technology," 2013.
- [135] F. Arneodo *et al.*, "Performance of a liquid argon time projection chamber exposed to the cern west area neutrino facility neutrino beam," *Phys. Rev. D*, vol. 74, p. 112001, 2006.
- [136] A. Ankowski *et al.*, "Measurement of through-going particle momentum by means of multiple scattering with the ICARUS T600 TPC," *Eur. Phys. J. C*, vol. 48, no. 2, pp. 667–676, 2006.

- [137] Y. Ge *et al.*, “ e/π^0 separation in ICARUS liquid argon time projection chamber,” ICARUS-TM 3-5, ETH Zurich, 2003.
- [138] J. Rico, *First study of the stopping muon sample with the ICARUS T600 detector*. PhD thesis, ETH Zurich, 2002.
- [139] A. Martinez, *Study of accelerator neutrino interactions in a liquid argon TPC*. PhD thesis, Universidad de Granada, 2007.
- [140] R. Brun and F. Rademakers, “ROOT - An object oriented data analysis framework,” *Nucl. Instrum. Meth. A*, vol. 389, no. 1-2, pp. 81–86, 1997.
- [141] D. Lussi, “Qscan.” <http://indico.cern.ch/conferenceOtherViews.py?view=standard&confId=129268> [05/2012], 2011.
- [142] I. Hrivnacova, “The Geant4 virtual Monte Carlo,” *J. Phys. Conf. Ser.*, vol. 396, p. 022024, 2012.
- [143] S. Agostinelli, J. Allison, K. Amako, J. Apostolakis, H. Araujo, P. Arce, M. Asai, D. Axen, S. Banerjee, G. Barrand, F. Behner, L. Bellagamba, J. Boudreau, L. Broglia, A. Brunengo, H. Burkhardt, S. Chauvie, J. Chuma, R. Chytracek, G. Cooperman, G. Cosmo, P. Degtyarenko, A. Dell’Acqua, G. Depaola, D. Dietrich, R. Enami, A. Feliciello, C. Ferguson, H. Fesefeldt, G. Folger, F. Foppiano, A. Forti, S. Garelli, S. Giani, R. Giannitrapani, D. Gibin, J. G. Cadenas, I. Gonzalez, G. G. Abril, G. Greeniaus, W. Greiner, V. Grichine, A. Grossheim, S. Guatelli, P. Gumplinger, R. Hamatsu, K. Hashimoto, H. Hasui, A. Heikkinen, A. Howard, V. Ivanchenko, A. Johnson, F. Jones, J. Kallenbach, N. Kanaya, M. Kawabata, Y. Kawabata, M. Kawaguti, S. Kelner, P. Kent, A. Kimura, T. Kodama, R. Kokoulin, M. Kossov, H. Kurashige, E. Lamanna, T. Lampn, V. Lara, V. Lefebvre, F. Lei, M. Liendl, W. Lockman, F. Longo, S. Magni, M. Maire, E. Medernach, K. Minamimoto, P. M. de Freitas, Y. Morita, K. Murakami, M. Nagamatu, R. Nartallo, P. Nieminen, T. Nishimura, K. Ohtsubo, M. Okamura, S. O’Neale, Y. Oohata, K. Paech, J. Perl, A. Pfeiffer, M. Pia, F. Ranjard, A. Rybin, S. Sadilov, E. D. Salvo, G. Santin, T. Sasaki, N. Savvas, Y. Sawada, S. Scherer, S. Sei, V. Sirotenko, D. Smith, N. Starkov, H. Stoecker, J. Sulkimo, M. Takahata, S. Tanaka, E. Tcherniaev, E. S. Tehrani, M. Tropeano, P. Truscott, H. Uno, L. Urban, P. Urban, M. Verderi, A. Walkden, W. Wander, H. Weber, J. Wellisch, T. Wenaus, D. Williams, D. Wright, T. Yamada, H. Yoshida, and D. Zschesche, “Geant4 - a simulation toolkit,” *Nuclear Instruments and Methods in Physics Research Section A: Accelerators, Spectrometers, Detectors and Associated Equipment*, vol. 506, no. 3, pp. 250 – 303, 2003.
- [144] J. Apostolakis *et al.*, “GEANT4 Physics Lists for HEP,” in *Nucl. Sc. Symp. Conf. Rec. IEEE*, pp. 833–836, 2008.
- [145] O. Araoka *et al.*, “A tagged low-momentum kaon test-beam exposure with a 250L LAr TPC (J-PARC T32),” *J. Phys. Conf. Ser.*, vol. 308, p. 012008, 2011, 1105.5818.
- [146] W. H. Press *et al.*, *Numerical recipes in C (2nd ed.): the art of scientific computing*. New York, NY, USA: Cambridge University Press, 1992.
- [147] P. Hough, “Method and means for recognizing complex patterns.” U.S. Patent 3.069.654, 1962.
- [148] M. Thomson, “Particle flow calorimetry and the pandorapfa algorithm,” *Nuclear Instruments and Methods in Physics Research Section A: Accelerators, Spectrometers, Detectors and Associated Equipment*, vol. 611,

- no. 1, pp. 25 – 40, 2009.
- [149] M. Thomson, “LAr Event Reconstruction with the PANDORA Software Development Kit. Talk given at UK Liquid Argon meeting in Manchester on 28/11/12.” 2012.
- [150] P. Amaudruz *et al.*, “The T2K Fine-Grained Detectors,” *Nucl.Instrum.Meth.*, vol. A696, pp. 1–31, 2012, 1204.3666.
- [151] G. Foster and V. Kashikhin, “Superconducting superferric dipole magnet with cold iron core for the vlhc,” *Applied Superconductivity, IEEE Transactions on*, vol. 12, pp. 111–115, Mar 2002.
- [152] G. Foster, V. Kashikhin, M. McAshan, P. Mazur, H. Piekarz, J. Volk, and R. Walker, “Conductor design for the vlhc transmission line magnet,” in *Particle Accelerator Conference, 1999. Proceedings of the 1999*, vol. 1, pp. 182–184 vol.1, 1999.
- [153] D. Adey *et al.*, “nuSTORM - Neutrinos from STORed Muons: Proposal to the Fermilab PAC,” 2013, 1308.6822.
- [154] A. Devred, I. Backbier, D. Bessette, G. Bevillard, M. Gardner, M. Jewell, N. Mitchell, I. Pong, and A. Vostner, “Status of iter conductor development and production,” *Applied Superconductivity, IEEE Transactions on*, vol. 22, pp. 4804909–4804909, June 2012.
- [155] S. Agarwalla *et al.*, “The mass-hierarchy and CP-violation discovery reach of the LBNO long-baseline neutrino experiment,” 2013, 1312.6520.
- [156] M. Nessi, “The CENF neutrino facility,” tech. rep., CERN, 2013.
- [157] C. Andreopoulos, A. Bell, D. Bhattacharya, F. Cavanna, J. Dobson, *et al.*, “The GENIE Neutrino Monte Carlo Generator,” *Nucl.Instrum.Meth.*, vol. A614, pp. 87–104, 2010, 0905.2517.
- [158] M. Calviani, A. Ferrari, W. Kozłowska, E. Nowak, and P. Sala, “The CENF neutrino fluxes, note to be published,” tech. rep., CERN, 2014.
- [159] see Equation 2.2 for a definition of reconstructed energy
- [160] P. de Peiro, (Neutrino 2012 poster), <http://t2k.org/docs/poster/034>.
- [161] The actual function is $u(E) = 1.004 \cdot E^5 - 5.083 \cdot E^4 + 10.082 \cdot E^3 - 10.280 \cdot E^2 + 6.431 \cdot E - 0.016$ for $[E] = \text{kV/cm}$ and $[u] = \text{mm}/\mu\text{s}$
- [162] O_2 represents in this case any electronegative impurity, oxygen being a very common one.
- [163] COMSOL Multiphysics: <http://www.comsol.com>
- [164] Heinzinger PNC 100000. Heinzinger electronic GmbH, Rosenheim, Germany. <http://www.heinzinger.com>.
- [165] It was manufactured at ELTOS Circuiti Stampati Professionali, Italy (<http://www.eltos.com/>).
- [166] COMSOL Multiphysics software, <http://www.comsol.com>
- [167] although the wire holders are made out of POM for the mechanical mockup, FR4 is contemplated for the final design
- [168] <http://cds.cern.ch/record/1552862/files/ATLAS-TDR-020.pdf>
- [169] GTT (Gaztransport & Technigaz), www.gtt.fr
- [170] The product in use is *FLUKA Copper(II)oxide purum, 98.0% (RT); 61202* from Sigma-Aldrich Chemie GmbH

- [171] ACD CRYO, Gutenbergstrasse 1 CH-4142 Muenchenstein Switzerland, www.acdcryo.com
- [172] <http://root.cern.ch>
- [173] <http://root.cern.ch/drupal/content/vmc>
- [174] <http://geant4.cern.ch>
- [175] http://www.linde-engineering.com/en/plant_components/cryogenic_tanks/index.html